

NANO-IONIC RADIATION SENSOR: MATERIALS ENGINEERING,  
DEVICE DESIGN, AND TESTING

by

Mahesh Satyanarayana Ailavajhala

A dissertation

submitted in partial fulfillment

of the requirements for the degree of

Doctor of Philosophy in Electrical and Computer Engineering

Boise State University

May 2014

© 2014

Mahesh Satyanarayana Ailavajhala

ALL RIGHTS RESERVED

BOISE STATE UNIVERSITY GRADUATE COLLEGE

**DEFENSE COMMITTEE AND FINAL READING APPROVALS**

of the dissertation submitted by

Mahesh Satyanarayana Ailavajhala

Dissertation Title: Nano-Ionic Radiation Sensor: Materials Engineering, Device Design, and Testing

Date of Final Oral Examination: 13 March 2014

The following individuals read and discussed the dissertation submitted by student Mahesh Satyanarayana Ailavajhala, and they evaluated his presentation and response to questions during the final oral examination. They found that the student passed the final oral examination.

Maria I. Mitkova, Ph.D.	Chair, Supervisory Committee
Darryl Butt, Ph.D.	Member, Supervisory Committee
Dmitri Tenne, Ph.D.	Member, Supervisory Committee
Vishal Saxena, Ph.D.	Member, Supervisory Committee
Carlo G. Pantano, Ph.D.	External Examiner

The final reading approval of the dissertation was granted by Maria I. Mitkova, Ph.D., Chair of the Supervisory Committee. The dissertation was approved for the Graduate College by John R. Pelton, Ph.D., Dean of the Graduate College.

DEDICATION

To My Parents

and

Grand Father: Late Dr. Ailavajhala Satyanarayana Murthy

## ACKNOWLEDGEMENTS

I would like to thank my advisor, Dr. Maria Mitkova, for her guidance, patience, and continued encouragement throughout my time at Boise State University.

Dr. Mitkova's guidance was vital for my understanding of chalcogenide glasses, and amorphous material. The conversations with her always included fruitful advice about research, and life, and it is a great pleasure to be her student during my tenure.

I would also like to convey my gratitude towards my advisory committee, Dr. Darryl P. Butt, Dr. Dmitri A. Tenne, and Dr. Vishal Saxena, for their guidance as well as being on my advisory committee. I am thankful to Dr. Hugh Barnaby, and Dr. Michael Kozicki, who were co-Primary Investigators on the project, for the conversations that aided in the interpretation of the accrued results. I would like to acknowledge the innumerable support that Muhammad Rizwan Latif has provided to my work, through discussions, proof reading, and help with exchanging ideas/theories. I would like to thank Kasandra Wolf for exchanging ideas, and aiding me in performing certain experiments. My gratitude to Peter Miranda, and Idaho Microfabrication Laboratory, who aided my training in various characterization techniques in order to make these studies possible. A special thank you to the many people: Dr. Diana Nesheva, Ping Chen, Yago Gonzalez-Velo, Ivan Esqueda, Pradeep Dandamudi, David Olesky, Bhes Pun, Tyler Nichol, June Guo, and Brendan Connolly.

I want to thank my parents, Raghuram, and Padmaja Ailavajhala, and my sister, Ramyasri Ailavajhala, for their continued support, and encouragement. My family has made it possible to pursue this degree.

This research has been made possible with financial support from: Boise State University Department of Electrical and Computer Engineering, Department of Energy – Nuclear Engineering in University Program (DOE-NEUP), NASA EPSCOR, and Department of Defense – Defense Threat Reduction Agency (DOD-DTRA).

## ABSTRACT

For decades, various radiation-detecting materials have been extensively researched, to find a better material or mechanism. Recently, there has been a growing need for smaller, and more effective materials or devices that are Integrated Circuits (IC) compatible, and can perform similar functions as bulkier Geiger counters, and other measurement options, which fail the requirement for easy, cheap, and accurate radiation dose measurements. Here arises the use of thin films of chalcogenide glasses, which have unique properties of high thermal stability along with high sensitivity towards short wavelength radiation.

In this work, the effect of  $\gamma$ -rays, generated from a  $^{60}\text{Co}$  source, on the properties of thin films chalcogenide glasses was studied. Various film compositions from different germanium containing chalcogenide glass systems, i.e., Ge-S, Ge-Se, and Ge-Te, were investigated. These materials are the most thermally stable among the chalcogenide glasses, therefore they were studied to get a broad perspective of the development of structures, and the effect of chemical bonding under different radiation doses.

Study of the bare films provided an insight into the structural changes, and allowed the creation of different device designs, which take advantage of these changes. The bare film investigations were performed using Raman spectroscopy, and Energy Dispersive X-ray Spectroscopy (EDS). The result of these studies revealed that the destruction, and reorganization of the structure that occurred depends on the original

structure of the host material. Gamma radiation-induced new structural formation were discovered, and related to the film structural organization, and the chemical bonding within the specific films. Additionally, X-ray Photoelectron spectroscopy (XPS), and Atomic Force Microscopy (AFM) provided insight into the topological transformation associated with the underlying structural changes. Along with the bare films, radiation-induced silver diffusion was studied to understand the role, and effect of silver during a radiation event. The introduction of silver creates different silver containing products that aid or hinder the increase in the film conductivity. These silver containing films were investigated using X-ray diffraction, and elemental mapping to determine the silver containing products, crystal sizes, rate of silver diffusion, and the oxidation rate due to radiation dose. These results were discussed based on the particular structures of the glasses, and the existing models. This information was also used as inputs in order to model, and simulate the real time diffusion of silver using COMSOL multiphysics software. Combined, these results provided a partial view of the mechanisms contributing to the device performance.

After careful considerations of the various effects on the conductivity of the films, several device designs were fabricated, and their electrical performances are presented as a function of radiation dose. Three distinct generations of devices were created, each of which has offered a different methodology for amplifying the effects determined in the film analysis. Two generations of devices (Gen. 1, and Gen. 2) were fabricated using a laterally diffusing silver source while Gen. 3 devices were created with a specific structure where the vertical diffusion of silver contributed to changes in conductivity. The structure of the Gen. 2 devices was derived through electric field simulations, and then



was fabricated using conventional photolithography processes. The conductivity of the three types of devices was measured by performing current vs. voltage measurements after discrete doses, after all the dynamic effects had ceased. Some devices show greater than four orders of magnitude change in current from pre radiation to post irradiation. This is a substantial change, which can be detected using significantly lower voltages when compared to the current dosimeters, allowing these sensors to be used in low power or energy saving applications. Additionally, a special circuit has been designed, which allows the capability to detect these changes in current.

## TABLE OF CONTENTS

DEDICATION .....	iv
ACKNOWLEDGEMENTS .....	v
ABSTRACT .....	vii
LIST OF TABLES .....	xiv
LIST OF FIGURES .....	xvi
LIST OF ABBREVIATIONS .....	xxvii
INTERACTION OF MATTER WITH LIGHT .....	1
Wave Particle Duality .....	1
Radiation .....	2
The Origin of $\gamma$ -rays .....	4
Characteristic of Nuclear Decay .....	5
Sources of Gamma Radiation .....	6
Gamma Ray Interaction with Matter .....	7
Compton Effect .....	10
Photoelectric Effect .....	13
Pair Production .....	14
TYPES OF DETECTORS .....	16
Gas-Filled Detectors .....	16
Geiger-Müller Counter .....	18

Semiconductor Detectors .....	19
Ge Crystals.....	20
Cadmium Zinc Telluride (CZT).....	22
CHALCOGENIDE GLASSES, AND RADIATION-INDUCED EFFECTS .....	27
Basics of Glasses.....	27
Sub-Bandgap Light .....	35
Structural Changes .....	35
Optical Properties.....	39
Gamma Radiation .....	44
Structural Changes .....	44
Optical Properties.....	50
Chalcogenide Glasses as Dosimeters.....	52
Silver Containing Chalcogenide Glasses .....	57
Silver Diffusion Properties .....	57
Cluster Bypass Model.....	62
Diffusion Products .....	64
Germanium Containing Glasses .....	70
FILM CHARACTERIZATION METHODS .....	75
Methods of FILM ANALYSIS.....	75
Spectrophotometer .....	75
X-ray Photoelectron Spectroscopy (XPS) .....	76
Energy Dispersive X-ray Spectroscopy (EDS).....	76
Raman Spectroscopy.....	79

Atomic Force Microscopy (AFM) .....	80
X-ray Diffraction (XRD) .....	81
FILM ANALYSIS .....	83
Film Fabrication.....	83
Bare Films.....	83
Silver Covered Films .....	86
Results, and Discussion .....	89
Bare Film Results.....	89
Discussion.....	104
Silver-Containing Film Results.....	113
Discussion.....	119
Silver Diffusion Simulations.....	122
Conclusion .....	131
GENERATION 1 DEVICES .....	133
Device Fabrication .....	133
UV Characterization .....	137
Gamma Ray Characterization.....	139
Ge-S Based Devices.....	139
Ge-Se Based Devices.....	142
Ge-Te Based Devices.....	144
Conclusion .....	146
GENERATION 2 DEVICES .....	148
Simulation Inputs .....	149

Simulation Outputs .....	152
Simulation Results .....	153
Mask Design .....	158
Process Flow .....	164
Al Deposition .....	165
Ag, and ChG Deposition.....	166
UV Characterization .....	168
Gamma Ray Characterization.....	170
Conclusion .....	176
GENERATION 3 DEVICES .....	177
Device Fabrication.....	177
Results.....	178
Discussion.....	186
Simulations .....	192
Conclusion .....	193
RADIATION SENSING CIRCUITRY .....	196
Background, and Circuit Requirements.....	196
Circuit Design, and Simulations .....	197
Fabricated Sensor Topology .....	208
Conclusion .....	210
CONCLUSIONS.....	211
REFERENCES .....	216

## LIST OF TABLES

Table 1	Compounds, and types of materials suitable for radiation detection [9] ..	20
Table 2	Comparison between CdTe, and CZT (with 10% Zn) [14] .....	22
Table 3	Bond energies for common atomic bonds in Chalcogenide glasses [37] .	36
Table 4	Room temperature, and high temperature conductivities of Binary $Ag_2X$ ( $X = S, Se, \text{ or } Te$ ) .....	66
Table 5	Standardized settings for compositional analysis using EDS method .....	77
Table 6	Silver dissolution settings for various chalcogenide glass compositions .	87
Table 7	Coefficients for silver diffusion simulations.....	124
Table 8	Silver diffusion coefficients for Ge-Se, and Ge-Te films .....	131
Table 9	Circular geometry simulation results for various sizes, and dimensions.	154
Table 10	Square geometry simulation results for various sizes, and dimensions..	154
Table 11	Triangle geometry simulation results for various sizes, and dimensions. .....	155
Table 12	Triangle, and rectangle geometry simulation result for various sizes, and dimensions. ....	156
Table 13	Antenna geometry simulation results for various sizes, and dimensions. .....	157
Table 14	Four types of silver source geometries used in the mask design for device fabrication. ....	160
Table 15	Aluminum electrode, and Silver source spacing on the small device mask to fabricate devices with relatively small dimensions. ....	161
Table 16	Aluminum electrode, and Silver source spacing on the big device mask to fabricate devices with relatively large dimensions. ....	161

Table 17	Device sizes, and location on the large device masks: Antenna geometry (A), No antenna (NA), Circle (C), and Square (S). ....	164
Table 18	Silver diffusion simulations captured at various radiation doses.....	175
Table 19	Material Properties used for Silvaco device modeling .....	192

## LIST OF FIGURES

Figure 1	<sup>60</sup> Co decay scheme: The decay of a neutron-activated Co atom, resulting in the emission of gamma ray photons. ....	7
Figure 2	Relates the photon energy to the atomic number of the material, showing the regions where each type of effect is prevalent [3]. The material used in this study resides in the Compton dominant effect, but the same material can also experience photoelectric effect depending on the photon energy. 9	9
Figure 3	Collision between a Gamma Ray, and an atom resulting in the Compton Effect.....	11
Figure 4	Relationship between the photon's scattering angle versus the electron scattering angle shown for different incident photon energies. The energies range from 0MeV to 500MeV [3].....	12
Figure 5	Gamma Ray interaction with an atom resulting in the photoelectric effect. ....	14
Figure 6	Photon incident near a nucleus resulting in the production of an electron, and a positron. The nucleus of the atom that is originally located in a specific region represented by the black circle has been moved to its new location.....	15
Figure 7	Structure of the ionization chamber [5]. Gas filled scintillators have a chamber filled with gas with two electrodes (anode, and cathode), and an external sensing circuit. Radiation causes the formation of electrons, and positive ions which are collected by their respective electrodes, and sensed by the external circuit.....	17
Figure 8	Change in voltage pulse due to collection of electron, and positive ion [5]. The effect of a generated ion, and electron on a DC voltage pulse is illustrated. Influx of a greater number of radiation photons creates large number of ions, resulting in a large RC, which correlates to longer pulse decay time. ....	18
Figure 9	Depiction of the functionality of Ge crystal-based sensor. A p-type metal (high workfunction), and n-type metal (low workfunction) are placed onto a Ge-crystal, and biased to form a large electric field, which aids in	



	separating, and collecting generated electron-hole pairs at the respective electrodes. ....	21
Figure 10	CdTe-ZnTe phase diagram [15]. The formation of these crystals with different molar fractions of ZnTe is illustrated in this figure. Increasing the molar quantity of ZnTe increases the liquidation temperature, but the incorporation of Zn enhances the crystal characteristics as shown in Table 2.....	23
Figure 11	Pressure vs. Temperature curve for different compositions of CZT [17]. The large melting temperature for the formation of CZT crystals can be mitigated by increasing the pressure within the melt chamber, thus effectively reducing the required temperature. Effective crystals have been formed at 769 K as shown in the graph above.....	25
Figure 12	Pocket size CdZnTe detector [20] © 2005 IEEE.....	26
Figure 13	Temperature vs. Viscosity for formation of glasses. The material that will be used to form glasses is placed in an ampoule, and the temperature of the ampoule is increased in stage 1. Once the melting temperature ( $T_m$ ) of the material is achieved at stage 2, the viscosity of the material greatly increases. The molten melt is set to achieve a quenching temperature ( $T_Q$ ), which is followed by removing the molten material, and quenching in air or ice bath in step 4, transitioning into step 5 at the glass transition temperature ( $T_G$ ). At step 5, a glass is formed that has a higher viscosity than the original material. ....	28
Figure 14	DSC measurements for various $Ge_xSe_{1-x}$ , and $Si_xSe_{1-x}$ compositions showing the transition from floppy-intermediate-rigid structure [31]. The application of Differential Scanning Calorimetry expounded that in addition to the floppy, and rigid phases, there is a transition region, which is classified as the intermediate phase. ....	31
Figure 15	Raman shift of CS units versus Pressure for various $Ge_xSe_{1-x}$ [23]. Various compositions from the Ge-Se systems were studied using Raman spectroscopy, and close observation of location of CS peak on the Raman spectra revealed stressors within the glasses. Glasses classified as rigid or floppy have the highest internal stress. When the glass composition converges to the intermediate phase, the internal stress is minimal or nonexistent as illustrated in this figure. ....	32
Figure 16	Phase diagram of Ge containing chalcogenide glasses (a) Ge-S, (b) Ge-Se, and (c) Ge-Te [36]. ....	34
Figure 17	Two location for sulfur atoms within a sulfur chain a) cis and b) trans. ..	37

Figure 18	Orthorhombic sulfur rings $S_8$ a) side view and b) front view. ....	37
Figure 19	Hexagonal Selenium chains a) configuration of the chains and b) top view of the chains. ....	38
Figure 20	Tellurium chains a) configuration of the chains and b) top view of the chains. ....	38
Figure 21	Absorption edge of a-Selenium [48]. ....	40
Figure 22	Transmission of $As_2S_3$ film versus illumination time using a 514.5 nm light source [56]. With increased illumination, new defects are formed that change the previously transparent light to partially or completely absorbed (photodarkening effect).....	42
Figure 23	Photodarkening showing the maximum reversible shift in the absorption edge as a function of temperature [57]. After illuminating the glasses causing photodarkening effect within the glasses, this study shows that by heating the glasses to a temperatures near the glass transition temperature, the change in bandgap can be reversed.....	43
Figure 24	Possible structural changes in $As_2S_3$ glasses ( $\bigcirc$ As), and ( $\bullet$ S) [22, 66].	48
Figure 25	Bond-switching model depicting the change to the neighboring structure post destruction-polymerization transformation [22]. An As-S bond is broken due to radiation, and due to the vicinity of a neighboring arsenic atom, As-As bond is formed. This newly formed bond rotates this molecule to accommodate the localized charges on the arsenic, and sulfur atom.....	49
Figure 26	Bond-twisting model proposed by Tanaka in 1990 [68]. This model was presented by Tanaka, which reveals that an atom can transition between the cis to trans sites to satisfy localized charges. ....	50
Figure 27	Optical transmission spectra of $v-As_2S_3$ before (1), after 1Grad radiation dose (2), annealed at various temperatures 330K, 370K, 380K, 395K, 420K, and 440K, shown in curves 3-8, respectively [71]. The pre-irradiation spectrum reveals that $As_2S_3$ has 30% transmission at 600 nm, exposure to 1Grad. $^{60}Co$ gamma rays resulted in a shift of this absorption edge towards higher wavelengths. Post exposure annealing of the glasses at various temperatures gradually returned the glasses to the pre-irradiation absorption spectrum. ....	51
Figure 28	<i>In situ</i> measurement of $As_{40}Se_{48}Te_{12}$ glasses, irradiated with $\alpha$ -source [86]. These glasses were biased with a 500V, and 750V constant DC bias, and exposed to radiation, and shuttered from the radiation. The results show a	

	high sensitivity, and an instantenous change due to exposure to radiation © 2009 IEEE.....	53
Figure 29	Resistivity of $\text{AsS}_{3.5}\text{Te}_{2.0}$ measured at dark, a) 1.3 krad, b) 5.2 krad, c) 24 krad, d) 110 krad, and e) 240 krad [87]. The trend that is observed from this study reveals that increasing the gamma dose causes a decrease in the resistivity.....	54
Figure 30	a) $\text{AsS}_{3.5}\text{Te}_{2.0}$ exposed to 73.3 krad gamma dose and b) $\text{AsSe}_{1.5}\text{Te}_{1.5}$ 36.6 krad gamma dose [87]. There are three stages: low conductivity pre exposure, high conductivity during exposure, and exponential decay of conductivity post exposure. The low conductivity is attributed to the bare glass conductivity. The high conductivity region is attributed to the formation of dynamic, and static changes, which enhance the conductivity of the material. Post exposure exponential decay is due to the dissapearance of the dynamic changes. ....	55
Figure 31	Step-like diffusion profile of Ag in $\text{As}_{30}\text{S}_{70}$ [94]. Silver diffuses up to a certain distance at which distance there is an abrupt change in the silver concentration. This abrupt change is evident in the above graph for 80, and 100 mins of exposure. ....	57
Figure 32	Temperature, and light intensity effect on silver diffusion in $\text{As}_{30}\text{S}_{70}$ glasses [101].....	59
Figure 33	Photodiffusion, and thermal diffusion of silver in $\text{Ge}_{20}\text{Se}_{80}$ [104]. In comparison, photodiffusion introduces a greater amount of silver in a shorter time into the chalcogenide glasses than thermal diffusion. ....	59
Figure 34	Electric field enhanced lateral silver diffusion in Al modified $\text{As}_2\text{Se}_3$ glasses [95]. The two aluminum electrodes were biased at positive, and negative voltage biases while the Ag source was unbiased. There is an evident growth of a silver bridge between the Ag source, and the negatively biased Al electrode illustrated in the figure. ....	60
Figure 35	Post induction period in lateral diffusion of silver [95]......	61
Figure 36	Illustration of the cluster bypass model: areas with diagonal lines represent the chalcogenide glass network, and the regions specified as doped salt are pathways within the glasses where silver can diffuse [111]. ....	64
Figure 37	High resolution TEM of photodoped Ag in GeSe chalcogenide glass. Dark regions represent the clusters, and pathways are created where silver can diffuse throughout the glassy film [112]. ....	64

Figure 38	Change in conductivity as a function of silver concentration in Ge-S glasses [115]. These measurements reveal that with the addition of 5 at.% of Ag incurs a 6 orders of magnitude increase in the glass conductivity. 67
Figure 39	Change in conductivity as a function of silver concentration in Ge-Se glasses [117]. Various studies confirm the finding that 10 at.% of silver results in 7 orders of magnitude change in conductivity. .... 68
Figure 40	Change in sheet resistance due to silver photodiffusion [95]. Chalcogenide glasses with a topological layer of silver films were fabricated, which were used to measure the sheet resistance during the exposure to light sources with different intensities. Results reveal a similar behavior in sheet resistance once an equivalent radiation dose has been achieved with different illumination sources. .... 69
Figure 41	Basic structural unit: (a) Bonding between Ge, and Chalcogen atom and (b) Single tetrahedral unit. .... 72
Figure 42	Corner-Shared Tetrahedral..... 72
Figure 43	Edge-Shared Tetrahedral. .... 72
Figure 44	Ethane-like bonding..... 73
Figure 45	Layered rocksalt-type structure a) molecular structure, b) formation of layered structure due to the existence of dative bonds [118], and c) origin of the dative bonding [118]..... 73
Figure 46	Glass transition temperature for a) $As_xS_{1-x}$ [119], b) $Ge_xS_{1-x}$ , and $Ge_xSe_{1-x}$ [120]..... 74
Figure 47	Sample spectrum achieved using EDS for Ge-S films on Si/SiO <sub>2</sub> substrate. This spectrum reveals the presence of Ge, Si, and S as the prominent peaks along with the presence of C, N, and O <sub>2</sub> ..... 78
Figure 48	Semi-Knudsen cell structure. The chalcogenide glass material was placed into the crucible source, and covered with the crucible with extremely small openings, which have been exaggerated in the figure to present the concept. .... 85
Figure 49	Illustration of chalcogenide films with circular silver sources. Silver sources were evaporated onto the bare chalcogenide film surface using a circular mask with openings of 2 mm separated by 1 mm. .... 89

Figure 50	Analyzed absorption spectra of films exposed to various exposure times of UV light using the Tauc procedure for a) $\text{Ge}_{25}\text{Se}_{75}$ in air, b) $\text{Ge}_{25}\text{Se}_{75}$ in vacuum, c) $\text{Ge}_{40}\text{Se}_{60}$ in air, and d) $\text{Ge}_{40}\text{Se}_{60}$ in vacuum.....	90
Figure 51	Analysis of the absorption spectra exhibited the changes in the optical bandgap of the films measured in air, and under vacuum for a) $\text{Ge}_{25}\text{Se}_{75}$ and b) $\text{Ge}_{40}\text{Se}_{60}$ . .....	91
Figure 52	Fitted XPS spectra for Ge 3d, and S 2p core peaks in Ge-S films.....	93
Figure 53	Analysis of the XPS spectra illustrating the change in % composition of Ge-O as a function of radiation dose. ....	94
Figure 54	EDS study quantifying the amount of oxidation in bare films for: a) $\text{Ge}_{25}\text{Se}_{75}$ , and $\text{Ge}_{10}\text{Te}_{90}$ , and b) $\text{Ge}_{40}\text{Se}_{60}$ , and $\text{Ge}_{40}\text{Te}_{60}$ . ....	95
Figure 55	Fitted Raman spectra of virgin, and radiated Ge-S films for a) $\text{Ge}_{20}\text{S}_{80}$ , b) $\text{Ge}_{30}\text{S}_{70}$ , c) $\text{Ge}_{33}\text{S}_{67}$ , and d) $\text{Ge}_{40}\text{S}_{60}$ . ....	97
Figure 56	Dependence of the ES/CS Raman modes ratio for the studied films at different doses. ....	97
Figure 57	Fitted Raman spectra of virgin, and radiated Ge-Se films for a) $\text{Ge}_{20}\text{Se}_{80}$ , b) $\text{Ge}_{30}\text{Se}_{70}$ , and c) $\text{Ge}_{40}\text{Se}_{60}$ . ....	99
Figure 58	Ge-Se Analysis of Raman Spectra: a) ES/CS Area ratio comparison and b) Se-Se band for $\text{Ge}_x\text{Se}_{1-x}$ ( $x=20,30,40$ ). ....	100
Figure 59	Fitted Raman spectra of virgin, and radiated Ge-Te films for a) $\text{Ge}_{20}\text{Te}_{80}$ and b) $\text{Ge}_{50}\text{Te}_{50}$ . ....	101
Figure 60	Analysis of Raman spectra for Ge-Te system: a) ES/CS Area comparison and b) change in rocksalt structure. ....	102
Figure 61	AFM surface analysis of $\text{Ge}_{20}\text{Se}_{80}$ sample measured at a) Prerad $R_q = 0.59$ nm, b) 20 krad $R_q = 0.90$ nm, and c) 100 krad $R_q = 1.34$ nm.....	103
Figure 62	AFM surface roughness analysis for various composition in the a) Ge-S, b) Ge-Se, and c) Ge-Te systems. ....	103
Figure 63	Cartoon illustrating CS to ES transition as exhibited in Ge-rich samples. Adapted with permission from [125] © 2011 American Chemical Society. Each triangle is a representation of a tetrahedral unit, which is connected to its neighboring tetrahedral by a corner (CS) or edge (ES). ....	110

Figure 64	Raman spectra of Ag containing films, bare films, and the difference spectrum. The difference spectrum reveals the formation of different types of thiogermanate groups. .... 114
Figure 65	XRD pattern of the Ge-S films measured at different radiation doses. .. 115
Figure 66	XRD spectra measured at different radiation doses for a) Ge <sub>20</sub> Se <sub>80</sub> and b) Ge <sub>40</sub> Se <sub>60</sub> ..... 116
Figure 67	XRD patterns measured at different doses for a) Ge <sub>10</sub> Te <sub>90</sub> b) Ge <sub>40</sub> Te <sub>60</sub> . 117
Figure 68	Amount of Ag concentration as a function of radiation dose for Ge-S glass films. .... 118
Figure 69	Amount of Ag concentration incorporated into the chalcogenide film as a function of radiation dose in Ge-Se glass films. .... 118
Figure 70	Crystal size variation as a function of radiation dose for β-Ag <sub>2</sub> Se in Ge <sub>20</sub> Se <sub>80</sub> , and Ge <sub>40</sub> Se <sub>60</sub> films derived using the Debye-Scherrer equation for cubic crystals. .... 121
Figure 71	Silver diffusion observed using films with silver source exposed to UV light after a) 0 hrs, b) 2.5 hrs, c) 3.5 hrs, and d) 6.5 hrs [143]. .... 123
Figure 72	Geometry of the simulated model used to resemble the films with lateral silver sources..... 125
Figure 73	Result of the COMSOL simulation of silver diffusion, where red represents that highest silver concentration, and blue represents the lowest silver concentration after a) 0hrs, b) 2.5hrs, c) 3.5 hrs, and d) 6.5 hrs. .. 125
Figure 74	Cut line concentration profile between two diagonal silver sources plotted at corresponding times to the observed images, and using the diffusion coefficient for 5.5x10 <sup>-11</sup> m <sup>2</sup> /sec..... 126
Figure 75	Measured silver diffusion using EDS for a) Ge <sub>20</sub> Se <sub>80</sub> and b) Ge <sub>40</sub> Se <sub>60</sub> . The measurement was performed from one silver source to another. Silver concentration is the highest in regions where silver has diffused, and regions that represent 0 Ag counts are the undoped chalcogenide film. 128
Figure 76	Taking the results from the EDS measurements (shown in Figure 77), silver diffusion distances have been calculated for a) floppy, and b) rigid films. .... 129

Figure 77	Experimental (black), and simulated (red) results of silver diffusion distance as a function of radiation dose for a) $\text{Ge}_{20}\text{Se}_{80}$ , b) $\text{Ge}_{40}\text{Se}_{60}$ , c) $\text{Ge}_{20}\text{Te}_{80}$ , and d) $\text{Ge}_{50}\text{Te}_{50}$ . .....	130
Figure 78	Shadow mask used for making Gen. 1 devices. Black circles represent openings that have been blocked, preventing the deposition of metals in this region. The deposition of metal is restricted to the areas represented by white circles. ....	133
Figure 79	Microscope image of one of the sputtered tungsten electrode, which exhibited the lack of adhesion between the electrode, and chalcogenide film. This buckling phenomenon is attributed to the large size of the W atom in comparison to the atoms in the chalcogenide film. ....	135
Figure 80	Crucible used for Al evaporation with the application of two wire thickness.....	136
Figure 81	Resistance-Voltage device characteristics under UV exposure for a) $\text{Ge}_{20}\text{Se}_{80}$ , b) $\text{Ge}_{30}\text{Se}_{70}$ , and c) $\text{Ge}_{40}\text{Se}_{60}$ .The black spectra (prior to UV exposure), red spectra (post UV exposure), and blue spectra (after device reset).....	138
Figure 82	Gamma ray device testing results for a) $\text{Ge}_{34.7}\text{S}_{65.3}$ and b) $\text{Ge}_{45.5}\text{S}_{54.6}$ . ....	139
Figure 83	Post fabrication of Ge-S Gen. 1 devices prior to process optimization. .	140
Figure 84	Optimized Gen. 1 devices post fabrication. ....	141
Figure 85	Current vs. Voltage characteristics for $\text{Ge}_{33}\text{S}_{67}$ devices after optimization. ....	142
Figure 86	Device testing results for a) $\text{Ge}_{20}\text{Se}_{80}$ , b) $\text{Ge}_{30}\text{Se}_{70}$ , and c) $\text{Ge}_{40}\text{Se}_{60}$ . ....	143
Figure 87	Device testing results for a) $\text{Ge}_{20}\text{Te}_{80}$ and b) $\text{Ge}_{50}\text{Te}_{50}$ . ....	145
Figure 88	Wire bonded Gen. 1 device final product a) Measurement scheme for testing, and identifying devices, b) Final DIP packaged $\text{Ge}_{40}\text{Se}_{60}$ devices, and c) Final DIP packaged $\text{Ge}_{20}\text{Se}_{80}$ devices.....	147
Figure 89	Comsol simulation of the distribution of electric field during the measurement for the Gen. 1 devices. ....	148
Figure 90	Electric field distribution, when silver electrodes biased at 0V instead of a floating voltage in Gen. 1 devices.....	150
Figure 91	Mask for creating Al electrodes for small devices.....	161

Figure 92	Mask for creating Ag electrodes for small devices.....	162
Figure 93	Mask for depositing chalcogenide films for small devices.....	162
Figure 94	Mask for creating Al electrodes for large devices. ....	162
Figure 95	Mask for creating Ag electrodes for large devices. ....	163
Figure 96	Mask for depositing Chalcogenide films for small devices.....	163
Figure 97	Gen 2. device fabrication process flow.....	167
Figure 98	Microscope image of Gen. 2 devices post fabrication.....	168
Figure 99	Reset procedure using a probe station to return the diffused silver to the silver source, and reuse the sensor.....	169
Figure 100	Current vs. Voltage plot for UV irradiated Gen. 2 device Prerad (black), 5 min rad (red), and post reset (green) characteristics. ....	169
Figure 101	Radiation dose vs. current characteristics for a) $\text{Ge}_{20}\text{Se}_{80}$ , b) $\text{Ge}_{40}\text{Se}_{60}$ , c) $\text{Ge}_{20}\text{Te}_{80}$ , and d) $\text{Ge}_{50}\text{Te}_{50}$ .....	170
Figure 102	Geometry of the simulated device to study the silver diffusion using COMSOL multiphysics software.....	173
Figure 103	Simulated Silver diffusion compared to the change in conductivity of the Gen. 2 devices as a function of radiation dose. The blue graph corresponds to the normalized silver concentration, and the black graph represents the change in conductivity of the device at discrete radiation doses.....	174
Figure 104	Final product of the wire bonded Gen. 2 devices. ....	176
Figure 105	Gen. 3 device cross section with film labels, and corresponding thicknesses. ....	178
Figure 106	Fitted Raman spectra of films at various radiation doses. ....	179
Figure 107	Analysis of the Raman spectra a) ES/CS Area ratio and b) ETH Area change .....	180
Figure 108	XRD pattern revealing the formation of various silver phases at different radiation dose exposures. ....	181
Figure 109	SEM surface images at various radiation doses a) 1.58 Mrad, b) 3.19 Mrad, c) 7.59 Mrad, and d) 14.82 Mrad. The clusters on the surface	



	correspond to silver surface deposition due to radiation-induced silver diffusion. ....	182
Figure 110	SEM analysis of the silver clusters on the film surface; the black graph corresponds to the mean radius of the clusters, and the blue graph represents the number of deposits per unit area. ....	182
Figure 111	AFM analysis of the surface of the films representing the film surface roughness (black), and the height of the silver clusters (blue). ....	183
Figure 112	EDS analysis confirming the oxidation in the studied system. Inset shows the development of the oxygen concentration with radiation dose. ....	184
Figure 113	UV characterization of Gen. 3 devices measured at different exposure times. ....	185
Figure 114	a) Current vs. Radiation dose measurements illustrating the development of the current and b) Current vs. Voltage curves of one of the radiated devices, measured at discrete radiation doses. ....	186
Figure 115	<i>In situ</i> measurement of current vs illumination time of Gen. 3 devices in vacuum, and in ambient using a UV light source. ....	191
Figure 116	a) Magnitude of impedance vs. frequency, and b) Phase of impedance vs. frequency for analytical model ( $Z_{mod}$ , $\theta_{mod}$ ), device simulations ( $Z_{sim}$ ; $\theta_{sim}$ ), and experimental data ( $Z_{dat}$ ; $\theta_{dat}$ ) for prerad impedance characteristics of one of the investigated devices. ....	193
Figure 117	Final product of the wire bonded Gen. 3 device. ....	195
Figure 118	Large voltage external sensing differentiating circuit [154]. ....	197
Figure 119	Device measurement setup using a semiconductor parameter analyzer. ....	198
Figure 120	Analogous circuit element substitution for radiation sensor. ....	198
Figure 121	Circuit schemes for a) charging, and b) discharging a capacitor. ....	200
Figure 122	Circuit concept design for measuring low currents. ....	201
Figure 123	Voltage reference Circuit block. ....	204
Figure 124	Radiation Sensing Circuit block. ....	204
Figure 125	Buffer Circuit block. ....	204

Figure 126	Output pass gates Circuit block .....	205
Figure 127	Top view of all circuit blocks, and their corresponding connections .....	205
Figure 128	Simulation results for (a) $I_{input}=33pA$ , (b) $I_{input}=250pA$ , (c) $I_{input}=250pA$ with $t_{low}$ closed, (d) $I_{input}=700pA$ with $t_{low}$ closed, (e) $I_{input}=700pA$ with $t_{low}$ , and $t_s$ closed, and (f) $I_{input}=920pA$ with $t_{low}$ , and $t_s$ closed .....	206
Figure 129	Concept of the cross section of final fabricated device. ....	208
Figure 130	Electron beam simulations validating the circuit topology using Casino Monte Carlo simulator. ....	209

## LIST OF ABBREVIATIONS

BSU	Boise State University
GC	Graduate College
TDC	Thesis, and Dissertation Coordinator
GM	Geiger-Müller counters
ChG	Chalcogenide Glass
DSC	Differential Scanning Calorimetry
T <sub>g</sub>	Glass Transition Temperature
EDS	Energy Dispersive X-ray Spectroscopy
XRD	X-ray Diffraction
XPS	X-ray Photoelectron Spectroscopy
AFM	Atomic Force Microscopy

## INTERACTION OF MATTER WITH LIGHT

Understanding the effects of electromagnetic radiation requires a brief introduction into electromagnetic waves, and photons. Albert Einstein described the dual nature of light, as containing wave, and particle characteristics. Light can diffract, and interfere with other light sources similar to electromagnetic waves. On the other hand, light can have similar properties that are possessed by particles. Particles obey the law of conservation of energy, which means that when a particle interacts with a material, the particle can transfer all or some of the initial energy to the material; similarly, light follows the same law.

### **Wave Particle Duality**

Max Plank stated in the early 1900s the relationship between the frequency of a radiation to the energy possessed by the radiation quanta [1]. In 1924, de Broglie confirmed the existence of the wave-particle duality that stated that the momentum of a photon is inversely proportional to the wavelength, which combined with the Plank's relationship gives rise to the equation that can be used to calculate the energy of a photon [1]. The wave particle duality, equation 1, states that the frequency ( $\nu$ ) of the light is proportional to the energy ( $E$ ) of the photon, and is inversely proportional to the wavelength ( $\lambda$ ) [1].

$$E = h * \nu = \frac{(h*c)}{\lambda} \quad (1)$$

From this equation, Planck's constant ( $h$ ), and speed of light ( $c$ ) are both constants that do not vary, therefore as wavelength ( $\lambda$ ) increases, the energy of the photon ( $E$ ) decreases, and vice versa. For example, a photon with a wavelength of  $100\ \mu\text{m}$  has energy of  $1.989 \times 10^{-21}\ \text{J}$ , which is significantly less than that of a photon with a wavelength of  $100\ \text{nm}$  with  $1.989 \times 10^{-18}\ \text{J}$  of energy. Interaction of a photon with a material can be quantified using this equation.

### **Radiation**

A source of radiation is classified as ionizing radiation if the energy is sufficient to remove at least the valence electron of an atom thereby ionizing the atom. The radiation source must contain energy greater than 4-25 eV to be considered as ionizing radiation [2]. Ionizing radiation is segmented into two parts, and depend on whether the radiation source consists of charged or uncharged particles [2]. The first type of radiation, known as directly ionizing radiation, consists of the interaction of charged particles with matter. The second type radiation is called indirectly ionizing radiation sources where uncharged particles or photons interact with the material.

In the case of directly ionized radiation, the radiation source, which is a charged particle, interacts with material through columbic interactions. A cumulative amount of columbic interactions will result in ionizing of an atom. For example, when electrons interact with a material, the incident electrons can interact with other electrons in the material that are in their path through columbic interactions. This interaction can ionize an atom if, and only if the energy of the incident electron has sufficient energy to ionize an atom within the material, i.e. the energy transferred to the bonded electrons is greater than binding energy. Another type of interaction between electrons, and materials is

through direct interaction by which energy transfer occurs, such as when an electron collides with a bonded electron, and transfers some or all of its energy to the stationary electron. A few types of directly ionized radiation are fast moving electrons, ions,  $\alpha$ , and  $\beta$  particles [2, 3]. In some situations, the result of the interaction between the charged particle, and the material could result in the creation of another indirectly ionized radiation. This is the case for the generation of x-rays through the Bremsstrahlung process [2].

The second type of radiation is known as indirectly ionized radiation where neutrally charged particles such as x, and  $\gamma$  rays, and neutrons interact with material [2]. In this case, the radiation source will transfer energy to a bonded electron. For example, photons are absorbed by bonded electrons, the effect of this absorption results in the energy transfer from the photon to electron. This type of radiation has a larger range of incident energies compared to directly ionized radiation, therefore these particles can penetrate deeper, and have a larger effect on the material [2]. Similar to where directly ionizing radiation can generate indirectly ionizing radiation, indirectly ionized radiation can also result in the production of Directly Ionized radiation. For example, when a photon with gamma ray characteristics interacts with an electron, it will transfer its energy to the electron, this causes the previously stationary electron to become excited, and scatter throughout the material creating other interactions characteristic to Directly Ionizing radiation. The result of most Indirectly Ionized Radiation is a highly excited electron, which can participate in Directly Ionized radiation.

The effects of these two types of radiation are significantly different, so it is necessary to compare one type of radiation to another. Exposure dose is the term that

compares different types of radiation. The dose is determined by the amount of energy deposited into a volume of material with a specific density thus arriving at the units J/kg. The factors that determine the dose are distance from the source, exposure time, dose rate, and density of the exposed material. There are two methods for achieving higher radiation doses, either by increasing the exposure time or by reducing the distance from the radiation source. Radiation dose is measured in various different units besides J/kg such as ergs, Gry, and rad. Conversions between these types of units are:  $1\text{J/kg} = 10^4\text{ erg/g} = 1\text{Gry} = 10^2\text{ rad}$ . To avoid confusion, the unit rad will be used in this dissertation as a standard unit of dose for gamma radiation, and  $\text{J/cm}^2$  for ultraviolet radiation.

### **The Origin of $\gamma$ -rays**

When a nucleus is in an excited state, the nucleus will decay to a stable state. This decay can happen by the emission of  $\alpha$ ,  $\beta$  or nucleus reaction, which will result in the emission of  $\gamma$ -rays. The  $\alpha$ -particles are the easiest detectable of these radiation types, which can consist of either a proton, and a neutron  $H_1^+$ ,  $H_2^+$  or 2 protons, and 2 neutrons, or  $He_4^{++}$  [4]. Alpha particles can be easily stopped or deterred with the application of an electric field, which is due to the size of the particle, and the assigned charge. Therefore, alpha particles do not have a large depth of penetration within material when compared with  $\beta$ -particles, and  $\gamma$ -rays. Compared to  $\alpha$ -particles, “ $\beta$ -particles requires roughly 1000 times as much matter to bring to rest” [4]. These types of particles are either positively charged or negatively charged, and have properties similar to fast moving electrons. Similar to electrons,  $\beta$ -particles are easily deflected by an applied electric, and magnetic fields. Due to the size of these particles, they penetrate deep into any material, and create collisions within the depth of the material. The third type of particles are called  $\gamma$ -rays,

and these rays are the most harmful because of their depth of penetration, and the resistance towards deflections from electric or magnetic fields. This type of radiation is considered as a high energy photons classified as electromagnetic waves such as radio waves, microwaves, and ultraviolet waves. Energy of these photons ranges from “few kilo electron volts to few Mega electron volts” [4].

### Characteristic of Nuclear Decay

The process of nuclear decay of a radioactive material “does not depend on the state of chemical combination, the temperature, pressure or the presence of other atoms or nuclei” [4]. It is difficult to predict when a specific nucleus will decay but the collective decay rate of the material can be predicted by calculating the half-life of the material. This equation can be derived by understanding that the decay is a first order reaction. It can be shown that if  $N$  is the number of nuclei within a specific material, then the rate of decay can be stated as  $\frac{dN}{dt}$ , and using a constant  $\lambda$  the following equation can be written to express the decay rate.

$$-\frac{dN}{dt} = \lambda N \quad (2)$$

$$\int -\frac{dN}{dt} * \frac{1}{N} * dt = \lambda \int dt \quad (3)$$

$$-\ln(N) = \lambda t + C \quad (4)$$

At time  $t=0$ , the number of nuclei within the material is going to be  $N_0$ , and using this fact, the value for  $C$  (integration constant) can be calculated.

$$-\ln(N_0) = C \quad (5)$$

The following equation is derived through substituting the value of  $C$  into equation 4.



$$-\ln ( N ) = \lambda t - \ln(N_0) \quad (6)$$

$$-\ln \left( \frac{N}{N_0} \right) = \lambda t \quad (7)$$

$$\frac{N}{N_0} = e^{-\lambda t} \quad (8)$$

In this manner, the number of remaining nuclei can be calculated if the initial number of nucleus  $N_0$ , and the decay constant  $\lambda$  are given for any material.

$$\frac{N}{N_0} = \frac{1}{2} = e^{-\lambda t_{1/2}} \quad (9)$$

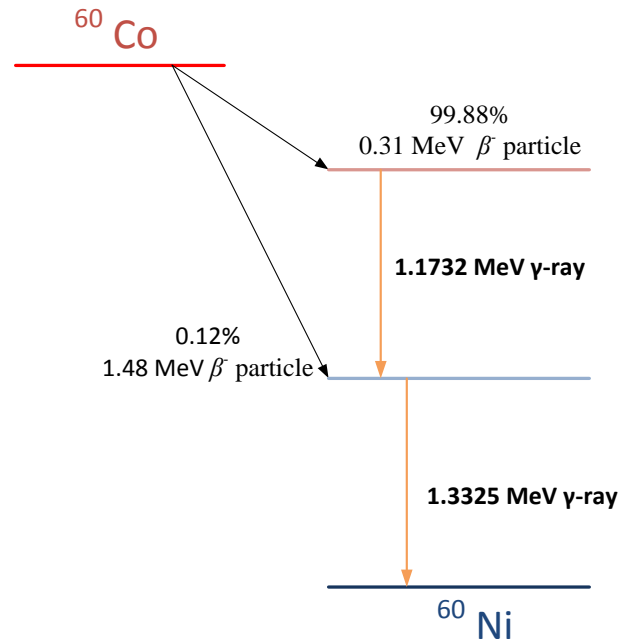
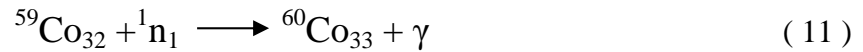
$$t_{1/2} = \frac{\ln(2)}{\lambda} = \frac{0.6931}{\lambda} \quad (10)$$

In the above equation,  $t_{1/2}$  is called the half-life of the nuclear species, which is defined as the time required for half of the unstable nuclei to decay [5]. Materials with short half-life are considered highly unstable when compared to material with long half-life.

### Sources of Gamma Radiation

One manner of generating  $\gamma$ -rays is through artificial neutron activation of a stable atom. This process is performed by forcing a neutron into the nucleus of an atom thus making the atom unstable [6]. An isotope of Cobalt -  $^{60}\text{Co}$  is generated in this manner. Elemental Cobalt has 59 protons, and neutrons, but if a neutron is forced into the nucleus causing the creation of a  $^{60}\text{Co}$ , the added neutron transfers the energy to the nucleus [6]. This reaction “increases the energy of the nucleus by 7.5MeV,” which is an excited state, and this atom cannot stay at this level [6]. The excess energy imparted to the nucleus is removed by emitting a  $\beta$ - particle, and a  $\gamma$ -ray photon from the nucleus. To balance this

extra energy, the atom will emit several gamma rays until the atom decays to its ground state. Gamma ray energies can range from 2.6 keV to 7.1 MeV ( $^{16}\text{N}$ ) [2].



**Figure 1**  ${}^{60}\text{Co}$  decay scheme: The decay of a neutron-activated Co atom, resulting in the emission of gamma ray photons.

From the figure above,  ${}^{60}\text{Co}$  decays to two levels emitting two distinct photons depending on the energy of the  $\beta$ -particle. When  ${}^{60}\text{Co}$  decays to  ${}^{60}\text{Ni}$ , 99.88% of the time, the  ${}^{60}\text{Co}$  emits 0.31 MeV  $\beta$  particles that results in the generation of a 1.1732 MeV  $\gamma$ -ray followed by another gamma ray with 1.3325 MeV energy. With 0.12% of the time, a 1.1732 MeV gamma ray is bypassed, and only a 1.3325 MeV photon is emitted in addition to a 1.48 MeV  $\beta$  particle.

### Gamma Ray Interaction with Matter

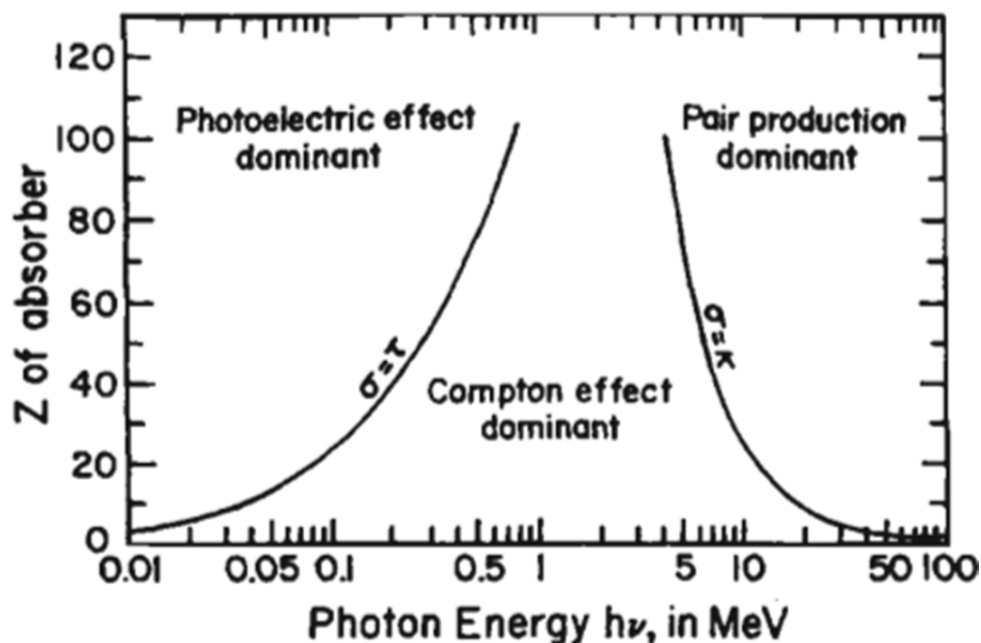
In this section, the discussion will focus more on the behavior of gamma rays after the interaction with material. There are two outcomes when gamma rays interact

with a material, gamma ray can diminish after interaction with a bonding site within the material or the energy of the gamma ray is attenuated, which then interacts with another bonding site. Whether the gamma ray diminishes or becomes attenuated is determined by the energy of the photon, and the type of interaction. Interactions between gamma rays, and material can be simply thought of as a transfer of energy between two masses. The following list describes the different types of effects that could occur [7].

1. Compton effect
2. Photoelectric effect
3. Pair production
4. Rayleigh Scattering
5. Photonuclear interactions

From this list of possible effects, the Compton Effect, Photoelectric effect, and Pair productions are the main types of outcomes that affect the atomic structure. These three types of effects defer on the quantum energy of the photon, energy transferred to an electron, and the neighboring conditions. Each of these three circumstances determines the type of interaction between a photon, and electron. In the case of the two other types of effects, a photon becomes redirected without the loss of energy known as photonuclear interactions [7]. The outcome of a Rayleigh scattering is an elastic scattering, which leaves the photon at a similar energy level but does not affect the atoms except to leave the nucleus at an excited state [4].

The three main types of effects are dominant in different energy ranges for different sized atoms. Figure 2 summarizes where a certain type of interaction is prevalent.



**Figure 2** Relates the photon energy to the atomic number of the material, showing the regions where each type of effect is prevalent [3]. The material used in this study resides in the Compton dominant effect, but the same material can also experience photoelectric effect depending on the photon energy.

The photon energy that corresponds to a specific effect changes as a function of the atomic number ( $Z$ ) of the material. These effects are dominant in the specific regions due to the energy of the photon, but other effects can also occur in these regions with the exception of pair production. Pair production requires a threshold energy of the photon. For this reason, pair production is only plausible at higher photon energies. In the case of the Compton Effect, the remnants of the original photon can create other types of interactions in a chain until the photon is diminished. In all three cases, if the photon is diminished or less energetic than its original state, the result of the interaction causes an electron to become ejected from an atom.

When the electron is ejected, it is also possible that another photon can be created. If gamma rays remove a bonded electron situated closer to the nucleus, when compared

to the electrons in the valence shell, then at least one X-ray is generated. For example, if an electron located in the K-shell is ejected from the bonding site, and there are electrons occupying the L, and M shells, which are located farther from the nucleus than the K-shell electrons. Then one electron will drop from the L-shell to occupy the newly vacated spot in the K-shell, and coincidentally an electron from M-shell will drop into the L-shell. In this manner, two characteristic X-rays are generated from the electron shifting into locations in the K, and L shells [5]. In the scope of this research, this type of interaction can be considered as minimal or non-existent.

When considering the interaction between energetic photons, such as  $\gamma$ -rays, with electrons, it is insufficient to only consider the loosely bound valence electrons. The bond energies between atoms is significantly less than the photon energy, therefore any electron within the material can interact with the photon, and can be freed from the atom. Hence, it is more appropriate to consider the interaction between a photon, and a free electron at rest, which can be determined by the following equation.

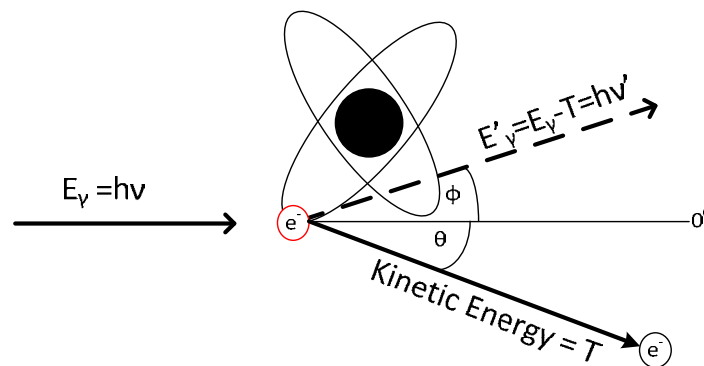
$$E_{electron\ at\ rest} = m_0 c^2 = (0.91095 \times 10^{-30} \text{ kg}) * (2.9979 \times 10^8 \text{ ms}^{-1})^2 = 0.511 \text{ MeV} \quad (12)$$

The photons generated by  $^{60}\text{Co}$  have energies of 1.1732 MeV, and 1.3325 MeV, which is significantly greater than the energy of an electron at rest shown in the previous equation.

### Compton Effect

The Compton Effect states that when a photon interaction with an electron, then the photon transfers some but not all of its energy to an electron, and after the interaction a remnant of the original photon remains. This type of energy transfer only occurs when

the photon energy is greater than the energy binding the electron to the atom, resulting in a less energetic photon, and a freed electron. Compton Effect occurs at energies higher than the required energy for photoelectric effect but lower than the required energy for pair production. A real world example of the Compton Effect is the “billiard ball” example, which shows the incident ball transfers some of its kinetic energy to the stationary target, but the incident ball contains more energy than that is required to move the stationary ball, and thus both ball travel at different directions after the collision [1]. The angle that both of the balls travel is the same because the two objects have a similar mass, but when considering a photon, and an electron, the two masses need to be taken into consideration. Therefore, the photon angle, and the electron angle are completely different. Obeying the law of conservation of momentum, remnant photon energy scatters at an angle ( $\Phi$ ), while the electron scatters at a different angle ( $\theta$ ), as shown in Figure 3.



**Figure 3** Collision between a Gamma Ray, and an atom resulting in the Compton Effect.

From the Law of Conservation of Energy, and Law of Conservation of Momentum, it is known that the incident energy has to equal the resultant energy.

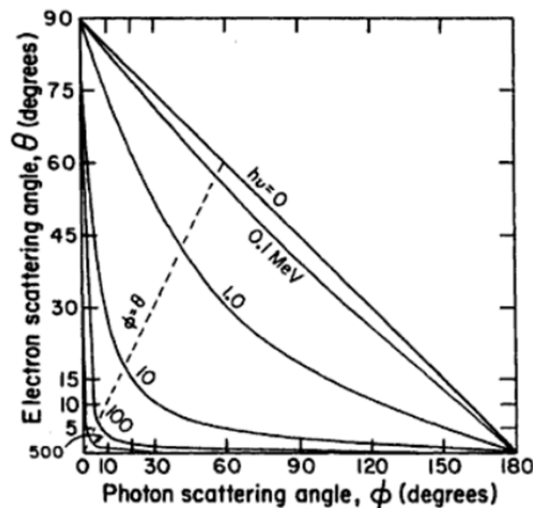
$$E = h\nu = h\nu' + T \quad (13)$$

In the above equation, energy of the incident photon ( $E$ ) is equal to the energy of the resultant photon ( $h\nu'$ ) plus the kinetic energy of the electron ( $T$ ). Converting every segment into momentum is valid since the momentum cannot be created or destroyed according to the law of conservation of momentum.

$$\frac{h\nu}{c} = \frac{h\nu'}{c} \cos \phi + \rho \cos \theta \quad (14)$$

$$E = \frac{h\nu}{c} = \frac{h\nu'}{c} \cos \phi + mv \cos \theta \quad (15)$$

Equation 14 is a manipulation of equation 13 where the kinetic energy term has been replaced with its equivalent momentum term, and equation 15 is the simplest form to calculate the deflection angles of the electron, and the photon [2]. Various deflection angles, and energies were calculated, and are shown below in Figure 4.



**Figure 4** Relationship between the photon's scattering angle versus the electron scattering angle shown for different incident photon energies. The energies range from 0MeV to 500MeV [3].

The amount of energy transferred to the electron is proportional to the angle of the incident photon with respect to the electron. "The greatest energy transferred to the electron occurs when the electron is ejected forward, and the photon is scattered

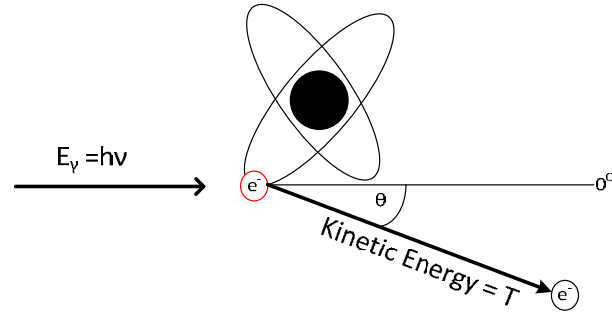
backward” [6]. “The lowest amount of energy transferred to the electron is when the electron is ejected at 90° while the photon does not change its direction” [6]. Since  $^{60}\text{Co}$  emits two photons of 1.17, and 1.33MeV, maximum energy transferred to the electron through Compton Effect can be calculated using equation 16.

$$E_{electron,max} = E_{\gamma} - \frac{m_0c^2}{2} = 1.3325 \text{ MeV} - \frac{0.255 \text{ MeV}}{2} = 1.205 \text{ MeV} \quad (16)$$

### Photoelectric Effect

In 1887, Hertz discovered a phenomenon, where a light photon can liberate a bounded electron from a metal causing a current flow in the metal. This phenomenon is known as the Photoelectric Effect, which occurs when a photon completely transfers the energy to an electron. Unlike in the case of Compton Effect, the photon completely transfers its energy to the electron, thus resulting in a free electron or an electron that is at a higher energy state, and the photon energy is exhausted. This effect is dominant for photon energies less than 0.511MeV [2]. When the energy of the photon is less than the binding energy, the electron absorbs the entire photon, and rises to a higher energy level. A combination of multiple photons adding together can free the electron. The other case that occurs in the photoelectric effect is evident when the photon energy is as large as the binding energy or slightly greater. The photon disappears after the interaction because the entire photon energy is transferred to the electron, causing the electron to become unbounded, and the remnant energy, which is a very small amount, is transferred to the atom. The recoiled atom has negligible kinetic energy but the momentum is not trivial.





**Figure 5** Gamma Ray interaction with an atom resulting in the photoelectric effect.

### Pair Production

This type of interaction occurs when the gamma ray passes in proximity to the nucleus of an atom, where there is a Coulombic field, which causes the atom to eject an electron, and a positron from the atom in addition to changing the location of the nucleus. Incident photon disappears because of this reaction, and the energy is transferred to the electron, and positron. Another type of pair production occurs when the interaction of photon energy, and material results in the production of two electrons, and a positron [2]. This process is called Triplet production, and only occurs when the incident photon energy is greater than the required energy for pair production [2]. Pair Production can only happen if the “minimum photon energy is at least  $2m_0c^2 = 1.022 \text{ MeV}$ ” [2]. The resultant positron can combine with another electron generating two gamma rays with 0.511 MeV of energy. This energy is less than the energy required for another Pair Production reaction, but it is sufficient for a Compton Effect, and/or Photoelectric Effect. To calculate the required photon energy for pair production is shown using the following equations.

$$E_{\text{photon},\text{min}} = h\nu = 2m_0c^2 + T^+ + T^- \quad (17)$$

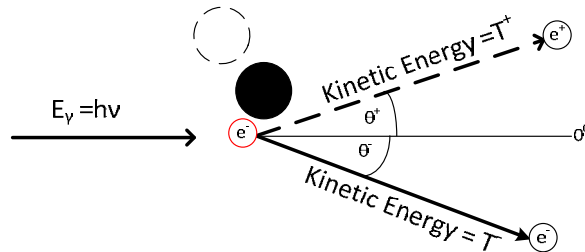
$$E_{\text{photon},\text{min}} = 1.022\text{MeV} + T^+ + T^- \quad (18)$$

Equations 17, and 18 pertain to calculating the required photon energy in pair production. From the two equations, the photon energy depends on the kinetic energy (T) of the particles. According to conservation of energy, the kinetic energy of the two particles as well as the energy required to overcome the Columbic force that binds the electron to the atom must be equal to the photon energy. An assumption can be made that equal energy is transferred to the electron, and positron. The values for  $T^+$ , and  $T^-$  can be estimated using equation 20.

$$T^{+,-} = \frac{h\nu - 1.022 \text{ MeV}}{2} \quad (19)$$

$$T_{60\text{Co},\text{max}}^{+,-} = \frac{1.33 \text{ MeV} - 1.022 \text{ MeV}}{2} = 156 \text{ keV} \quad (20)$$

Triplet production on the other hand is similar to the same equations as the pair production but with the addition of another term for the kinetic energy of the extra electron.



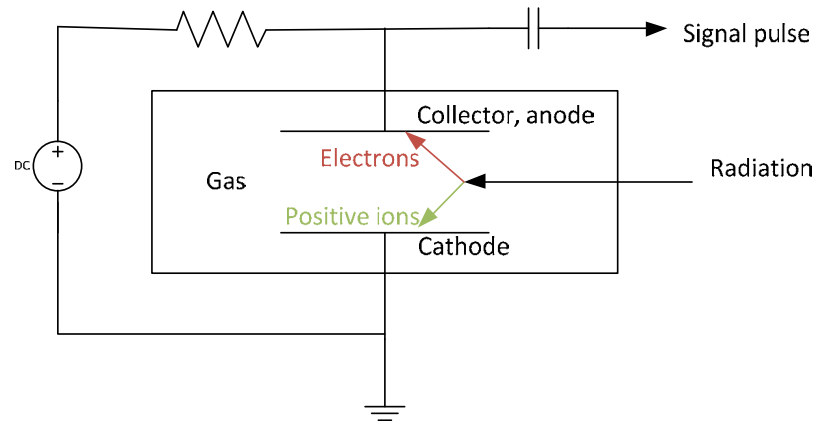
**Figure 6** Photon incident near a nucleus resulting in the production of an electron, and a positron. The nucleus of the atom that is originally located in a specific region represented by the black circle has been moved to its new location.

## TYPES OF DETECTORS

There are different methods to measure radiation exposure, which can be either differentiated by the type of radiation or the mechanisms that govern the performance of the detector. A majority of the detectors work under the properties of ionization where the radiation ionizes a material, and the generated charged particles are used to measure the exposure. “Ionization chambers, proportional counters, Geiger-Müller counters, semiconductor radiation detectors, cloud chambers, and spark chambers” are types of detectors that detect charge particle generation [8]. Of these types of detectors, Ionization chambers, proportional counters, and Geiger-Müller counters are the oldest, and these detectors are still used.

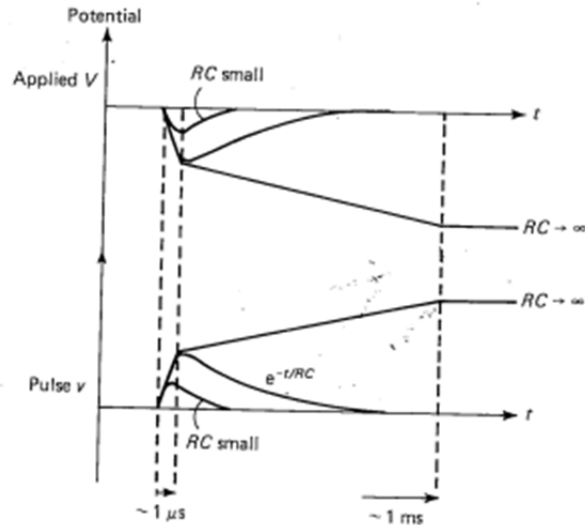
### **Gas-Filled Detectors**

This type of detector consists of a chamber containing two electrodes is filled with a specific gas. When radiation is incident on this chamber, the gas becomes ionized, and the generated electrons are collected using two electrodes located inside the chamber. The ionized particles are collected using charge pulses or measuring the change in current to detect the presence of radiation. The setup for this type of detector is shown in the figure below.



**Figure 7** Structure of the ionization chamber [5]. Gas filled scintillators have a chamber filled with gas with two electrodes (anode, and cathode), and an external sensing circuit. Radiation causes the formation of electrons, and positive ions which are collected by their respective electrodes, and sensed by the external circuit.

Based on this type of geometry, the electric field is uniform between the anode, and cathode. When radiation is incident inside the chamber, electrons, and ions are generated, and the electrons will move towards the anode. This will cause a decrease in the voltage, and using a pulse to collect the newly generated charge, the signal changes similar to the figure shown below [5].



**Figure 8** Change in voltage pulse due to collection of electron, and positive ion [5]. The effect of a generated ion, and electron on a DC voltage pulse is illustrated. Influx of a greater number of radiation photons creates large number of ions, resulting in a large RC, which correlates to longer pulse decay time.

### Geiger-Müller Counter

Geiger-Müller (GM) counters are a type of gas scintillators that operate using high voltage bias (600V for halogen-quenched, and 1000V for organically quenched counters), which can sense single ionization events using the avalanche mechanism [5].

When an electron is generated under a large electric field, the electron collides with other atoms generating multiple carriers. Due to the large voltage, a problem arises if the gas inside the chamber has a high ionization potential. Sometimes, in the presence of radiation, more than one electron is generated; the second electron can also begin a chain reaction, generating more electrons, which will eventually form a plasma inside the chamber. To prevent this from occurring, 5-10% halogens or organic gas is added to the gas mixture, which act as a positive charge carrier since these gasses have low ionization potential [2]. These gasses will prevent the generation of large number of electrons, thus preventing the generation of extraneous carriers that can corrupt the data [2].

## Semiconductor Detectors

Advances in material characterizations, and development of novel material compounds have created a new type of detecting materials. Semiconductors offer advantages in reducing the voltage required to sense singly occurring ionization events when compared to gas-filled detectors or Geiger Müller counters. This segment of detecting material has the capability to create smaller, effective, and inexpensive radiation detectors. Armantrout *et al.* generated a list of promising materials, and requirements for creating radiation detectors using semiconductors [9]. There are three main obstacles that a suitable material should surpass to become as a promising detector [9].

1. Material must have very high resistivities ( $>1\text{M}\Omega$ )
2. Limited number of charge traps
3. Should not have polarizing effects

The first requirement addresses the issue of photodark currents where the material should have a high order of difference between on, and off current for viable sensor application. Second requirement is necessary because all radiation sensors are charge-collecting materials, either as PN diodes or as PIN diodes. The presence of traps greatly diminishes the ability of generated charges to reach the contact. This is the main reason that the novel materials are all defect free crystals, which try to avoid this issue. To enhance the performance of semiconductors, direct, and wideband gap material are preferred.

Armantrout has determined various groups of materials, which are Elemental Group IVB, Binary IV-IV, III-V, III-VI, II-VI, IV-VI, n-VIIB, Pseudo Ternary/Ternary

Compounds [9]. The following table presents a few examples of compounds of these types of materials that have shown response to radiation.

**Table 1**      **Compounds, and types of materials suitable for radiation detection [9]**

Group IVB	Sn	Ge
Binary IV-VI	SiGe	SiC
Binary III-V	InP	GaAs
Binary III-VI	GaTe	GaSe
Binary II-VI	CdTe	CdSe
Binary IV-VI	PbS	PbSe(Te)
Binary n-VIIB	HgI <sub>2</sub>	PbI <sub>2</sub>
Pseudo Ternary/ Ternary Compounds	CdZnTe	CdMnTe

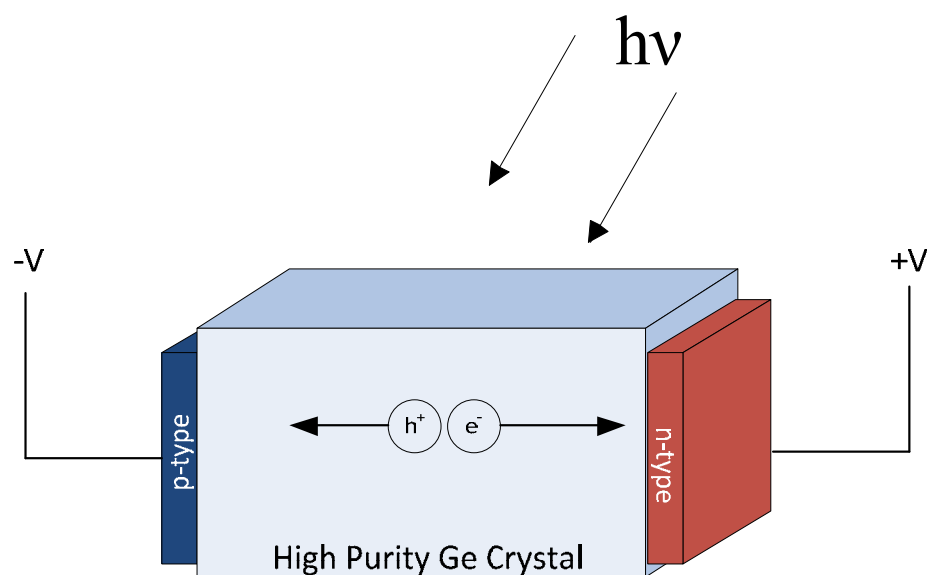
Of these various groups of materials, SiC of the group Binary IV-IV, and CdZnTe from the group Binary II-VI are the most novel, and thoroughly researched materials.

### Ge Crystals

Application of semiconductor based radiation detectors began in the early 1960s with the use of Germanium (Ge) detectors [10]. A benefit of using Ge detectors was the small size compared to gas-filled scintillators. To use germanium for radiation detection, high purity crystals are created using the Czochralski growth method [11]. The primary concern for creating Ge crystals is the incorporation of impurities within the crystal. Impurities that could affect the performance of the detector are elements such as Ga, Al, etc. that can be electrically active [11]. Germanium detectors are created using a p-n junction structure, and under a reverse electric bias. The detector is operated in depletion mode, which generates very large electric fields within the crystal. The pn-junction is created by using n, and p-type metal contacts on the crystal. Various metals can be

applied towards the p-type contact ranging from Au, Cr, Pt, and Al to name a few [12]. The n-type contacts on the other hand have been created by evaporating lithium [12]. When radiation is incident on the Ge crystal, electron-hole pair is produced. Since the detector is biased in depletion mode, the large electric field will attract the generated charged particles to their respective electrodes, where the particles are collected, and registered by the external circuitry.

Main disadvantage of this type of detector is that lithium can easily diffuse into the crystal at room temperature, which degrades the contact. To prevent the degradation of the electrode, the detector must be operated at 77K, which limits the “lifetime, operating, storing, and transporting detectors” [10].



**Figure 9** Depiction of the functionality of Ge crystal-based sensor. A p-type metal (high workfunction), and n-type metal (low workfunction) are placed onto a Ge-crystal, and biased to form a large electric field, which aids in separating, and collecting generated electron-hole pairs at the respective electrodes.

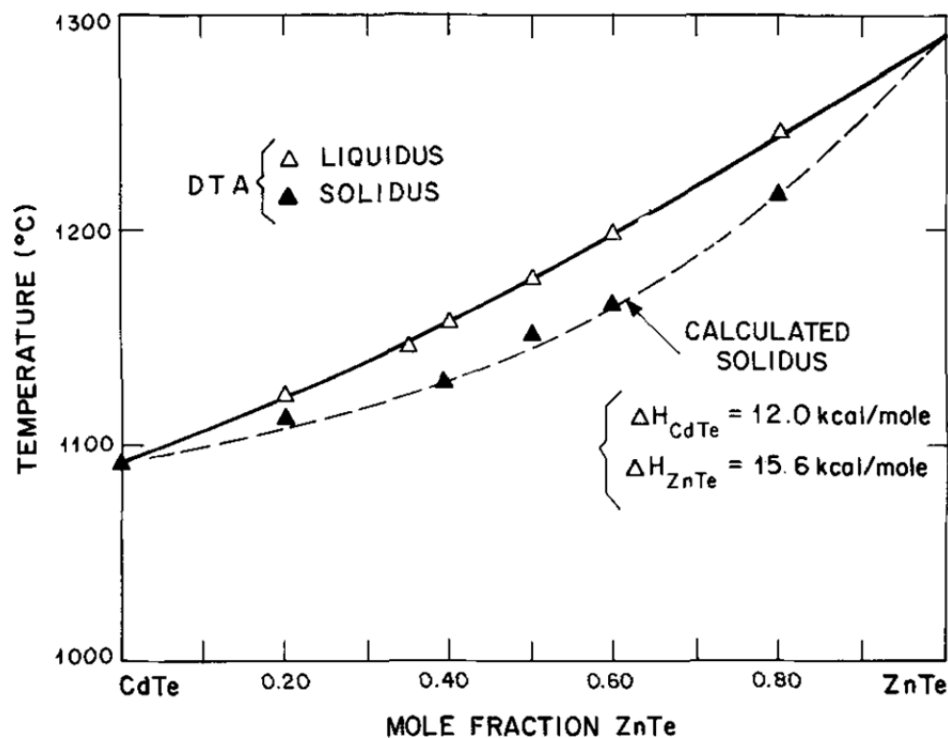


### Cadmium Zinc Telluride (CZT)

The cooling of Germanium crystals has proved to be a difficult obstacle to overcome for applications outside of laboratory, and accelerator settings. This led the researchers to look for new materials with the capability to measure radiation at room temperature. For these purposes, Cadmium Telluride (CdTe), and Cadmium Zinc Telluride (CZT) are viable materials because they are direct band gap material with very high resistivity to reduce the leakage currents, which are among the primary requirements for a suitable semiconductor for radiation sensing [13]. Fabrication of either CdTe or CZT begins with the creation of CdTe crystals, and uses dopants to achieve the required properties. Chlorine is used as the dopant in CdTe, and Zinc in the fabrication of CZT. The addition of Zinc increases the bandgap of the material [14]. The following table summarizes the comparison between CdTe, and CZT.

**Table 2 Comparison between CdTe, and CZT (with 10% Zn) [14]**

Characteristics	CdTe (Cl)	CZT
Bandgap (eV)	1.47	1.65
Mobility ( $\frac{cm^2}{V \cdot sec}$ )	e: 1000-1100 h: 80	e: 1000-1100 h: 50
Resistivity ( $\Omega \cdot cm$ )	$1-3 \times 10^9$	$0.5-1 \times 10^{11}$
Operating Electric Fields ( $\frac{V}{cm}$ )	300-500	900-1500

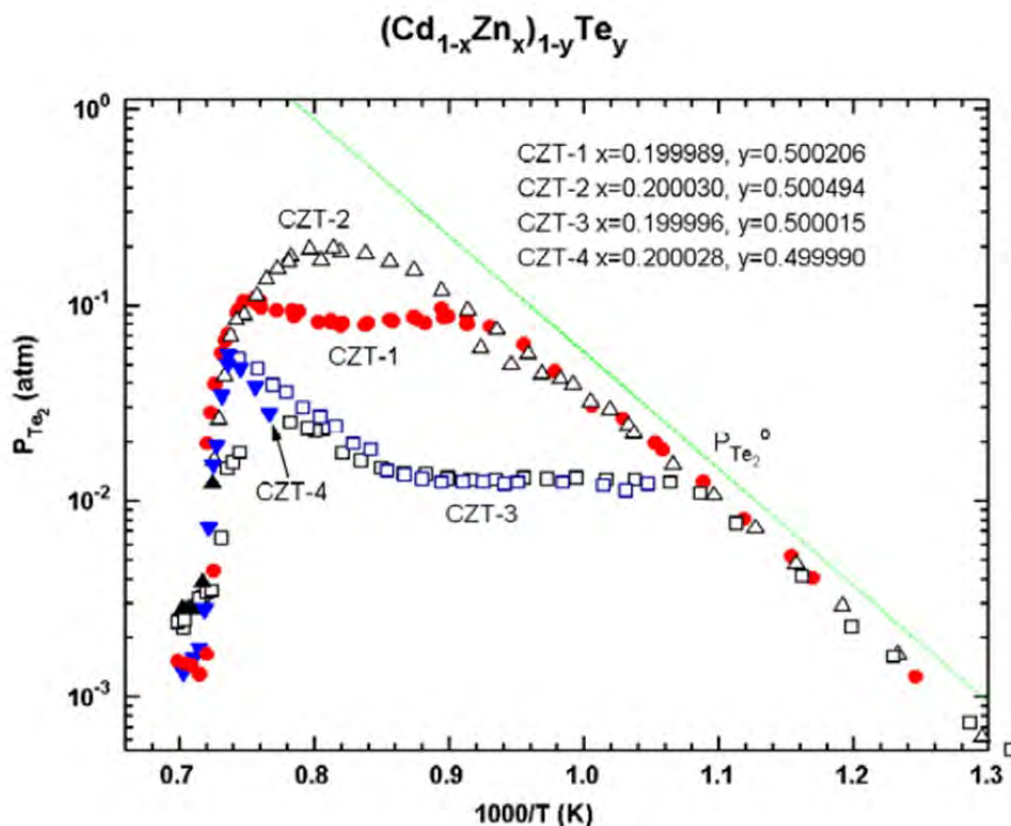


**Figure 10** CdTe-ZnTe phase diagram [15]. The formation of these crystals with different molar fractions of ZnTe is illustrated in this figure. Increasing the molar quantity of ZnTe increases the liquidation temperature, but the incorporation of Zn enhances the crystal characteristics as shown in Table 2.

Figure 10 represents the liquidus, and solidus curve for a melt containing various compositions of CdTe, and ZnTe. The upper curve in the figure corresponds to the melting temperature of the material, while the bottom curve represents the temperature of crystallization for different mole fractions of ZnTe within the CdTe. There are different methods to create CZT crystals, of which high pressure (HP), low pressure (LP) Bridgman, and Physical Vapor transport are the most prominent methods [13]. The process of fabricating crystals begins with melting Cadmium, and Tellurium in separate areas in a hydrogen-enriched environment. Hydrogen is used to prevent the introduction of oxygen into the melt because oxygen will easily form an highly resistive oxide layer, degrading the performance of the crystal [16]. After separately melting the elements,

these two melts are reacted together at the melting temperature. At this point of the growth process, dopants such as Zinc, and Chlorine are introduced into the melt [17]. To generate crystals, the liquid alloy is slowly cooled, which produces the final crystals. Growth of crystals requires either the temperature to be greater than 1100 °C or a high pressure as described in the pressure vs. temperature graph shown by Su, and Lehoczky [18]. The crystals must be crack free, defect free, and highly homogenous; otherwise, the process must be restarted until high-quality crystals are achieved. The entire process is highly expensive, and has a very low yield, therefore this reflects the cost, and the availability of such crystals.

The fabricated crystals can either be p-type or n-type conductive material depending on the growth process of the crystals [19]. Detector properties can be optimized by engineering the Fermi level to make the material have n-type conductive properties since the lifetime of the carriers is greater, but this in turn reduces the resistivity of the material [17]. The detector structure consists of the specific thickness, and two electrodes are placed on either side of the crystal, and then using a voltage large enough to create  $1000\text{V}/\text{cm}^2$  electric field within the crystal [13].



**Figure 11** Pressure vs. Temperature curve for different compositions of CZT [17]. The large melting temperature for the formation of CZT crystals can be mitigated by increasing the pressure within the melt chamber, thus effectively reducing the required temperature. Effective crystals have been formed at 769 K as shown in the graph above.

When a photon interacts with the material, the generated electron/hole becomes separated by the applied electric field, and then captured by their respective contacts, which are then detected by the external measuring circuitry. This high electric field is necessary to be able to detect single radiation effects. Another drawback for using CZT crystals is the inefficiency to capture holes because the generation of holes becomes trap centers, and if a photon induced electron is generated near this trap [19]. The electron, and the trap recombine, and the circuitry does not detect this electron, so this generated

electron is invisible. This would not be a big problem for p-type material with the capability to capture the electron, and affect the conductivity of the material.

Recent developments in the field of radiation sensors have allowed the creation of an easily transportable CZT detector. The group of Luke *et al.* have created a small “Pocket-size” detector with a  $2 \text{ cm}^3$  volume CZT sensor with all self-enclosed components to detect radiation [20]. Package consists of a high voltage source, power converters, and a separate segment of the circuit board dedicated to the digital, and analog circuit components [20].



**Figure 12** Pocket size CdZnTe detector [20] © 2005 IEEE.

## CHALCOGENIDE GLASSES, AND RADIATION-INDUCED EFFECTS

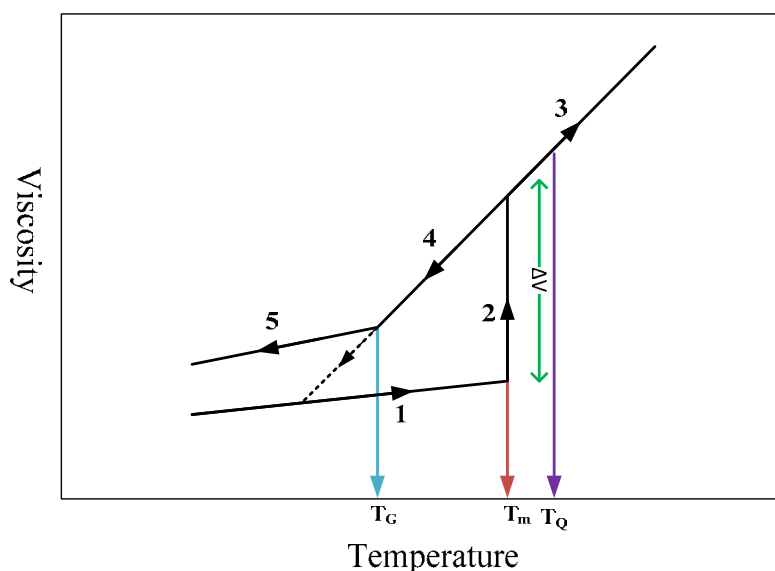
Chalcogenide Glasses (ChG) are a segment of materials that are considered as amorphous semiconductors. These materials have been researched for various applications such as memory, photolithography, chemical sensing, as well as radiation sensing [21, 22]. Compared to the other possible applications for ChG, radiation sensing is a very novel, and promising research area because of the range of structural changes that are possible, and the lack of research in this aspect.

### **Basics of Glasses**

All materials are classified in one of four forms based on entropy, and structural order. The materials with the highest entropy are either gasses or plasma while the lowest entropy characteristic for solids. Solids consist of three main groups of materials, which are single crystalline, poly crystalline, and amorphous. Single crystalline materials have high range order with the exception of very few defects. The atoms are arranged in a distinct pattern of periodically repeated unit cells, for example, single crystalline Si. Poly crystalline materials on the other hand have the benefits derived from the single crystalline structure with the addition of grain boundaries. These types of materials have multiple crystalline structures separated by boundaries, which has specific benefits, for example, the use of poly crystalline Si as a gate electrode in CMOS technology.

The third type of solids is known as amorphous materials where the structure of the material has short range order but there is no long range order. Chalcogenide glasses

are an example of materials with such characteristics that are direct result of the production of glasses. Glasses are conventionally produced using the melt quench technique, which begins by taking measured amounts of pure elements in pellets or powder form, corresponding to a specific composition, sealed inside evacuated ampoules. The next procedure is to place the sealed ampoule into a specialized furnace, which raises the temperature until all the materials are in molten liquid form. At this point, the furnace is rocked to ensure complete mixture of all the elements. This step is followed by a quick quench to solidify the mixture but also maintaining the amorphous nature of the glasses by freezing the equilibrium characteristic of the liquid mixture. This process is summarized in the following figure, which shows the temperature as a function of viscosity.



**Figure 13** Temperature vs. Viscosity for formation of glasses. The material that will be used to form glasses is placed in an ampoule, and the temperature of the ampoule is increased in stage 1. Once the melting temperature ( $T_m$ ) of the material is achieved at stage 2, the viscosity of the material greatly increases. The molten melt is set to achieve a quenching temperature ( $T_Q$ ), which is followed by removing the molten material, and quenching in air or ice bath in step 4, transitioning into step 5 at the glass transition temperature ( $T_G$ ). At step 5, a glass is formed that has a higher viscosity than the original material.

In the figure above, material is heated in step 1, and once the elements reaches a melting temperature ( $T_m$ ), the viscosity of the material drastically increases when it becomes a liquid. After reaching the molten state, in step 3, the molten liquid is removed from the furnace, and is immediately quenched in air, water, or ice bath, depending on the required quench rate. When the molten alloy is quenched at a fast rate (step 4), then the resultant material is in glass form, and the viscosity of the material is higher than the viscosity of the initial material. The characteristic temperature for the transition from liquid to solid state is called glass transition temperature ( $T_G$ ). Slow cooling rate will follow the dotted line in Figure 13, and reach a similar viscosity of the original material, therefore achieving a crystalline structure by which the material will reach its equilibrium state. Crystalline material has the lowest entropy, therefore if the system is allowed to slowly cool, the atoms can form a structured order, but a fast cooling rate prevents the material from achieving this molecular organization. The primary concern for glasses is to ensure the temperature of the glass is sufficiently lower than the glass transition temperature. When the temperature of the glass begins to approach the glass transition temperature, the glass will begin to liquefy, and without the proper cooling rate, material could become semi crystalline, which has completely different properties than the amorphous glass.

It is possible to create glasses out of most materials, but most material only form glasses in specified compositions, and using specified cooling rates. These specific compositions are known as the glass forming regions, and are studied in detail since glasses from various compounds have many capabilities. One of the main explanations towards the ability to form glasses is given by the bond constraint theory, which was



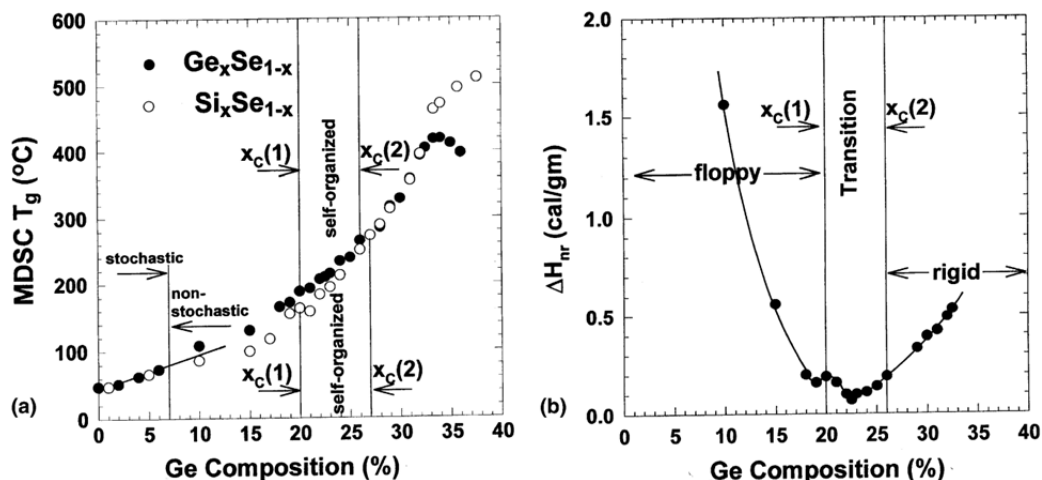
theorized by Phillips [23]. According to this theory, ideally the compositions with mean coordination number of 2.4 can easily form glasses. This ideal mean coordination number creates a situation where the number of constraints per atom is equal to the degrees of freedom for each atom. Mean coordination number can be calculated using the following equation for an arbitrary alloy with elements A, and B, in a compound  $A_xB_{100-x}$ .

$$r = Z_A(x/100) + Z_B((100 - x)/100) \quad (21)$$

Where  $Z_A$  is the coordination number or the number of additional valance electrons that are required to satisfy the 8-N rule for element A, and similarly  $Z_B$  is the coordination number of element B. For example, the mean coordination number for  $Ge_{20}Se_{80}$  is 2.4. Further research into the relationship between the glass formation regions, and the mean coordination number revealed that structural properties are also correlated to the coordination number. It was shown by M. Thorpe that  $r = 2.4$  is the transition point from floppy ( $r < 2.4$ ) to rigid ( $r > 2.4$ ) structure of the glasses [24-28]. When a structure is floppy, it means that there is greater degree of flexibility between bonds, resulting in an overall flexible glass, while rigid structure have considerably less freedom. Floppy structures are primarily chalcogen-rich glasses. Recently, P. Boolchand has stated that in addition to the floppy, and rigid glass phases, there exists an intermediate phase where the glasses are non-stressed rigid, and they do not age [29-32]. Hence, using the bond constraint theory, information about glass formation region, and structural properties of glasses, compositions can be used to determine the purpose, and application of said glasses.

Intermediate phase offers many different benefits such as stated by Boolchand *et al.* using Differential Scanning Calorimetry (DSC) where in the intermediate phase the

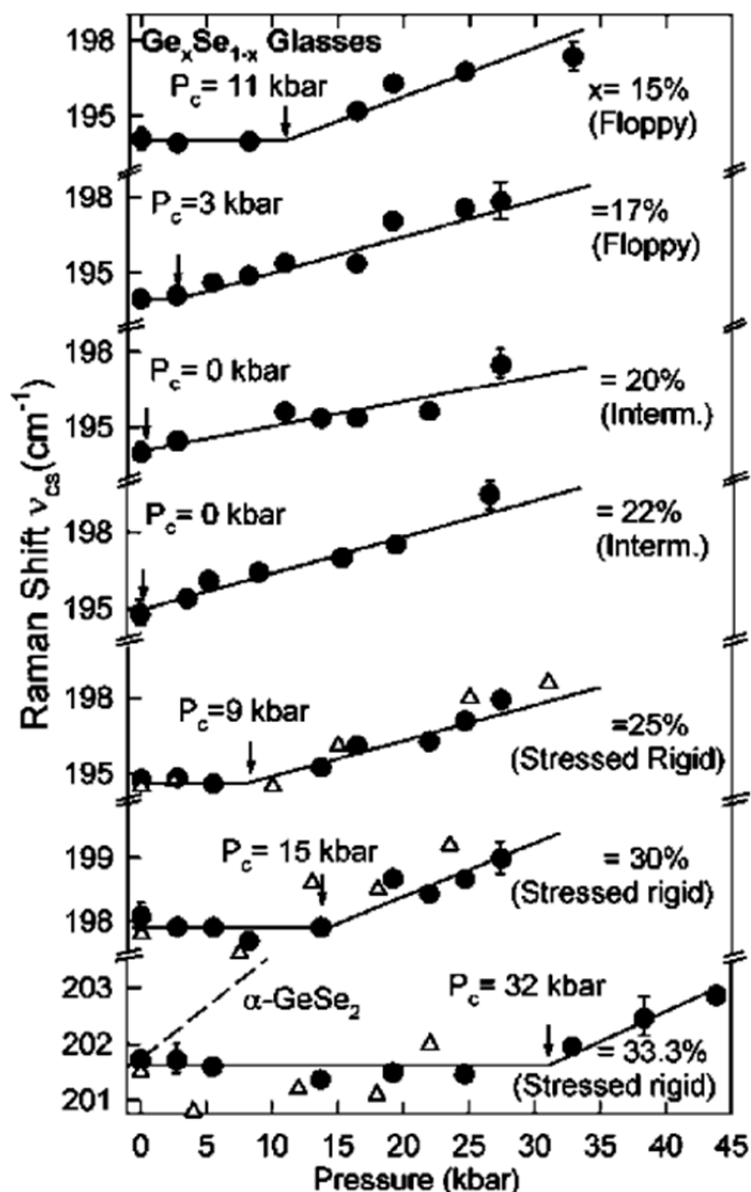
non-reversing heat-flow parameter is minimal, which was equated to glass's structure resembling the structure of the material in liquid state in the sense that the stress within the structural is minimal at this composition [29, 33-35]. This transition is shown in the figure below for various chalcogenide glasses, which is a comparison between the coordination numbers to the non-reversing heat-flow parameter.



**Figure 14** DSC measurements for various  $\text{Ge}_x\text{Se}_{1-x}$ , and  $\text{Si}_x\text{Se}_{1-x}$  compositions showing the transition from floppy-intermediate-rigid structure [31]. The application of Differential Scanning Calorimetry expounded that in addition to the floppy, and rigid phases, there is a transition region, which is classified as the intermediate phase.

This study was also performed in combination with Raman spectroscopy, and DSC where the stresses within the system were studied, and analyzed. The combination of the DSC, and the Raman illustrated that the floppy glasses were under constrained, and the stressed rigid structures were over constrained as shown by the Phillips-Thorpe theory. While the intermediate phase is optimally constrained with the minimal pressure, hence the effect of ageing is greatly reduced in this type of system [30]. This is shown in Figure 15, which shows the pressure for various compositions within the  $\text{Ge}_x\text{Se}_{1-x}$  system.

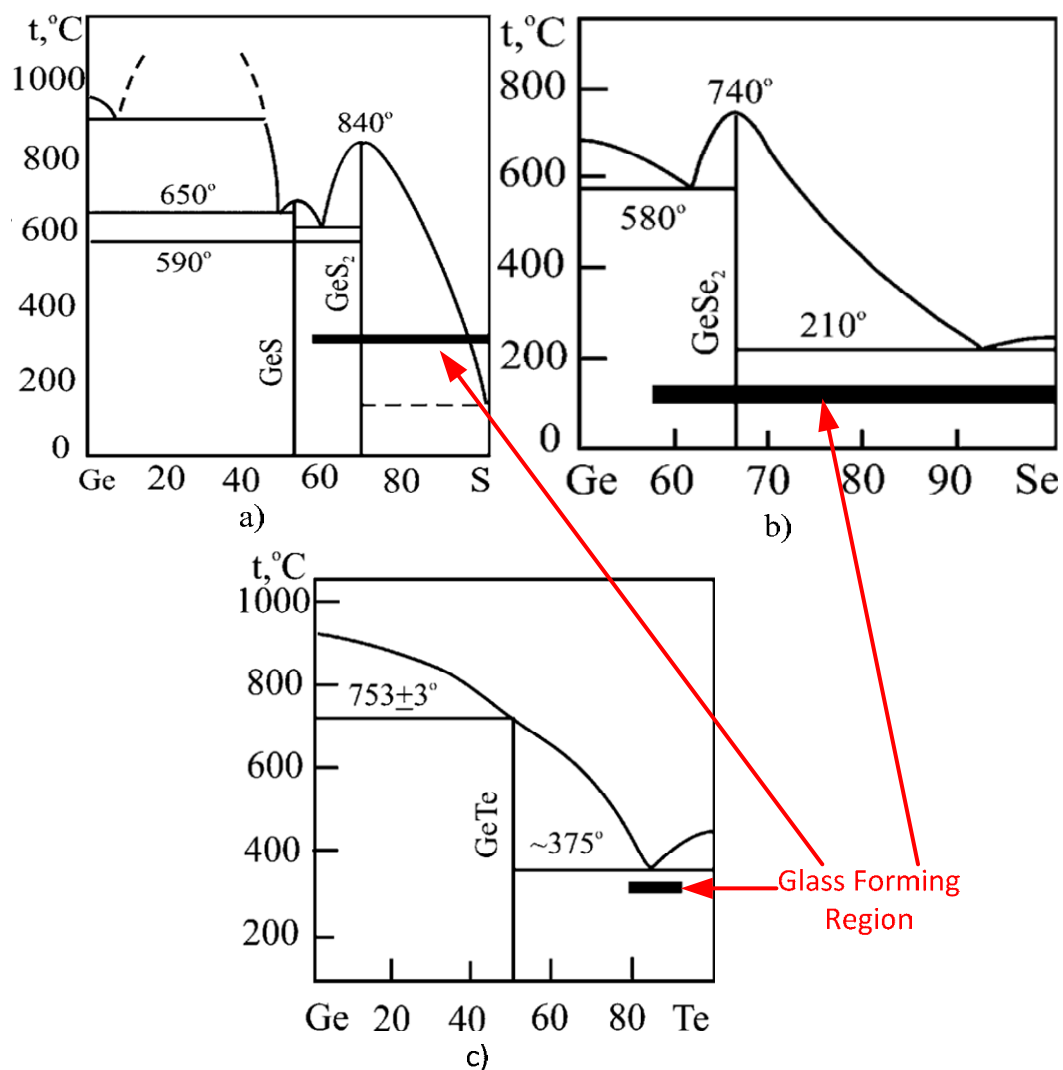
It was also mentioned that the glasses described as floppy, and rigid are known as “fragile liquids” while the glasses in the intermediate phase are shown to have characteristics described as “strong liquids” [29, 33]. These classifications are derived from the connectivity within the system.



**Figure 15** Raman shift of CS units versus Pressure for various  $\text{Ge}_x\text{Se}_{1-x}$  [23]. Various compositions from the Ge-Se systems were studied using Raman spectroscopy, and close observation of location of CS peak on the Raman spectra revealed stressors within the glasses. Glasses classified as rigid or floppy have the highest internal stress. When the glass composition converges to the intermediate phase, the internal stress is minimal or nonexistent as illustrated in this figure.

A segment of glasses are known as Chalcogenide glasses are created using the above mentioned glass formation method, but the primary difference between these glasses to other glassy material is the inclusion of group VI elements such as Sulfur (S), Selenium (Se), or Tellurium (Te) within the composition of the glass alloy. These three elements are also known as chalcogen elements, and thus glasses created from these elements are known as chalcogenide glasses. Chalcogenide glasses range from glasses created with only S, Se, or Te to binary compounds, which consist of other elements in combination with the chalcogen elements to more complex alloys, with the only requirement being the presence of at least one of the chalcogen atoms in the glass composition. There is no end to the possible compounds that can be created, and each combination is used for a specific purpose because of the structure, the bonding between the elements, and properties of each unique combination.

Glass formation, and phase diagrams are an important method of studying the properties of chalcogenide glass. The formation of glasses using chalcogen elements has been researched, and a specific trend has been determined between the different chalcogen atoms. Elemental Sulfur can be alloyed into a glass when heated to a temperature greater than 160°C, and then quenched at -27°C [36]. Selenium has a  $T_G$  of 40°C, but tellurium cannot form a glass [36]. This data follows the general trend for glass formation capability of chalcogenide glasses, where selenium has the largest ability followed by sulfur, and tellurium has the smallest ability. The glass formation capability of chalcogenide glasses is highly dependent on their connectivity. For example, introduction of Ge significantly increases the coordination of the glasses since germanium is usually four-fold coordinated creating a three dimensional structure.



**Figure 16** Phase diagram of Ge containing chalcogenide glasses (a) Ge-S, (b) Ge-Se, and (c) Ge-Te [36].

Study of phase diagrams reveal an abundance of information from melting temperature, and glass formation region for various compositions of a specific binary glass compound. The phase diagrams for Germanium (Ge) containing glasses show  $\text{Ge}_x\text{S}_{1-x}$  ( $10 \text{ at.}\% \leq x \leq 47.6 \text{ at.}\%$ ),  $\text{Ge}_x\text{Se}_{1-x}$  ( $0 \text{ at.}\% \leq x \leq 40 \text{ at.}\%$ ), and  $\text{Ge}_x\text{Te}_{1-x}$  ( $12 \text{ at.}\% \leq x \leq 22 \text{ at.}\%$ ) [36]. In sulfur, and selenium containing glasses, the stoichiometry glass composition ( $\text{GeS}_2$ , and  $\text{GeSe}_2$ ) can be synthesized. The wider the glass formation region

enables the ability to study different structures, which are prominent in chalcogen-rich glasses, and other structures that might only be available in chalcogen poor compositions.

The availability of lone pair electrons, and the mixture between the covalent, and van der Waals bonding between the elements in the chalcogenide glasses gives rise to the photoinduced effects within these materials. In the following sections, chalcogenide glasses have been characterized using two types of photons (sub-bandgap light, and gamma rays), which will be discussed in detail, and their structural changes, as well as the photon effects on the optical properties of chalcogenide glasses.

### **Sub-Bandgap Light**

#### Structural Changes

Prior to discussing the structural changes induced by sub-bandgap light, it is important to discuss the properties of the chalcogen atoms since these atoms determine the unique properties of these types of glasses. Sulfur, Selenium, and Tellurium as a group have specific properties that are characteristically unique in the world of glasses, but each of these elements vary in their own unique manner. The sizes of the atoms increase from Sulfur to Selenium to Tellurium, and this is inversely proportional to the bond strengths of atoms. For example, Te-Te bonding is weaker than Se-Se bonding, and in turn weaker bonding energy than S-S. This pattern is similar for the bonding energy of some combinations of chalcogen atom with other elements for the prominent chalcogenide glasses are shown in the following table.

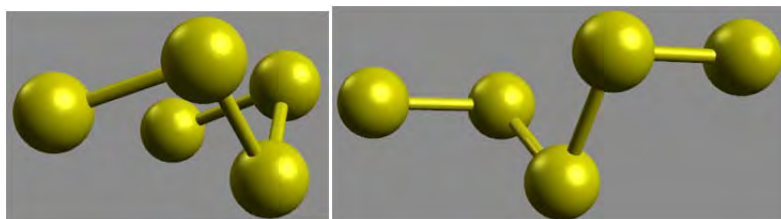
**Table 3** Bond energies for common atomic bonds in Chalcogenide glasses [37]

Bond	$E$ (kJ/mol)	Bond	$E$ (kJ/mol)	Bond	$E$ (kJ/mol)
S-S	280	P-P	225	Sb-Sb	175
Se-Se	225	P-S	270	Sb-S	230
Se-Te	195	P-Se	240	Sb-Te	195
S-Se	255	As-As	200	Si-Si	225
Se-Te	220	As-S	260	Si-Te	220
		As-Se	230	Ge-Ge	185
		As-Te	205	Ge-S	265
				Ge-Se	230
				Ge-Te	200

Another pattern that arises from the bonding energies is the thermal stability of the glasses. Glasses containing Te have the lowest  $T_g$ , and this transition temperature increases to sulfur containing glasses in the following manner:  $S > Se > Te$ .

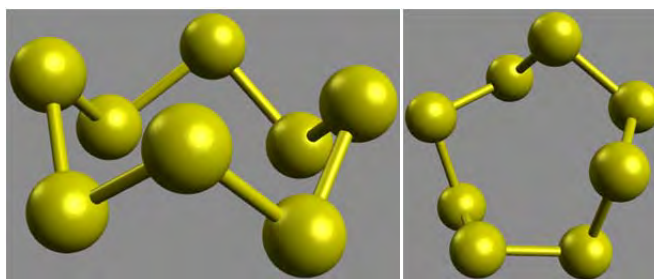
Chalcogen atoms have two electrons in the  $s$  shell, and four in the  $p$  shell. Two of the  $s$ -shell electrons, which have opposite spins, will bond with each other. The  $p$ -shell electrons are the reason chalcogenide glasses are highly researched because the electrical, and optical capabilities are derived from these electrons. Two of the  $p$ -shell electrons will become lone pair electrons forming an electron pair, and the other two electrons will covalently bond with other atoms. When glasses are created with only chalcogen atoms, the following unique properties were discovered, which will be explained individually.

Sulfur atoms create chains with other sulfur atoms where the angle between the atoms is  $105^\circ$ . Within a chain, there are two specific locations where each of the sulfur atoms can be located. These locations are known as eclipsed (cis) or staggered (trans) configurations as shown in the figure below [36].



**Figure 17** Two location for sulfur atoms within a sulfur chain a) cis and b) trans.

Crystalline sulfur forms orthorhombic chains with 8 sulfurs with a trans configuration at bond angles of  $105^\circ$ . This orthorhombic structure is shown below.

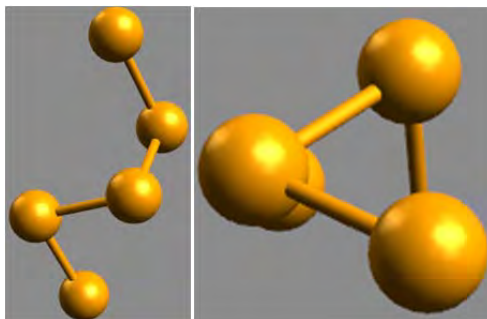


**Figure 18** Orthorhombic sulfur rings  $S_8$  a) side view and b) front view.

In sulfur-rich glasses, the sulfur rings can phase separate from the remainder of the glass network, which is the main reason for the smaller glass formation region in comparison to the selenium atoms. Additionally, sulfur has a significantly higher partial molar volume, which is an attribute that is unique to sulfur-containing glass in contrast to the other two chalcogen-containing glasses.

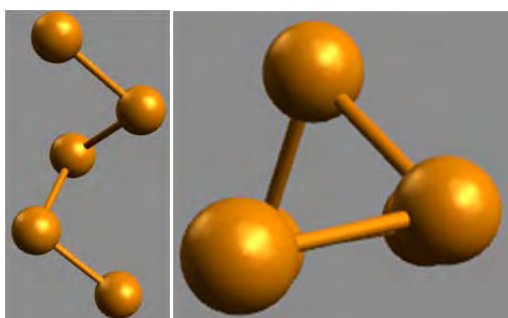
Selenium on the other hand has more of a hexagonal chain, which are held together using Van der Waals forces [38]. These chains are created from parallel chains unlike in the case of the Sulfur orthorhombic rings, and each atom has a bond angle of approximately  $103.1^\circ$  [38].





**Figure 19 Hexagonal Selenium chains a) configuration of the chains and b) top view of the chains.**

Similar to Selenium, Tellurium also forms long spiraling hexagonal chains held together with Van der Waals forces [39]. These chains are shown in the figure below.



**Figure 20 Tellurium chains a) configuration of the chains and b) top view of the chains.**

Tellurium is considered as a semi-metal, and has characteristics similar to metals, such as having a very narrow bandgap, high conductivity, and are lustrous in appearance.

The lack of order in the chalcogenide glasses, and the presence of lone pair p-shell electrons provide chalcogenide glasses unique electrical, and optical properties when compared with crystalline material. These qualities are derived from the energy band diagram, and the presence of localized states. In crystalline material such as undoped intrinsic silicon, there exist two energy states, conduction band (CB), and

valence band (VB), which are occupied by an abundance of electrons, and holes at room temperature. Between these bands, there are no other states, so for an electron to transition between the VB, and occupy a state in the CB, the electron must acquire sufficient energy to overcome the band gap energy. Ideally, in these materials, the Fermi level, which provides information on whether there is an abundance of holes or electrons within the material, is situated in the middle of the band gap, suggesting similar number of electrons, and holes at 0 K or ideally intrinsic (undoped) semiconductors.

Chalcogenide glasses on the other hand, have band tail states, and localized states along with the two band states [40-42]. These extra states are attributed to the presence of lone pair electrons as well as the amorphous structure of the glasses. The localized states between the CB, and VB are primarily due to the presence of the lone pair electrons, while the band tail states are attributed to the Van der Waal's forces between layers of atoms [43]. Localized states are trap locations within the band gap where electrons from the valence band can hop into, on their path towards the conduction band. Tail states on the other hand are locations near the band gap, and are known as Urbach tail states. These states are occupied with many electrons that can participate in the various changes due to interaction with photons. The investigation by Utsugi and Mizushima stated that electron-phonon interactions are responsible for the generation of the Urbach tails [44-46]. The Urbach tail states are responsible for setting the absorption edge for glasses, and photons with energy near the band gap affect these states.

### Optical Properties

The absorption edge of chalcogenide glasses is very important characteristic, since the material is highly transparent for wavelengths greater than the absorption edge.

This highly transparent region is usually contained within the infrared, and near infrared regions of the electromagnetic spectrum, where these glasses are useful for telecommunication applications as either waveguides or fiber optics [47]. Wavelengths shorter than the absorption edge are completely absorbed, which is useful for radiation sensing purposes. For these reasons, study of the absorption edge is of the highest priority to ensure using the appropriate glasses for the specific purposes. Illuminating chalcogenide glasses using sub-bandgap light or light sources with wavelengths near the absorption edge will result in defect formation creating unique optical properties. The absorption edge for a-selenium has been studied, and the band gap is 2.1eV, and the absorption edge is located at 540 nm, as shown in the figure below [48].

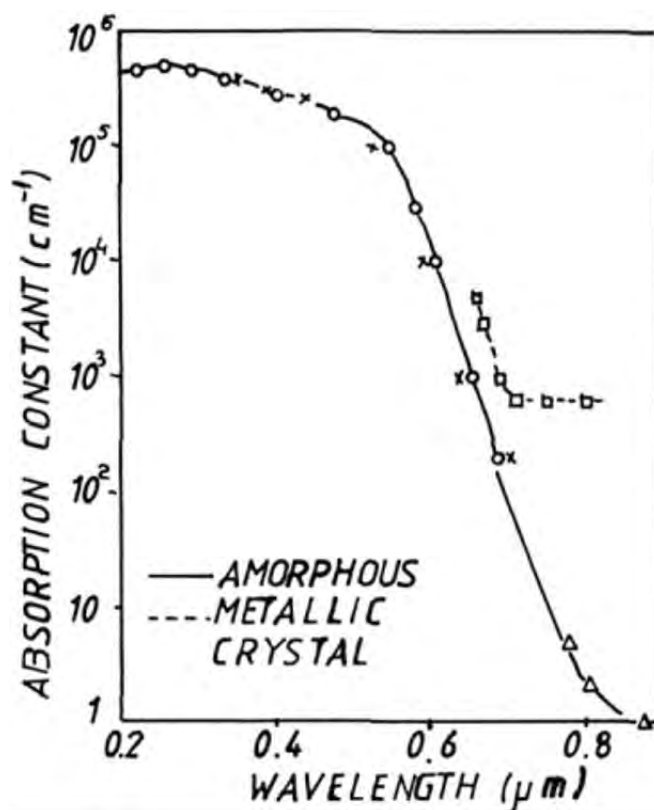
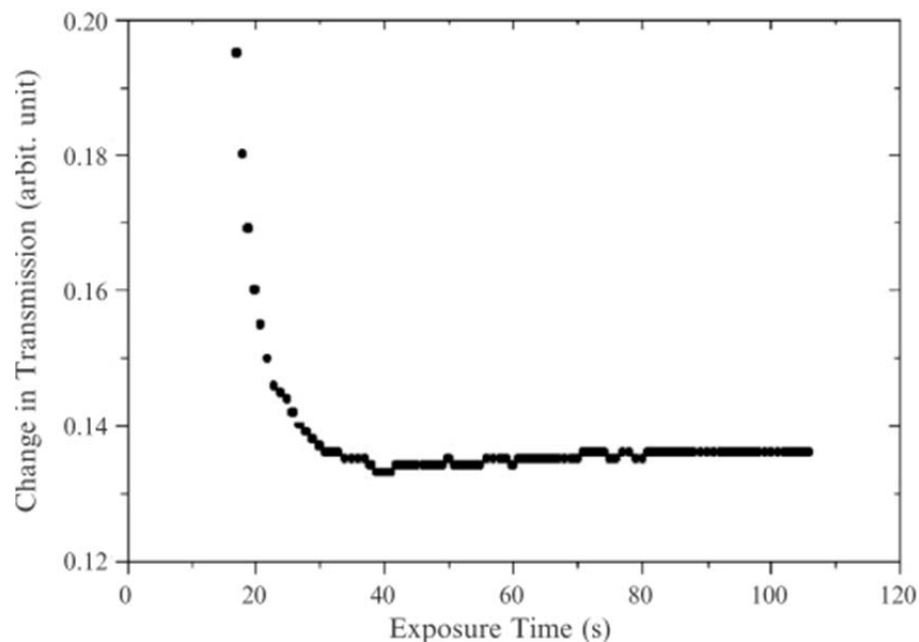


Figure 21 Absorption edge of a-Selenium [48].

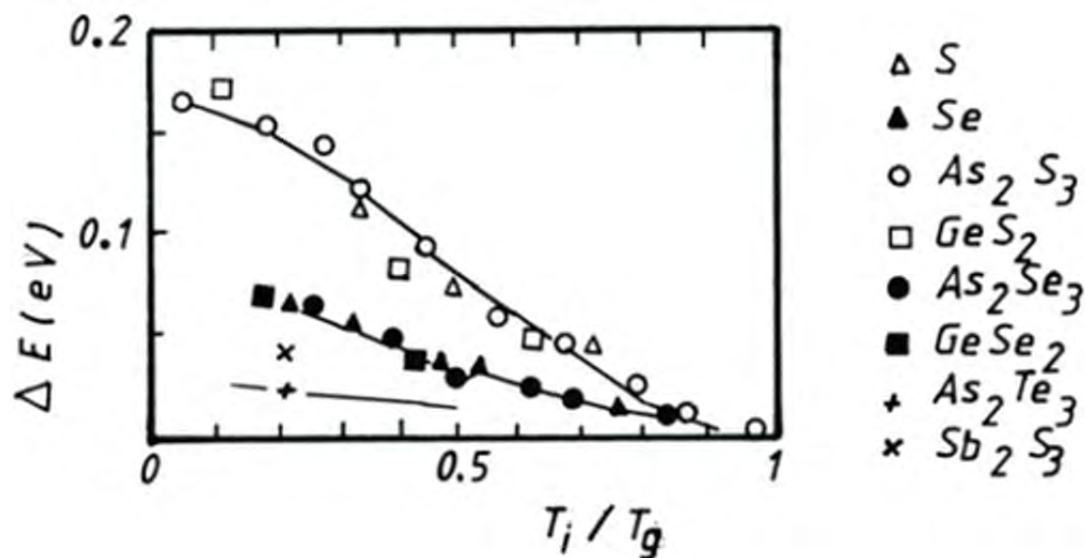
Sulfur, and Tellurium also have similar absorption spectra, which can be modified through photon irradiation [20, 49]. Two types of effects occur due to photon irradiation, which are known as either photodarkening or photobleaching. In the case of photodarkening, the absorption edge of the glass properties is shifted to longer wavelengths, such as what occurs when the absorption edge of a-Se to shift towards 600 nm or higher after photon irradiation. This type of result is attributed to bond breaking, and molecular rearrangement, which rearranges the traps, thereby decreasing the bandgap of the material. There are two possible theories explaining the phenomenon, broadening of the valence band thus changing the bandgap, while the other theory states that the extended states contribute to the change in the bandgap due to excited charge carriers [45, 50-55]. The change in the bandgap occurs when the photon interacts with the material, which breaks bonds within material, creating defects. These defects are located within the bandgap of the material, and act as localized states. With an increased number of generated defects, the bandgap of the material experiences a reduction since there are an abundant number of defect sites in near proximity of one another, and an electron requires minimal energy to hop from one defect to another. By effectively reducing the bandgap, illumination by light with higher wavelengths is sufficient to begin photoconduction. Photodarkening has been a very interesting, and highly researched topic, since the possibilities are nearly endless because the ability to change the properties from transparent to completely absorbed by illumination is valuable [56]. An example of such optical effects has been shown in the book *Optical Non-linearities in Chalcogenide Glasses, and their application*, photodarkening has been observed in  $As_2S_3$  films by

irradiation using a 514.5 nm laser [56]. The result is shown in the figure below comparing the change in film transmissivity as function of irradiation time.



**Figure 22** Transmission of  $\text{As}_2\text{S}_3$  film versus illumination time using a 514.5 nm light source [56]. With increased illumination, new defects are formed that change the previously transparent light to partially or completely absorbed (photodarkening effect).

These changes are also reversible by annealing for certain types of glasses, and have been studied for various films, such as chalcogen only as well as binary compounds such as Ge, and As combined with chalcogen atoms [25, 57].



**Figure 23** Photodarkening showing the maximum reversible shift in the absorption edge as a function of temperature [57]. After illuminating the glasses causing photodarkening effect within the glasses, this study shows that by heating the glasses to a temperatures near the glass transition temperature, the change in bandgap can be reversed.

The figure above shows that the change in absorption edge is nearly negligible at temperatures close to the glass transition temperature, which has been equated to the annealing process of those effects [57].

Similar to the process of photodarkening, the reverse effect is called photobleaching, where the absorption edge moves to lower wavelengths. This effect is prominent in Ge-containing chalcogenide glasses, and has been attributed to the structural changes as well as the oxidation of Ge atoms within the glasses [27, 28, 55, 58].

Recently, D. Arsova, and E. Vateva have shown that Ge-As-S films exhibit a dual nature, both photodarkening, and photobleaching properties [59]. This study was performed under vacuum to prevent oxidation, which has been shown by Tanaka *et. al.* as it can cause photobleaching [55]. From this study, it is shown that the films can be initially photodarkened, but after sufficient illumination, the effect can be reversed due to

the structural changes that occur [59]. In addition to Arsova *et al.*, many other groups recently reported the coexistence of photodarkening, and photobleaching. The reported results reveal a fast photodarkening, which occurs within the initial illumination, followed by a slow photobleaching [60-62]. The previous measurements were made post factum, and thus unable to capture the dynamic changes, but some researchers have observed that during irradiation, the glasses undergo a switching behavior where the material switches from photodarkening to photobleaching, and vice versa, while the overall spectra follows the trend observed, which displays only photodarkening or photobleaching [35, 63].

### **Gamma Radiation**

Gamma rays offer similar structural changes as sub-bandgap photons, but this type of radiation possesses a significantly greater amount of energy per photon. Therefore, it is expected that the observed structural changes under gamma radiation should be greater than the changes observed due to sub-bandgap light.

#### Structural Changes

Structural changes within chalcogenide glasses in the presence of  $^{60}\text{Co}$  gamma radiation was first observed by Starodubcev *et al.* in 1961 [29]. Following this discovery, Stanford Ovshinsky reported that radiation-induced changes have not been registered until  $10^7$ - $10^8$  rad dose [32]. After this dose, changes in microhardness, Young's modulus, internal friction, and geometrical dimensions exhibited a change, and this change is stable up to 7 months post radiation exposure [29]. The other unique property of chalcogenide glasses is the ability to reverse the structural changes, and return the original pre radiation

state of the glasses. In bulk glasses that have been exposed to radiation, to return the material to the initial state, the glass was heated to 10-30K less than the glass transition temperature [64]. By heating the glass close to this temperature, the damage inflicted by gamma radiation is reversed [64].

Many of the structural changes that have been reported have been compiled by the research group of Oleg Shpotyuk [22]. In the various research articles published by the aforementioned research group, they investigated the radiation-induced changes in vitreous chalcogenides in the Arsenic containing chalcogenide glasses. These investigations have been performed using a  $^{60}\text{Co}$  gamma radiation emitting source, and the structural changes resulted after exposure to this source has been identified as destruction-polymerization transformation [22].

It has been stated that gamma ray irradiation causes two types of changes: static, and dynamic changes. The latter type of change occurs during the presence of radiation, such as creating defects, and disappear after the cession of radiation exposure, while static changes on the other hand are stable after the exposure to radiation. Examples of static changes are destruction-polymerization transformations.

Destruction-polymerization transformation is a process where either heteropolar bonds are broken, and transformed into homopolar bonds (equation 22) or vice versa (equation 23), as shown in the following chemical reactions in the Ge-S binary glasses.



The specific transformation is dependent on the atoms that participated in the covalent bond that was destroyed by gamma radiation as well as the neighboring defects.

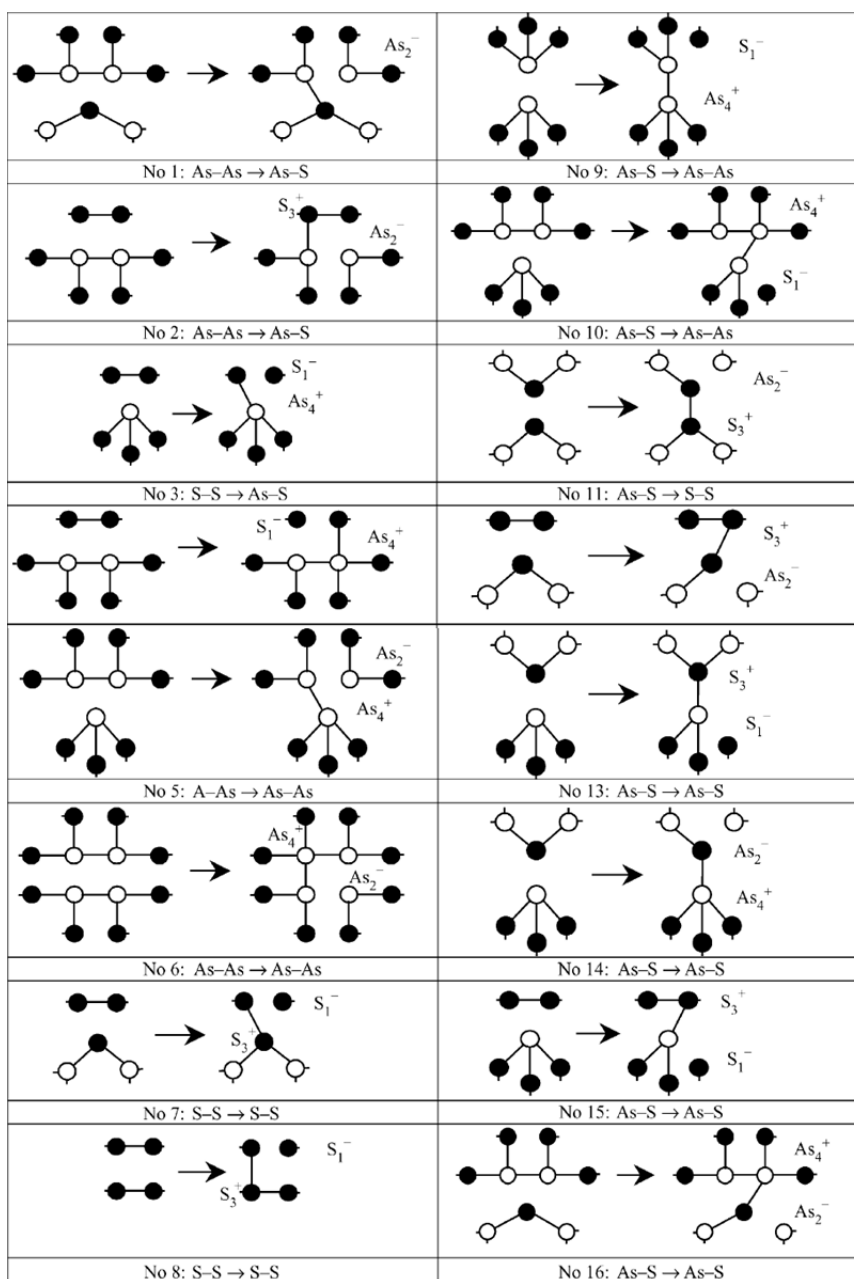


In the occasion where a bond is destroyed in an area where there are no available defects that can accept the newly created change, a new bond can be created, which does not comply with the 8-N rule [65]. The resultant bond will consist of one atom being over-coordinated (more than 8 valence electrons), and another being under-coordinated (less than 8 valence electrons) [22]. This new coordinated bond, which does not exist in steady state, and therefore this bond is also known as a wrong bond, and accompanies a charge on the respective atoms. The over-coordinated atom is assessed with a positive charge, and the under-coordinated atom consists of a negative charge [22]. After extensive research into these structural changes, specific rules have been created to understand all the various changes that can occur in the presence of  $\gamma$ -rays [22].

1. All interaction can be narrowed down to a single broken bond transforming to a created bond.
2. The high energy of the  $\gamma$ -rays allows for the creation of weaker bonds instead of strong bonds. The newly created bond has a bonding energy that is significantly less than the bonding energy of the previously existing strong bond. For future clarification, the creation of weaker bonds in the place of stronger bonds will from now onwards be referred to as “wrong bonds.”
3. In similar vein as rule #2, it is also possible to destroy a homopolar bond, resulting in the formation of a strong heteropolar bond in addition to an under-coordinated atom with lower electronegativity (i.e., bond transitions 1, 2 in Figure 24).

4. The final rule was not observed in these glasses due to low density of the material. In highly packed material, such as crystalline material, a broken bond can result in many subsequent structural changes in the short or medium range order to achieve the lowest entropy state.

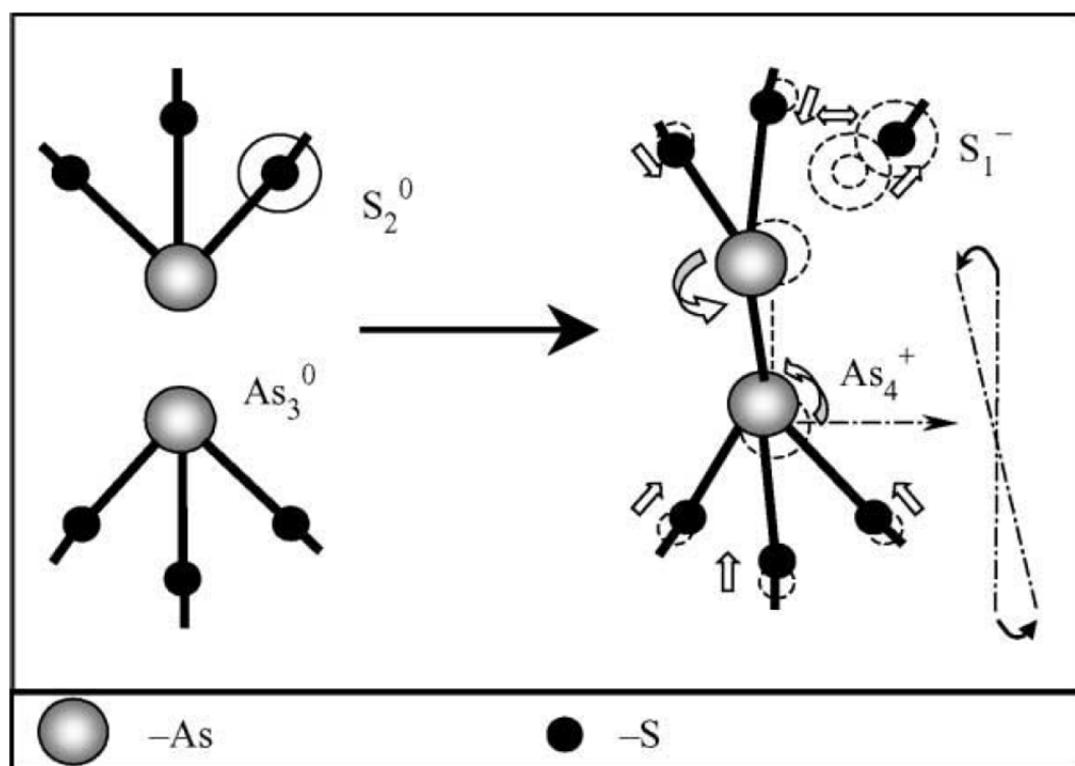
The above mentioned rules have been applied to the system with As-S, and illustrated in the Figure 24. Structural changes depicted in 1-4 correspond to homopolar to heteropolar changes, and the changes in 9-12 represent the heteropolar to homopolar changes. These changes can be easily detected since the bond prior to the destruction is significantly different from the post irradiation bond. The following changes depicted in 5-8, and 13-16 are more difficult to detect since the broken bond is replaced with a similar bond, and thus is undetectable with the exception of local molecular rearrangements.



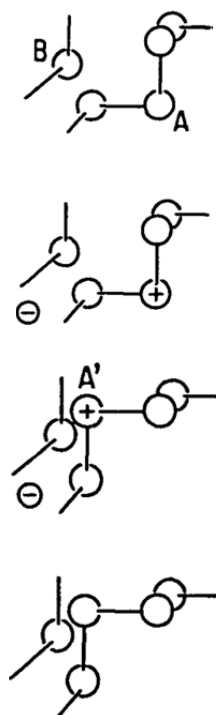
**Figure 24** Possible structural changes in  $\text{As}_2\text{S}_3$  glasses ( $\circ$  As), and ( $\bullet$  S) [22, 66].

Until this point, single bond destruction, and polymerization has been discussed, but within glasses, and materials, the single bond is connected to the neighboring molecular structure. Changing one bond, and the creation of a local charge causes a ripple effect to the connected molecular structure. These types of changes are known as a bond-

switching process, and is described by the bond-twisting model [22, 67]. In addition to molecular rearrangements, this type of structural change also results in creating new voids or openings within the structure. The following figures depict various types of molecular rearrangements that can occur within these types of glasses.



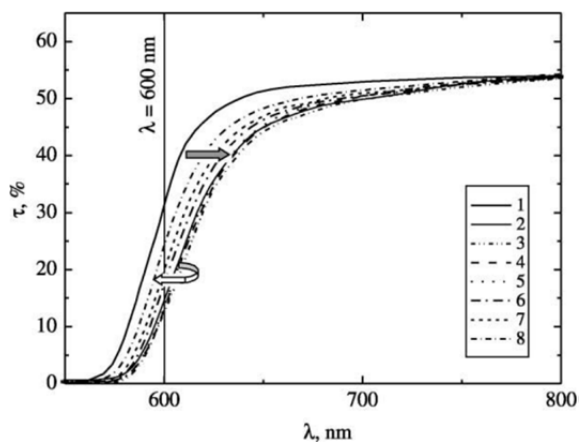
**Figure 25** Bond-switching model depicting the change to the neighboring structure post destruction-polymerization transformation [22]. An As-S bond is broken due to radiation, and due to the vicinity of a neighboring arsenic atom, As-As bond is formed. This newly formed bond rotates this molecule to accommodate the localized charges on the arsenic, and sulfur atom.



**Figure 26** Bond-twisting model proposed by Tanaka in 1990 [68]. This model was presented by Tanaka, which reveals that an atom can transition between the cis to trans sites to satisfy localized charges.

### Optical Properties

With the various structural changes described in the above section, it is expected that these changes will contribute to a change in the optical properties of the glasses. In the studied bulk chalcogenide glasses, it was observed that changes in the optical properties occur after 50 Mrad [22, 51, 69, 70]. These glasses were 1 mm in diameter, and therefore the changes required a significant amount of dose to become detectable. The absorption spectra shown below illustrates the photodarkening behavior of As-S chalcogenide glasses under gamma radiation in addition to the reversibility of these effects by annealing the glass at various temperatures [22].



**Figure 27** Optical transmission spectra of  $v\text{-As}_2\text{S}_3$  before (1), after 1Grad radiation dose (2), annealed at various temperatures 330K, 370K, 380K, 395K, 420K, and 440K, shown in curves 3-8, respectively [71]. The pre-irradiation spectrum reveals that  $\text{As}_2\text{S}_3$  has 30% transmission at 600 nm, exposure to 1Grad.  $^{60}\text{Co}$  gamma rays resulted in a shift of this absorption edge towards higher wavelengths. Post exposure annealing of the glasses at various temperatures gradually returned the glasses to the pre-irradiation absorption spectrum.

Other investigations were performed at lower radiation doses with similar glass dimensions 2-3 mm in Ge-As-Se glasses [72]. In this study, it was revealed that the composition of the glasses determines the sensitivity towards radiation [72]. The researchers varied the amount of  $\text{GeSe}_2$  glass with respect to the amount of  $\text{As}_2\text{S}_3$  glass, and studied the optical bandgap variation from the pre-irradiated measurement to post irradiated measurement [72]. The glasses containing the highest amount of  $\text{GeSe}_2$  glass composition obtained the highest change in the bandgap while the lowest concentration of Ge-containing glass did not obtain any change in bandgap up to 5 Mrad [72]. This result suggests that germanium containing chalcogenide glasses are more sensitive to low doses of gamma radiation when compared to arsenic containing glasses. Other research groups confirmed similar results in other bulk chalcogenide glasses that were irradiated at various radiation doses [73-80]. Another prominent study using bulk glasses was performed on a highly Se-rich glasses to study the change in conductivity, and the

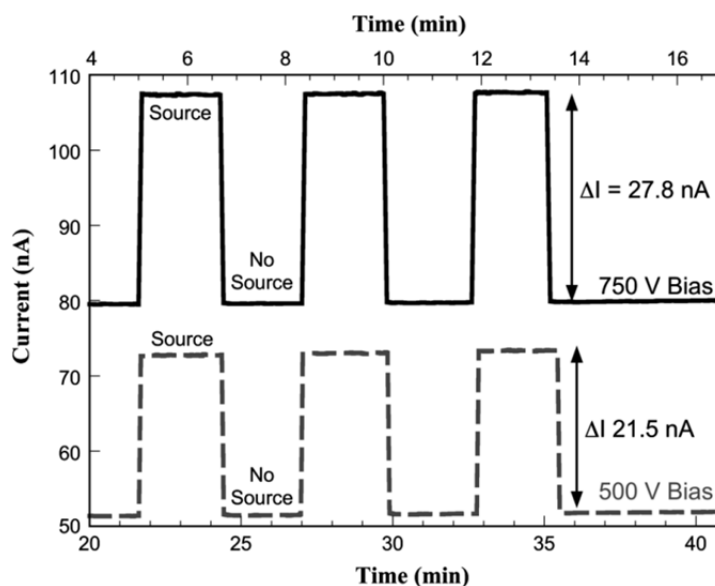
Current vs. Voltage behavior of bulk  $\text{Se}_{92}\text{Sn}_8$  glasses [81]. This study uncovered that in such Se-rich glasses, the density of states, and the bandgap of the material have a monotonic increase up to 2Mrad [81]. After 2Mrad, the density of states, and bandgap decrease [81]. The cause for these changes is still under research.

The aforementioned optical studies have been performed on bulk glasses, which have the benefit of being able to produce a high signal for the analysis purposes, but it is difficult to detect subtle changes that could predict the start of the structural changes. This capability is achievable in thin chalcogenide films, which do not produce a high signal to noise ratio due to lack of physical material but subtle changes are easily detectable. Some research regarding thin films performed on  $\text{Se}_{76}\text{Te}_{15}\text{Sb}_9$  thin films on transparent glass substrate [82]. From transmittance, and reflectance measurements, the absorption edge showed an increase in the transmittance as well as increasing the calculated absorption coefficient [82]. Other research has been performed on  $a\text{-Se}_{90}\text{In}_{10-x}\text{Sn}_x$  [83],  $\text{SbSe}_{2.5}$  [84] and  $\text{Se}_{70}\text{S}_{30-x}\text{Sb}_x$  [85] to name a few. These studies revealed that at high radiation dose, and with high Se concentration films, it is possible to crystallize Se [84]. Additionally, increasing the gamma radiation dose in all three compositions leads to a bandgap decreases, which parallels the observations in bulk glasses. The consensus from studying various types of glasses, and types expounded that Arsenic, and Germanium containing glasses are highly sensitive towards gamma radiation, and these types of glasses exhibit the greatest structural changes.

#### Chalcogenide Glasses as Dosimeters

Application of chalcogenide glasses for radiation sensing has recently been investigated due to the above-mentioned structural, and optical changes in the presence of

gamma radiation. The benefits of creating these changes will result in a change in the conductivity of the material. In current research, the effects that were studied were static in nature, but the dynamic changes, which are difficult to detect, also play a major role in the conductivity. To study the static, and dynamic changes in conductivity, various studies were performed on pure chalcogenide glasses. One such study consisted of studying various amorphous semiconductors [86]. The authors studied four types of bulk glasses  $\text{CdGe}_{0.85}\text{As}_2$ ,  $\text{As}_{40}\text{Se}_{48}\text{Te}_{12}$ ,  $\text{As}_{40}\text{Se}_{60}$ , and  $\text{As}_{40}\text{Se}_{48}\text{Te}_{12}$  under gamma radiation, and  $\alpha$ -source [86]. Exposure to the  $\alpha$ -source generated a change of 36 nA in the current vs. voltage characteristics from the pre irradiation state to the post irradiation state in  $\text{CdGe}_{0.85}\text{As}_2$  glasses [86]. Similarly, the  $\text{As}_{40}\text{Se}_{48}\text{Te}_{12}$  bulk glasses were also tested, but these glasses were tested in situ to capture all the effects. In this experiment, the glass was either exposed to or shuttered from the  $\alpha$ -source, while a constant voltage bias was applied to the material [86]. Below is the resultant figure from this experiment.

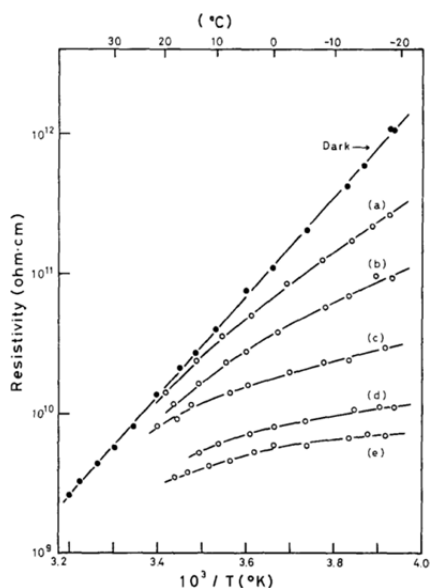


**Figure 28** *In situ* measurement of  $\text{As}_{40}\text{Se}_{48}\text{Te}_{12}$  glasses, irradiated with  $\alpha$ -source [86]. These glasses were biased with a 500V, and 750V constant DC bias, and exposed to radiation, and shuttered from the radiation. The results show a high sensitivity, and an instantaneous change due to exposure to radiation © 2009 IEEE.



Based on the graph shown above, it can be stated that the sensitivity of such amorphous material is very high, and this effect can be applicable for detecting radiation. Additionally, for applications similar to CZT, and Ge detectors mentioned in the previous chapter, the amplification of the electric field across the material greatly increases the ionization current, and in  $\text{As}_{40}\text{Se}_{60}$  glasses the DC ionization current is linearly dependent on the applied electric field [86].

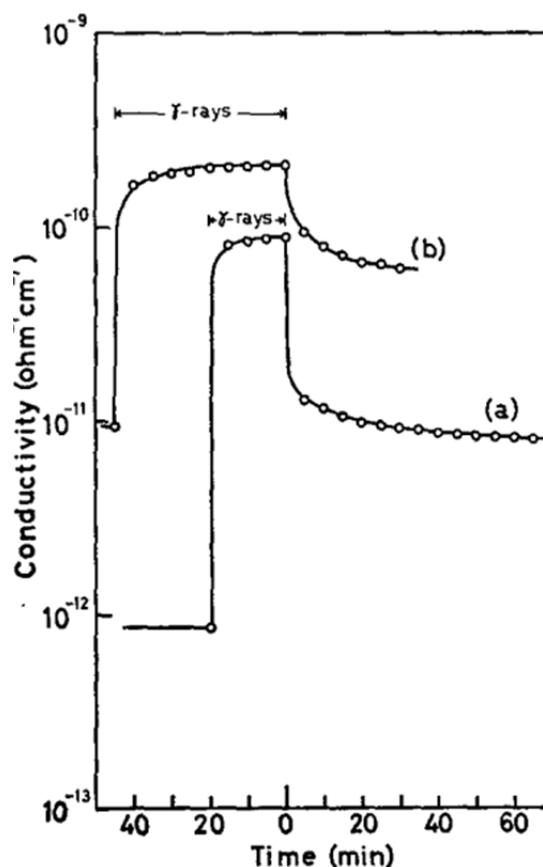
Other research conducted on the application of chalcogenide glasses as radiation dosimeters exhibited that the steady state character of  $\text{AsS}_{3.5}\text{Te}_{2.0}$ , and  $\text{AsSe}_{1.5}\text{Te}_{1.5}$  show a decrease in resistivity when measured at discrete radiation doses [87].



**Figure 29** Resistivity of  $\text{AsS}_{3.5}\text{Te}_{2.0}$  measured at dark, a) 1.3 krad, b) 5.2 krad, c) 24 krad, d) 110 krad, and e) 240 krad [87]. The trend that is observed from this study reveals that increasing the gamma dose causes a decrease in the resistivity.

The results in Figure 29 were acquired after irradiation when all the dynamic changes have been subsided. Even though the results depict the changes due to the static behavior of the glasses, there is an important aspect presented in this data. The static

nature of the glasses present a decrease in the resistivity, thus it can be deduced that the *in situ* measurement of the current vs. voltage measurement would reveal an instantaneous rise in the current when exposed to gamma radiation. This type of experiment was performed by Minami *et al.*, as shown below [87].



**Figure 30** a)  $\text{AsS}_{3.5}\text{Te}_{2.0}$  exposed to 73.3 krad gamma dose and b)  $\text{AsSe}_{1.5}\text{Te}_{1.5}$  36.6 krad gamma dose [87]. There are three stages: low conductivity pre exposure, high conductivity during exposure, and exponential decay of conductivity post exposure. The low conductivity is attributed to the bare glass conductivity. The high conductivity region is attributed to the formation of dynamic, and static changes, which enhance the conductivity of the material. Post exposure exponential decay is due to the disappearance of the dynamic changes.

There are a few specifics regarding Figure 30 that require further explanation.

Initially prior to the exposure to radiation, the conductivity of the glasses is extremely low,  $10^{-11}$ , and  $10^{-12} \Omega^{-1} \text{cm}^{-1}$  for the selenium containing, and sulfur containing glasses

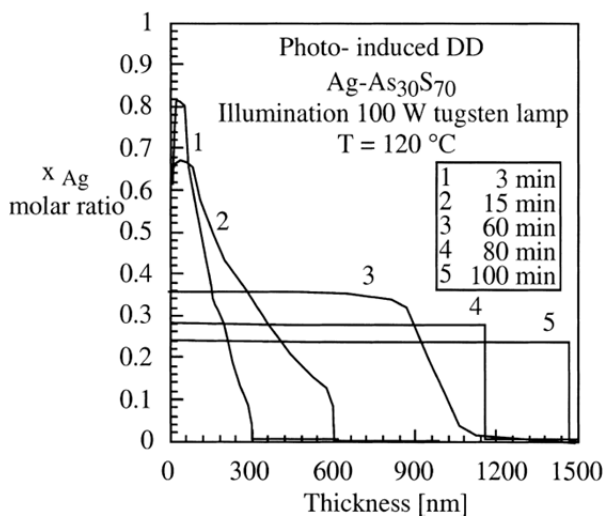
respectively. After initial exposure to  $\gamma$ -rays, the conductivity incurs a sharp rise due to the newly generated defects, localized electric fields, and structural changes. Immediately after the shutter to the radiation source is closed, there is an instantaneous decline in the conductivity, which is attributed to the disappearance of the dynamic changes. As these changes vanish, the conductivity declines but does not incur the same instantaneous change as observed when the material was initially exposed to the radiation source. Eventually a majority of the charges, and defects recombine, which alters the conductivity of the material to a value similar to the original pre-irradiation state.

This type of decay can be minimized with the aid of a methodology, which can capture both the static, and dynamic changes, and represents an integral change in the material conductivity. Here arises the use of metals such as silver (Ag) atoms as dopants that can become ionized by the radiation, and binds with the newly formed defects thus capturing, and freezing the newly formed defects in order to become sensed. Unfortunately, there is no prior or current research related to investigating this issue under the presence of gamma radiation, which contributes to the novelty of this research. On the other hand, silver incorporation into chalcogenide glasses has been thoroughly investigated using sub-bandgap light. Since the exposure to gamma rays, and sub-bandgap light produces similar changes in bare chalcogenide glass, it is expected that these results can be extrapolated to gamma radiation.

## Silver Containing Chalcogenide Glasses

### Silver Diffusion Properties

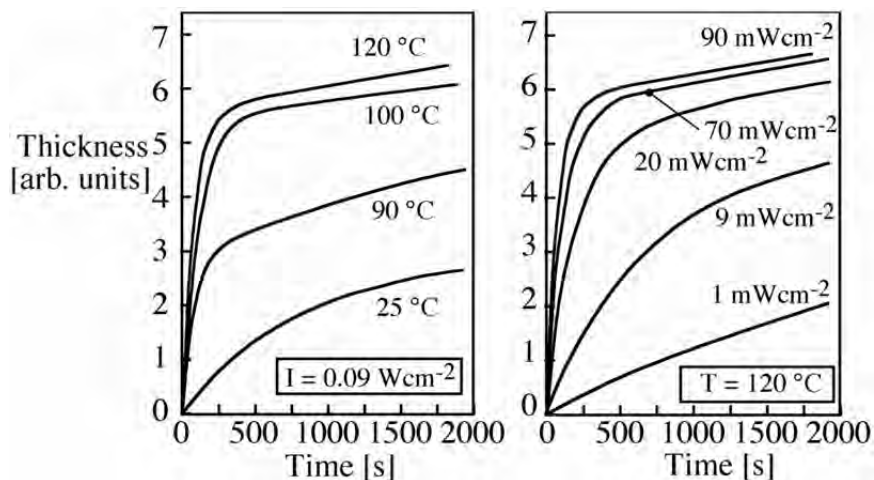
The addition of silver into chalcogenide glasses enhances the optical, electrical, and mechanical properties of these glasses for the application as sensors, batteries, memory devices, and optical recordings [88-94]. All of these types of discoveries were only possible due to the unique properties that are derived when silver diffuses into chalcogenide glasses. Silver diffusion has specific characteristics, which have been compiled, and explained in detail [94]. When silver diffuses into chalcogenide glasses, the process follows Fick's laws of diffusion with a small caveat. Under conventional diffusion processes, the diffusing material will diffuse up to a point, and then exponentially decrease in concentration, but silver diffusion has been observed to have a step-like diffusion profile [94]. Step-like diffusion profile is highly convenient because once silver has diffused to a specific distance, the silver concentration is uniform up to that distance, and no silver diffuses beyond this point, as shown in Figure 31.



**Figure 31** Step-like diffusion profile of Ag in As<sub>30</sub>S<sub>70</sub> [94]. Silver diffuses up to a certain distance at which distance there is an abrupt change in the silver concentration. This abrupt change is evident in the above graph for 80, and 100 mins of exposure.

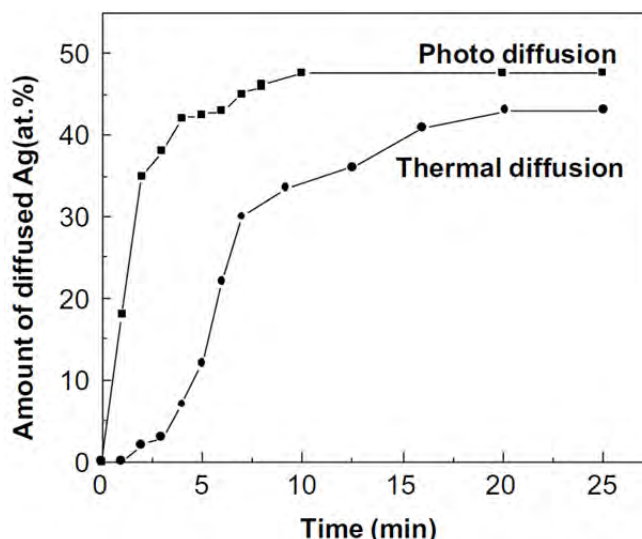
Silver diffusion occurs in three stages explored in detail by Kolobov, and Elliot [95]. The three stages of silver diffusion include an induction period, effective photodissolution, and exhaustion stages [95]. The diffusion rate is minimal in the induction period, followed by the maximum diffusion rate in the effective region, and then when the silver source begins to become exhausted, the rate decreases until silver concentration is uniform throughout the chalcogenide glass. Some researchers claim that the induction period does not exist since the diffusion rate is minimal, and difficult to detect [96, 97]. At the end of the induction period, arises the effective dissolution region where researchers found a square root of time dependence on the silver film thickness [98-100]. The final stage of the silver diffusion is the exhaustion of silver.

The three primary factors that affect the three stages of silver diffusion are temperature, light intensity, and electric field. There are many other mechanisms that affect silver diffusion but the above-mentioned three factors greatly change the diffusion of silver. According to Fick's laws of diffusion, temperature is a primary mechanism that drives the diffusion of diffusing species into a medium. Similarly, silver in chalcogenide glasses also behaves in a similar manner as shown by Wagner [101]. The next major mechanism is silver diffusion through light illumination also known as photodiffusion. The diffusion of silver can occur in the dark, but the diffusion rate is significantly higher when the chalcogenide glass with silver is exposed to light illumination [94, 97, 101-103]. Increasing the light intensity drastically decreases the time required to achieve silver saturation. The following figure illustrates the dependence of the silver thickness on the temperature, and the illumination intensity [101].



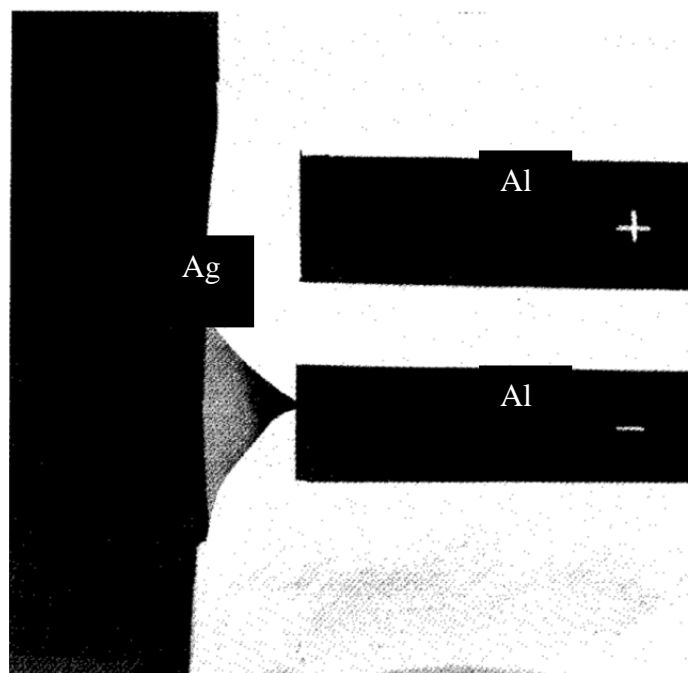
**Figure 32** Temperature, and light intensity effect on silver diffusion in  $\text{As}_{30}\text{S}_{70}$  glasses [101].

Even though, both temperature and light illumination can increase the silver diffusion rate within chalcogenide glasses, the group of Mitkova *et al.* have shown that photodiffusion of Ag results in a faster introduction, and higher silver concentration when compared to thermal diffusion [104]. Increased illumination times results in an increase in the amount of diffused silver within the matrix of the  $\text{Ge}_{20}\text{Se}_{80}$  glass, as shown in Figure 33 [104].



**Figure 33** Photodiffusion, and thermal diffusion of silver in  $\text{Ge}_{20}\text{Se}_{80}$  [104]. In comparison, photodiffusion introduces a greater amount of silver in a shorter time into the chalcogenide glasses than thermal diffusion.

The third mechanism involves the effect of electric field on the diffusion of silver. This is the primary mechanism behind the novel chalcogenide glass based non-volatile memory known as Programmable Metallization Cell (PMC) [88, 105]. Electric field effect is evident in Figure 34 where two inert aluminum electrodes were biased at positive, and negative electric potentials, and a silver electrode was maintained unbiased [95]. The energy provided by the electric field is sufficient to create a red-ox reaction between the silver electrode, and the negatively biased aluminum electrode.

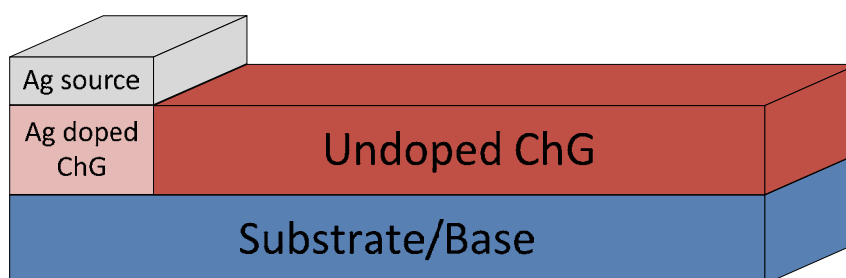


**Figure 34** Electric field enhanced lateral silver diffusion in Al modified  $As_2Se_3$  glasses [95]. The two aluminum electrodes were biased at positive, and negative voltage biases while the Ag source was unbiased. There is an evident growth of a silver bridge between the Ag source, and the negatively biased Al electrode illustrated in the figure.

In addition to directly influencing silver diffusion, the application of an electric field can aid in photodiffusion [106]. When the applied electric field is greater than

125V/m, the electric field directly affects the movement of silver ions in  $\text{As}_2\text{Se}_3$  glasses [106].

For the purposes of a radiation sensing, photodiffusion of silver is the primary mechanism behind the functionality of these devices. Therefore, from this point onwards, the discussion of silver diffusion will pertain to photo-induced silver diffusion unless otherwise specified. There are two types of silver diffusion, lateral, and vertical silver diffusion. The mechanics of both types of diffusion are similar in nature, where the three stages of diffusion, and the same mechanisms that drive vertical diffusion are also valid for lateral diffusion. Initial discoveries were performed on vertically stacked sandwich films, therefore the induction period is difficult to detect since this stage could occur during the deposition of the topological layer of silver. On the other hand, in lateral diffusion, the induction period is classified as the time where the topological layer has diffused vertically in the chalcogenide glass as shown in the figure below.



**Figure 35 Post induction period in lateral diffusion of silver [95].**

At this point of time, the diffusion front is confined to the immediate area underneath silver source, which is followed by lateral movement of the Ag doped area until the source of pure silver is completely exhausted. Another important aspect that governs the diffusion rate is the direction of the light source, i.e. the light source directed



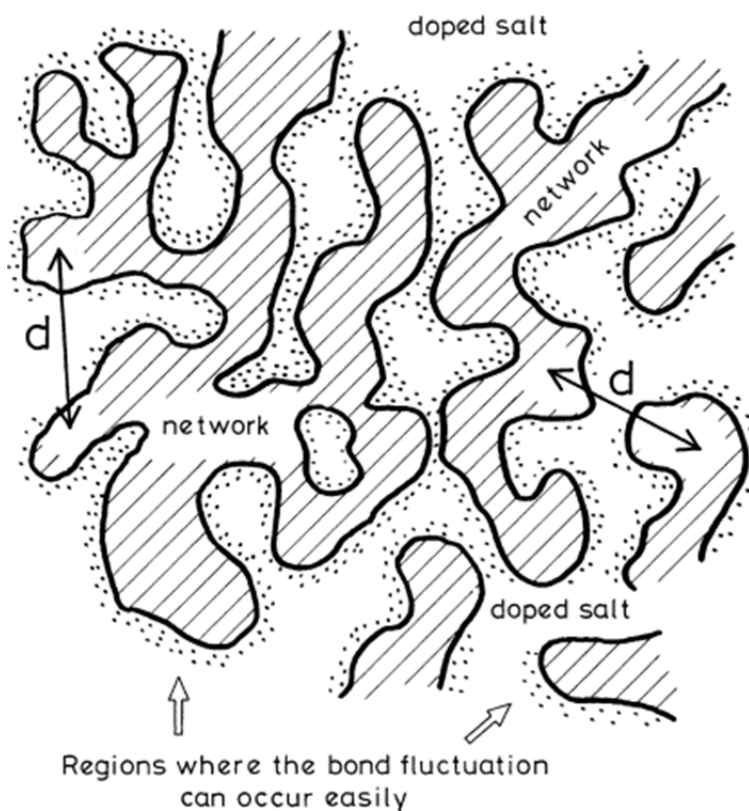
at the silver film or the light illuminated from the backside of a transparent substrate. The intensity of the light source when located on the opposite side of the substrate will be significantly less than when placing the light source on the silver side, due to the attenuating factors that drastically reduce the intensity because of the interaction with the substrate, and the chalcogenide film [95].

Neutral silver atoms do not randomly diffuse into chalcogenide glasses. They are first required to be ionized forming  $\text{Ag}^+$  ions. In the previous example, the light source directly ionizes the silver atoms, creating  $\text{Ag}^+$  ions that can diffuse into the chalcogenide structure [107-109]. Another method for ionizing silver is the capture of a free hole by a silver atom creating a  $\text{Ag}^+$  ion [107-109]. Three additional methods for creating  $\text{Ag}^+$  ions are the chemical reaction between the silver atom, and chalcogen atom resulting in the formation of a silver containing compound, the movement of silver ions due to the presence of a concentration gradient, and the dissolution of homopolar bonds between chalcogen atoms that attract silver atoms forming silver-chalcogen molecules [107-109]. It is important to mention that each of these ionization methods is interdependent; therefore, it is difficult to isolate one method from another. The combination of these methods provides the remarkable properties for a myriad of applications.

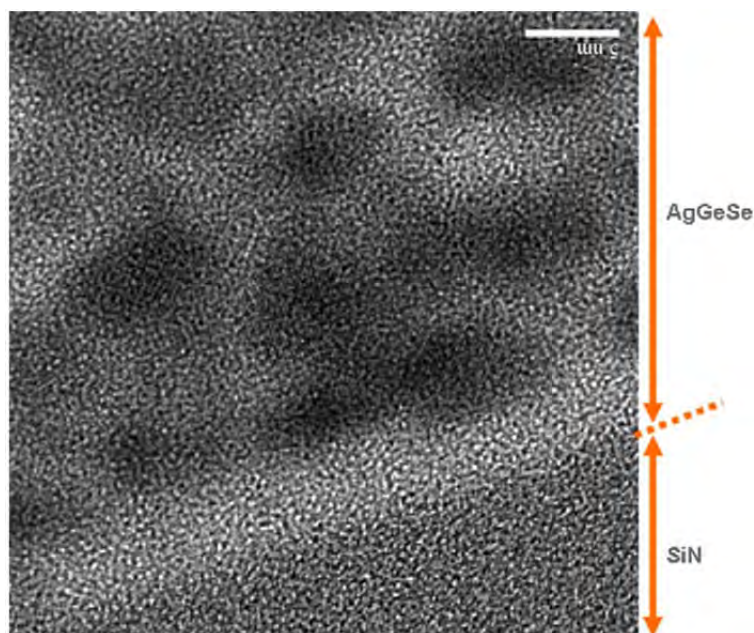
#### Cluster Bypass Model

After ionization, silver ions do not randomly move throughout the structure. The movement of these ions is highly dependent on the neighboring structure, and the free volume of the amorphous film. Research into the macroscopic structure of the glasses revealed that the free volume in Ge-Se glass varies between 10-15% where the highest amount of free volume is available within  $\text{Ge}_{33}\text{Se}_{67}$  glasses, and the lowest volume is in

the Se-rich films [110]. The free volume within chalcogenide glasses creates a localized network, which has been explored in the cluster bypass model [51]. Along with the cluster pathway model, other models have been proposed to describe the diffusion of silver within these materials such as the, anderson-Stuart model or Percolation model [76-78]. The cluster pathway model is an appropriate method to visualize the free volume within chalcogenide glasses, and the possible regions of silver diffusion. This model states that there are two types of regions within the glass with distinct densities. The first region consists of clusters of highly dense chalcogenide glass network separated by van der Waals forces, which corresponds to the low density area [111]. The regions outside of the highly dense clusters are considered as the preferred regions or pathways for ion conduction [111]. A visual of this type of model is represented in Figure 36.



**Figure 36** Illustration of the cluster bypass model: areas with diagonal lines represent the chalcogenide glass network, and the regions specified as doped salt are pathways within the glasses where silver can diffuse [111].



**Figure 37** High resolution TEM of photodoped Ag in GeSe chalcogenide glass. Dark regions represent the clusters, and pathways are created where silver can diffuse throughout the glassy film [112].

### Diffusion Products

In the section above, the cluster bypass model illustrated the presence of pathways for silver diffusion, but silver ions do not completely diffuse from one end of the pathway to the other unless there is a large enough force that attracts the ionized silver particles. For example, in the Programmable Metallization Cell (PMC) devices, there is an applied electric field, which attracts/repels silver ions. On the other hand, when the chalcogenide glass, and silver are exposed to sub-bandgap light or gamma radiation, the silver ion diffuses through the pathway until it is captured by a negatively charged defect. After the silver ion, and defect combine, a new molecule is formed that has a significantly different conductivity when compared to the bare chalcogenide glass. To discuss the change in

conductivity, it is important to consider the photodoping mechanism from the perspective of the energy band diagram. When the chalcogenide glass is illuminated by a light source, an electron in the valence band, localized states, or band tail states is excited to the conduction band [80]. The hole generated during the illumination, which is also near the silver/chalcogenide interface, is captured by a silver atom creating a silver ion [80]. This silver ion is attracted to a negative defect, resulting in the creation of a localized state situated in the middle of the bandgap [80]. This new state acts like a level within the bandgap, and reduces the bandgap of the glass, which in turn increases the conductivity of the material, thus increasing the sensitivity to higher wavelengths than the bare material [80]. Increasing the illumination time will generate a greater number of electron-hole pairs, and thus increase the silver incorporation into the chalcogenide glass matrix, which also decreases the bandgap of the material. Similar observations of decreased bandgap have been made by researchers investigating  $\text{AgSbSe}_2$ ,  $\text{Ag}_{10}\text{Te}_{90}$ , and  $\text{Ag}_x\text{As}_{50-x}\text{Te}_{50}$  ( $3 \leq x \leq 20$ ) thin films under gamma radiation [85, 86, 113].

The physics behind the change in conductivity can be explained by the changes in the bandgap, but a question can arise regarding the origin of these changes; is it due to the creation of pure silver or silver containing diffusion products? This question can be answered based on the background chalcogenide structure since each specific glass composition will reveal its characteristic silver containing diffusion products. For radiation sensing, it was revealed in the previous section that the prime candidates for radiation sensing are As, and Ge based chalcogenide glasses, but Ge containing glasses present higher sensitivities, therefore the following discussion will be focused on Ge-Ch binary glass systems.

There are two types of silver containing products, binary, and ternary, where the binary consists of  $\text{Ag}_2\text{X}$  ( $\text{X} = \text{S}, \text{Se}, \text{or Te}$ ). For example, in the Ag-Se system, the binary compound forms an orthorhombic ( $\beta$ -phase) or body centered cubic ( $\alpha$ -phase) structures [114]. The  $\beta$ -phase is the primary stable phase at room temperature, while the  $\alpha$ -phase is only stable at higher temperature:  $\text{Ag}_2\text{S} > 179^\circ\text{C}$ ,  $\text{Ag}_2\text{Se} > 133^\circ\text{C}$ ,  $\text{Ag}_2\text{Te} > 150^\circ\text{C}$ . This phase is the most tightly packed crystal when compared to the  $\beta$ -phase. In addition to the structure, the  $\alpha$ -phase is also a super ion conductor in comparison to the  $\beta$ -phase, which is narrow band semiconductor. The following table compares the conductivities of the binary compounds with respect to each phase.

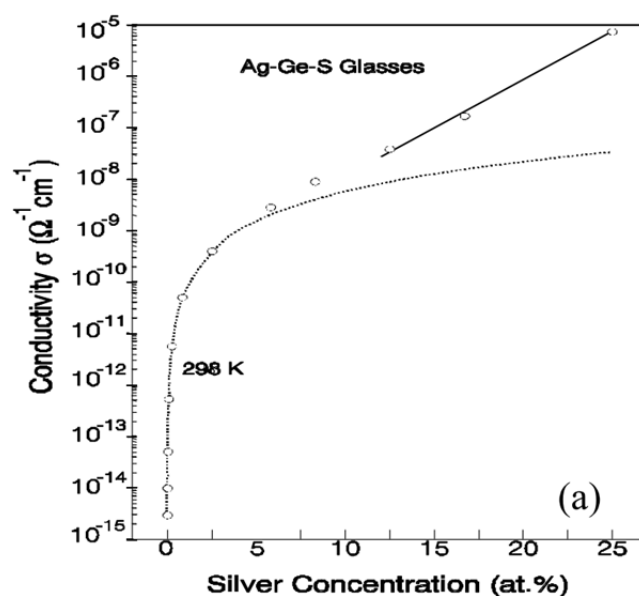
**Table 4** Room temperature, and high temperature conductivities of Binary  $\text{Ag}_2\text{X}$  ( $\text{X} = \text{S}, \text{Se}, \text{or Te}$ )

Binary Silver-Chalcogenide	Conductivity of $\alpha$ -phase ( $\Omega^{-1} \text{cm}^{-1}$ )	Conductivity of $\beta$ -phase ( $\Omega^{-1} \text{cm}^{-1}$ )
$\text{Ag}_2\text{S}$	4.1 [114]	$6 \times 10^{-3}$ [88]
$\text{Ag}_2\text{Se}$	3.1 [114]	$9.8 \times 10^{-6}$ [89]
$\text{Ag}_2\text{Te}$	1.0 [114]	$4.3 \times 10^3$ [91]

The other type of Ag-containing diffusion product is the ternary phase, which is a combination Ag-chalcogen atom-Ge atoms. Unlike the binary phase, the ternary is purely semiconductor in nature.

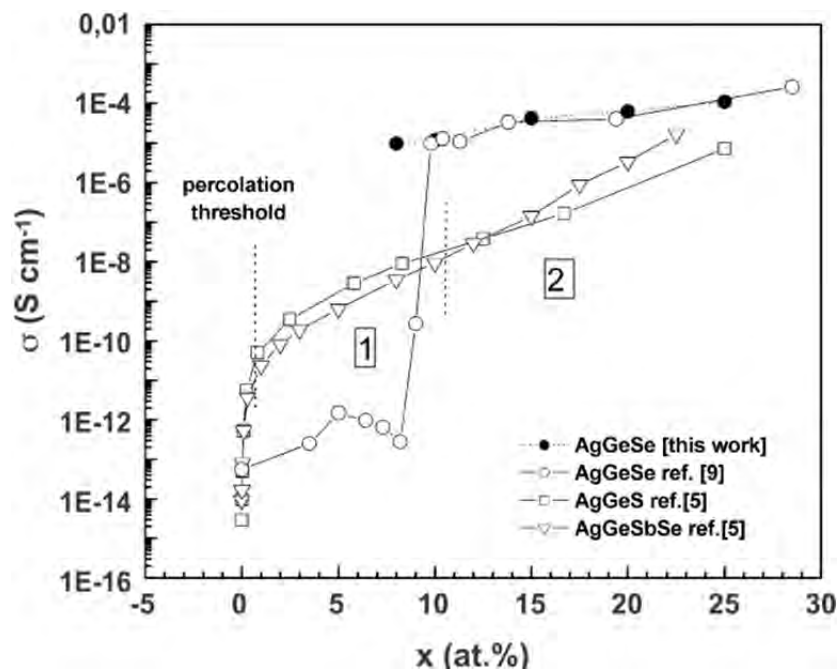
Measuring the conductivity of Ag-photodoped chalcogenide glass using sub-bandgap light or gamma radiation does not result in the contribution from only the conductivity of the binary phase or the ternary phase but a combination of these two phases in addition to the bare glass. During the photodoping process, silver atoms are incrementally introduced into the backbone structure, therefore it is important to

understand the complete picture, which has been presented in this section, i.e. the behavior of silver in chalcogenide glass, the regions of the glass that are amicable for silver movement, and finally the byproducts generated when silver bonds with the glass. It is expected that incremental addition of silver will similarly incrementally increase the conductivity of the highly resistive amorphous backbone glass due to the incorporation of higher conductivity regions within the glasses. Experiments performed by M. Ribes *et al.* report a strong effect of silver on the change in conductivity of the glasses [115]. Glasses for this experiment were produced by taking specific amount of germanium, sulfur, and silver, and creating glassy alloys [115]. By varying the silver concentration of the glasses, measurements revealed that the addition of only 5 at. % of silver into the glass matrix created a 6 orders of magnitude change in the conductivity of the glasses, as shown in Figure 38 [115].



**Figure 38** Change in conductivity as a function of silver concentration in Ge-S glasses [115]. These measurements reveal that with the addition of 5 at.% of Ag incurs a 6 orders of magnitude increase in the glass conductivity.

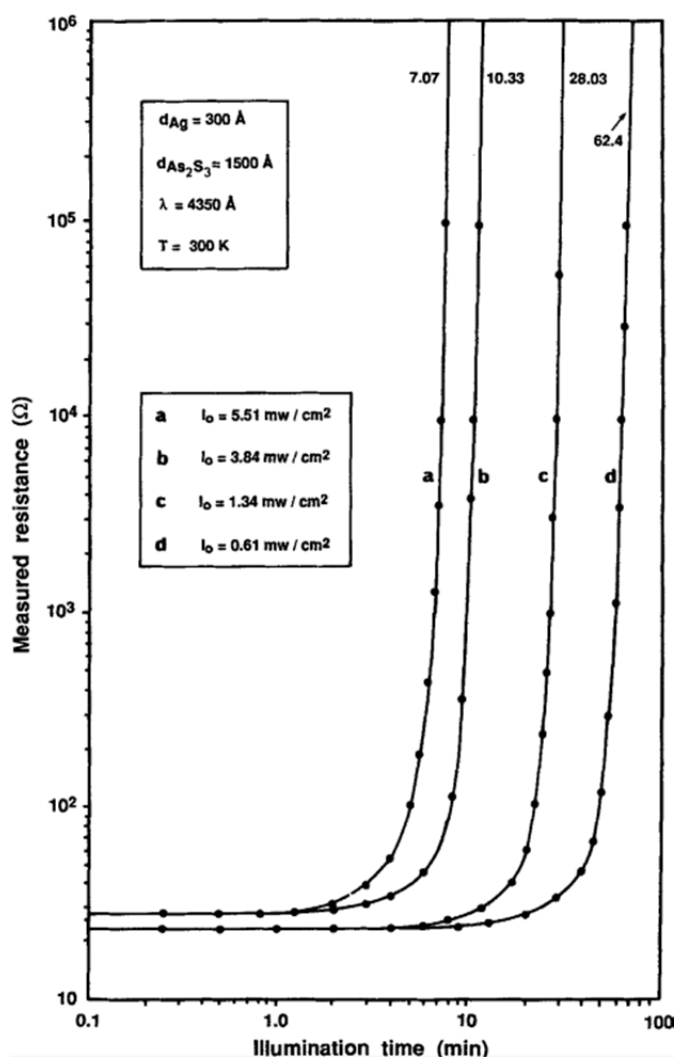
A similar result has been confirmed by Ureña *et al.* in Ge-Se chalcogenide system, who observed that with 10 at. % of silver, results in 7 orders of magnitude increase in the conductivity [116]. This result is shown in Figure 39.



**Figure 39** Change in conductivity as a function of silver concentration in Ge-Se glasses [117]. Various studies confirm the finding that 10 at.% of silver results in 7 orders of magnitude change in conductivity.

Therefore, it can be summarized from the previous two types of studies that the introduction of a very small amount of silver into the chalcogenide glasses creates a significant change in the conductivity. These studies are related to glassy alloys containing specific atomic percentage of silver, but photodoping using sub-bandgap or gamma radiation will introduce an unspecified amount of silver, which is a function of the illumination dose, and thickness of the silver source. To determine whether photodoping will result in a similar change in conductivity, a corollary experiment performed by Kolobov, and Elliott can be considered [95]. In this experiment, a film of

chalcogenide glass was created, which was covered with a thin layer of a continuous film of silver, and the entire stack was illuminated by various intensities of visible light while constantly monitoring the sheet resistance of the stack [95]. Their experiment demonstrated that using a high intensity light for short period of time or a low intensity light for a longer time resulted in a similar behavior [95].



**Figure 40** Change in sheet resistance due to silver photodiffusion [95]. Chalcogenide glasses with a topological layer of silver films were fabricated, which were used to measure the sheet resistance during the exposure to light sources with different intensities. Results reveal a similar behavior in sheet resistance once an equivalent radiation dose has been achieved with different illumination sources.



Therefore, it can be concluded that the change in conductivity observed by Ribes *et. al.* [115], and Ureña *et. al.* [117] is in cohesion, if the films were photodiffused with silver instead of creating silver containing alloys.

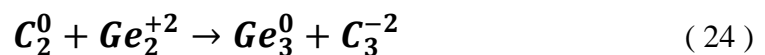
### **Germanium Containing Glasses**

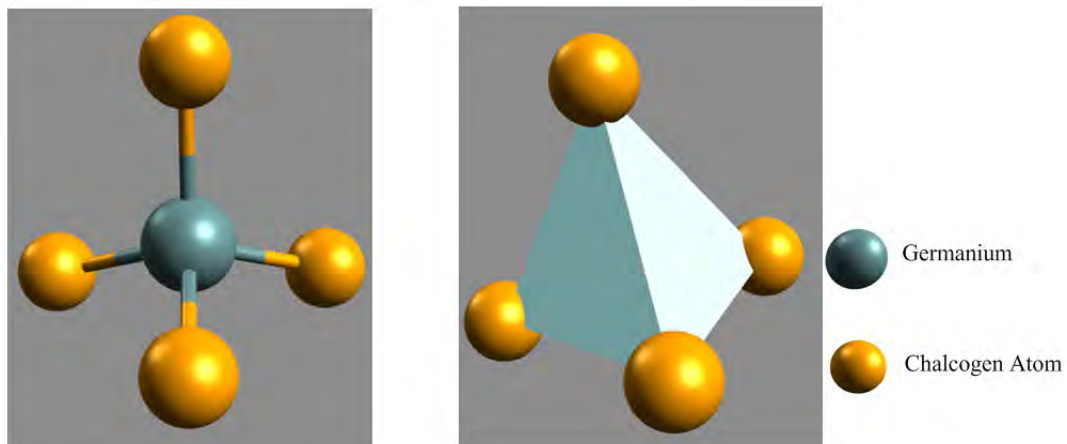
Until this point, it was shown that certain types of chalcogenide glasses are highly sensitive towards gamma radiation, the conductivity of these glasses increases in the presence of gamma radiation but subsides after the cessation of radiation. The addition of silver into the glasses will aid in capturing the changes that occur due to radiation, and the addition of silver enhances the conductivity change with the incorporation of less than 10 at.% of silver.

For radiation sensing purposes, arsenic, and germanium based glasses are highly sensitive, but out of these two types of glasses, germanium containing glasses offer unique properties when compared to arsenic based glasses. The primary difference between these two types of glasses is attributed to the four fold coordinated Ge atom in comparison to the three fold coordinated As atom. This leads to the formation of highly coordinated glasses, which result in a high glass temperature i.e., the thermal stability of the glasses is higher, and Ge-containing glasses are not as toxic as the As-containing counterparts. The tetrahedral shape is considered the strongest molecular geometry, which provides Ge-containing glasses better structural properties than ones containing Arsenic.

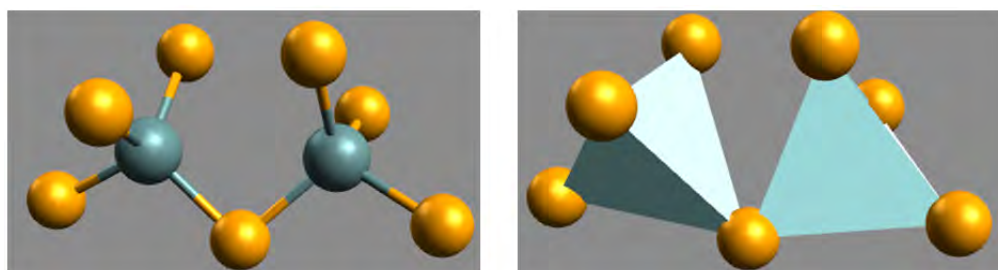
The tetrahedral structure is created with a germanium atom at its center surrounded by chalcogen atoms as the basic unit structure (see Figure 41). Each base tetrahedron is connected to each other by one of three main structures depending on the

availability of chalcogen atoms in the vicinity. In chalcogen-rich glasses, two tetrahedrals are connected using a single chalcogen atom, therefore connecting the two tetrahedral by their corners forming corner-shared structure (see Figure 42). The corner-shared structure consists of seven chalcogen, and two germanium atoms. Reducing the number of chalcogen atoms available for bonding results in the creation of edge-shared structures where two tetrahedrons are sharing two adjacent chalcogen atoms, consisting of six chalcogen atoms, and two germanium atoms (see Figure 43). The third type of structure occurs in a situation where germanium atoms do not have sufficient chalcogen atoms in the vicinity to create four heteropolar bonds, so the germanium atoms are forced to bond with another germanium to create a structure called ethane-like (see Figure 44). There exists another type of structure that is prevalent in chalcogen depleted glasses, where both the germanium, and chalcogen atoms are three-fold coordinated. This type of structure is known as layered rocksalt structure. This structure occurs only when there is a Ge atom with an unsatisfied bond in a location where all neighboring chalcogen atoms have sufficient bonds to fulfill the 8-N rule. In this situation, the Ge atom forms a dative bond with the lone pair p-electrons of a neighboring chalcogen atom. The two electrons required to satisfy a bond are supplied by the chalcogen atom, and these electrons orbit around both the chalcogen atom, and the Ge atom in this type of a bond. This creates layers of the rocksalt structure, which are separated by van der walls forces (see Figure 45). Additional description of dative bonding, such as origins, and detection of this bond, are explained in detail [118]. An added benefit of the layered structure is the generation of a -2 columbic charge attributed to the chalcogen atom, as shown in the equation below.

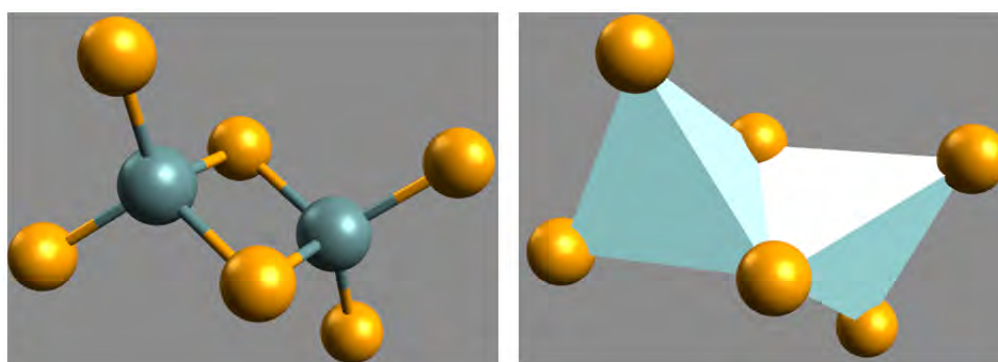




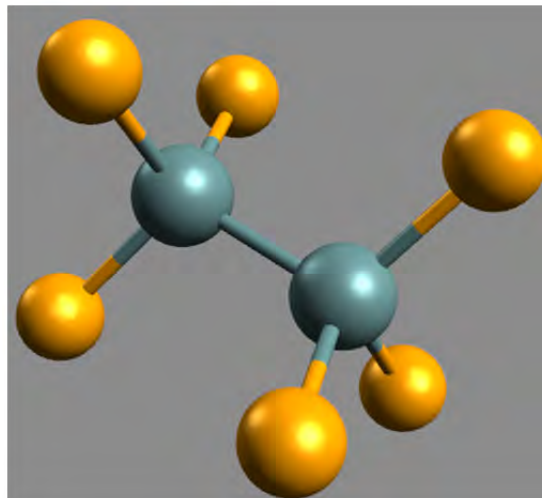
**Figure 41 Basic structural unit: (a) Bonding between Ge, and Chalcogen atom and (b) Single tetrahedral unit.**



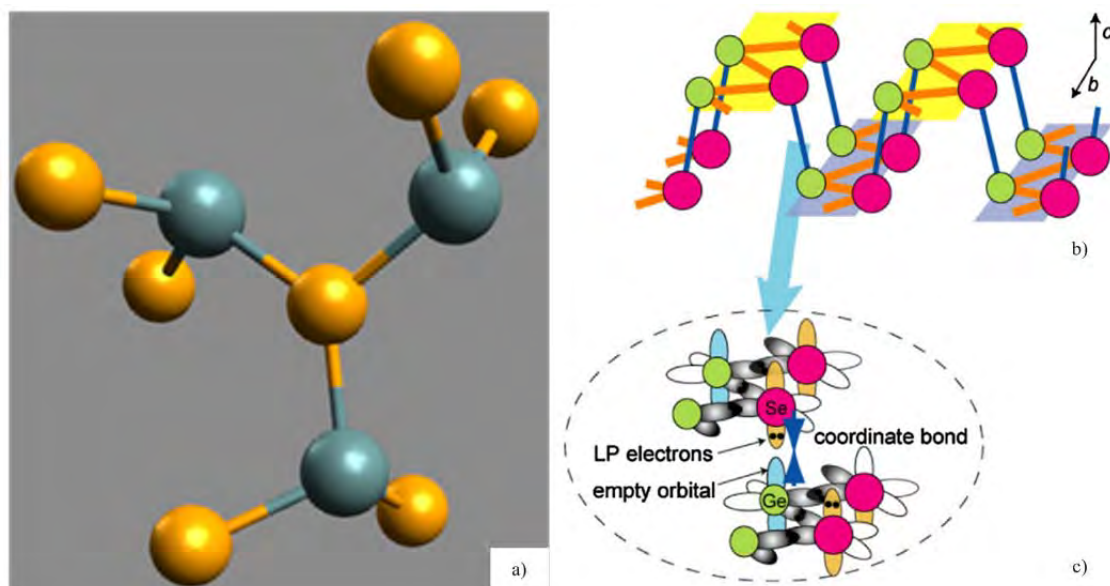
**Figure 42 Corner-Shared Tetrahedral.**



**Figure 43 Edge-Shared Tetrahedral.**



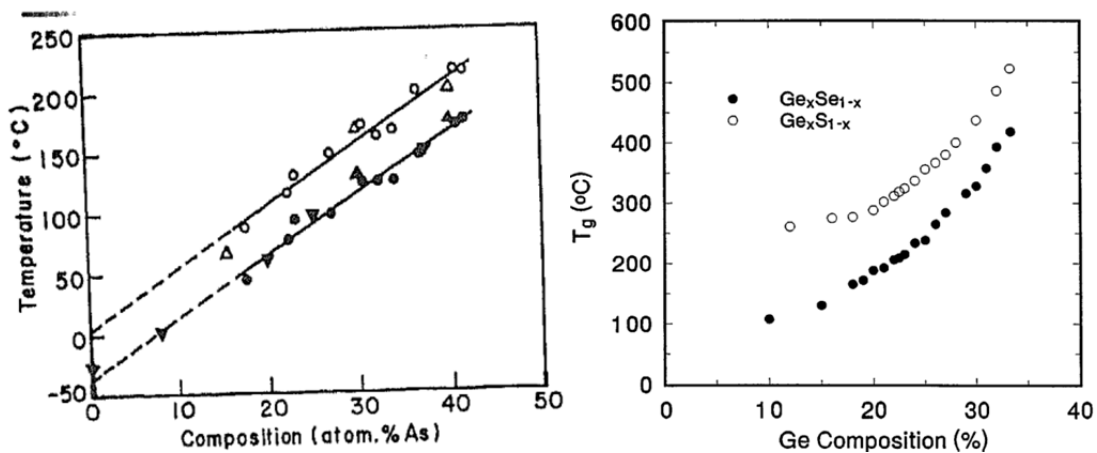
**Figure 44 Ethane-like bonding.**



**Figure 45 Layered rocksalt-type structure a) molecular structure, b) formation of layered structure due to the existence of dative bonds [118], and c) origin of the dative bonding [118].**

The tetrahedral structure in combination with the above mentioned structural units enhance the glass transition temperature ( $T_g$ ) in Ge-containing glasses. The benefit of a higher glass transition temperature allows the flexibility for the application of these types of sensors in a myriad of environments. For example, the glass transition temperature of

$\text{As}_{40}\text{S}_{60}$ , which is three-fold coordinated is  $212^\circ\text{C}$ , while the four-fold coordinated Ge-containing glasses exhibit a higher  $T_g$ , as illustrated in the Figure 46 a), and b) [119, 120].



**Figure 46** Glass transition temperature for a)  $\text{As}_x\text{S}_{1-x}$  [119], b)  $\text{Ge}_x\text{S}_{1-x}$ , and  $\text{Ge}_x\text{Se}_{1-x}$  [120].

## FILM CHARACTERIZATION METHODS

### **Methods of FILM ANALYSIS**

Various methods have been applied to aid in the characterization of the films.

Each type of analysis offers a different perspective towards enlightening the mystery that is related to the radiation-induced effects in chalcogenide glasses. Energy dispersive X-ray Spectroscopy, Raman Spectroscopy, Atomic Force spectroscopy, X-ray Photoelectron spectroscopy, and X-ray Diffraction are the methods used in this dissertation. Prior to presenting the results of these experiments, it is important to understand the different capabilities of each type of method.

#### Spectrophotometer

The use of spectrophotometer offers a unique insight into the absorption edge of the films, and through special processing methods could lead to the determination of the bandgap of the material. The optical bandgap measurements were performed on a Cary 5000 UV-Vis-NIR spectrophotometer. The photometer was placed in absorbance spectroscopy mode. The machine cycled through various wavelengths of light, and the intensity of the incident light, and the intensity after passing through the film were recorded giving rise to the complete absorption spectra. The range of measured wavelengths was from 200 nm to 2000 nm at a rate of 7 samples/second. The sampling rate was deemed appropriate since the long exposure to the light source can induce photoinduced effects, which have been limited by the short exposures while striking the ideal balance for achieving the accurate spectra.

### X-ray Photoelectron Spectroscopy (XPS)

X-ray photoelectron spectroscopy is a highly effective method to investigate the structure, and chemical composition of materials. This method is useful for studying the surface of the films, and determining the exact chemical bonding of all the atoms in the top few layers of the film. The spectra were measured using a Scienta ESCA-300 spectrometer with a monochromatic Al K $\alpha$  X-ray with energy of 1.487 keV. The instrument was operating in a 0.4 eV Fermi-level width mode for Ag, and a Full width at half maximum of 0.54 eV for Ag 3d<sub>5/2</sub> core level peak. Surface charging due to the photoelectron emission was minimized by flooding the surface of the film with low energy (<10eV) electrons, and the raw data were calibrated with a gold thin film, which has a 4f<sub>7/2</sub> line positioned at 84.0 eV. The raw data was analyzed using the CASA-XPS software, and the core level spectra were determined by subtracting the Shirley background, and assuming a Voigt line-shape for the peaks. A  $\pm 0.05$  eV error in the peak position, and  $\pm 2\%$  error in the area for each component is expected with this method.

### Energy Dispersive X-ray Spectroscopy (EDS)

Films were characterized using Energy Dispersive X-ray Spectroscopy (EDS), a method that is capable of detecting the presence of different elements in a film, and studying the film compositions down to 1-micron depth. Determining the accurate film composition aids in understanding the behavior of the samples under radiation since the source composition, and the deposited film compositions can vary. EDS was performed using the LEO 1430VP Scanning Electron Microscope with an Oxford X-ray Detector as well as a Hitachi S-3400N-II Scanning Electron Microscope with an Oxford Instruments Energy + EDS system. This method was performed by applying a voltage bias across a

tungsten filament, which generates a stream of electrons that were directed at the sample using a set of apertures, and beam aligners. Once the electrons interact with the material, X-rays were generated, which were collected, and analyzed to study the composition of the film. Each atom creates a characteristic X-ray corresponding to a specific energy, and thus the elements that are present within the studied film can be determined. To maintain consistency between various samples, the following settings were used for all the EDS analysis.

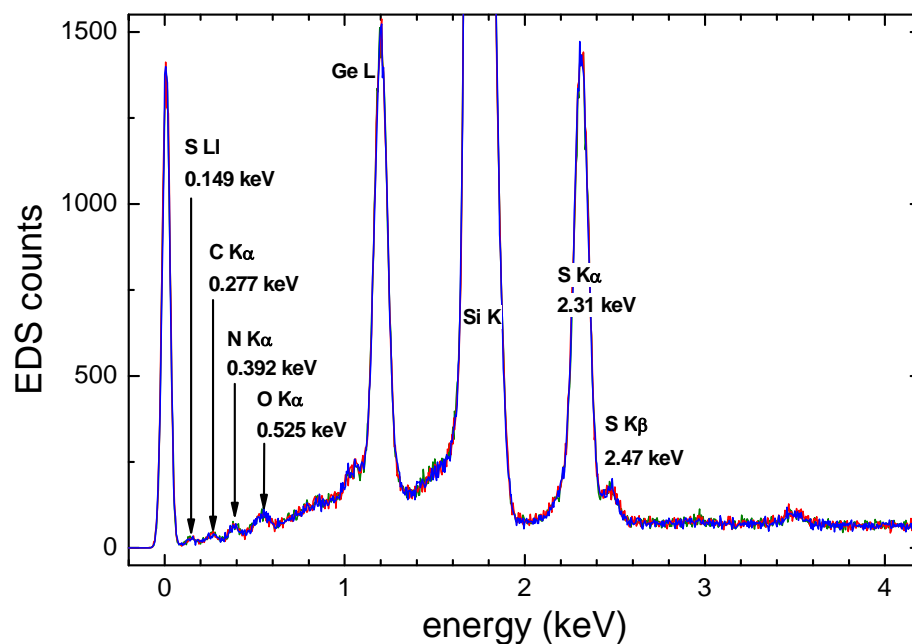
**Table 5**      **Standardized settings for compositional analysis using EDS method**

Electron Accelerating Voltage	20kV
Working Distance	10mm
Zoom (magnification)	2kX
# of pts per sample	5pts

The primary, and secondary X-rays for all the elements within these types of chalcogenide glasses reside between 0 kV to 10 kV. It is of common practice to have an accelerating voltage that is at least two times greater than the farthest peak location, since the electrons can scatter off the sides or other locations, and arrive at the surface of the sample with various energies. Adjusting the accelerating voltage for the electrons to twice the energy of the most energetic X-rays originating from the sample ensures that the majority of the generated electrons reach the sample with more energy than the most energetic X-rays. This enhances the signal from the sample, and generates an accurate compositional analysis of the material. A working distance of 10 mm is required to ensure a consistent calibration of the detector from one scan to another. Variations of the working distance can alter the counts, which correlates to the strength of the X-ray signal,



and is crucial for appropriate calibration of the detector. Similarly, a 2 kX zoom ensures that the data collected from each sample is not from a very small area, or a very large area. This specific zoom has been experimentally determined to measure a large enough area at the same time it is not too large of an area that the resultant composition consists of contaminants. Finally acquiring spectra from five locations provides sufficient statistics about the entire film where an average composition, and the standard deviation can be calculated. Prior to measuring the composition of any of the samples, the beam intensity, and the software were initially calibrated with a copper film. An example of the spectrum from EDS analysis is shown in Figure 47.



**Figure 47** Sample spectrum achieved using EDS for Ge-S films on Si/SiO<sub>2</sub> substrate. This spectrum reveals the presence of Ge, Si, and S as the prominent peaks along with the presence of C, N, and O<sub>2</sub>.

Software used by the EDS machine created by the Oxford Company compares the area under the various peak locations, and then provides the user with a composition of

the sample. The X-ray peaks for various elements have already been determined, so using a library of elements, the software detects a specific element when the peak intensity is greater than the noise of the spectrum. Once the software provides a specific composition of the films, it is possible to compare only the elements are of interest such as Ge, and chalcogen, while the sample picks up carbon, silicon, and other elements that could be present in nature. The result is then normalized to 100% to find the exact composition in the following manner  $\text{Ge}_x\text{ChG}_{1-x}$ .

### Raman Spectroscopy

Structural analysis of the various films is vital for understanding the initial film, and the subsequent changes that arise due to the introduction of radiation. Specific structural units are revealed through the analysis of the Raman spectra. This type of analysis was performed using a high precision laser, which only emits a laser light with a wavelength at 441.6 nm. This laser was focused onto a ~0.1 mm diameter spot onto the film using an intensity of 50 mW with the aid of various optical lenses. The laser light scatters off the sample, which was then collected by a charge-coupled device (CCD). Inside the material, light is scattered, which occurs when a photon passes near an electron cloud of a molecule, and the photon is absorbed by the electrons [97]. This results in the atom acquiring a higher electronic state, but this state occurs during a brief period of time because the energy contained within the electrons is immediately released as a scattering light before the nucleus of the atom reacts to this change in energy [97]. The acquired energy is stated to cause the electrons to acquire a virtual state, and the relaxation of the electrons from this state to the equilibrium state causes the release of a photon with the specific characteristics related to this transition [97]. The photon energy does not affect a

single electron but the energy is transferred to vibrations of atoms present within the material [97]. The resultant Raman spectra will consist of Gaussian peaks corresponding to the scattering intensity of specific structures. The intensity of each peak is proportional to the number of specific structures. To analyze the overall spectra with multiple peaks, such as the spectra for chalcogenide glasses, the baseline noise from all the spectra was removed followed by normalizing the spectra in order to compare different scans without extraneous variables.

One part of the Raman spectroscopy method that was taken into consideration was the creation of laser-induced effects due to the Raman laser, which can alter the gamma radiation-induced changes. The laser light (441.6 nm) used in this analysis is less than the absorption edge, which means that the laser light has enough energy to produce photoinduced effects in the chalcogenide films. These laser-induced changes are indistinguishable from the radiation-induced changes, therefore to avoid these effects all the samples were placed in an evacuated closed-cycle He cryostat, and measured at 77 K to diminish the laser light-induced structural changes. This method was verified by performing multiple scans, which confirmed that the resulting spectrum did not change from one scan to another.

#### Atomic Force Microscopy (AFM)

Atomic Force Microscopy technique is a useful method of studying the roughness, and the deformation of the film. There are three modes of operation to measure the surface roughness: contact mode, non-contact mode, and tapping mode. Sample roughness was measured using the tapping mode, which applies the least amount of force onto the surface, and is not a constant pressure, which could change the

roughness of the neighboring area during a scan. This method was performed by taking a Si tip at the end of a flexible cantilever beam, which was excited by a resonance frequency causing the probe tip to traverse the surface of the chalcogenide film. The amplitude of the oscillation, and the phase of the modulations vary as a function of the sample surface. This data is recorded, and converted into a roughness measurement. All of the AFM scans were performed at 0.5  $\mu\text{m}/\text{sec}$  rate since the slower the AFM scan speed will result in a better tip traction, and improvement on the overall resolution. The measurements were performed at ambient atmosphere, and in a dark environment. Due to the change in the structure as a result of radiation-induced bond destruction, and reorganization, the structure is altered, and slight changes in the structure are detectable using this technique. The scans were performed on a 25  $\mu\text{m}^2$  square area, and the samples were analyzed to determine the surface roughness.

#### X-ray Diffraction (XRD)

X-ray diffraction is a powerful technique, which provides a different perspective into film characterization that is not possible by the other techniques. XRD can detect the formation of crystalline phases within the films such as silver containing molecules, which can arise when silver diffuses into chalcogenide glass films. X-ray Diffraction can detect all the silver-containing phases because these molecules are crystalline in nature, and are represented using sharp peaks in the XRD pattern.

The XRD patterns were obtained using a Bruker AXS D8 Discover X-Ray Diffractometer equipped with a Hi-Star area detector. Each sample was placed onto the surface of a zero background plate that was subsequently centered on the stage. Correct placement of the sample in XYZ space was achieved using a video microscope with laser

assist focus. Beam conditions included a Cu anode at 40 kV, and 40 mA to produce Cu  $K\alpha_1$  radiation ( $\lambda=1.5406 \text{ \AA}$ ) through Göbel mirror for collimated beam. Diffracted x-rays were collected using a two-dimensional general area diffraction detection system (GADDS) set up for a single run, 2 frames, and coupled (step) mode, with rotating sample stage. Runtime for each frame was 1200 s. Debye ring data were integrated over  $\chi$ , and integrated frame data were combined for the final XRD pattern.

## FILM ANALYSIS

Prior to creating a sensor design, it is important to study the radiation-induced changes in the chalcogenide glasses. For this purpose, it is first essential to understand the film structures that will facilitate the device performance. Therefore, the study of the bare films, and the effect of silver due to radiation are of the utmost importance.

### Film Fabrication

#### Bare Films

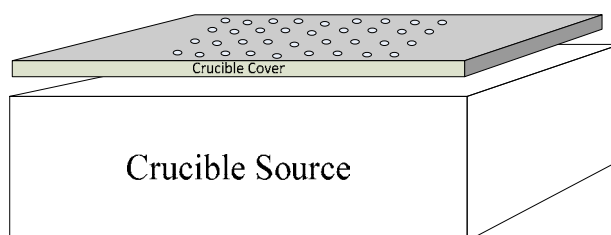
Films, and devices based on these films were created on two types of substrates of which one is the conventional silicon substrate used in semiconductor industry. The second type of substrate used for bare film analysis consisted of borosilicate glass, which was used to assess the optical properties of the films. Silicon wafers used for film preparation were 4" in diameter, 380  $\mu\text{m}$  thickness, with  $\langle 100 \rangle$  orientation, boron doped p-type, and single side polished. Films were prepared on the polished side of the wafer, but prior to film deposition, a thermally grown oxide was placed which insulates the electrical currents through the film from traversing into the substrate. Silicon wafers have a resistivity of  $1^{-10} \frac{\Omega}{\text{cm}}$ , which is significantly less than the resistivity of the chalcogenide glass film, hence the necessity of an insulating layer. Thermally grown oxide is an expedited method for generating a good oxide layer. This oxide was grown using a high temperature furnace, with a bubbler attachment that generates water vapors, which react with the wafer generating an oxide layer. The furnace was heated to 1100°C, and the

wafers were placed into the furnace for 30 minutes growing 200-250 nm of oxide. Wafer is now ready for film deposition, and device fabrication.

Prior to the film preparation, it is important to mention the method of creating bulk glasses from 99.99% pure elements. This method is widely known as the melt quench technique, where pure elements of germanium, and a specific chalcogen element for example Sulfur, are measured to correspond to a composition of the final glass. For example, when creating  $\text{GeS}_2$ , for a specific weight of pure germanium, the weight of sulfur placed into a sealed, and evacuated ampoule will be twice that of Ge. The sealed ampoule is placed into a specialized furnace, and glass is formed by the method stated in the *Basics of Glasses* section. After synthesizing the bulk glasses, a small portion of the entire glass was weighed to limit the wastage of glass, and using only the required amount of glass for a specific thickness. The measured amount of glass was then placed in a mortar, and pestle, and ground up into small pieces but not to a fine powder. Small pieces of the bulk glass are easier to evaporate when compared to large pieces. These pieces were then placed into a specialized crucible used for evaporation.

The specialized crucible is shaped in the form of a semi-Knudsen cell that allows the ability to maintain a uniform pressure of the contents, and composition of the glass material. Thermal evaporation works on the properties of partial pressure of the atoms, where atoms of similar partial pressure will evaporate at similar rates, and maintain the composition of the source material. In the case of the chalcogenide glasses used in this dissertation, the components have varied partial pressures. The germanium atoms have a low partial pressure while the chalcogen atoms have a significantly high partial pressure. This implies that the chalcogen atoms will evaporate with a significantly higher rate than

the Ge atoms. Therefore, a special crucible is required that will maintain a similar pressure, ensuring the composition of the source material is transferred to the evaporated film, which is shown in the figure below.



**Figure 48** Semi-Knudsen cell structure. The chalcogenide glass material was placed into the crucible source, and covered with the crucible with extremely small openings, which have been exaggerated in the figure to present the concept.

The actual openings are very small, and hard to see, but the image above is an exaggeration to present the idea of the structure. Evaporation was performed in a Cressington 308R Low-Pressure thermal evaporation system, which was evacuated to  $1 \times 10^{-6}$  bar at room temperature. Deposition rate is an important aspect that determines the film structure, uniformity, and composition. All three aspects are highly vital for studying the material properties of the films. A non-uniform film will result in films of different thicknesses. Usually it is acceptable for a  $\pm 10$  nm of thickness variation in a 100 nm thick film, but this variation can be disastrous for films of 30 nm thickness. In a similar vein, film structure, and composition are dependent on rate, where a fast deposition rate will result in an inaccurate composition, thickness variations, and more defects in the film structure. Therefore, the deposition of the films was standardized to 0.05 nm/sec, which allows them to achieve uniform film thickness, and reproducible compositions. In this manner, films of various compositions, and thicknesses were produced to study the



radiation-induced effects. All the films were evaporated on a large segment of wafer to allow for fabrication of different types of samples using the same film.

The only variation from this deposition method was the fabrication on a glass substrate to study the optical properties of the films. The glass substrate used in this study was an alkali free borosilicate glass, which was prepared by a thorough cleaning of the glass substrate to enhance the adhesive properties, and remove any contaminants from the surface of the substrate. The substrate was then placed inside the evaporator to deposit a 500 nm thick chalcogenide film. This specific thickness was selected to ensure that a thicker sample would provide an improved signal, and create a greater number of defects, which can be used to characterize the properties of the chalcogenide glasses.

### Silver Covered Films

Besides the above described bare films, two additional types of samples were fabricated simultaneously to study the different aspects of the research. The first type of sample was a bare film topped with a continuous film of silver. Second type of film was similar to the bare film topped with silver, but instead of creating a continuous layer, 100 nm thick circular silver sources were created using a shadow mask with 2 mm diameter openings, and 1 mm spacing between adjacent openings. Since both types of samples were created from the same bare film, other variations relating to the film deposition, and other discrepancies were avoided. Samples with the topological silver, and circular silver sources were fabricated under similar conditions as the film deposition, but instead of depositing chalcogenide film, 99.99% pure silver beads are initially cleaned with Isopropanol alcohol to remove any surface contaminants, and then placed into a boat. Fifty nanometers of topological silver was evaporated on top of the chalcogenide glass

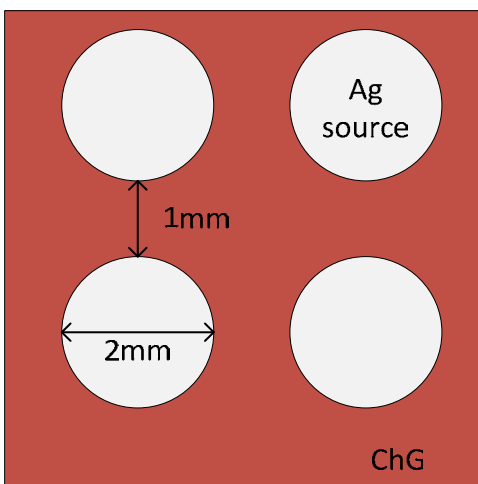
film for the continuous silver films. During radiation, some of the silver from this continuous film will diffuse into the chalcogenide glass. To evaluate the amount of diffused Ag, the excess topologically located silver film was dissolved, revealing the silver doped chalcogenide film. The samples were submerged into a solution of  $\text{Fe}(\text{NO}_3)_3$ , and deionized (DI) water. Different compositions have shown to react differently to the  $\text{Fe}(\text{NO}_3)_3$  solution where the various variables were altered to find the ideal settings of rotational speed of the stirrer, temperature of the hotplate, and the amount of  $\text{Fe}(\text{NO}_3)_3$  added to the DI water. These experiments were performed using a isotemp hotplate, the solution was mixed in a 50 ml beaker, and the solution was poured into a large petri dish to evenly spread the solution across the sample. The various settings, and specifications for different sample compositions are summarized in the table below.

**Table 6 Silver dissolution settings for various chalcogenide glass compositions**

Film Composition	Amount of $\text{Fe}(\text{NO}_3)_3$ (grams)	Time	Temp	Rotation Speed
$\text{Ge}_{20}\text{S}_{80}$	5.795	5-10 seconds	Room Temp	500 rpm
$\text{Ge}_{30}\text{S}_{70}$	5.795	5-10 seconds	Room Temp	500 rpm
$\text{Ge}_{33}\text{S}_{67}$	5.795	5-10 seconds	Room Temp	500 rpm
$\text{Ge}_{40}\text{S}_{60}$	5.795	5-10 seconds	Room Temp	500 rpm
$\text{Ge}_{20}\text{Se}_{80}$	14.4875	2-2:30 minutes	40°C	500 rpm
$\text{Ge}_{30}\text{Se}_{70}$	11.5997	2 minutes	40°C	500 rpm
$\text{Ge}_{40}\text{Se}_{60}$	14.4875	2-2:30 minutes	40°C	500 rpm

The problem that arises from the topological layer of silver films is associated with the introduction of silver through the evaporation process. When evaporating the topological layer of silver, it is unavoidable that a portion of the silver film reacts with the chalcogenide film, which starts the diffusion processes prior to exposure to gamma rays. Any additional energy provided to the film through temperature variation or light exposure would continue these processes, leading to inaccurate results. To circumvent these problems, virgin samples were used as controls, where these films experienced the same environmental changes as the irradiated samples, but were not exposed to radiation. By comparing the changes observed in the irradiated samples to the virgin samples reveals the actual nature of the radiation-induced changes.

Additionally, circular silver sources were created to minimize the issue of introduction of silver in the virgin samples. Even though silver diffusion during evaporation is unavoidable, the distance between the sources ensures that the silver diffusion does not completely saturate the chalcogenide film prior to exposure to radiation. An added benefit of these films is the ability to achieve higher radiation doses. In the topologically deposited silver film, diffusion stops after the silver saturates the film thickness, but as discussed earlier, the lateral diffusion begins at this step, and continues until the 1 mm distance between adjacent silver sources is saturated.



**Figure 49** Illustration of chalcogenide films with circular silver sources. Silver sources were evaporated onto the bare chalcogenide film surface using a circular mask with openings of 2 mm separated by 1 mm.

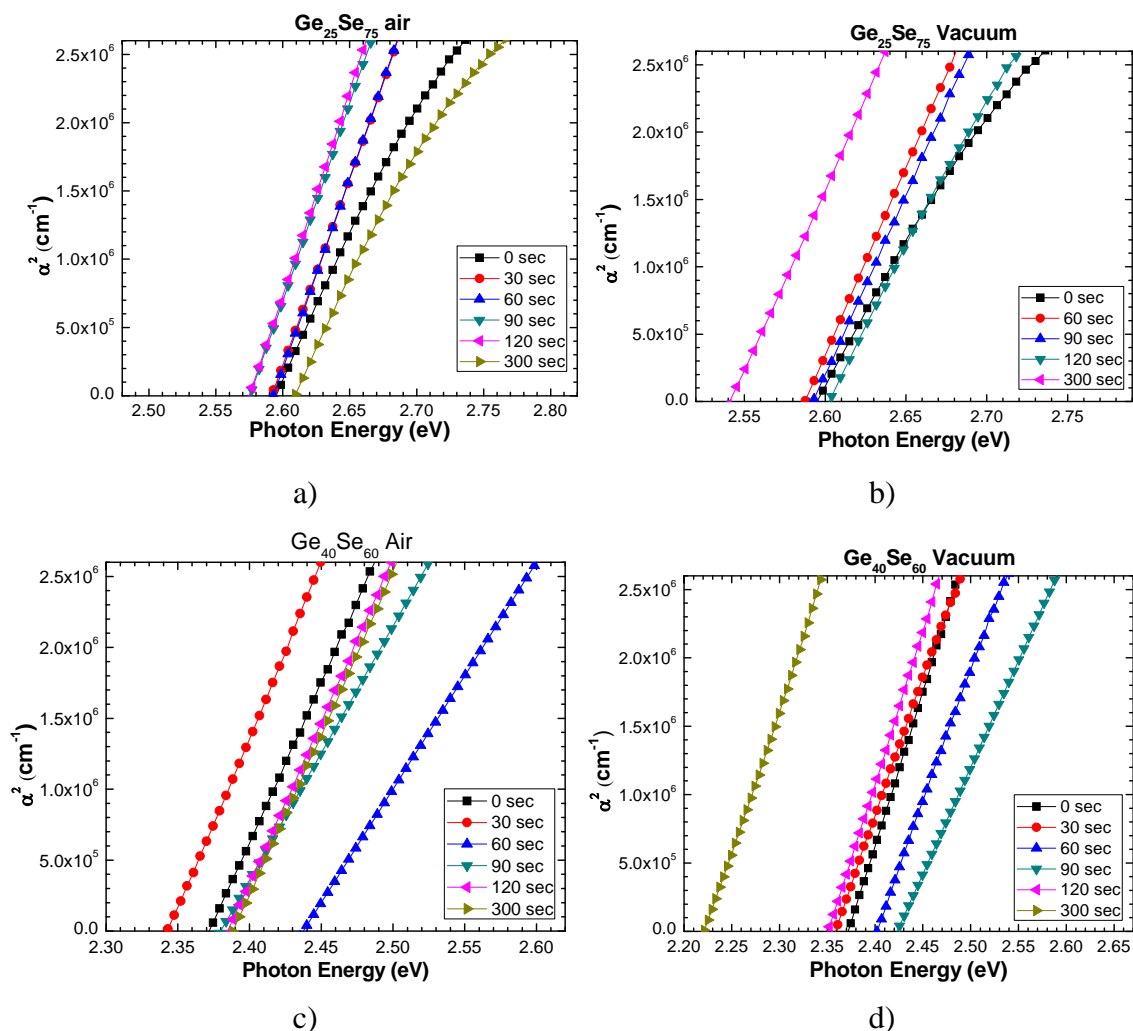
### Results and Discussion

The film analysis is presented in three parts, bare film analysis, silver containing films, and silver diffusion simulations. By separating the results in this manner, it allows to differentiate the effects in the chalcogenide glass followed by the effect of silver introduction. The silver diffusion simulations provide an insight into the combination of processes.

#### Bare Film Results

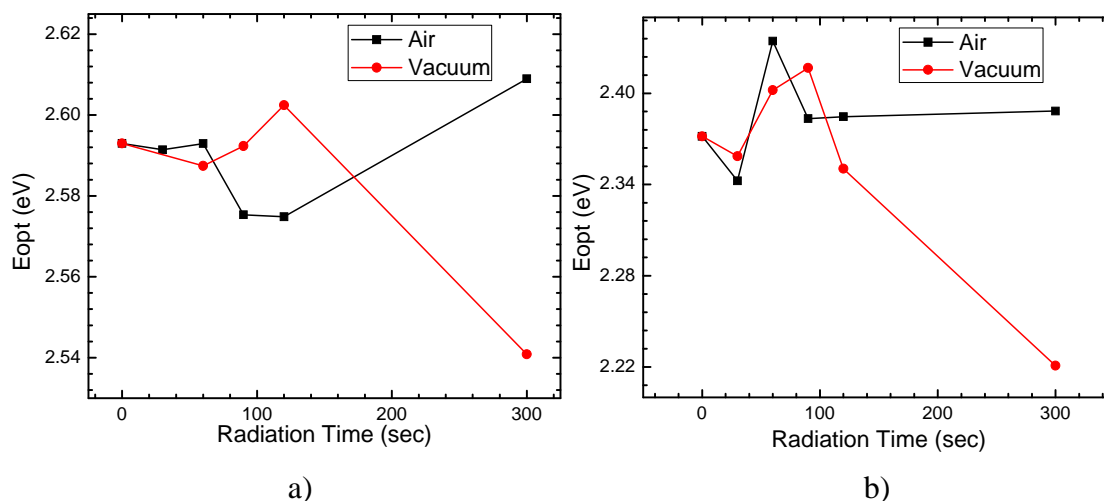
##### Optical Bandgap

The optical bandgap study revealed the bandgap of the material, and the effect of defect formation due to radiation exposure, which can affect the conductivity of the film. The samples with high chalcogenide content, and high Ge content were studied in ambient air, and vacuum. The optical bandgap was analyzed using the Tauc procedure [41], revealing the following spectra (Figure 50) for Ge-Se films in air, and in vacuum.



**Figure 50** Analyzed absorption spectra of films exposed to various exposure times of UV light using the Tauc procedure for a)  $\text{Ge}_{25}\text{Se}_{75}$  in air, b)  $\text{Ge}_{25}\text{Se}_{75}$  in vacuum, c)  $\text{Ge}_{40}\text{Se}_{60}$  in air, and d)  $\text{Ge}_{40}\text{Se}_{60}$  in vacuum.

Extrapolating the analyzed spectrum divulges the bandgap of the material, which has been analyzed, and is shown in Figure 51.



**Figure 51** Analysis of the absorption spectra exhibited the changes in the optical bandgap of the films measured in air, and under vacuum for a)  $Ge_{25}Se_{75}$  and b)  $Ge_{40}Se_{60}$ .

The measurements performed in air are similar to the observations by other research groups [35, 59-61, 63], where in the Se-rich samples there is an initial photodarkening followed by a slow photobleaching effect. In the initial radiation, the bandgap has a small decrease, but then the sample undergoes a slight increase in the bandgap, which can be negligible due to the short period of time and resolution of the spectrometer to capture small changes that have been detected by the other groups. After 60 seconds, the films exhibit a significant decrease in the bandgap, which is maintained up to 120 seconds. The films after long irradiation (300 seconds) illustrate a drastic increase in the bandgap to a level greater than the bandgap of the virgin films. The samples that were irradiated in vacuum from this composition demonstrate a similar trend as the films irradiated in air, but with a small caveat. Films irradiated in vacuum show a delayed trend, where the same trend that occurred in the samples irradiated in air occurs after a longer irradiation exposure for the sample irradiated in vacuum. Samples that have been irradiated in air were performed using a predefined setup where the UV light source

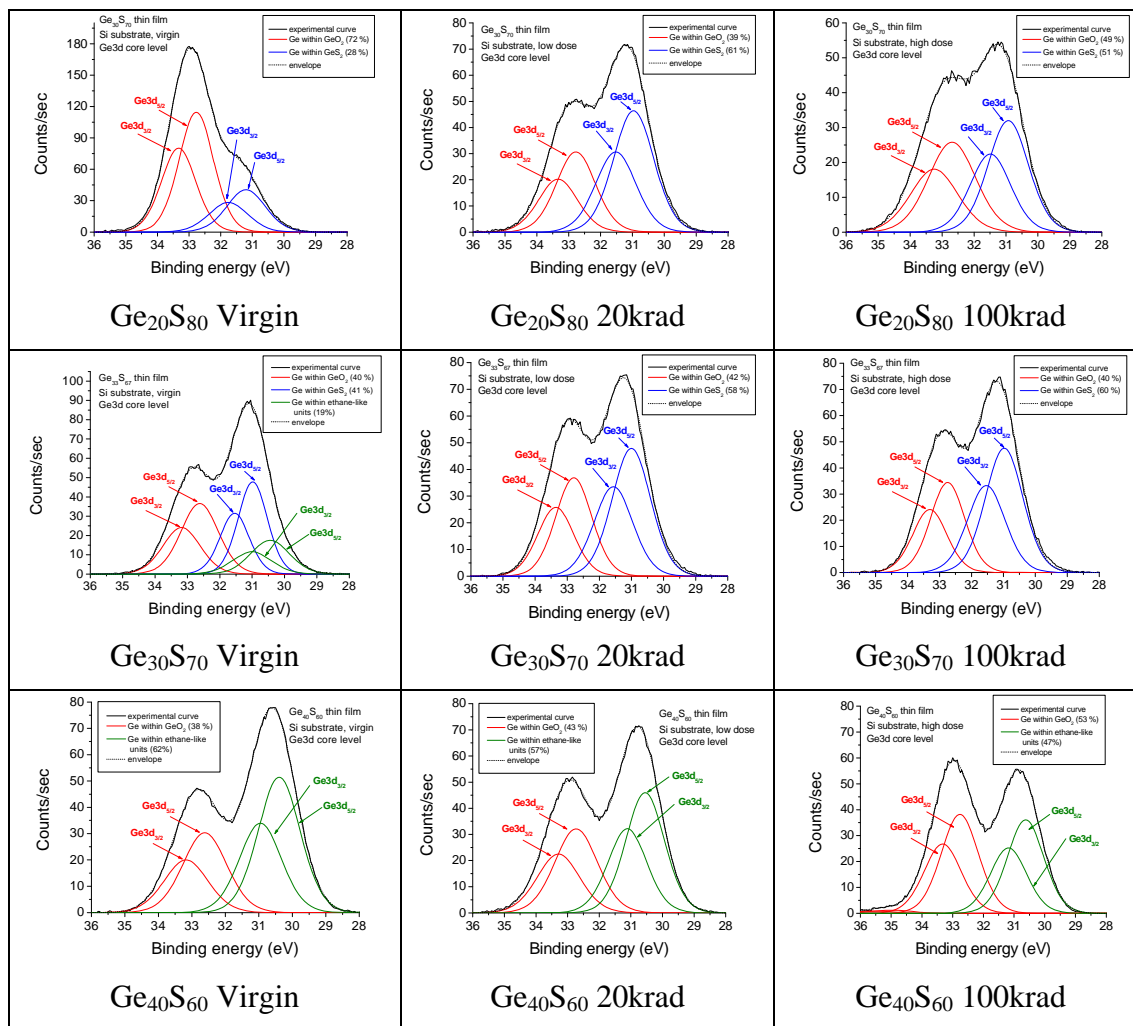
was set up exactly 3 ft away from the sample, and the light photons were parallelized onto the samples using a stationary optical lens. On the other hand, the samples in vacuum were irradiated at approximately 3 ft, but without the optical lens due to logistics issues that prevented the accurate placement of the lenses. Without the collimating lenses, the light scatters in different directions, and the intensity of light arriving at the sample is less than in the other setup. Therefore, the observed changes in the vacuum occur at slightly longer time intervals. For example, the slight decrease in the bandgap observed in the samples irradiated in air at the 30 second irradiation time is similar to the decrease at the 60 second in the vacuum sample. Similarly, the increase observed between 30, and 60 seconds in air is exhibited between 60 seconds, and 120 seconds. This trend is followed by a large decrease in the bandgap of the material.

The Ge-rich samples (see Figure 51 b) irradiated in air experience an initial decrease in the bandgap, but addition exposure to UV light causes a significant increase, which is then followed by a stabilization of the bandgap to a level greater than the virgin sample. In the Ge-rich samples measured in vacuum, there is an initial photodarkening, which is not as large of a decrease in the bandgap as the sample measured in air. Increasing the radiation time, caused an increase in the bandgap. Without the effect of oxygen, the samples undergo a greater photodarkening process, as shown in the measured bandgap after 90 seconds.

#### X-ray Photoelectron Spectroscopy

The X-ray photoelectron spectroscopy is a surface-sensitive method with a majority of the photoelectrons being collected without scattering from around top 4 nm (~15 atomic layers). The kinetic energy of photoelectrons of Ge 3d core level is around

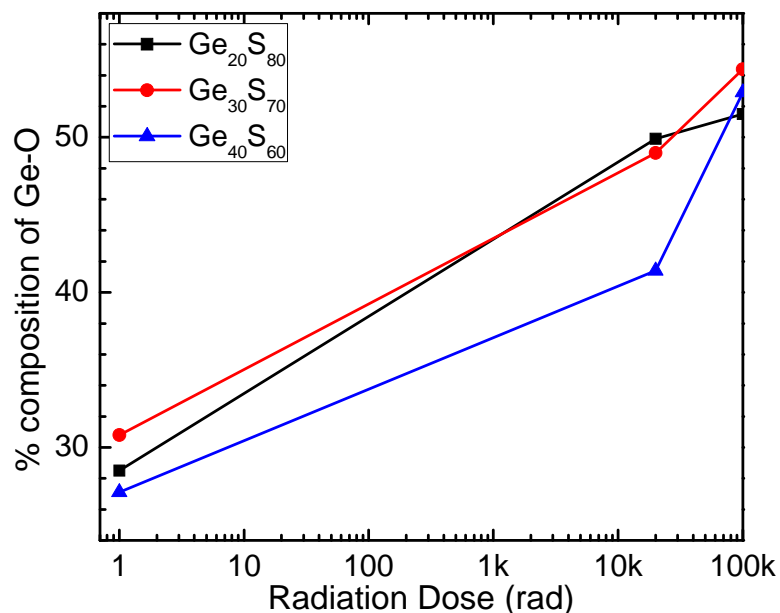
1454 eV. From the binding energy of its core electrons, information regarding the specific atomic surroundings of the top layer of atoms can be determined. X-ray photoelectron spectroscopy study has been performed on the Ge-S system in order to understand the change in the interface of the chalcogenide glasses. The Ge 3d, and S 2p core level XPS spectra are plotted in the Figure 52.



**Figure 52** Fitted XPS spectra for Ge 3d, and S 2p core peaks in Ge-S films.

The fitted data from the XPS spectra have been analyzed, which expounded that the composition of the Ge-O bonds increased with radiation dose as shown in the figure below.



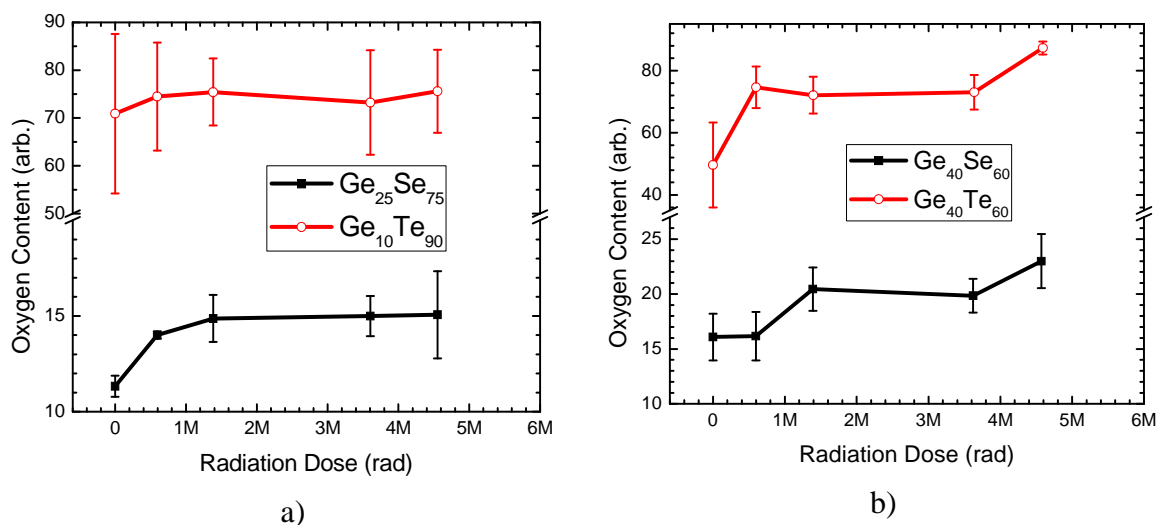


**Figure 53** Analysis of the XPS spectra illustrating the change in % composition of Ge-O as a function of radiation dose.

The study exhibited an increased amount of oxidation of the Ge atoms regardless of the composition. Oxygen on the surface was present even in the virgin case, and the increase of oxygen content describes that the broken Ge-S bonds were replaced with Ge-O bonds due to the abundance of oxygen during radiation.

#### Film Oxidation Using EDS

When considering Ge-containing systems, oxidation is a specific concern. This effect can be accelerated by radiation due to the formation of dangling bonds, which are ready to react with oxygen from the surrounding atmosphere. To investigate this effect, film oxidation measurements were performed as a function of radiation dose for the other two studied systems—Ge-Se, and Ge-Te. As expected, the Ge-rich glasses are more perceptible to oxidation, while those containing predominantly chalcogen atoms are stable, and the amount of oxygen included in their structure remains almost unchanged with radiation, as presented in Figure 54 a), and b).



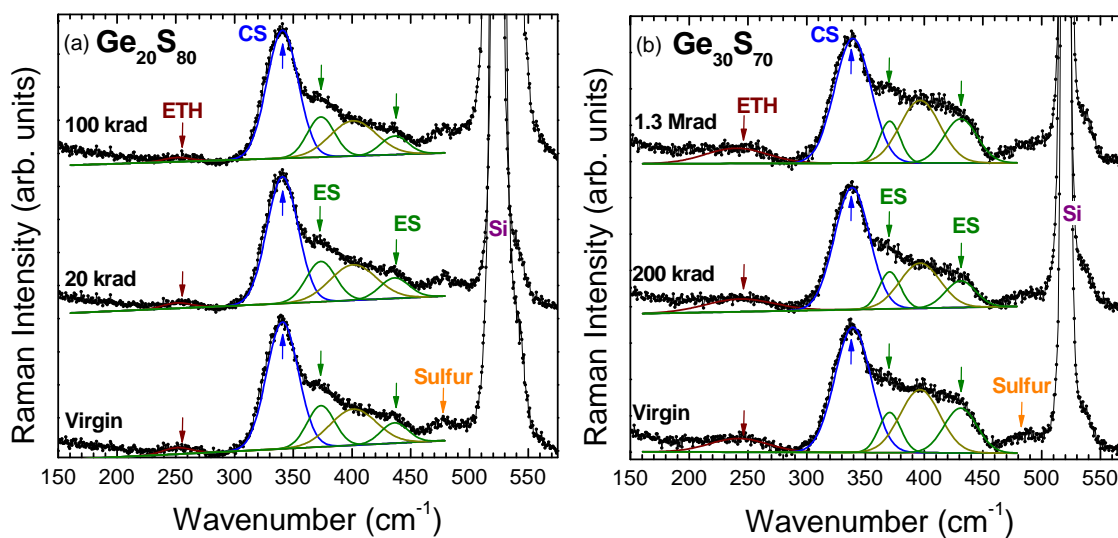
**Figure 54** EDS study quantifying the amount of oxidation in bare films for: a) Ge<sub>25</sub>Se<sub>75</sub>, and Ge<sub>10</sub>Te<sub>90</sub>, and b) Ge<sub>40</sub>Se<sub>60</sub>, and Ge<sub>40</sub>Te<sub>60</sub>.

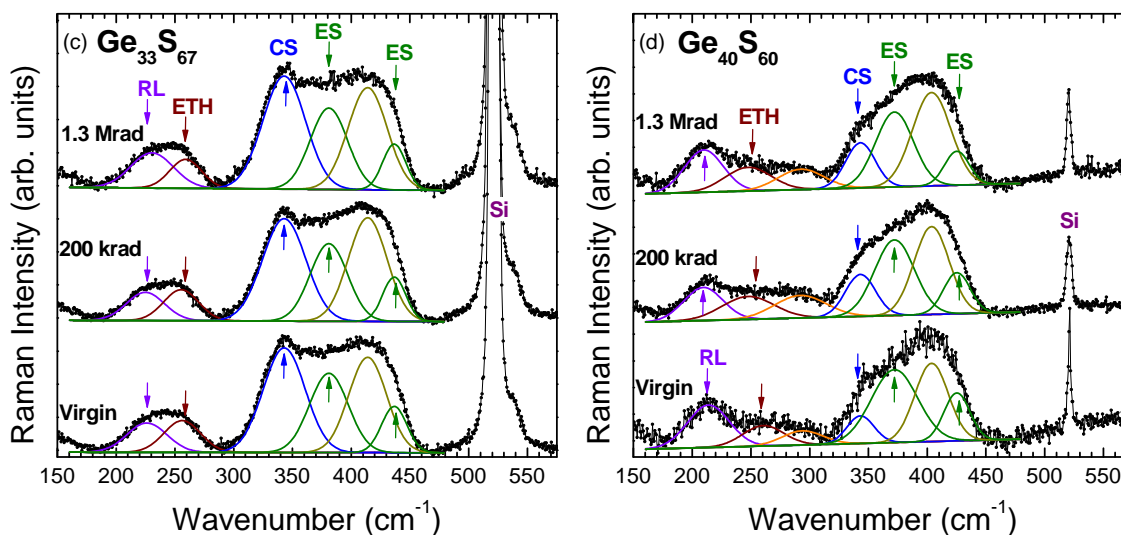
#### Raman Spectroscopy Based Structural Study

Raman spectroscopy analysis provides an insight into the structural changes exhibited in the films. Various compositions of the Ge-S, Ge-Se, and Ge-Te chalcogenide structures were studied at different discrete doses to investigate the structural changes observed in these types of glasses. Analysis of each type of system will be performed separately since each system has its unique characteristics.

Some specific vibrational modes are characteristic to Ge-S glasses that are represented by peak locations in the Raman spectra. Figure 55 (a)-(d) shows the normalized Raman spectra of virgin, and gamma irradiated with two different doses for Ge<sub>20</sub>S<sub>80</sub>, Ge<sub>30</sub>S<sub>70</sub>, Ge<sub>33</sub>S<sub>67</sub>, and Ge<sub>40</sub>S<sub>60</sub> thin films, respectively. In the virgin samples, there is a systematic increase of ethane-like mode (ETH) around 250 cm<sup>-1</sup>, and edge-sharing tetrahedral mode (ES) around 430 cm<sup>-1</sup> at the expense of the corner sharing tetrahedral mode (CS) around 340 cm<sup>-1</sup> with increasing of the Ge content. For the very Ge-rich composition, peaks in the region 200-300 cm<sup>-1</sup>, and the region below 175 cm<sup>-1</sup>

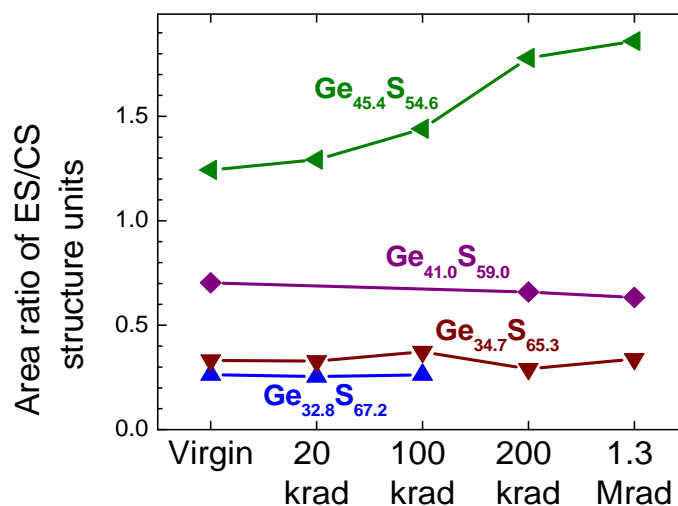
appear. These features are consistent with the results reported by Kotsalas, and Raptis [121]. In addition to the peaks, there is a large continuous background in the spectra at the high Ge concentration. The low frequency scattering for this system has been studied in terms of the relative intensity of boson peak, and fraction model so far. However, in the studied case, the background component is quite strong at frequencies higher than  $100\text{ cm}^{-1}$  and the relative intensity of the background component to that of the peak component becomes larger with increasing Ge concentration. At Ge concentration of approximately 40%, the background component persists at least up to  $400\text{ cm}^{-1}$ , which is no longer the low-frequency region.





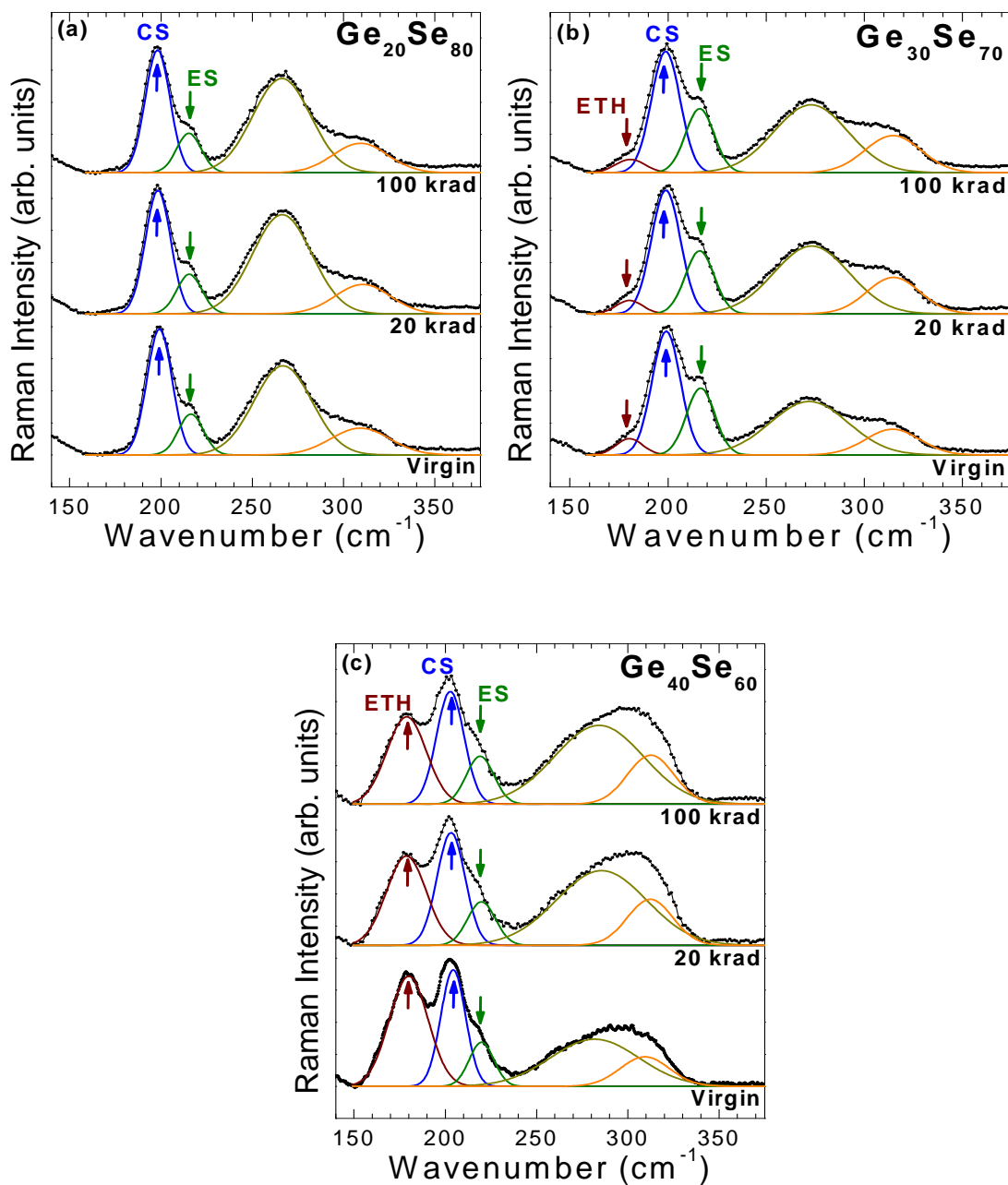
**Figure 55** Fitted Raman spectra of virgin, and radiated Ge-S films for a)  $\text{Ge}_{20}\text{S}_{80}$ , b)  $\text{Ge}_{30}\text{S}_{70}$ , c)  $\text{Ge}_{33}\text{S}_{67}$ , and d)  $\text{Ge}_{40}\text{S}_{60}$ .

Deconvolution of the Ge-S spectra revealed that the structural changes were limited in the range of studied radiation doses. The most expressed difference has been registered for samples with composition  $\text{Ge}_{40}\text{S}_{60}$ , where a clear tendency towards the increase of the ES/CS structural units' area ratio has been well expressed, as shown in Figure 56.



**Figure 56** Dependence of the ES/CS Raman modes ratio for the studied films at different doses.

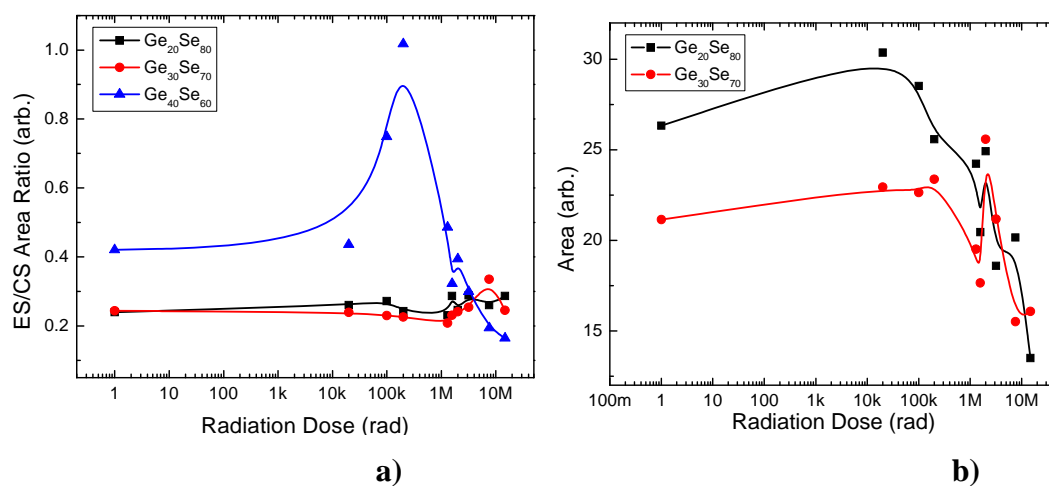
Similar spectra for  $\text{Ge}_{20}\text{Se}_{80}$ ,  $\text{Ge}_{30}\text{Se}_{70}$ , and  $\text{Ge}_{40}\text{Se}_{60}$  thin films are depicted on Figure 57(a), (b), and (c). In the spectra of  $\text{Ge}_{20}\text{Se}_{80}$  films, one can distinguish 4 bands located at 199, 216, 263, and  $310\text{ cm}^{-1}$ . Based on the commonly accepted interpretation [122-125], the first band ( $A_1$ ) is assigned to symmetric stretching vibrations of Se atoms on the Ge-Se-Ge linkages that are corner-sharing between  $\text{GeSe}_4$  tetrahedra, and the second one ( $A_1^c$ ) - to the breathing mode of a pair of Se atoms that are edge-sharing between two neighboring  $\text{GeSe}_4$  tetrahedra. The third band in these Se-enriched samples is normally assigned to Se-Se stretching vibrations in Se chains, and rings [126, 127]. According to the computational studies based on different models [63, 127, 128], the last band is due to an asymmetric vibration in the  $\text{GeSe}_4$  edge-shared tetrahedra. This type of motion involves the Ge atom moving towards two of its Se neighbors which are moving towards it as well, while its two other Se neighbors move away from it. In the spectra of the two other compositions ( $x=0.3$ , and  $0.4$ ), a fifth band at  $\sim 178\text{ cm}^{-1}$  is observed that originate from Ge-Ge, and vibrations in ethane-like structures ( $\text{Se}_3\text{-Ge-G e-Se}_3$  units) [122, 129]. Besides, at these compositions, the band at  $263\text{ cm}^{-1}$  shifts to the higher energies with increasing Ge content, and in the films with  $x=0.4$ , both initially resolved bands at 263, and  $310\text{ cm}^{-1}$  merge into a broad, and intense band. In addition to the scattering from the asymmetric vibrations of  $\text{GeSe}_4$  edge-sharing tetrahedra contribution to this band may come from vibrations in ethane-like units, and the asymmetric T2 mode (two bond stretching while two bonds shrink) of the  $\text{GeSe}_4$  tetrahedron ( $285\text{ cm}^{-1}$ ) [124, 128, 130]. The following plots are a small sampling of all the Raman spectra collected during the span of the research.



**Figure 57** Fitted Raman spectra of virgin, and irradiated Ge-Se films for a)  $\text{Ge}_{20}\text{Se}_{80}$ , b)  $\text{Ge}_{30}\text{Se}_{70}$ , and c)  $\text{Ge}_{40}\text{Se}_{60}$ .

A trend observed in these films is the increase in the ES/CS ratio after irradiation incurs a significant increase in the ratio up to 1Mrad followed by a decrease in the ratio in the  $\text{Ge}_{40}\text{Se}_{60}$  films, as shown in Figure 58 a. The other two compositions do not exhibit the same significant change in the ES/CS ratio unlike in the  $\text{Ge}_{40}\text{Se}_{60}$  samples. Such a

structural conversion could be due to increased temperatures as suggested by Edwards, and Sen [125]. However, it can be stated with a large degree of certainty that the temperature in the  $^{60}\text{Co}$  chamber did not increase over the room temperature because of the low radiation dose rate applied during the experiments [22]. This structural transition is clearly the result of  $\gamma$  radiation.

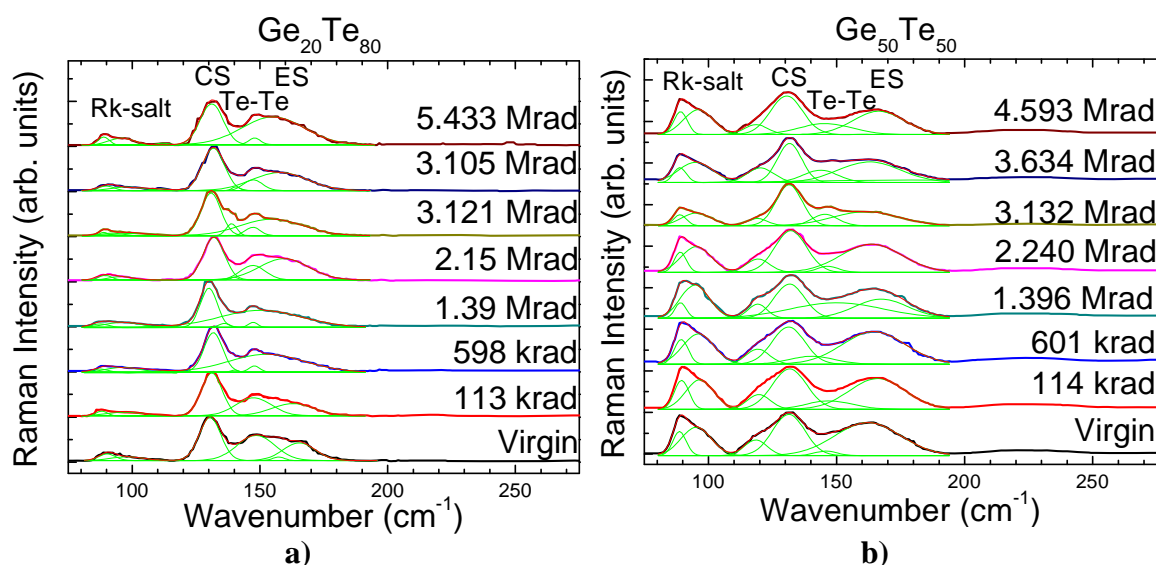


**Figure 58** Ge-Se Analysis of Raman Spectra: a) ES/CS Area ratio comparison and b) Se-Se band for  $\text{Ge}_x\text{Se}_{1-x}$  ( $x=20,30,40$ ).

The Se-rich glasses do not show a significant change in the shape, and the area of the bands because of radiation. A more detailed consideration of the  $\text{Ge}_x\text{Se}_{1-x}$  spectra, reveals at large radiation doses, there is a significant decrease of the  $263\text{ cm}^{-1}$  band (Se-Se band) in the irradiated  $\text{Ge}_{20}\text{Se}_{80}$  samples. This same type of bonding in the  $\text{Ge}_{30}\text{Se}_{70}$  films does not incur a similar change.

The Raman spectra for  $\text{Ge}_{20}\text{Te}_{80}$ , and  $\text{Ge}_{50}\text{Te}_{50}$  are presented in the Figure 59 (a)-(b). Regardless of the composition of the film, there are four primary bands located at  $88\text{ cm}^{-1}$ ,  $127\text{ cm}^{-1}$ ,  $150\text{ cm}^{-1}$ , and  $162\text{ cm}^{-1}$  corresponding to rocksalt (3-fold Te), corner-shared structure, Te-Te bonding, and edge-shared structures, respectively [131-133]. The

other bands that are present at  $95\text{ cm}^{-1}$ , and  $118\text{ cm}^{-1}$  correspond to the rocksalt, and the corner-shared structures [131-133]. The Raman spectra for this system of glasses consists of at least 2 different peaks for each type of structure, but the aforementioned list of band locations, which have been ascribed in the fitted Raman results, are accepted as the primary bands for Ge-Te chalcogenide glass system. It is also important to mention that the peak arising at  $150\text{ cm}^{-1}$ , which is ascribed to the Te-Te, is derived from the study of a-Te, and c-Te material [131]. The Raman spectra for a-Te reveals a peak at  $150\text{ cm}^{-1}$  while the crystalline phase produces a band at  $123\text{ cm}^{-1}$ , therefore it can be concluded that both types of films are partially amorphous due to the presence of this specific peak [131]. A definite confirmation of the amorphous nature of these films will be provided using the XRD investigations of the films.

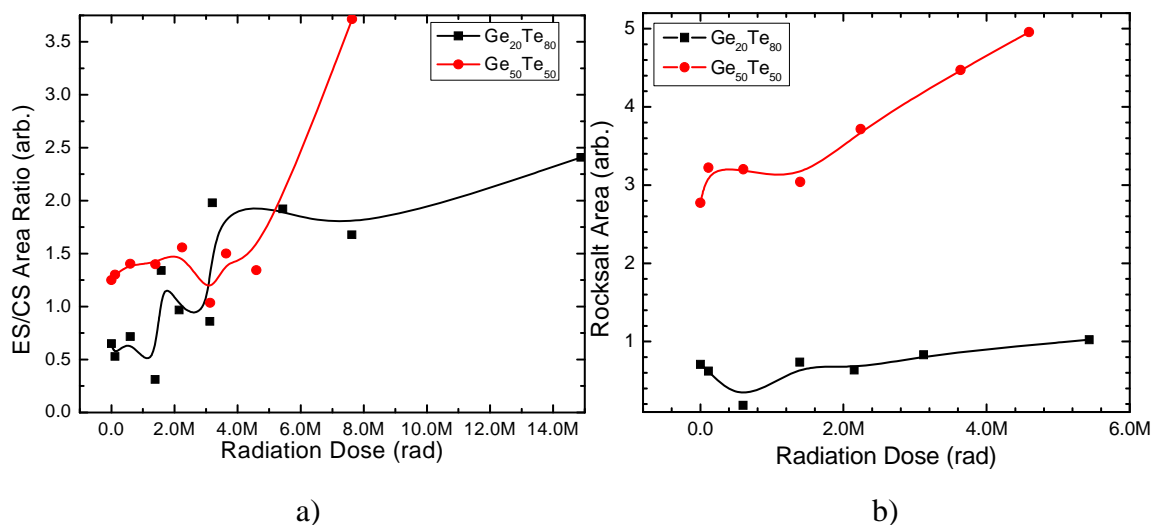


**Figure 59** Fitted Raman spectra of virgin, and irradiated Ge-Te films for a)  $\text{Ge}_{20}\text{Te}_{80}$  and b)  $\text{Ge}_{50}\text{Te}_{50}$ .

Application of tellurium offers different characteristics that have been observed by this structural analysis method. The Raman spectra for chalcogen-rich, and germanium-rich samples were analyzed revealing an increase in the ES/CS structural units in both



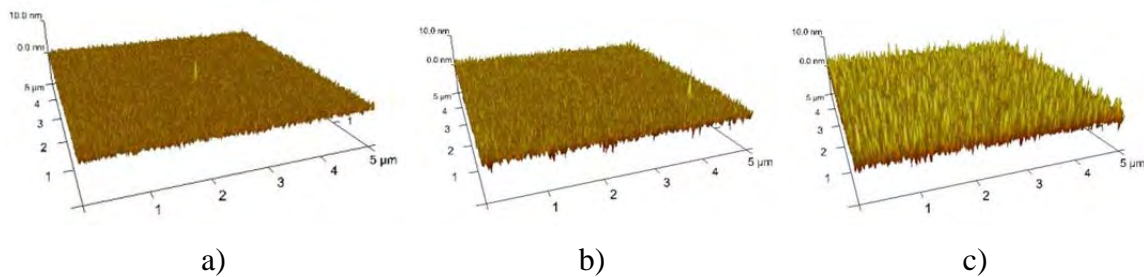
samples while the change observed in the Ge-rich samples was comparatively greater. The tellurium-containing sample offers a unique ability to analyze the rocksalt structure, and under radiation conditions, the analysis divulged that Ge-rich samples undergo a larger change as shown in Figure 60 b).



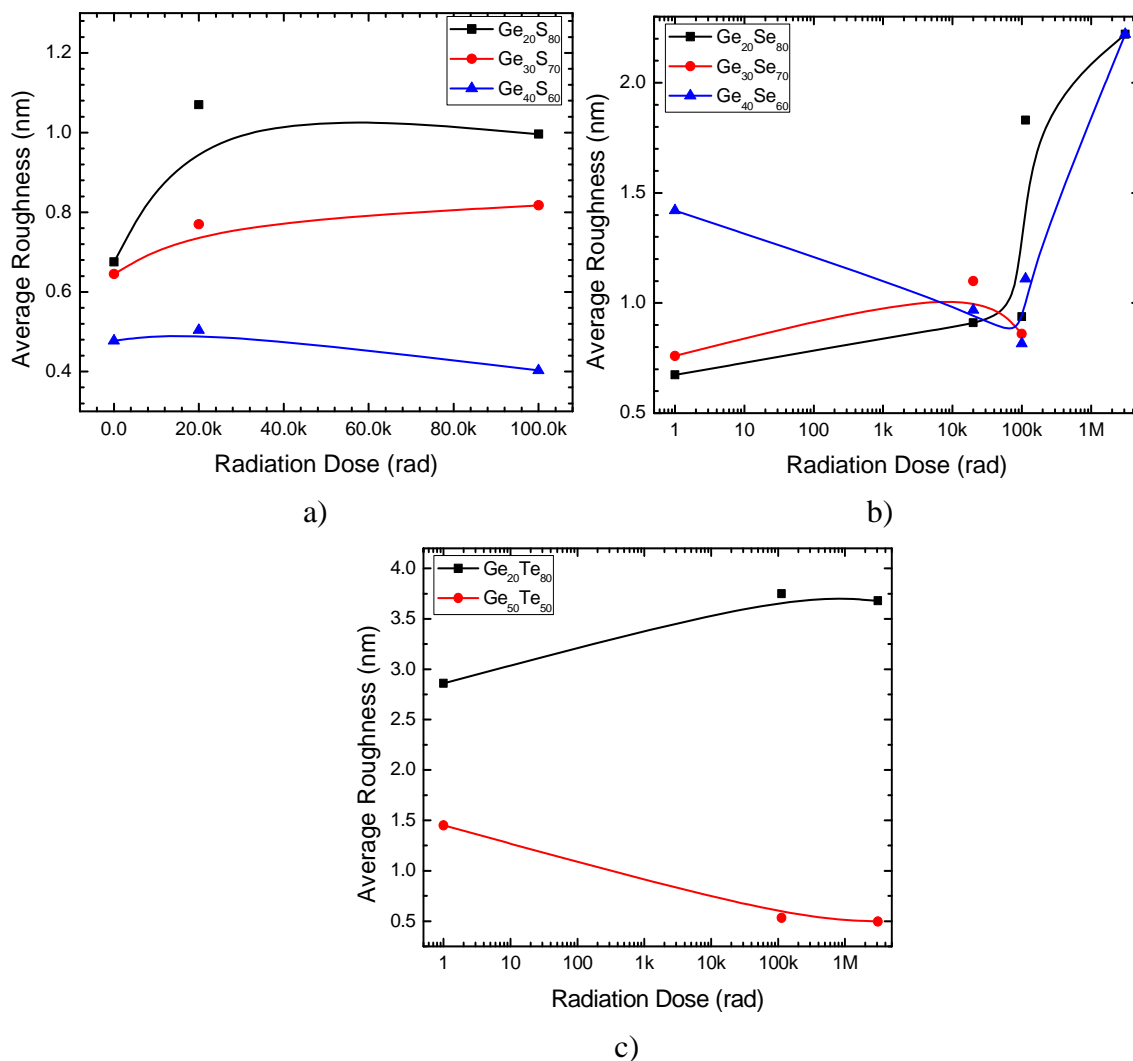
**Figure 60 Analysis of Raman spectra for Ge-Te system: a) ES/CS Area comparison and b) change in rocksalt structure.**

#### Atomic Force Microscopy Surface Analysis

The AFM study of the sample surface shows the variation of film roughness. There are unique trends that are consistent with the three types of systems, which exhibit an increase in the roughness with all three types of systems with samples that were chalcogen-rich. Samples with compositions near the stoichiometric do not exhibit significant changes in the roughness. In the Ge-rich samples from the Ge-S, and Ge-Te film samples reveal a decrease in the roughness with increasing radiation dose, while Ge-Se presents a similar trend for the low radiation doses, which is followed by an inflection point at 100 krad that is followed by a significant increase in the roughness. Films that are chalcogen-rich in general present a greater surface roughness.



**Figure 61** AFM surface analysis of  $\text{Ge}_{20}\text{Se}_{80}$  sample measured at a) Prerad  $R_q = 0.59$  nm, b) 20 krad  $R_q = 0.90$  nm, and c) 100 krad  $R_q = 1.34$  nm



**Figure 62** AFM surface roughness analysis for various composition in the a) Ge-S, b) Ge-Se, and c) Ge-Te systems.

## Discussion

### Ge-Se System

The comparison of the deconvoluted data for the Raman spectra of each composition for the Ge-Se system does not show significant changes in the shape, and the area of the bands as a result of radiation (see Figure 57 a). Selenium-rich samples do not show a significant change with the exception of decrease in the Se-Se bonds, which occurs after a specific radiation dose threshold. Up to this point, the underlying effects that occur are due to the formation of defects arising from the creation of electron-hole pairs. The electron hole formation is confirmed by the bandgap decrease after 60 seconds (see Figure 51 a). This change in bandgap continues until 300 seconds, where the generated defects begin the recombination process since the absorbed dose is large enough to create a substantial number of defects. As a result, the distance between neighboring defects becomes short enough to assist in their recombination. This recombination process will increase the bandgap of the material to the original state, but the experimental result shows that the bandgap after a large absorbed dose is greater than the virgin sample. Since the bandgap of the films is significantly greater than the virgin sample, it suggests that in addition to defect recombination other factors partake in this behavior. The cause behind this increase in the bandgap is due to the formation of heteropolar bonds, which researchers have stated could contribute by increasing the bandgap of the films [35, 59, 60, 62].

Here arises the observation in the Raman spectra, which reveals the reduction of Se-Se bonding. Reduction of the Se-Se bonds is attributed to the transformation from homopolar bonding to heteropolar bonding. The change in the Se-Se bonding is minimal

up to 1 Mrad, which suggests that the photodarkening that is exhibited up to 90 seconds is primarily attributed to the formation of electron-hole pairs. After 120 seconds, the two underlying effects, defect recombination, and the homopolar to heteropolar transformation, are prevalent.

Another confirmation of the formation of electron hole pairs at low radiation doses is visible in the AFM surface roughness analysis (see Figure 62 b). The overall trend of the roughness increases with radiation dose, but in the initial radiation dose range, there is a small increase in the roughness. Additional radiation exposure reveals a large increase in the roughness, which concurs with the homopolar to heteropolar bond transformation, and the subsequent molecular rearrangements. It can be stated with a large certainty that oxygen does not play a significant role on the radiation-induced changes of these glasses, which is exhibited in the EDS analysis (see Figure 54 a). The oxygen content is minimal, and the change observed is within the resolution of the method.

In the Ge-rich films, Ge-Ge bonds are the weakest among all existing bonds in the studied systems, and can be mostly affected by the radiation. Once the bond is broken, the elements are quite reactive, and can easily react with the atmospheric oxygen. Because of this, Ge is known to oxidize in these glasses. Raman spectroscopy is unable to detect the formation of Ge-O bonds because of their low intensity of their vibrations. However, EDS analysis of the films revealed the increased oxygen content in the films as shown in Figure 54 b). The oxygen in the virgin sample is due to the detection of oxygen from the SiO<sub>2</sub> substrate, but the oxygen content continues to increase at every discrete radiation dose increment. Since the Raman study, and other analytical methods have been

performed under vacuum, it can be concluded that the oxidation occurred during the radiation exposure.

The effect of oxidation was also determined in the optical bandgap measurements for these types of films (see Figure 51 b). The Ge-rich samples irradiated in air experience an initial decrease in the bandgap due to defect formation, but with additional exposure to the UV light, creating a combination of two distinct effects. The two effects are the formation of heteropolar bonds, which are prevalent in the Se-rich samples, can also occur in Ge-rich samples in addition to photooxidation as mentioned by K. Tanaka [55]. In the initial stages (between 0 seconds, and 60 seconds), the defect formation, and bond switching effects are dominant, but as the system reaches a steady state after 60 seconds, the effect of photooxidation supersedes the other effects, and therefore the bandgap of the material does not change with addition radiation exposure. In the samples measured in vacuum, there is an initial photodarkening, which is accompanied with a smaller decrease in the bandgap when compared to the sample measured in air, due to the difference in the intensity of the UV light source. Increasing the radiation time, caused an increase in the bandgap, but this change is characteristic for the formation of homopolar bonding since the effect of oxygen has been removed from the system. Without the effect of oxygen, the samples undergo a greater photodarkening process, as shown in the measured bandgap after 90 seconds.

Similar to the bandgap studies, two distinct changes were also captured by the AFM study (see Figure 62 b). Introduction of oxygen into the films forms Ge-O bonds, which are significantly shorter than the other bonds that are prevalent within this glass structure, thus affecting the films' roughness. Since the AFM method is a surface analysis

added to the fact that the rate of oxidation at the surface is significantly larger than in the bulk, the effects of oxidation are immediately detected using this method. When Ge-O bonds are formed, the resultant film constriction will cause a decrease in the surface roughness, which is exhibited up to 100 krad. After the surface has been saturated with Ge-O bonds, additional radiation dose creates newer defects that cause a decrease in the ES/CS ratio (see Figure 58 a). This transformation causes local structural rearrangements, which increase the surface roughness.

Changes observed in the Se-rich, and Ge-rich samples are not exhibited in the  $\text{Ge}_{30}\text{Se}_{70}$  films. The Raman spectra, and AFM do not exhibit any detectable changes. The application of this type of film for radiation sensing is not ideal since it is difficult to predict what type of structural changes occurs within these films. We suggest that the reason for the lack of sensitivity of this material is due to the fact that this composition is very close to the stoichiometric one, and hence the number of wrong bonds in the films is limited. The introduction of radiation causes the destruction of one type of structural unit, and due to the near stoichiometric composition of these films, a similar structural unit is formed thus resulting in a lack of changes in the Raman spectra. Since the resultant structure, post radiation exposure is similar to prior radiation; the local rearrangements are minimal, thus representing the uniform surface roughness.

### Ge-S System

After studying the changes in Ge-Se system, it is important for application purposes to use the best material with the highest temperature tolerance. Sulfur containing glasses have a larger  $T_g$ , and thus are useful for different applications. Ideally,

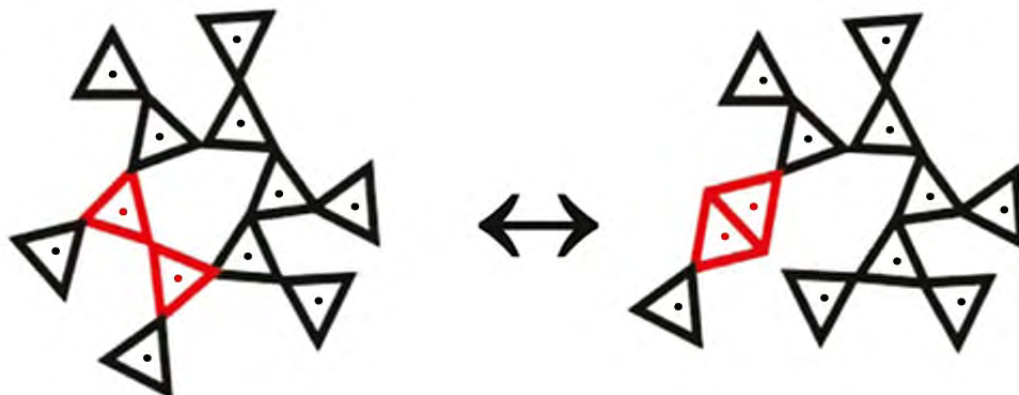
if the Ge-S films exhibit similar changes to the Ge-Se in addition to the increased  $T_g$ , this combination would make Ge-S system more appealing for radiation sensor design.

Based on the radiation data of the Raman spectra, it can be suggested that for the S-rich glasses, due to the lack of structural changes in the range of studied radiation doses, the changes in these types of films is attributed to the formation of electron-hole pairs (see Figure 55 a). Due to the similarities between the Ge-S, and Ge-Se systems, the observed bandgap changes in the Ge-Se are also applicable for these films. These electron hole pairs are suggested as the primary mechanism of these films' reaction to radiation, which is empowered by the high concentration of chalcogen atoms with lone pair electrons. This creates internal electric fields produced by non-equilibrium, radiation-induced effects such as  $C_1^+$ , and  $C_3^+$  centers [134]. They are the reason for the reduction of the optical band gap reported by Xia *et al.* [74]. The structural data points to the fact that at the conditions of our experiments there is no significant detectable bond breaking, and structural reorganization for these chalcogen-rich glasses, which for example has been obtained for chalcogen-rich Ge-Sb-S glasses at 770 Mrad radiation dose, which is much higher than the doses used in the this dissertation [135]. The exaggerated change in the surface roughness observed in the Se-rich films is not present in the S-rich films. We attribute this to the fact that the chemical bonding in this system is significantly stronger than in the previously regarded case, and the smaller cross section of the S atoms, which reduces the effect of radiation. Even though structural changes are undetected by Raman spectroscopy, structural changes do occur in these films as confirmed by the AFM analysis (see Figure 62 a). The destruction, and reorganization of the structure that occurs as a result of radiation changes the roughness of the films. The

exaggerated change in the surface roughness observed in the Se-rich films is not present in the S-rich films due to surface oxidation expounded using the XPS methodology (see Figure 53). Oxidation, and the formation of Ge-O bonds in this film composition is extremely rare. The reason behind the detection of the Ge-O bonds is ascribed to the size of the atoms within the film. In the previous case, where germanium, and selenium are similarly sized, the probability that a selenium atom becomes ionized is equal to the germanium atom. For the system containing sulfur, the sulfur atoms are significantly smaller than the germanium atoms, thus the likelihood of germanium ionization is greater than sulfur. Due to this difference, the surface oxidation rate of sulfur-rich films is similar to the germanium-rich films.

For the glasses with 40 at. % Ge, due to the reduced amount of nearby tetrahedra, restructuring of the system becomes possible. In this case,  $\text{Ge}^{2+}$  can be regarded as a modifier in the system, which contributes to breaking up the bridging sulfur. It is for this reason that radiation induces formation of a higher number of edge-sharing structural units in the Ge-rich films breaking some of the existing bonds, which has the important consequence of opening the entire structure of the films as illustrated in Figure 63 [136]. For the Ge-rich glasses, the disconnection of the network, and decreasing of the S bridging atoms makes the rigid structure more susceptible to bond reorganization as a result of radiation. Increase of the sensitivity with increase of the Ge concentration has been reported also by Donghui et al. [73].





**Figure 63** Cartoon illustrating CS to ES transition as exhibited in Ge-rich samples. Adapted with permission from [125] © 2011 American Chemical Society. Each triangle is a representation of a tetrahedral unit, which is connected to its neighboring tetrahedral by a corner (CS) or edge (ES).

The AFM roughness reveals a decrease in the roughness similar to the decrease observed in Ge-rich Ge-Se films. Surface oxidation observed in the XPS confirms that oxidation contributes to the decrease in the surface roughness. Similar to the Ge-Se system, the compositions of  $\text{Ge}_{30}\text{S}_{70}$ , and  $\text{Ge}_{33}\text{S}_{67}$  do not exhibit any detectable changes.

When comparing Ge-Se, and Ge-S, the observed structural changes in sulfur containing glasses are not as large as the selenium containing system. Larger the structural change, allows for greater sensitivity towards radiation, and a better radiation sensor.

#### Ge-Te System

Up to this point, selenium, and sulfur containing systems have been analyzed, but the introduction of tellurium will offer its own unique properties for radiation sensing. Compared to the selenium, and sulfur atoms, tellurium atoms are significantly larger, offering a bigger atomic cross section, which increases the probability of ionization.

In the case of Te-rich films, the lone pair electrons located on the tellurium atom do not participate in the bonding. They rather split into filled bands, and occupy a band location higher than the location of the bonded electrons, therefore, forming the top of the valence band. Due to this arrangement of electrons, this material is considered as a lone pair (LP) semiconductor in nature. Because of the presence of density of states within the band gap, contributing to the p-type conductivity as suggested by Chopra *et. al.* [34], this material is also considered as a narrow gap semiconductor. Radiation introduces many long-term stable transient effects such as the rise of rocksalt structure, as observed by the Raman spectroscopy in Figure 59 a. There is an interesting tendency, which states that with increasing radiation dose, dynamic destruction, and transformation occurs between the ES, and rocksalt structural units. By this transmutation, the area of the peak corresponding to the rocksalt structural units fluctuates between 0.62 to 0.78 arb. units. Such transient effects have been described as arising because of defect formation on metastable states followed by local rearrangement of the molecular structure. The energy possessed by  $\gamma$  radiation is sufficient for overcoming the barrier for generating these effects, leading to the formation of new structures, not characteristic for this particular composition [35]. Note that the rocksalt structure contains dative bonds where both Ge, and Te appear three-fold coordinated with the two electrons for the dative bond supplied by the Te atom. In this manner Te becomes polarized with a high negative charge on it. This regrouping of the structure contributes to phase separation in the system. Indeed Jóvári *et. al.* [137] report on two glass transition temperatures for these types of samples, very close to this composition even without radiation. The structural changes observed in the Raman spectra result in an increased surface roughness similar to the trend observed

in the other systems (see Figure 62 c). Furthermore, oxidation does not play a role in the Te-rich films, due to the low concentration of germanium in addition to the lack of change in the oxygen content in the EDS study (see Figure 54 a).

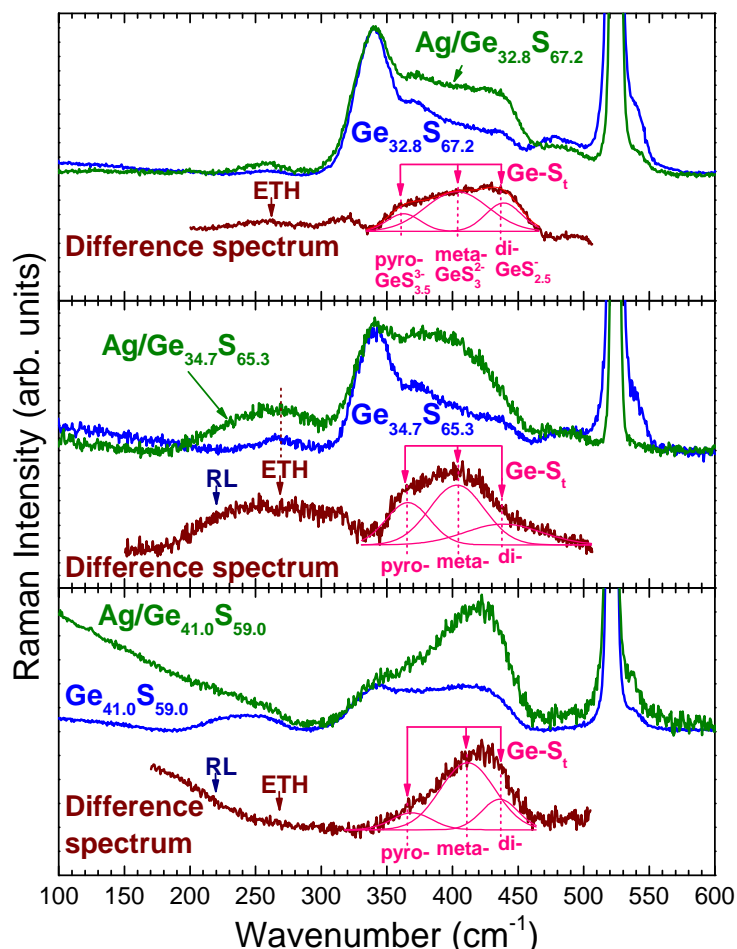
The main structural characteristic of Ge-rich Ge-Te compositions, that differentiates them from the previous compositions is the formation of distorted rocksalt structure with a vibrational band below  $100\text{ cm}^{-1}$  [133], containing a dative bond (see Figure 59 b). It is interesting to note that in a dative bond, the length of this type of bond is equal to any of the other covalent bonds between Ge-Te atoms up to the second decimal digit ( $2.77\text{ \AA}$ ), which makes the nature of this bonding indistinguishable from other bonds within the system [138]. Radiation aids in the formation of such bonds, since this type of bonding satisfies all requirements within a glass composition. Ideally, each Ge atom would prefer bonding with 4 Te atoms to create the tetrahedral structure, the corner-sharing building block, but due to the lack of free Te atoms in this composition to fulfill this type of bonding, dative bonds are formed instead of the covalent bond. As described in the earlier sections, the dative bond is the weakest bond, and thus easily broken, which exposes germanium atoms to the oxygen present in the ambient atmosphere. Due to this exposure, the oxygen content increases with radiation dose, and reaches saturation in the studied radiation dose range as shown in Figure 54 b. Therefore, the surface roughness of the films concurrently incurs a decrease in roughness with increased radiation dose. The incorporation of tellurium creates unique structures that could be beneficial for creating radiation sensors, but it is important to recall the polarizability of the tellurium atom, which would reduce the effects occurring in these films.

### Silver-Containing Film Results

Studying the bare films offers a small insight into the radiation-induced changes, but creating an effective radiation sensor requires the analysis of the films after the introduction of silver. Silver has the capability of amplifying specific properties, and attenuating other characteristics, which could prove to be beneficial for the sensor design.

### Raman Spectroscopy

When silver bonds with the structure of the Ge-S system, the newly formed molecular changes are detectable using Raman spectroscopy, since Ag becomes part of the network [139]. However, these changes are not detectable in the other two systems (Ge-Se, and Ge-Te) because of the phase separation of the Ag products in the glasses ( $\text{Ag}_2\text{Se}$ , and  $\text{Ag}_2\text{Te}$ ) are Raman silent. In the Ge-S system, adding Ag atoms to the backbone structure tends to break sulfur bridges, and form Ag cations terminated by S anion pairs. The tentative mode assignments of the Ge-S<sub>t</sub> modes are shown in Figure 64. For these samples, the spectra decreases in counts, and shows a sloped background by increasing the Ag content. There are a number of terminal Ge-S modes, which progressively grow in scattering strength with higher radiation dose. This further proves that when silver enters the network, it preferably breaks sulfur bridges instead of Ge-Ge bonds, leading to a predominant increase of ETH modes compared to other modes.

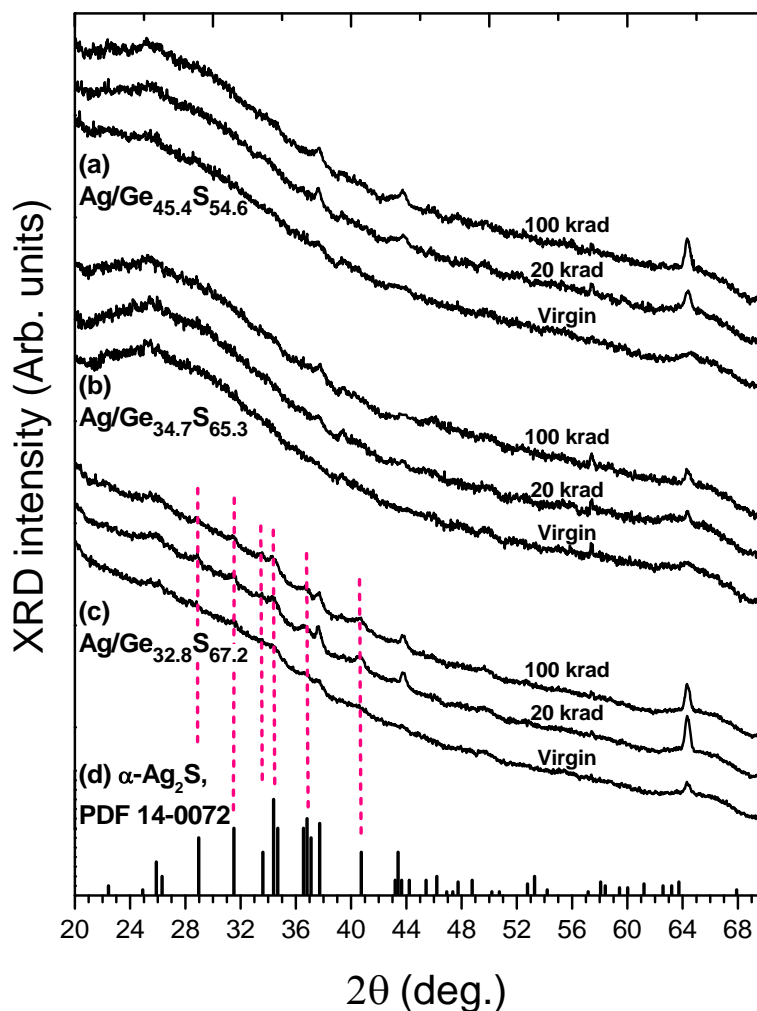


**Figure 64** Raman spectra of Ag containing films, bare films, and the difference spectrum. The difference spectrum reveals the formation of different types of thiogermanate groups.

The modes that are detectable using Raman spectroscopy are known as thiogermanate groups, which are different types of Ge-S-Ag ternary groups. The development of thiogermanate bonds ( $\text{GeS}^-$ ) forming pyro- ( $\text{GeS}_{3.5}^{3-}$ ), meta- ( $\text{GeS}_{2.5}^{2-}$ ), and di- ( $\text{GeS}_{2.5}^-$ ) thiogermanate tetrahedra, as suggested by Kamitsos *et al.* [139] was observed. Note the dominance of the metathiogermanate tetrahedra, which after accommodation of Ag form stoichiometry that is specific for this system—the  $\text{Ag}_2\text{GeS}_3$  ternary. It is not visible on the XRD spectra because it becomes part of the amorphous

network. On the other hand, the binary form of the molecule  $\text{Ag}_2\text{S}$  is Raman silent, which can only be detected using X-ray diffraction.

### X-ray Diffraction

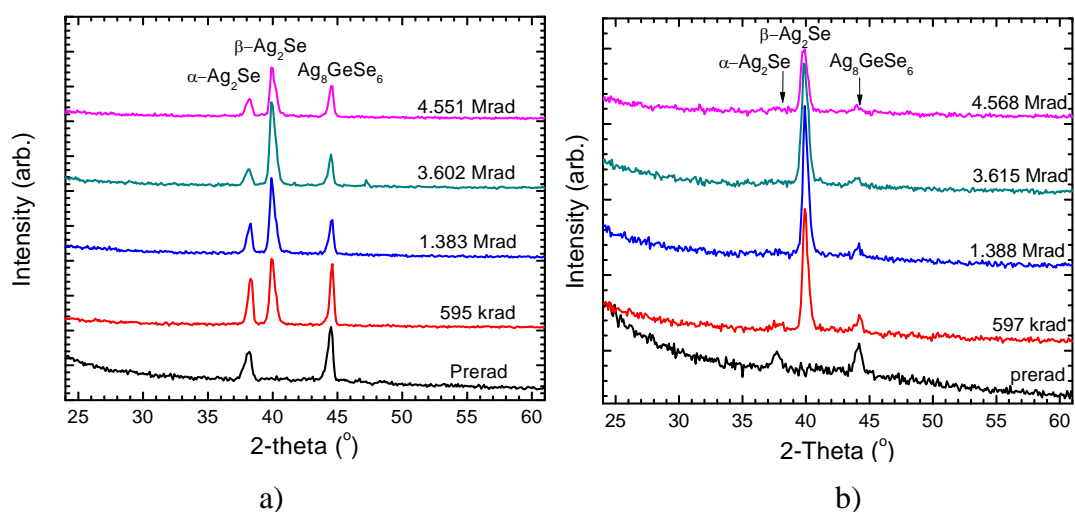


**Figure 65** XRD pattern of the Ge-S films measured at different radiation doses.

The molecular composition of the Ag diffused films was studied by XRD spectroscopy. Figure 65 illustrates the reaction products forming after Ag diffusion at room temperature. In general, the films are amorphous, and there are no strongly expressed crystalline molecular peaks. Only the binary composition  $\text{Ag}_2\text{S}$  was identifiable using the JCPDS card 75-1061. These peaks are present only in the spectra

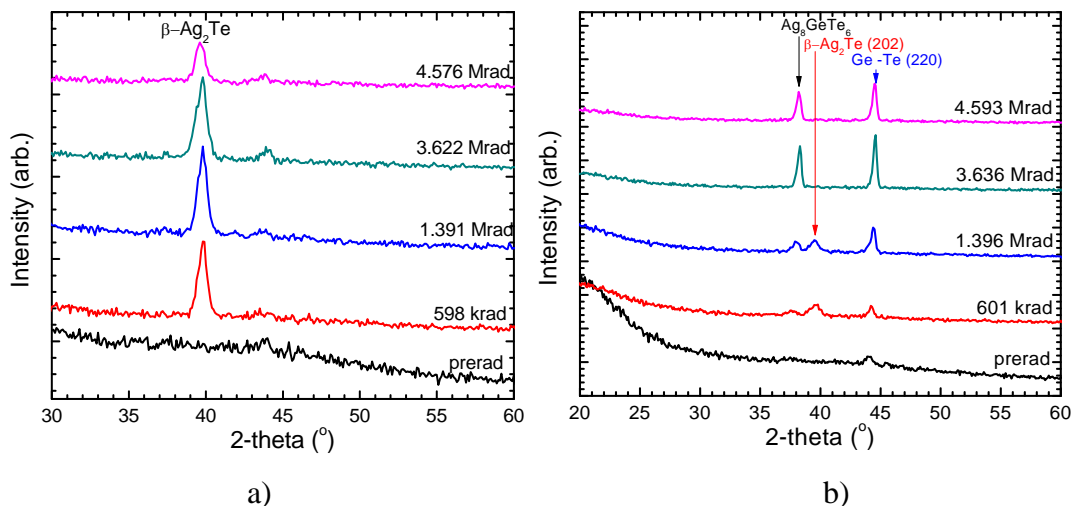
for  $\text{Ge}_{32.8}\text{S}_{67.3}$  films. There are some peaks that could be associated with the presence of  $\text{Ag}_2\text{GeS}_3$  (JCPDS card 83–1247) but they are wide, and with small intensity that suggests the crystalline clusters related to them are very small, and the structure is predominantly amorphous. There are also some small peaks that have been identified as pure Ag, and the origin of which is assumed to be originating from traces of non-dissolved Ag clusters from the surface of the samples after the Ag etch, since they are available on the virgin samples.

In the Ge-Se containing system, there are few specific structures to describe that arise after the incorporation of silver. There are three specific silver containing molecules located at  $38^\circ$ ,  $40^\circ$ , and  $45^\circ$ , corresponding to  $\alpha\text{-Ag}_2\text{Se}$ ,  $\beta\text{-Ag}_2\text{Se}$ , and  $\text{Ag}_8\text{GeSe}_6$ , respectively. With increased radiation dose, the size of the  $\alpha\text{-Ag}_2\text{Se}$  decreases. Simultaneously, the  $\beta\text{-Ag}_2\text{Se}$  develops in both Ge-Se compositions. The analyzed data is shown in Figure 66.



**Figure 66** XRD spectra measured at different radiation doses for a)  $\text{Ge}_{20}\text{Se}_{80}$  and b)  $\text{Ge}_{40}\text{Se}_{60}$ .

Diffusion of Ag into the Ge-Te films results in different diffusion products depending on the backbone. When introduced in Te-rich films, Ag reacts with Te from the Te chains, and forms  $\text{Ag}_2\text{Te}$ , which phase separates. In the case of introduction in the Ge-rich network, ternary  $\text{Ag}_8\text{GeTe}_6$  is the major crystalline phase forming, as shown in Figure 67 a), and b). In this system, the high polarizability of Te has to be accounted for which the tellurium atom can be assigned a positive charge. This can repel the Ag ions diffusion. In the Ge-rich Ge-Te films, due to irradiation, there is an increase in the formation of Ge-Te crystals with increased radiation dose.



**Figure 67** XRD patterns measured at different doses for a)  $\text{Ge}_{10}\text{Te}_{90}$  b)  $\text{Ge}_{40}\text{Te}_{60}$ .

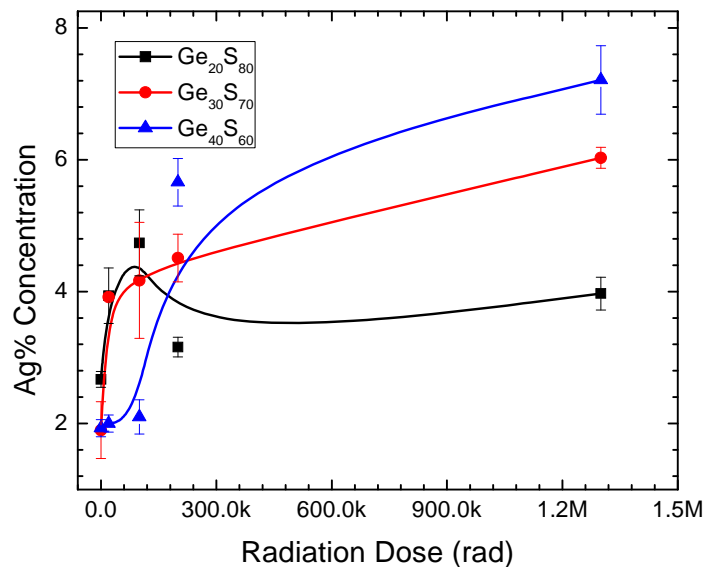
#### Energy Dispersive X-ray Spectroscopy (EDS)

As studies have shown [115, 117], silver concentration directly correlates to the conductivity of the films. Investigation into the silver concentration changes as a function of dose has been performed using EDS, and the results for Ge-S are shown in Figure 68.

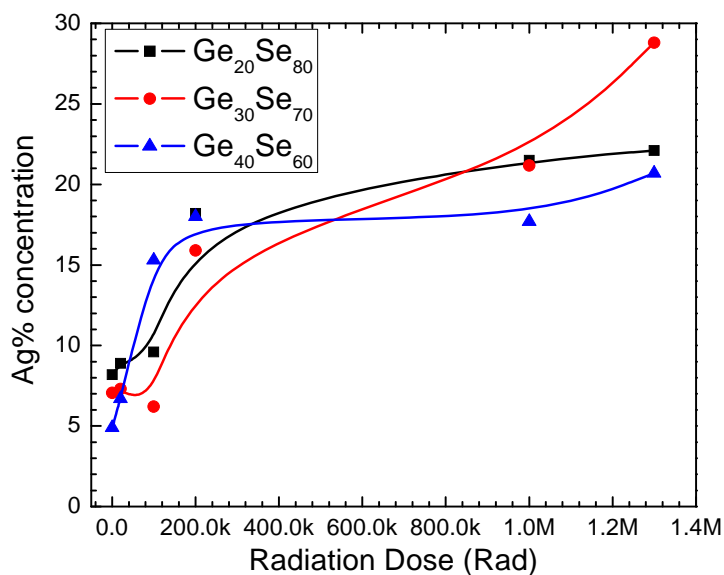
Silver concentration in Ge-Se system incurs an instantaneous rise with the lowest measured radiation dose in all the compositions. The concentration increases with



increasing germanium concentration up to 30 at.% Se. This trend is due to the formation of the layered structure creating localized fields that increase the attraction of silver ions.



**Figure 68** Amount of Ag concentration as a function of radiation dose for Ge-S glass films.



**Figure 69** Amount of Ag concentration incorporated into the chalcogenide film as a function of radiation dose in Ge-Se glass films.

## Discussion

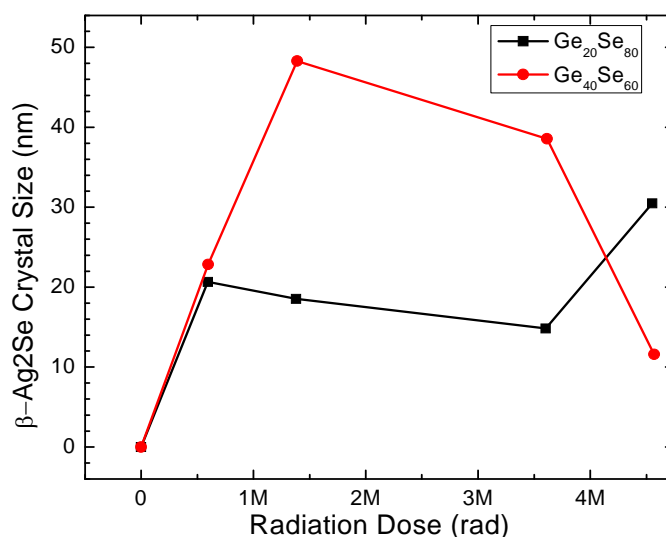
### Ge-S System

Once introduced into a noncrystalline or glassy phase within the Ge-S system, Ag could form stoichiometric solids, and could be included as an additive in the base network [140]. These additive can either segregate [139, 140] as separate phases or uniformly mix [140] with the base glass to form homogeneous solid electrolyte glasses. The fate of Ag strongly depends upon the matrix in which it is introduced. As revealed by the XRD studies for the case when Ag diffuses in  $\text{Ge}_{20}\text{S}_{80}$  film, part of it phase separates, and forms  $\text{Ag}_2\text{S}$  reacting with S from the S chains, and rings. The sizes of the peaks are small, suggesting small crystals are being formed, which therefore do not have a significant impact on the conductivity. On the other hand, the EDS analysis exhibited that the silver concentration increases with radiation dose in all of the compositions. There is an aspect that needs to be addressed about this result. Initially the non-irradiated samples have a small amount of silver. This is attributed to the small size, and fast mobility of the silver. When the silver film was evaporated onto the chalcogenide glass, the silver atoms that reach the film surface have some extra energy that will allow some silver to diffuse into the chalcogenide film while a majority of it will remain above the film. Therefore, some silver has entered the film for the non-irradiated samples. The S-rich samples immediately incorporate a large amount of silver due to the high affinity of the silver atom to the chalcogen atom. The  $\text{Ge}_{30}\text{S}_{70}$  films also exhibit a similar trend as the S-rich films, but the silver content continues to increase with increasing radiation dose. Ge-rich films react in a different method to the previous two types of films, where there is an

initial period of low silver incorporation followed by a drastic rise in the silver content. This behavior is attributed to the structural changes revealed in the bare film analysis.

### Ge-Se System

In the Ge-Se system, there are traces from  $\alpha$ -Ag<sub>2</sub>Se even in the initial films (see Figure 66). This phase is the superconductor phase, which highly contributes to the change in conductivity, when compared to the other two phases that are present in these films. For the Se-rich phases, the ternary Ag<sub>8</sub>GeSe<sub>4</sub> forms simultaneously with the  $\beta$ -Ag<sub>2</sub>Se. This is also the most abundant phase after Ag diffusion into Ge<sub>40</sub>Se<sub>60</sub>. The size of the  $\alpha$ -Ag<sub>2</sub>Se crystals diminishes after irradiation, presumably due to a polymorph transition to a  $\beta$  phase in both compositions. This  $\beta$ -Ag<sub>2</sub>Se is also the phase that predominantly develops during  $\gamma$ -radiation-induced Ag diffusion, as revealed by the XRD spectra. The  $\beta$ -Ag<sub>2</sub>Se is semiconductor with a low ionic conductivity component [141], which does not drastically contribute to the conductivity of the Ag radiation diffused films. The size of the beta phase has been analyzed using the Scherrer equation [142].



**Figure 70** Crystal size variation as a function of radiation dose for  $\beta$ -Ag<sub>2</sub>Se in Ge<sub>20</sub>Se<sub>80</sub>, and Ge<sub>40</sub>Se<sub>60</sub> films derived using the Debye-Scherrer equation for cubic crystals.

Close inspection of the crystal size analysis expounded that immediate exposure to radiation incurs an immediate rise in the formation of these types of crystals. Regardless of the backbone chalcogenide system, a similar crystal size is recorded at the initial stage of radiation dose. Beyond this initial radiation dose, the underlying structural changes dictate the size of the crystals. In the chalcogen-rich samples, since e-h pair formation limits the size of the crystals in the initial radiation doses. At higher radiation doses, the increased number of e-h pairs, and decrease in homopolar bonding, which increases the size of the crystals as exhibited by the crystal size measured at the highest radiation dose. The Ge-rich samples, due to the transition of ES/CS, and other structural changes exhibited in the Raman spectra, cause the formation of bigger crystal sizes. After a significant radiation dose, the oxidation effect discovered using the EDS oxidation (see Figure 54 b), limits the size of the crystals in the Ge-rich samples.

From the EDS analysis, the amount of silver incorporated into the chalcogenide films shows a consistent increase with an increase in radiation dose in Ge-Se system. There is a sharp rise in the silver content around 100krad from an initial 5-8% to approximately 15-18%. As shown earlier, a small amount of silver is required to cause a significant change in the electrical performance of the sensor. This combination of the higher silver incorporation with the large crystal sizes reveals that the addition of silver amplifies the structural changes observed in the bare film analysis.

### Ge-Te System

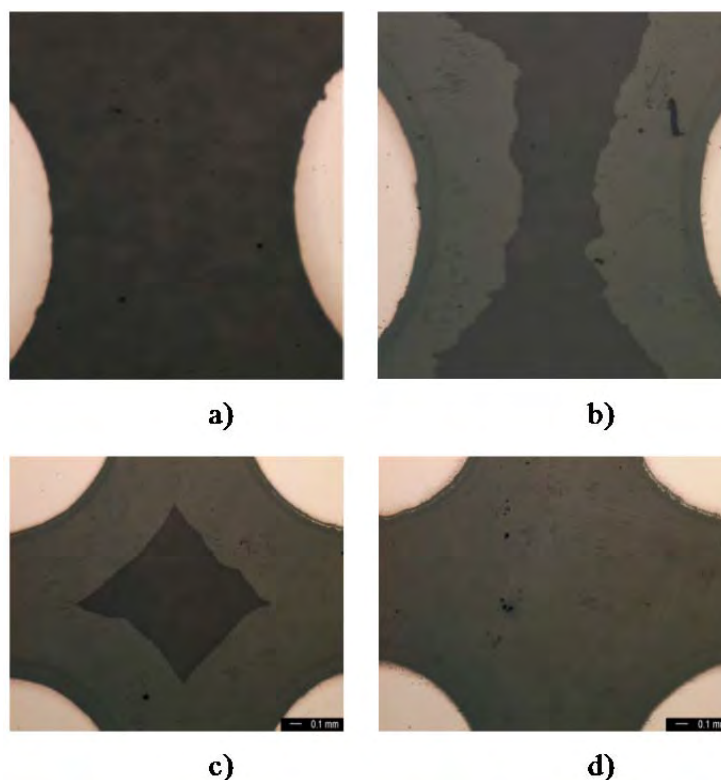
Initial introduction of Ag in the Ge-Te films has not been established, which is related to the film structure, and also to the positive charge coupled with the tetrahedrally connected Te atoms which repel the Ag ion diffusion. In the tellurium richer films, due to presence of tellurium chains, the preferred phase is the binary  $\text{Ag}_2\text{Te}$ , which develops from the initial radiation exposure, and is present with additional radiation exposure.

In the Ge-rich Ge-Te films, due to irradiation there is a phase separation resulting in the formation of Ge-Te crystals. The germanium-rich films consist of the formation of both the binary, and the ternary phases. Binary phase develops with the lowest radiation dose, but this phase disappears after 1.3 Mrad radiation dose due to the lack of free tellurium atoms. This phase is destroyed, and morphs into the ternary phase, which has a higher probability of formation, which can satisfy the bonding requirements of the Ge, and Te atoms. Another effect that plays a role in this composition is the presence of the dative bonding, which couples a tellurium atom with a negative charge, which attracts  $\text{Ag}^+$  ions. Due to this attraction, the resultant molecule is  $\text{Ag}_8\text{GeTe}_6$ , where the covalent bond requirements for Ag are satisfied with minimal disturbances to the neighboring molecules.

### Silver Diffusion Simulations

Silver diffusion studies offer a unique insight into predicting the sensitivity of the radiation sensor with the prior knowledge of the composition, and distance from the silver source to the measuring electrodes. Prior to investigating the silver diffusion using gamma radiation, it is important to confirm whether the simulation models are accurate. This confirmation was performed in collaboration with Dr. Michael Kozicki, and Dr.

Pradeep Dandamudi at Arizona State University, by taking images of films with circular silver sources before, and after discrete doses after illuminating with UV light. The diffusion profile achieved using UV light is shown in the figure below after  $0 \text{ J/cm}^2$ ,  $19.22 \text{ J/cm}^2$ ,  $33.64 \text{ J/cm}^2$ , and  $43.25 \text{ J/cm}^2$  doses. The corresponding times for the images are 0 hrs, 2.5 hrs, 3.5 hrs, and 6.5 hrs, respectively.



**Figure 71** Silver diffusion observed using films with silver source exposed to UV light after a) 0 hrs, b) 2.5 hrs, c) 3.5 hrs, and d) 6.5 hrs [143].

In the images above, the unirradiated sample consists of the two silver electrodes with large areas of undoped chalcogenide glass film. Increasing the absorbed dose to  $19.22 \text{ J/cm}^2$  resulted in a small but uniform diffusion distance, which continues with increasing UV dose until  $43.25 \text{ J/cm}^2$ , where the silver has completely diffused into the chalcogenide glass. Based on the images shown above, after 3.5 hrs of exposure, the observed diffusion distance is approximately 0.5 mm from each of the electrode bridging

the 1 mm distance. This value was used to determine the rate of diffusion (m/sec). Another quantity required to make the accurate simulation was to provide the diffusion coefficient ( $\text{m}^2/\text{sec}$ ) of the silver ions in  $\text{Ge}_{20}\text{Se}_{80}$  chalcogenide glass. This value was obtained from a literature review. As it is commonly known, silver does not have a constant diffusion coefficient, but rather this value is dependent on the silver concentration within the chalcogenide glass. Using the following coefficients, the initial baseline simulations were performed.

**Table 7** Coefficients for silver diffusion simulations

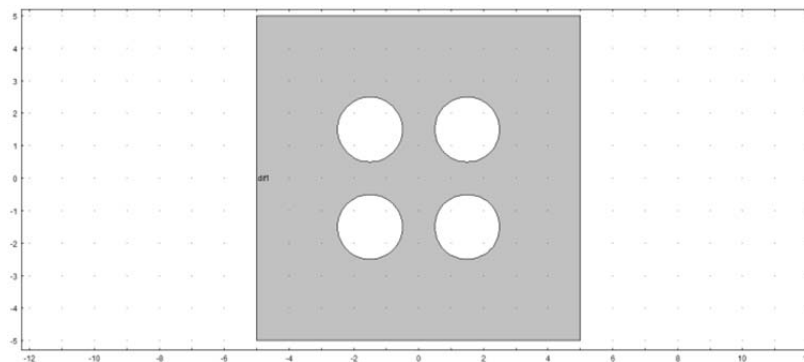
Diffusion coefficient ( $\mathcal{D}_{Ag}$ )	$5.5 \times 10^{-11} \text{ m}^2/\text{sec}$
Maximum concentration	$1 \text{ mol}/\text{m}^3$
$a$	0

These diffusion simulations were performed by applying an adjusted Fick's diffusion laws, and calculating the diffusion dependent on time using COMSOL simulations. The equation is shown below:

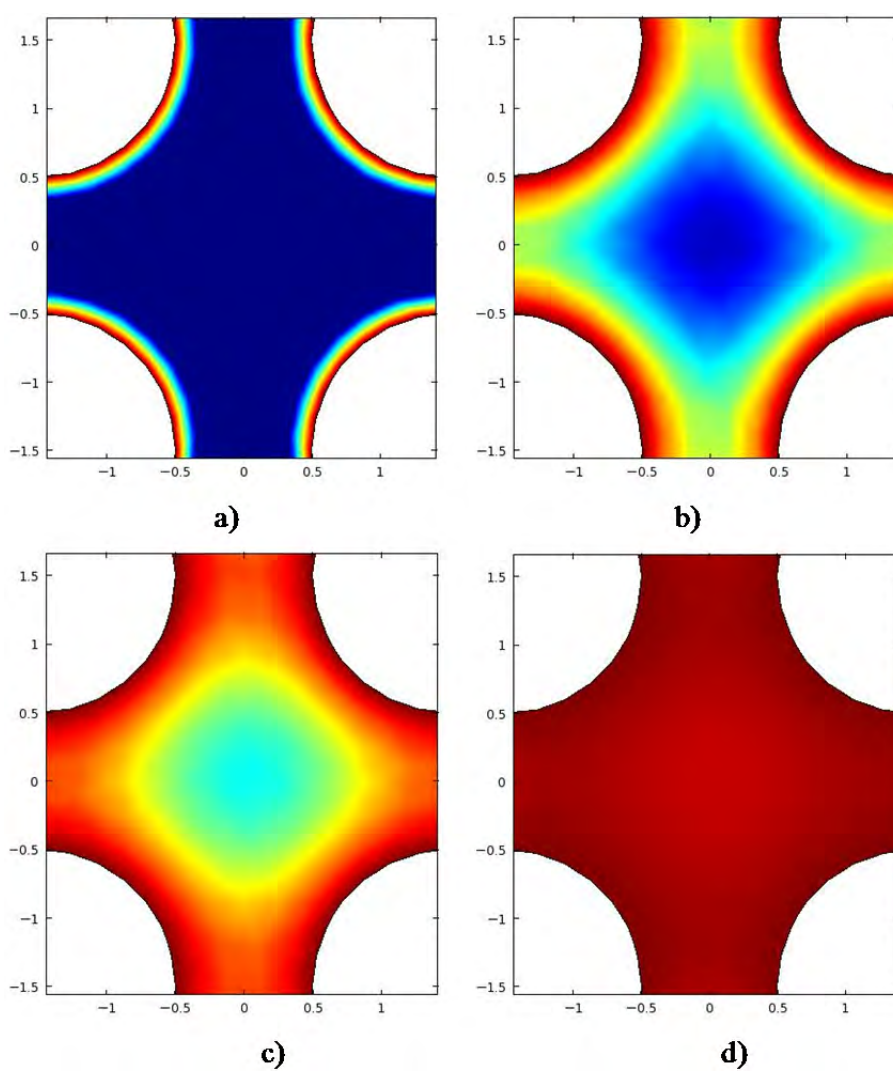
$$\mathbf{0} = \frac{\partial^2 \mathbf{u}}{\partial t^2} + \nabla \cdot (-\mathcal{D}_{Ag} \nabla \mathbf{u}) + a \mathbf{u} \quad (25)$$

Where  $u$  is the concentration of silver,  $\mathcal{D}_{Ag}$  is the diffusion coefficient, and  $a$  is a correction term, which allows the ability to closely resemble the experimental result. During the simulation, only the diffusion coefficient, and the  $a$  terms were manipulated.

After determining the appropriate equation, and the values for the simulation, the device was then modeled as the fabricated devices with a large square area representing the blanket chalcogenide film, and 4 circular (1 mm radius) circles were placed as shown in the figure below. The horizontal, and vertical spacing of the electrodes was 1 mm.



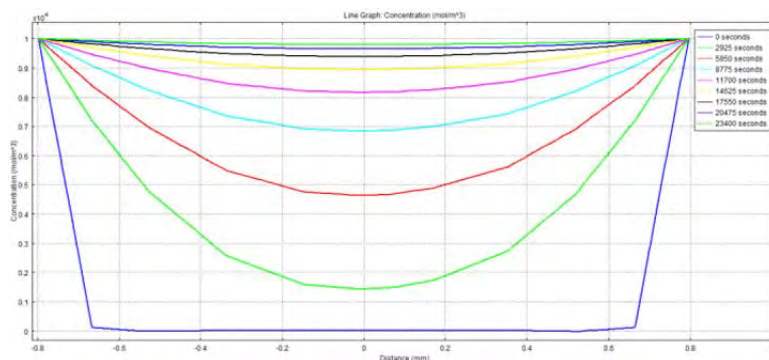
**Figure 72** Geometry of the simulated model used to resemble the films with lateral silver sources.



**Figure 73** Result of the COMSOL simulation of silver diffusion, where red represents that highest silver concentration, and blue represents the lowest silver concentration after a) 0hrs, b) 2.5hrs, c) 3.5 hrs, and d) 6.5 hrs.



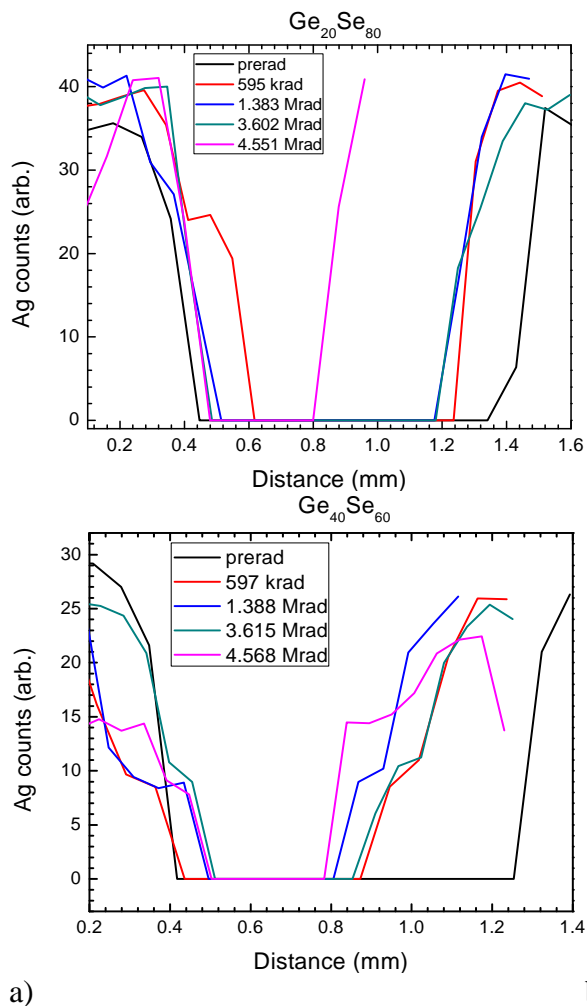
The modeling results show a good correlation with the observed diffusion, suggesting that this method is an appropriate approximation of the silver diffusion. Below is a graph of the concentration between two diagonal silver sources. By iteratively adjusting the diffusion coefficient to  $5.5 \times 10^{-11} \text{ m}^2/\text{sec}$ , a solution similar to the experimental result is achieved as shown in the following graph.



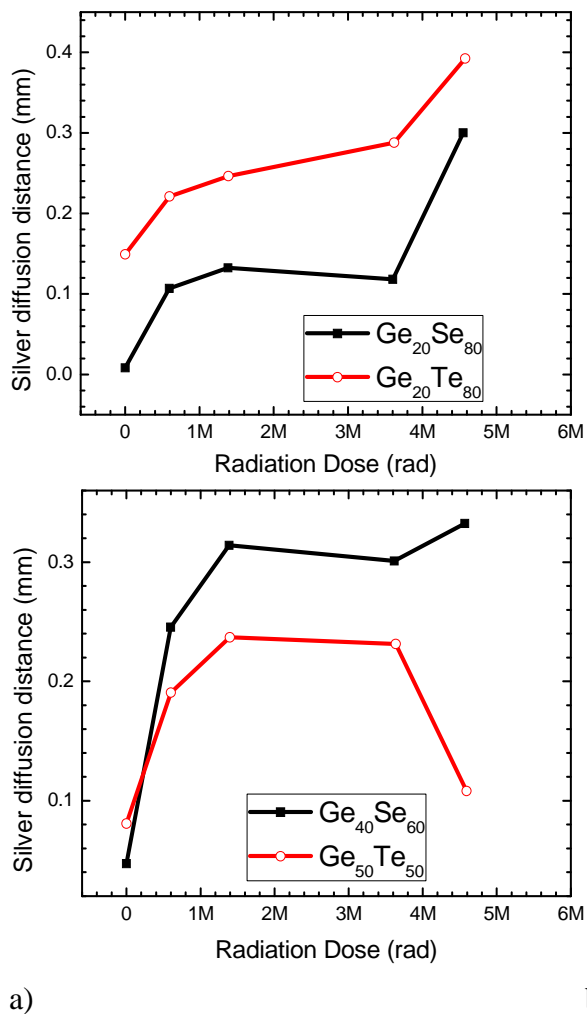
**Figure 74** Cut line concentration profile between two diagonal silver sources plotted at corresponding times to the observed images, and using the diffusion coefficient for  $5.5 \times 10^{-11} \text{ m}^2/\text{sec}$ .

After determining that this methodology is an appropriate approach towards modeling silver diffusion, experimental measurements were performed using circular silver sources as shown in Figure 74, but rather than illuminating the films with a UV source the films were exposed to gamma rays. The exact silver diffusion distance has been determined through compositional analysis of the films using EDS. The structure of the circular silver sources on the bare films presents a good opportunity to characterize Ag diffusion as a function of the radiation dose through mapping of the Ag concentration between the two inert electrodes on which the conductivity of the devices is characterized.

The radiation field distribution during the experiments is uniform around the irradiated film, which results in lateral Ag diffusion. The actual data collected for  $\text{Ge}_{20}\text{Se}_{80}$ , and  $\text{Ge}_{40}\text{Se}_{60}$  films are shown in Figure 75 a, and b, respectively. The experimentally acquired data resembles the shape, and the concentration distribution characteristic for silver diffusion in chalcogenide glasses. Furthermore Figure 76 a, and b represent the particular concentration distribution for floppy chalcogenide films containing Se, and Te (a), and rigid films containing Se, and Te (b). For all Ge-Se, and Ge-Te films, the distance of diffused Ag increases with increased radiation dose. However, for the rigid Te containing films, the Ag diffusion distance actually decreases at high dose levels.

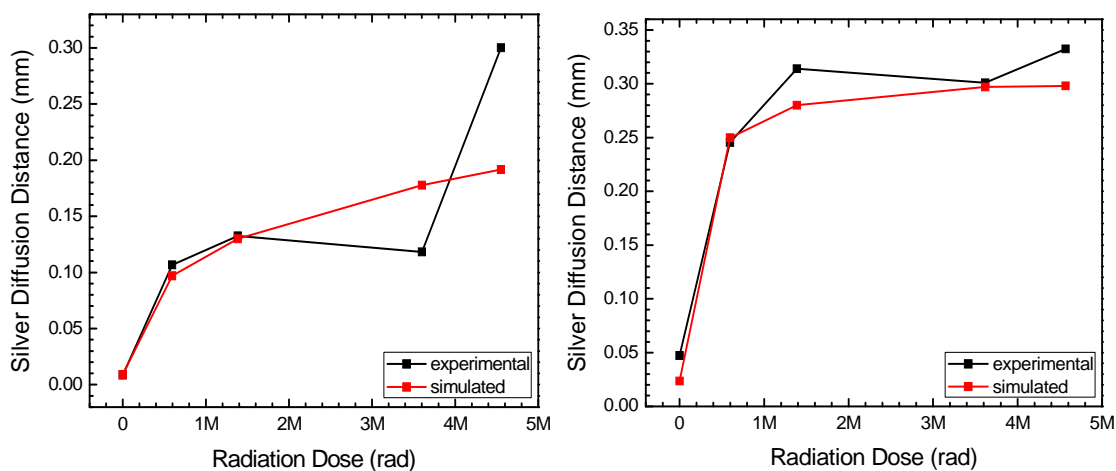


**Figure 75** Measured silver diffusion using EDS for a)  $\text{Ge}_{20}\text{Se}_{80}$  and b)  $\text{Ge}_{40}\text{Se}_{60}$ . The measurement was performed from one silver source to another. Silver concentration is the highest in regions where silver has diffused, and regions that represent 0 Ag counts are the undoped chalcogenide film.



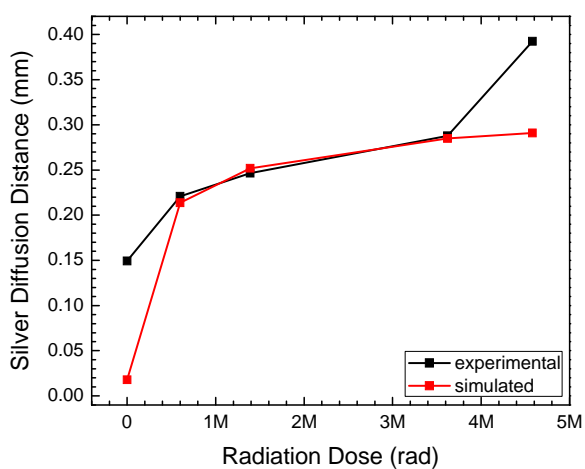
**Figure 76** Taking the results from the EDS measurements (shown in Figure 77), silver diffusion distances have been calculated for a) floppy, and b) rigid films.

These experimental values have been used to simulate the diffusion mechanics of silver from the initial state to the end of the gamma ray exposure. The same equation that has been utilized for the UV baseline simulations has been modified for the gamma-irradiated measurements, and the result of this simulation is compared to the measured silver diffusion data shown below.

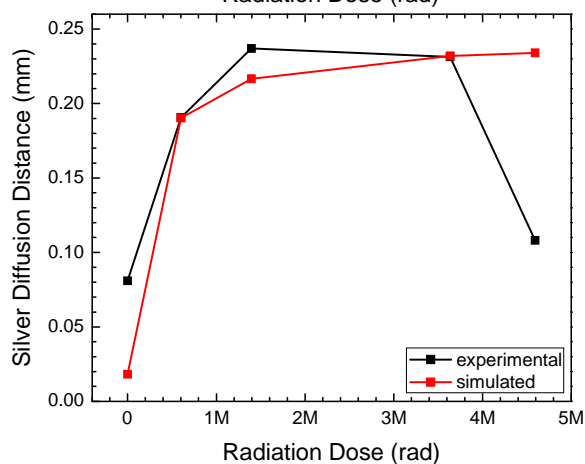


a)

b)



c)



d)

**Figure 77** Experimental (black), and simulated (red) results of silver diffusion distance as a function of radiation dose for a)  $\text{Ge}_{20}\text{Se}_{80}$ , b)  $\text{Ge}_{40}\text{Se}_{60}$ , c)  $\text{Ge}_{20}\text{Te}_{80}$ , and d)  $\text{Ge}_{50}\text{Te}_{50}$ .

The simulated results, and the experimentally measured results correlate with one another. The coefficients that serve as inputs to the diffusion equation have been tabulated for each composition, and are summarized in the following table.

**Table 8 Silver diffusion coefficients for Ge-Se, and Ge-Te films**

<b>Film Composition</b>	<b><math>\mathcal{D}_{Ag}</math> (m<sup>2</sup>/sec)</b>	<b><math>\alpha</math> (m<sup>3</sup>/sec)</b>
Ge <sub>21.82</sub> Se <sub>78.18</sub>	$2.8 \times 10^{-12}$	$-1.8 \times 10^{-7}$
Ge <sub>43.60</sub> Se <sub>56.40</sub>	$8.5 \times 10^{-12}$	0
Ge <sub>10.65</sub> Te <sub>89.35</sub>	$4.2 \times 10^{-11}$	$2.2 \times 10^{-6}$
Ge <sub>48.22</sub> Te <sub>51.78</sub>	$3.25 \times 10^{-11}$	$4.5 \times 10^{-6}$

### Conclusion

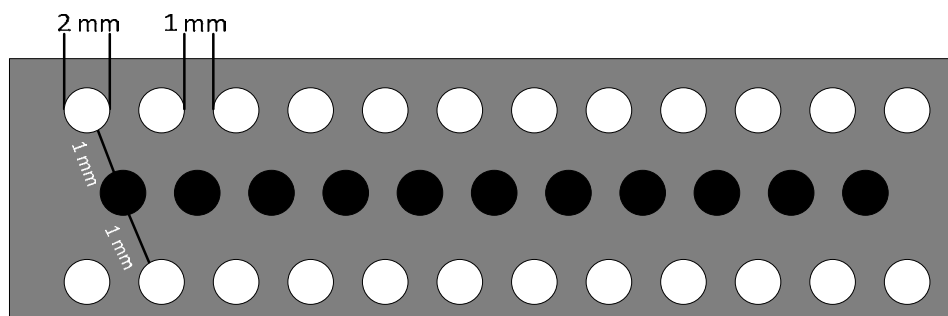
Study of the material properties allows the ability to make a choice regarding the appropriate type of material for the specific application, and provide a basis for designing a sensor based on these materials. Investigations of gamma radiation effects on the Ge-S, Ge-Se, and Ge-Te films revealed that germanium-rich films in all three compositions in addition to the Ge<sub>20</sub>Te<sub>80</sub> films exhibit a specific structural change that has been detected by Raman spectroscopy, while the chalcogen-rich compositions of the Ge-S, and Ge-Se films do not show any structural changes. In the chalcogen-rich films, it was determined that the formation of electron-hole pairs dominates the changes observed in these films, and this result has been confirmed by the optical bandgap measurements. Initially there is no change in the bandgap of the film, but with increased UV exposure created new defects that decreased the bandgap of the material creating a photodarkening effect within the films. The surface roughness of all the chalcogen-rich films increases with radiation, and the XRD study revealed the formation of binary molecules, which aid in the change in the conductivity of the films.

The change observed in the germanium-rich films is attributed to the transformation of edge-shared tetrahedra to corner-shared units, which opens the structure of the films, thus to allow diffusion of fast moving ions such as silver. The other aspect that is prominent within these films is the effect of oxidation. Optical measurements provided evidence that in the presence of oxygen, and with additional radiation the films undergo photobleaching effect, which is not present in the films irradiated under vacuum. The XPS study also confirms the finding of topological oxidation, which can occur with increased radiation exposure. Additionally, the EDS measurements illustrated the increase in oxidation with radiation dose, which is in line with the other observation in these film compositions. The formation of different types of binary, and ternary compounds illustrated by the XRD study suggests that the conductivity of the films could change as a function of radiation dose. The silver diffusion simulations, and silver concentration measurements of all the films show that a device created with these films has the capability to display a significant change in conductivity due to radiation dose.

## GENERATION 1 DEVICES

### Device Fabrication

The bare chalcogenide film used for the film analysis was also used to create devices using a shadow mask with silver sources, and non-diffusive electrodes. The non-diffusive metal was used to measure the change in conductivity of the films. Various metals were applied for creating the non-diffusive metal electrodes, of which tungsten, mixture of tungsten, and chromium, and aluminum were selected as appropriate for this purpose. The electrodes were deposited in specific regions of the wafer using a circular shadow mask similar to the figure shown below.



**Figure 78** Shadow mask used for making Gen. 1 devices. Black circles represent openings that have been blocked, preventing the deposition of metals in this region. The deposition of metal is restricted to the areas represented by white circles.

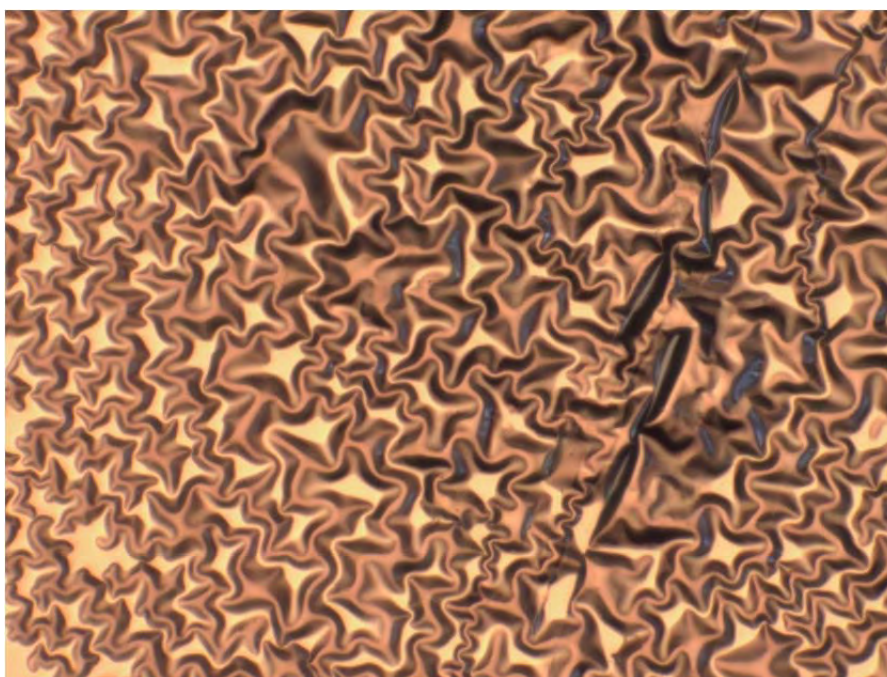
In the image above, the circles represented in white are openings where the metals were deposited onto the film, while the black circles represent areas where the openings have been closed off, and metal was not deposited in these areas. The method of creating the devices begins by taking a portion of the wafer covered by the bare film, and placing



the shadow mask on top of the film, such that the mask is in direct contact with the film a method similar to contact lithography, which is tightly secured. The Ag evaporation was performed inside the Cressington 308R evaporator. As previously described, regarding the evaporation of topologically deposited silver on the bare films, silver was evaporated into the openings of the mask onto the films. To avoid issues regarding sample variations, samples covered with topological silver, films with circular silver sources, and devices were prepared at the same time. In this manner, the initial devices had 50 nm thick Ag electrodes, but later it was observed that increasing the thickness of the Ag electrode to 100 nm allows the capability to measure the device at higher radiation doses in addition to the capability to reset the device by electrically drawing back the silver towards the Ag electrode.

Next, it is important to create another electrode to measure the conductivity of the chalcogenide film. Silver source cannot be used to measure the film since silver can diffuse under an applied electric field [144], therefore another metal, that does not diffuse under the influence of the applied electric field, is required to measure the conductivity of the films. These electrodes were also deposited using the shadow mask used for creating the silver source, but to avoid overlapping the silver electrode with the other metal electrode, the mask was shifted such that the black circles (illustrated in Figure 78) were aligned over the Ag sources, and the rows of open areas are situated equidistant from a nearby silver source. Originally, the first versions of the devices were prepared with sputtered tungsten used as the inert electrode. Tungsten was sputtered using an AJA sputtering system, which has the capability of generating either a RF or DC plasma. The system was evacuated to less than  $1 \times 10^{-7}$  torr, and using RF plasma, for 15 minutes,

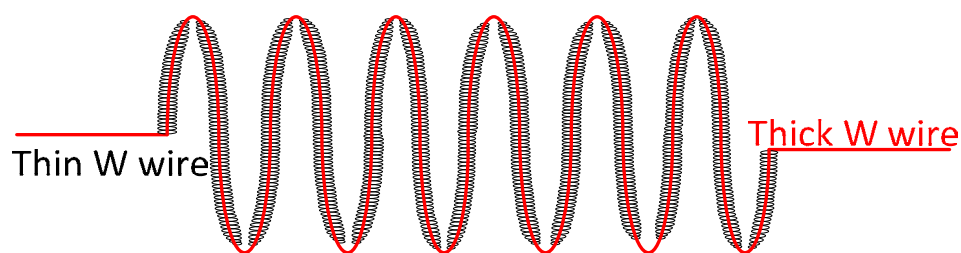
approximately 150 nm of tungsten were deposited. The problem with tungsten is that some of the electrodes expressed a lack of adhesion between the tungsten, and chalcogenide glass interface, while other electrodes on the same sample had excellent adhesion. The range of adhesion reduced the overall yield of functioning devices. The electrodes that exhibited a lack of adhesion were easily removed, and the surface of the electrode is shown in Figure 79.



**Figure 79** Microscope image of one of the sputtered tungsten electrode, which exhibited the lack of adhesion between the electrode, and chalcogenide film. This buckling phenomenon is attributed to the large size of the W atom in comparison to the atoms in the chalcogenide film.

The overall yield was improved by dual deposition of chromium followed by tungsten to increase the adhesion. This new procedure was also performed on the AJA sputtering system. Initially there was a 1 minute RF clean performed on the open areas of the mask immediately followed by a 50 nm chromium deposition. Near the end of the chromium deposition, the shutter holding the tungsten electrode was opened such that for

a duration of 1 minute both chromium, and tungsten were deposited to increase the adhesion of the tungsten. Finally, only the tungsten shutter was opened until a thickness of 100 nm was deposited. While this technique was a viable solution, it is established that aluminum does not incur any adverse reaction to radiation, and is a better metal under radiation conditions [145, 146]. Therefore, it was determined that aluminum has the same adhesion properties as the Cr + W co-deposited electrodes. The thermally evaporated aluminum showed consistent results with adhesion, and ease of deposition. It is also easily wire bondable. Due to these significant advantages that are derived from the use of aluminum, a change in the inert electrode was made from sputtered tungsten, and chromium to thermally evaporated aluminum. Thermal evaporation of aluminum was performed in the Cressington 308R thermal evaporation system using a specially designed crucible unlike the ones for silver, and chalcogenide film. The source of aluminum was aluminum foil, which has been thoroughly cleaned using Acetone followed by Isopropanol alcohol to remove the various contaminants. The foil was wrapped around two different thicknesses of tungsten wire, where the thinnest wire was wrapped around the thicker wire, as shown in the figure below.



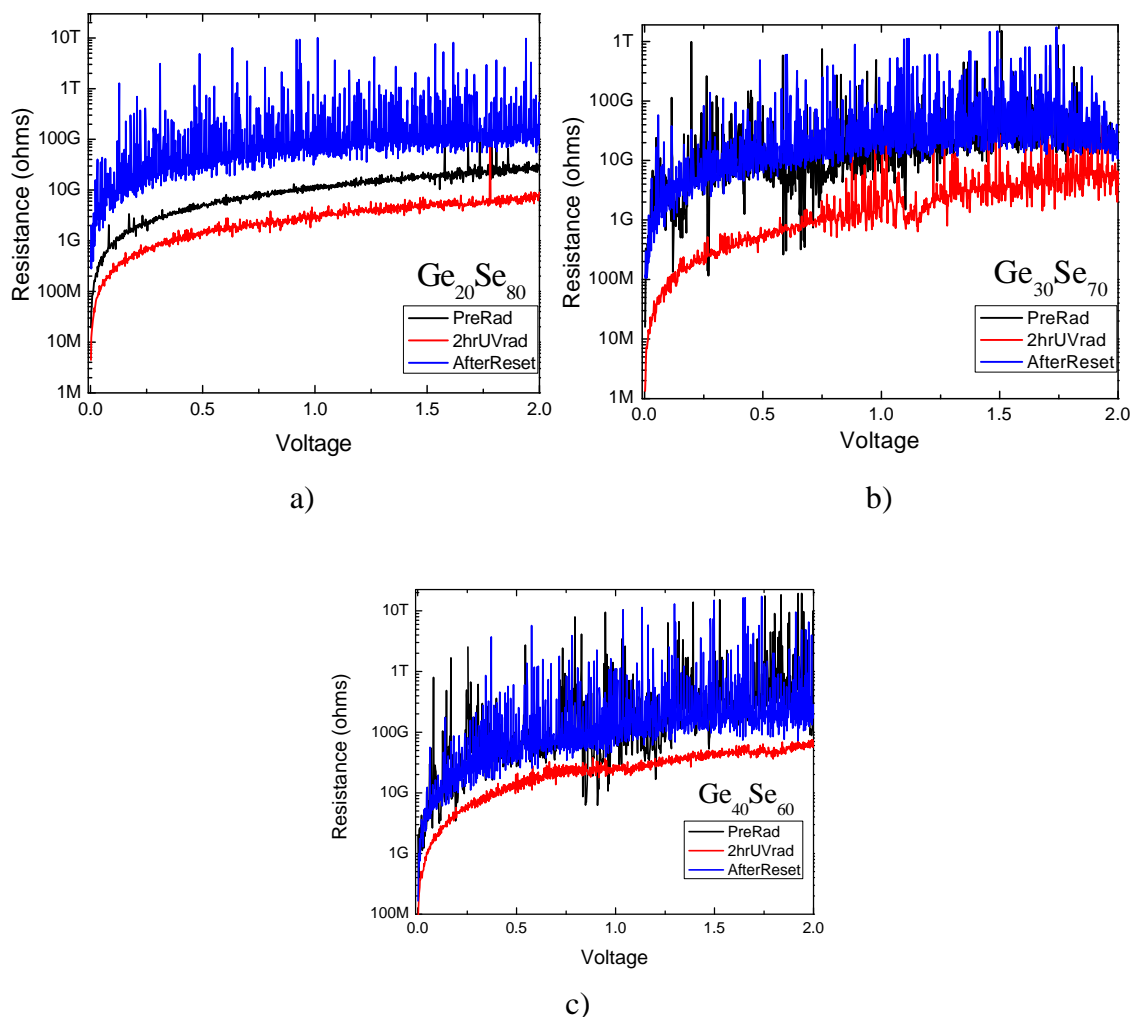
**Figure 80** Crucible used for Al evaporation with the application of two wire thickness.

Evaporation was performed at  $1 \times 10^{-6}$  bar, and initially a shutter was placed above the aluminum crucible, which helps evaporate any impurities in the aluminum foil, leaving behind a molten liquid of aluminum. Once the foil has melted into a molten liquid, the shutter was opened allowing for the evaporation of pure aluminum onto the mask, and chalcogenide film. The only issue that arose due to the switch to aluminum was the high oxidizing ability of aluminum. Aluminum oxide is a dielectric, so to prevent the oxygen from interacting with the surface of the aluminum, a cap consisting of a 20 nm layer of silver was deposited without breaking vacuum to prevent the introduction of oxygen between the silver layer, and aluminum. This silver thickness was significantly smaller in comparison to the aluminum thickness such that the silver does not come in contact with the chalcogenide glass film, which can change the conductivity of the film.

### **UV Characterization**

These devices were initially tested using a  $1.5 \text{ W/cm}^2$  UV radiation source, and measured after discrete radiation doses. This test provides the viability of each device. The devices were measured using a HP 4146 parameter analyzer using a DC voltage sweep between 0 V, and 2 V. Using gold probes, and a faraday cage, the entire measuring station has been isolated from any external noise source, and charge buildup using specialized cables. The probes have been placed on two adjacent Al electrodes, and the current between these two electrodes has been measured, and recorded during the DC voltage sweep. The results have been analyzed, and are shown in the figures below for 3 compositions from the Ge-Se system. The device has been reset by connecting the Al electrodes together, and applying a positive voltage (2V). Simultaneously, the silver sources were contacted, and placed at a ground potential to create a large electric field

between the silver source, and the Al electrodes. This appropriate voltage bias in addition to the large voltage creates an electric field, which forces the flow of electrons towards the Al electrode, and concurrently ionizes the silver atoms creating positively charged silver ions, which become attracted towards the silver source. In this manner, a significant amount of silver that has diffused as a result of radiation would be expected to return to the source, and thus reset the device for repeat usages.



**Figure 81** Resistance-Voltage device characteristics under UV exposure for a)  $\text{Ge}_{20}\text{Se}_{80}$ , b)  $\text{Ge}_{30}\text{Se}_{70}$ , and c)  $\text{Ge}_{40}\text{Se}_{60}$ . The black spectra (prior to UV exposure), red spectra (post UV exposure), and blue spectra (after device reset).

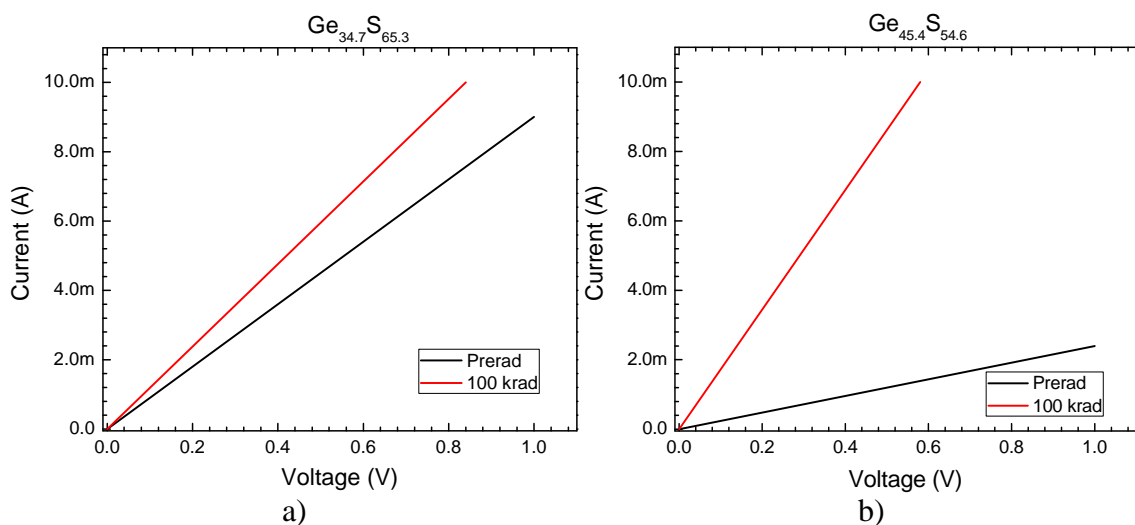
These results show conclusively that the device is suitable for sensing radiation, and it can be reversed to the initial condition. The UV radiation causes a measurable change in the conductivity of the three film compositions from the Ge-Se films. After device reset, the conductivity of the film returns to the original state or to a state with significantly less conductivity depending on the time, and the reverse field applied.

### Gamma Ray Characterization

Following the UV characterization experiment, it was determined that the devices were fully functional using the ascribed process flow above. The next step was to irradiate the devices using gamma radiation, and measure the conductivity of the devices after discrete radiation doses. This type of characterization was performed for Ge-S, Ge-Se, and Ge-Te Gen. 1 devices.

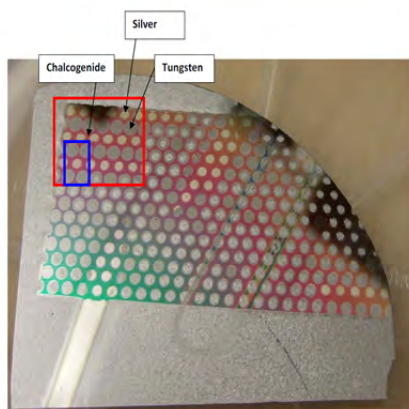
#### Ge-S Based Devices

The Ge-S devices were prepared, and tested, and the results are summarized in the figures shown below.



**Figure 82** Gamma ray device testing results for a) Ge<sub>34.7</sub>S<sub>65.3</sub> and b) Ge<sub>45.5</sub>S<sub>54.6</sub>.

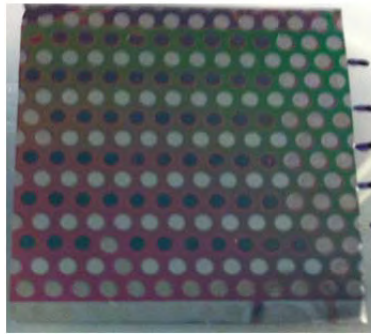
The results reveal a high preradiation conductivity. The change of the device conductivity in the  $\text{Ge}_{35}\text{S}_{65}$  devices is minimal while the change observed in the  $\text{Ge}_{45}\text{S}_{55}$  device is large. This lack of change in the S-richer device leads back to the material characteristics, where the Raman spectra for the corresponding films do not represent any noticeable change. The change in conductivity in this device is due to the effect of defect formation, and concurrent recombination. On the other hand, the change in the Ge-richer devices are ascribed to the structural changes resulting in the opening of the film structure leading to the increased silver diffusion. The radiation dose range measured in this experiment is small that the effects of oxidation can be negligible, and thus the change in conductivity is directly related to the structural changes than any other extraneous effects. The significantly higher amount of conductivity is attributed to the distance between the measuring electrodes, which was significantly smaller as shown in the image of the devices.



**Figure 83** Post fabrication of Ge-S Gen. 1 devices prior to process optimization.

It is known that the resistivity of the material is directly proportional to the distance between the measuring electrodes. Therefore, reducing the distance between the

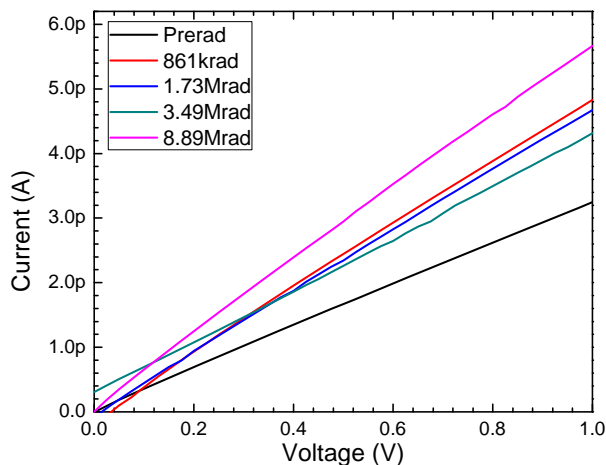
measuring electrodes decreases the resistivity of the material, which increases the measured current. This type of spacing is not consistent, thus the results derived from the initial measurements had a large deviation. With additional fine tuning of the fabrication process as well as the switch to thermal evaporation of aluminum allowed the creation of consistent spacing between the electrodes, which improves the reliability. The devices shown below represent the evenly spaced devices resulting in a consistent measurement between adjacent devices.



**Figure 84**      **Optimized Gen. 1 devices post fabrication.**

The success of the new updates to the process flow enhanced the ability to create a significant number of devices at once. Initially, the process flow design could create a maximum 12 devices, but the increased consistency enabled the creation of 52 devices, which are shown in Figure 84.



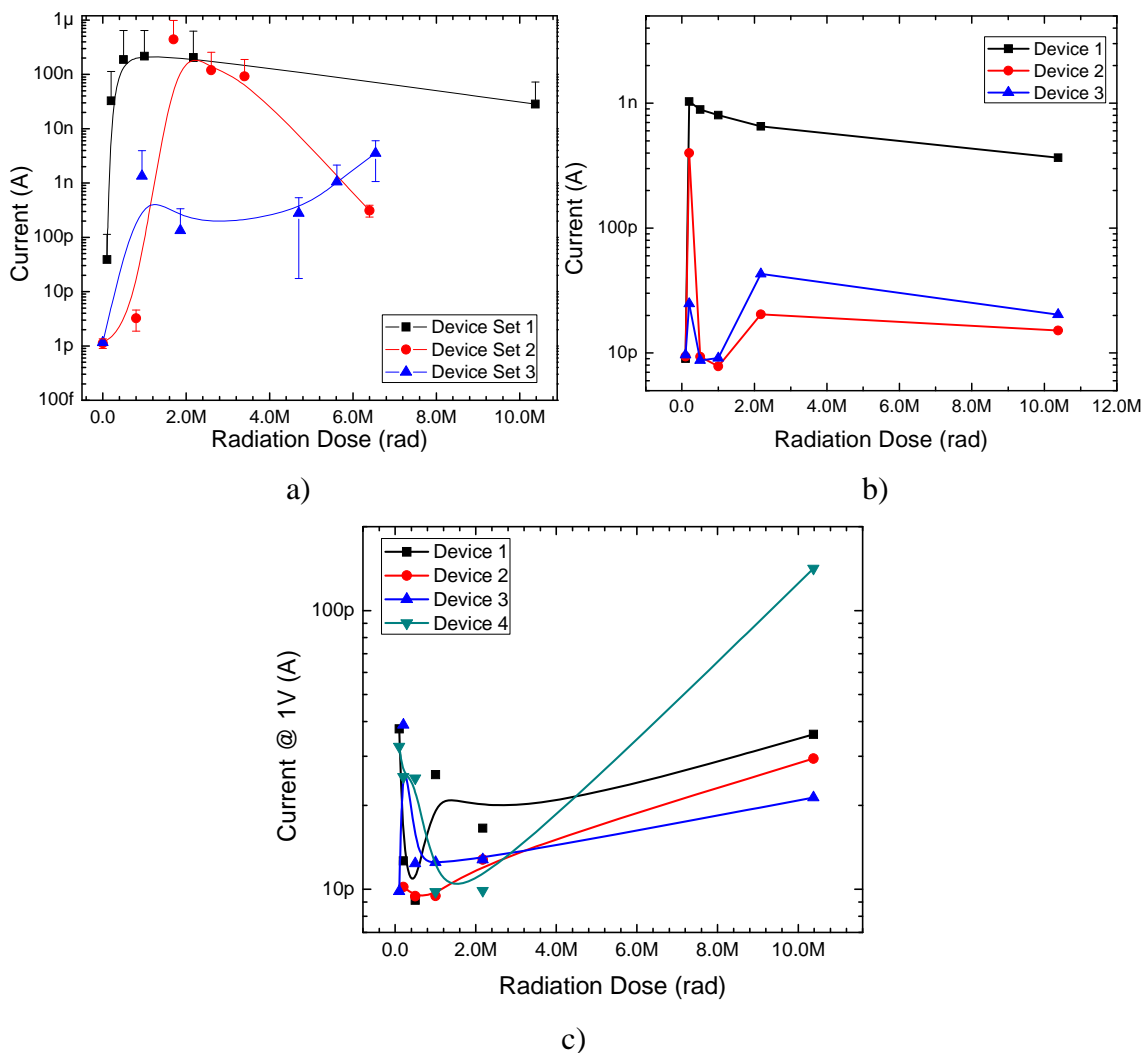


**Figure 85** Current vs. Voltage characteristics for  $\text{Ge}_{33}\text{S}_{67}$  devices after optimization.

The measured devices after optimization revealed a similar trend as previous version of the device, where the change in conductivity is minimal. It can be concluded from these results that the distance of the devices is an important aspect to consider regarding the conductivity of the material, but the sensitivity of the device is highly dependent on the material properties, and the reaction of the material to radiation.

### Ge-Se Based Devices

Based on the material analysis, the Ge-Se system has revealed a higher sensitivity; therefore, devices were fabricated using the optimized process flow with the Ge-Se system. The results from various radiation experiments are summarized in the figures below.



**Figure 86** Device testing results for a) Ge<sub>20</sub>Se<sub>80</sub>, b) Ge<sub>30</sub>Se<sub>70</sub>, and c) Ge<sub>40</sub>Se<sub>60</sub>.

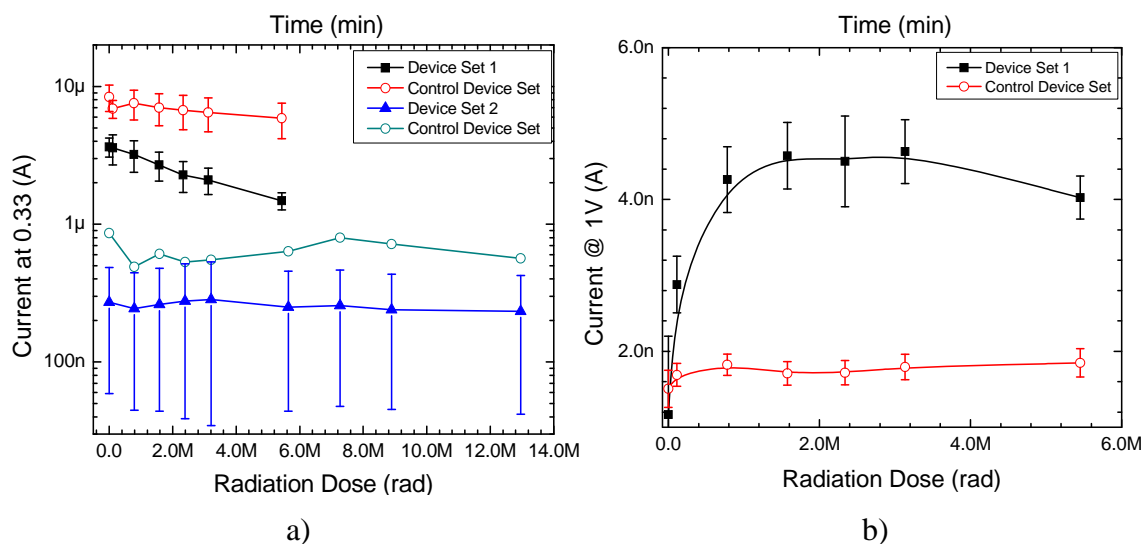
The data presented in Figure 86 a-c were compiled from multiple radiation experiments with around 4-5 devices per radiation experiment in Ge<sub>20</sub>Se<sub>80</sub> results. The results for the chalcogen-rich devices reveal an immediate increase in the conductivity at low radiation doses attributed to the formation of defects on the chalcogen atoms, and the presence of the binary phase as illustrated from the film analysis. There was five or six orders of magnitude change in conductivity in the some of the devices i.e. device sets 1, and 2, respectively. This change in conductivity is sustained (static change) since the devices were measured 15-30 minutes post irradiation exposure. Therefore, the observed

conductivity changes are actual changes to the material, which are frozen in time due to the inclusion of silver. The large increase in the conductivity is followed by a decrease in the conductivity in these compositions, which is attributed to the recombination of defects.

The germanium-rich devices reveal a unique trend that is a combination of all the film characteristics. The devices do not show a significant change in conductivity at low radiation doses like the  $\text{Ge}_{20}\text{Se}_{80}$  devices, but rather begin to show the preliminary changes at higher doses. The structural changes, and the distance of the silver sources play a significant role in determining the dose, which exhibits the greatest change in the conductivity. These two components need to be taken into consideration for improving the design of the radiation sensor. Through various radiation experiments, the  $\text{Ge}_{30}\text{Se}_{70}$  devices did not reveal any substantial changes unlike the  $\text{Ge}_{20}\text{Se}_{80}$  or the  $\text{Ge}_{40}\text{Se}_{60}$  devices.

#### Ge-Te Based Devices

Tellurium based devices were also tested, and the measurements were performed similar to the other devices, with a small caveat. The addition of tellurium significantly increases the conductivity of the pure chalcogenide glass without the addition of silver, thus the compliance limitations of the measurement device were adjusted to accurately measure the conductivity of the material. The collected device data is shown in Figure 87 for  $\text{Ge}_{20}\text{Te}_{80}$ , and  $\text{Ge}_{50}\text{Te}_{50}$ .



**Figure 87** Device testing results for a)  $\text{Ge}_{20}\text{Te}_{80}$  and b)  $\text{Ge}_{50}\text{Te}_{50}$ .

The devices that are labeled as control, and represented by open circles in both device compositions are devices that have been prepared, and experienced the same environmental factors as the measured devices. The only difference between the control devices to the other devices was the exposure towards gamma radiation. The control devices were shielded from the radiation, and did not experience any radiation conditions, while the other devices have been placed inside the gamma radiation environment. These control devices were measured at the same time intervals as the radiated devices. Both of these device data (control, and irradiated) were compiled together on the same graph for comparison purposes, but the control devices will be discussed with respect to current vs. time, while the irradiated samples will be discussed with respect to current vs. radiation dose.

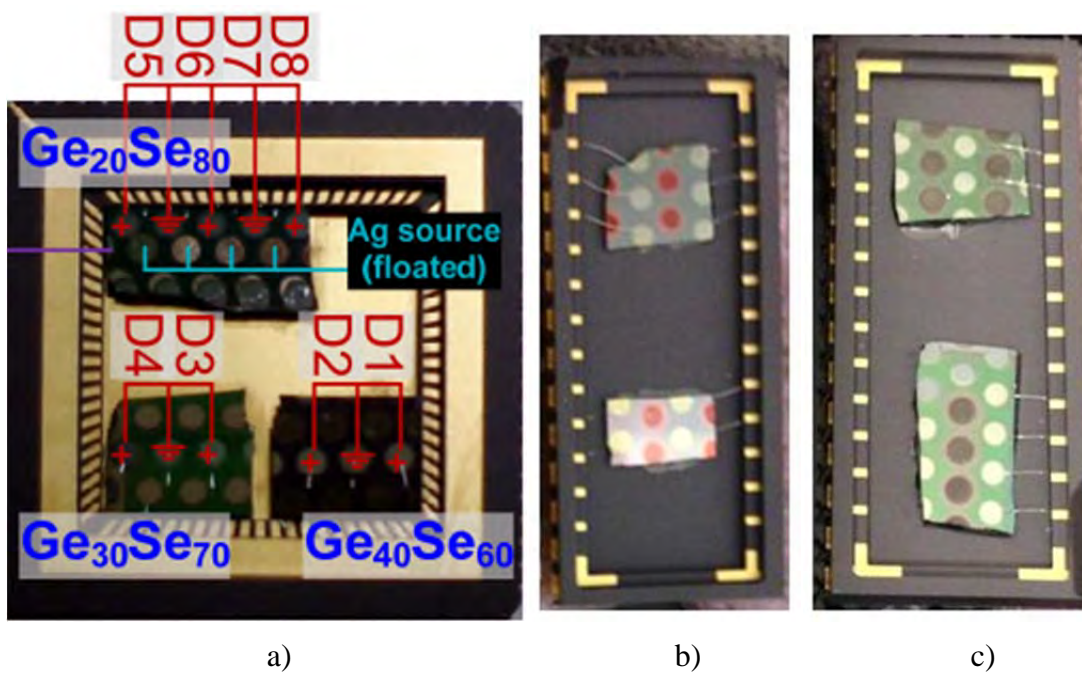
The tellurium-rich devices exhibit a high conductivity prior to radiation exposure, and after radiation exposure, the device conductivity decreases linearly in a semilog-linear graph. This behavior is attributed to the lower conductivity of the silver containing

Ge-Te films, which include  $\text{Ag}_2\text{Te}$  with a conductivity of  $4.3 \times 10^3 \Omega^{-1} \text{cm}^{-1}$  [91], in addition to the polarizability of the tellurium atom, which can create this decline in the conductivity [147]. During the decrease in the conductivity, the control devices do not exhibit any change in conductivity thus confirming that the exhibited response is purely radiation based effects. In the germanium-rich devices, more specifically in the  $\text{Ge}_{50}\text{Te}_{50}$  devices, the devices show the capability to react at low radiation doses but the change is minimal. This behavior is highly dependent on the oxidation effects, which suppresses the other effects within this device composition.

### **Conclusion**

Gen. 1 devices were prepared, and studied under UV, and gamma radiation conditions for Ge-S, Ge-Se, and Ge-Te systems. The devices were initially prepared with tungsten electrodes, and through process optimization, the final devices were created using thermally evaporated aluminum with thin film of silver to prevent oxidation. The Ge-S devices revealed that the distance between the electrodes, and the corresponding distance to the silver source has a significant impact on the conductivity of the devices. Selenium containing devices show promise for a good device performance, where a considerable number of devices revealed at least five orders of magnitude change in the conductivity of the device due to the exposure to radiation. The devices containing tellurium offer a new type of conductivity change that is unique to this chalcogenide system, which is not prevalent in the other devices. With increased radiation dose, the conductivity of the devices decreased. The outstanding issues with this type of device structure are the lack of freedom to vary the device sizes, the significant distance between

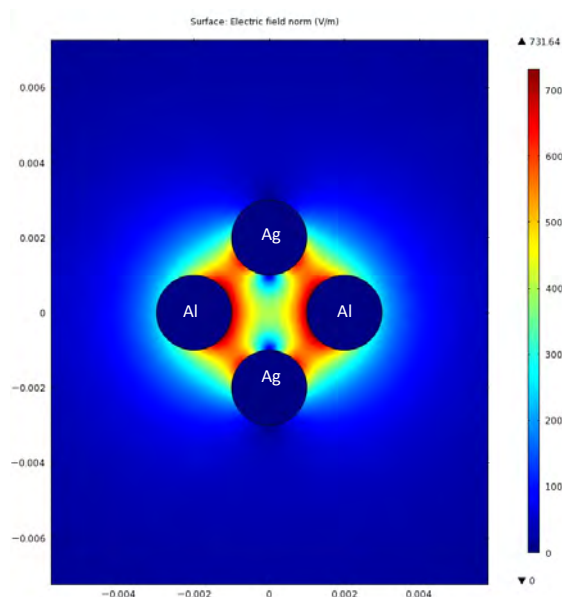
the sensing electrodes, and the silver source, which contribute to the reduction of consistency between different radiation experiments.



**Figure 88** Wire bonded Gen. 1 device final product a) Measurement scheme for testing, and identifying devices, b) Final DIP packaged  $\text{Ge}_{40}\text{Se}_{60}$  devices, and c) Final DIP packaged  $\text{Ge}_{20}\text{Se}_{80}$  devices

## GENERATION 2 DEVICES

The Gen. 1 devices are useful for measuring the performance of a device with one specific geometry, spacing, and dimensions of the electrodes at discrete radiation doses. However, the Gen. 1 devices are not suitable for changing the geometry as well as the ability to measure insitu radiation. The main drawback for making insitu measurements is the application of a constant DC voltage bias in order to measure the change in resistance as a function of time. Applying a constant voltage bias on the Gen. 1 devices will result in an electric field distribution as shown in Figure 89. Similar to radiation-induced silver diffusion, electric fields can also cause silver diffusion. Kang *et al.* have reported the effect of the electric field on silver diffusion, which shows that electric fields greater than 125V/m can cause a large transfer of silver ions in  $\text{As}_2\text{Se}_3$  films [106].



**Figure 89** Comsol simulation of the distribution of electric field during the measurement for the Gen. 1 devices.

In the above figure, the largest electric fields are located around the aluminum (non-diffusive) electrodes, but with the silver sources in the vicinity, the maximum electric fields extend to silver sources. The electric field strength around the silver source is significantly greater than the electric field required to cause silver transport within the film. Therefore, if the Gen. 1 device was used to measure the current *in situ*, then it is difficult to determine whether the change in resistivity is due to radiation or electric field induced silver diffusion, although the net effect is applicable for the device performance. Hence, here arises the necessity to determine a specific geometry that considers the electric field influence, and eliminates this incorporation into the final design. For this purpose, COMSOL Multiphysics software simulations were performed, which applies the Poisson equations to calculate the electrical voltage, electric fields, and electrical energy density at various locations in a given geometry.

$$\nabla \cdot \mathbf{D} = \rho \quad (26)$$

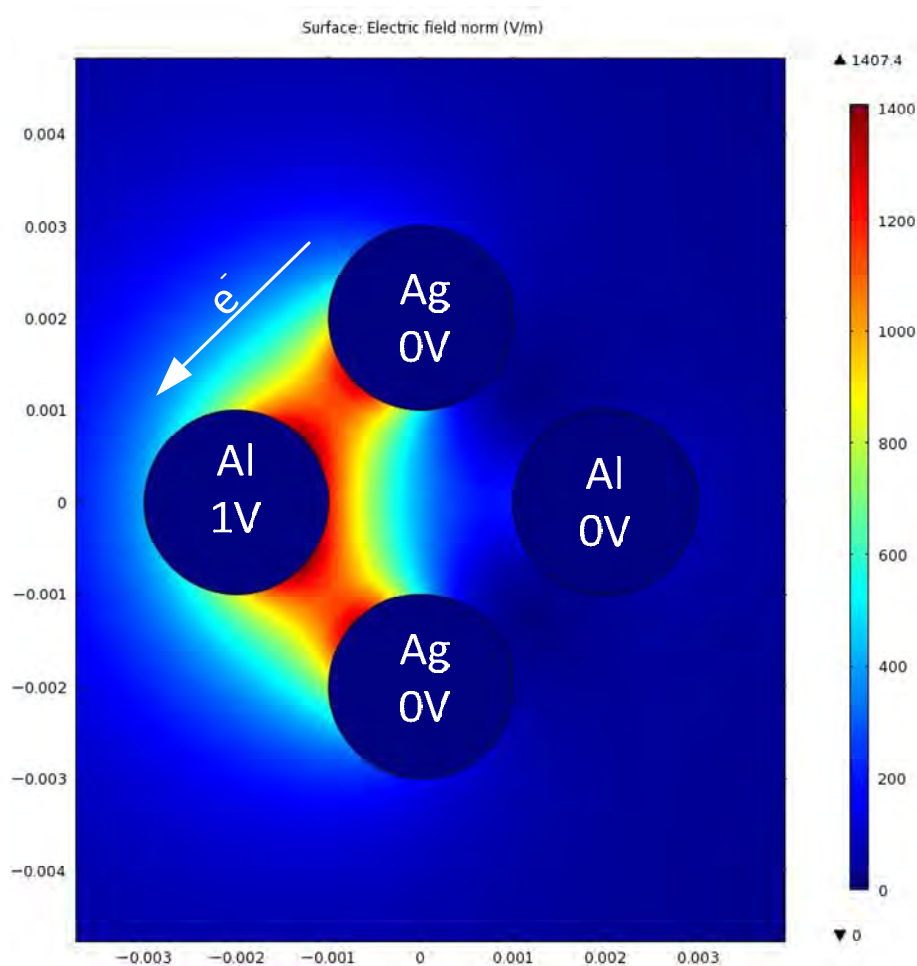
$$\mathbf{E} = -\nabla V \quad (27)$$

### Simulation Inputs

Application of the Poisson equations requires some user defined inputs, which are geometries, and spacing of the electrodes, voltages applied to the electrodes, and the permittivity of the material. Geometries, and spacing of the electrodes determines the effect, and distance of the electric fields, and electrical energy density. These two variables can be used to manipulate the field distributions, which is crucial to ensure the measurements exclude the effect of the bias voltage effects. The results were extrapolated for a 100 nm out of plane thickness, which corresponds to the thickness of the chalcogenide film, which was used during device fabrication.



The second user input is the electric potentials, which were constant in all the simulations in order to be able to compare the effect of varying the different geometries. The left, and right aluminum electrodes were placed at one volt, and zero volt biases, respectively. Silver electrodes on the other hand were left to be at a floating voltage potential because placing a voltage bias on those electrodes will create a large electric field between the left electrode, and the silver electrodes, preventing the silver to diffuse towards the left electrode as shown in the figure below.



**Figure 90** Electric field distribution, when silver electrodes biased at 0V instead of a floating voltage in Gen. 1 devices.

The flow of electrons is in the opposite direction to direction to that of the silver ions, hence, applying a bias voltage on the silver electrode will oppose the diffusion of silver towards the left electrode. For this reason, proper electrode biasing is extremely important. Equally important is the selection of an appropriate bias voltage. Chalcogenide glasses are very resistive material, which is an advantage for radiation sensing, but if the bias voltage is very low, the resultant current is also extremely low. With low currents, arises the problem of identifying the signal from the noise within the system. From previous experiments, it was determined that the current at 1V was the most stable, and noise free, while ensuring against electric field induced silver diffusion. For this reason, all the geometries were simulated with 1V potential difference between the left, and the right electrode.

Third user defined parameter that is required for the simulations is the relative permittivity of the material. The relative permittivity will provide a quantitative comparison of the ability to store charge in a material to air [148]. Various studies were performed quantifying the relative permittivity of bulk chalcogenide glasses [110]. Thin film chalcogenide glasses on the other hand have different characteristics depending on the deposition methods, rate of deposition, and deposition conditions. For these reasons, it is difficult to get an exact value for thin film chalcogenide glasses, but an assumption can be made that the values correlating to the bulk glasses are approximate to the thin film values. Thermal evaporation of thin films transfers whole structural units from bulk material to the film surface, so the properties of the thin films are similar to the bulk glasses with a small deviation from these values. A justification for making this assumption is that the use of a different relative permittivity value will only alter the

quantitative value regarding the electric fields, but it will not alter the location of the electric fields. The reason for performing these simulations is to observe the distribution of the electric fields, and minimize their effect, hence slight differences in the permittivity values can be tolerated. The numerical value of the relative permittivity that was selected for the simulations correlates to the bulk glass with a  $\text{Ge}_{20}\text{Se}_{80}$  composition, which is 6.98 [110].

### **Simulation Outputs**

The outcomes of the Poisson equations are plots, which illustrate electric potential, electric field, and electric energy density distributions within the device. Electric potential shows the distribution of the voltage at different locations, which is important to determine the induced voltage on the silver electrodes. This result shows a small portion of the big picture because the voltage only shows the direction of the ion, and electron movement, but it is necessary to know the strength, and the capability of the bias to affect the ions. For this part of the picture, the electric field distributions, and the energy density results show where the bias has the greatest influence on the movement of silver ions. The ultimate goal of this simulation is to determine the distribution of the electric field created by the application of a voltage bias, and couple it with a specific device geometry, which does not affect the device performance.

Similar to the study of the electric field distribution, the electrical energy density result is an important aspect for consideration. Electrical energy density quantitatively describes the amount of energy given to a charged particle in a specific location, due to interaction with an electric field. To calculate the total energy imparted to the particle, it

is important to consider the effect of the electrical, and magnetic fields on the charged particle, which is given in equation 28.

$$U = \eta_E + \eta_H \quad (28)$$

In the above equation, U is the total energy, which has contributions from both the magnetic ( $\eta_H$ ), and electric ( $\eta_E$ ) fields.

$$\eta_E = \frac{\text{Energy}}{\text{Volume}} = \frac{1}{2} \mathbf{E} \cdot \mathbf{D} = \frac{1}{2} \epsilon \mathbf{E}^2 \quad (29)$$

The term energy density means the amount energy within a defined volume. This consists of a relationship between the Electric field (E), and Electric Displacement field (D) as shown in the equation above. Displacement field is a function of the Electric field, and the dielectric constant of the material ( $\epsilon$ ), which is then substituted in for D.

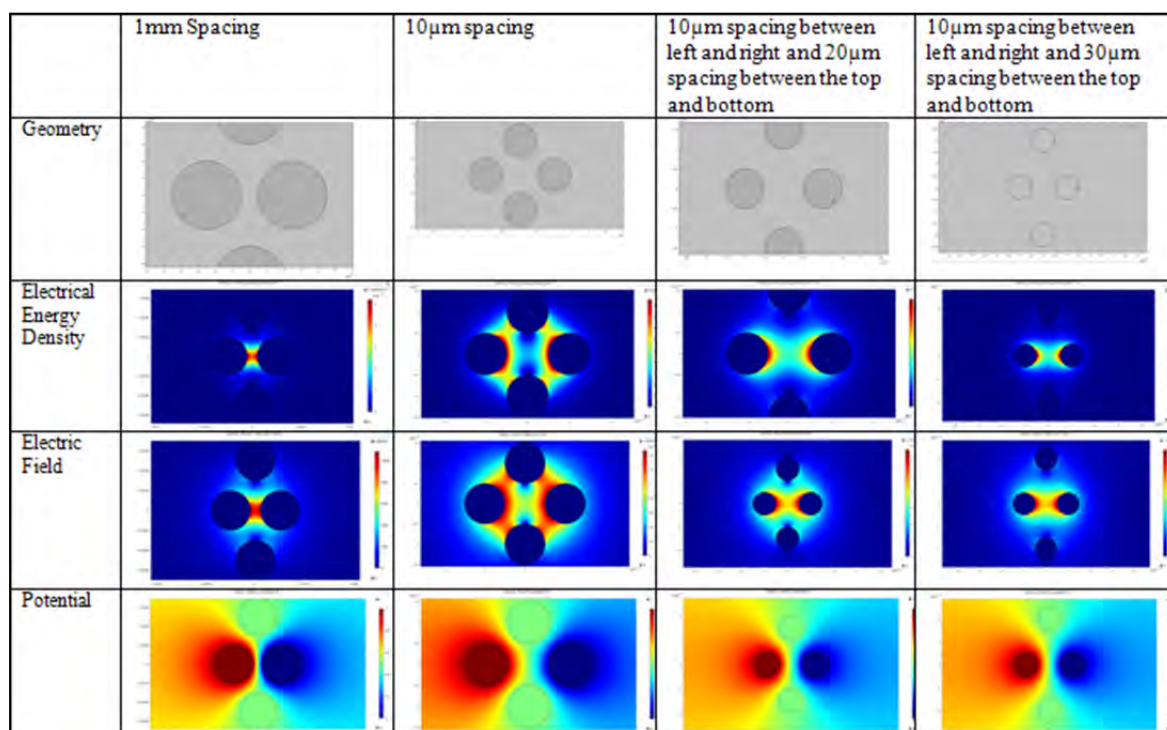
$$\eta_H = \frac{\text{Energy}}{\text{Volume}} = \frac{1}{2} \mathbf{H} \cdot \mathbf{B} = \frac{1}{2} \left[ \frac{\mathbf{B}^2}{\mu} \right] \quad (30)$$

Similarly, the energy density due to the magnetic field is a relationship between the Magnetizing field (H), and the Magnetic displacement Field (B). The H field is an inverse relationship between the displacement field, and the magnetic permeability of the material ( $\mu$ ).

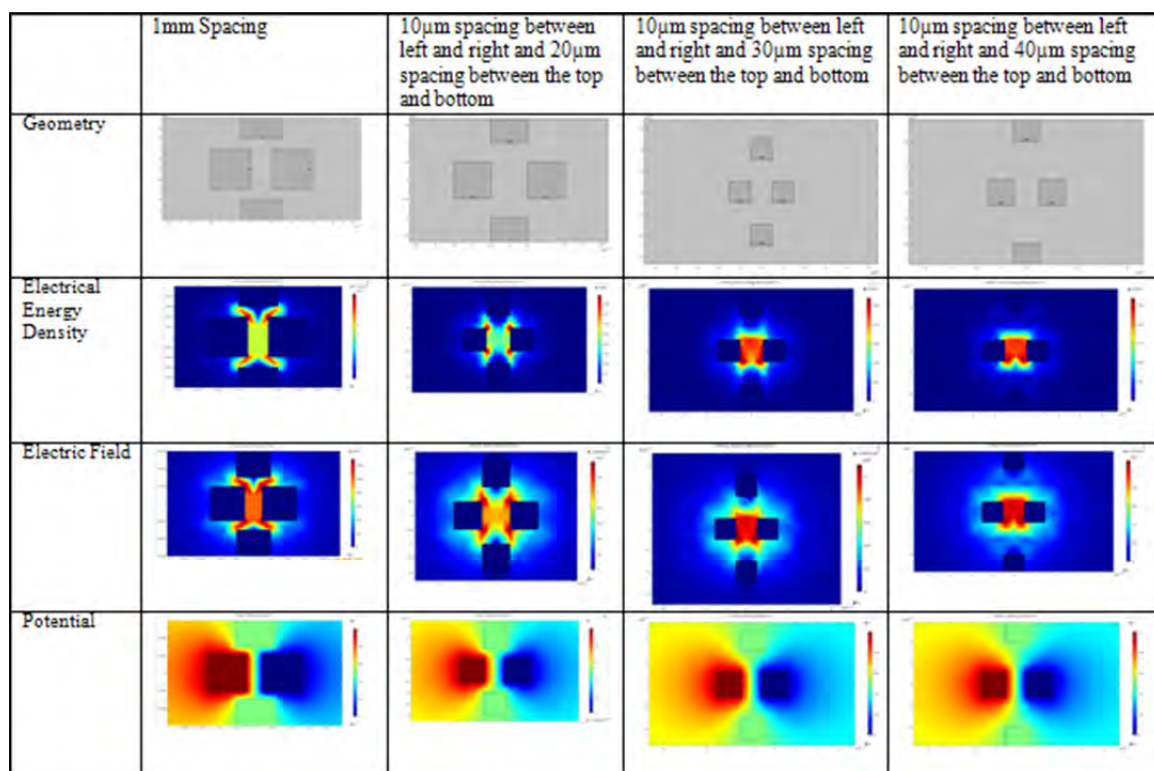
### Simulation Results

Initially, basic geometry shapes such as circles, squares, and triangles were simulated, and the outputs are shown below.




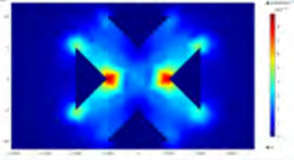
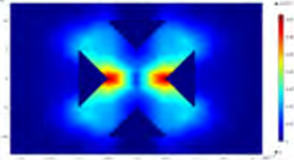
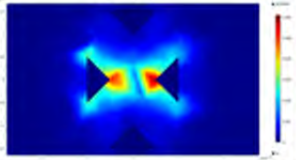
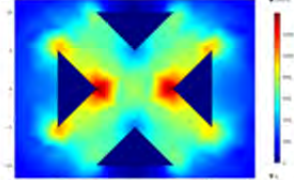
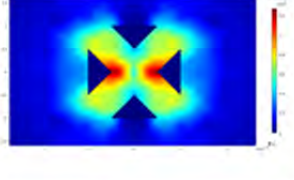
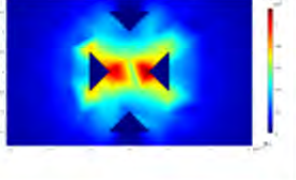
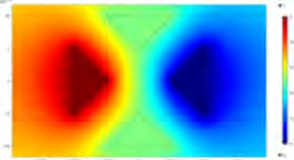
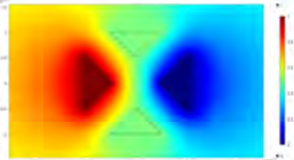
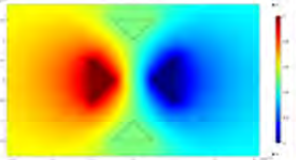
**Table 9** Circular geometry simulation results for various sizes, and dimensions.



**Table 10** Square geometry simulation results for various sizes, and dimensions.

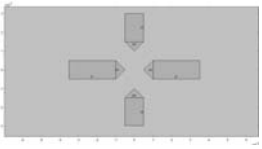
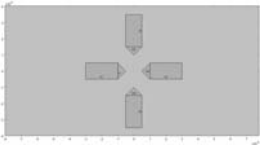
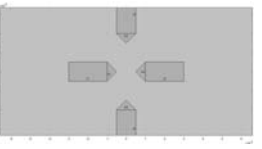
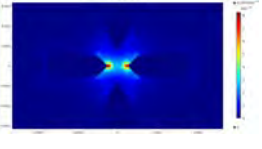
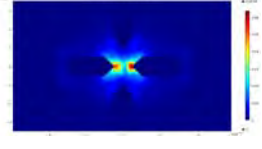
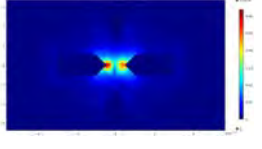
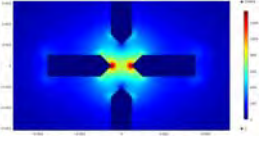
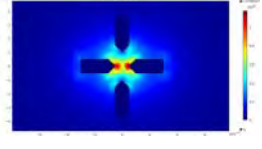
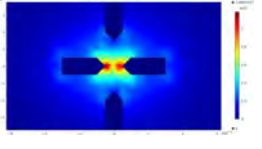
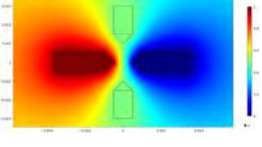
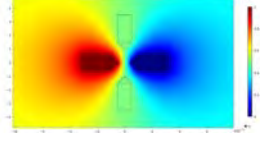
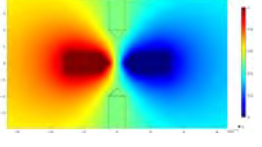


**Table 11 Triangle geometry simulation results for various sizes, and dimensions.**

	1mm Spacing	10 $\mu$ m spacing	10 $\mu$ m spacing between left and right and 20 $\mu$ m spacing between the top and bottom
Geometry			
Electrical Energy Density			
Electric Field			
Potential			

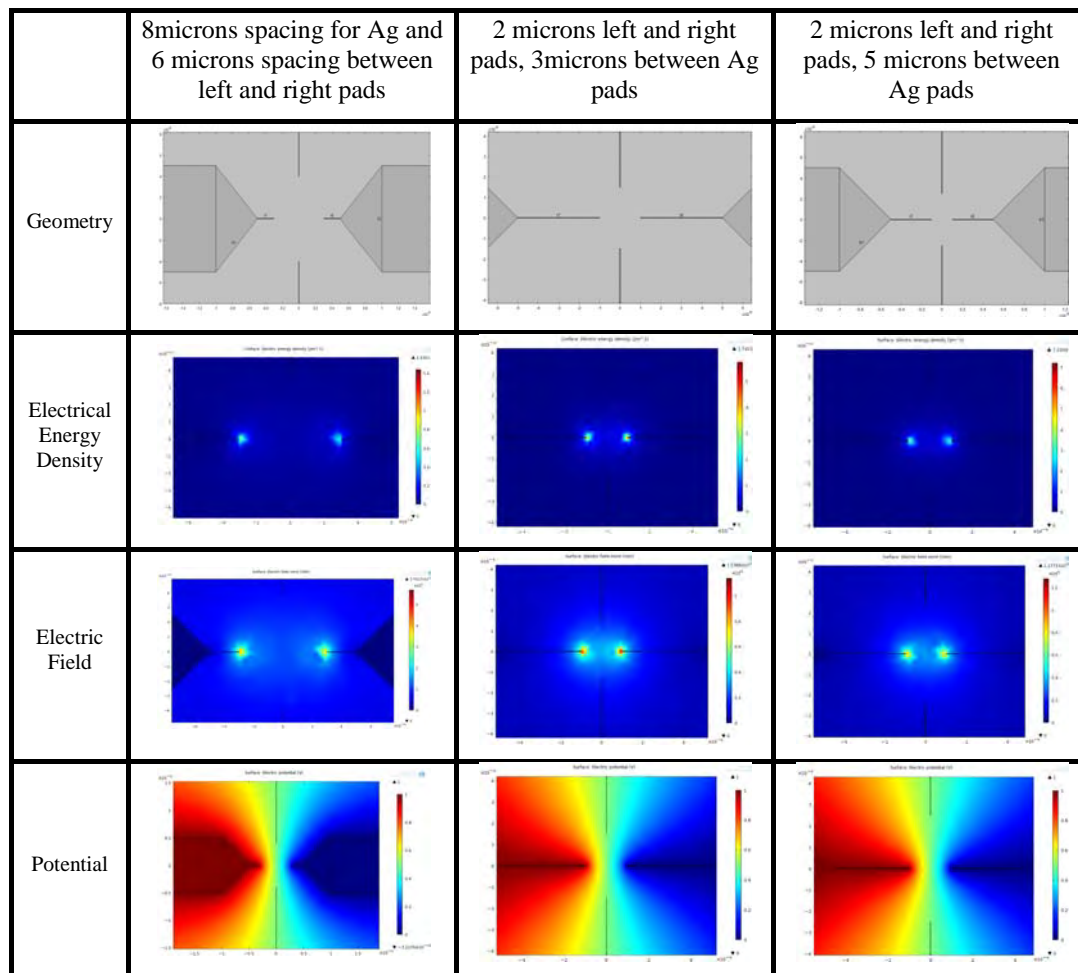
Comparing the results in Table 9-10 for the basic shapes shows that with very small spacing (10  $\mu$ m Al spacing), all three shapes are poor at isolating the electric fields from the silver electrodes. The triangle shape in comparison has isolated the peak electric field, and energy density to a confined space at the tip of the triangle. The disadvantage of the triangle geometry is that the energy density distribution extends in all directions around the left, and right aluminum electrodes, but this is not a big problem for the squares, which reveals that the energy density is confined to the area between the Al electrodes. Combination of a triangle shape connected to a long rectangle will focus the fields between the two triangles, and prevent any dispersive electric fields. This type of design has been simulated, and shown below in Table 12.

**Table 12 Triangle, and rectangle geometry simulation result for various sizes, and dimensions.**

	1mm Spacing	10 $\mu$ m spacing	10 $\mu$ m spacing between left and right and 20 $\mu$ m spacing between the top and bottom
Geometry			
Electrical Energy Density			
Electric Field			
Potential			

This new type of structure, has improved on the previous versions in the aspect of isolating the maximum electric energy density between the two Al electrodes, while the electric field is still affects the silver electrode. To constrict the electric field distribution, the square shaped geometry performed better than the other geometries in confining the electric fields, so the addition of very thin, and long rectangular shapes should theoretically minimize the electric fields. Addition of a very thin rectangle is called an antenna structure, which was simulated, and the results are shown below in Table 13.

**Table 13** Antenna geometry simulation results for various sizes, and dimensions.



This type of device structure is ideal for the purposes of a sensor since the electric fields are completely confined to the region between the two aluminum electrodes, and the silver source can be placed in vicinity without experiencing these large electric fields. The figure corresponding to aluminum spacing of 2  $\mu\text{m}$ , and 3  $\mu\text{m}$  spacing of the silver electrode is the best ratio for the spacing because the silver electrode is just outside the electric field. As soon as one silver atom becomes ionized, the electric field can attract this ion towards the non-diffusive electrodes. In this manner, the electric field aids in the



silver diffusion rather than being the primary reason for silver diffusion. Additionally, the applied voltage bias on the Al electrodes does not play a role in the silver diffusion, therefore the sensing voltages can be increased until the measured current is within the sensing range of the external circuit.

### **Mask Design**

Conventional masks for semiconductor photolithography are created with either fused silica or soda lime glass, which can be very expensive since any small defect in the glass is disastrous for fabricating the devices. These types of masks are necessary for devices with very small, and precise dimensions, but for a radiation sensor, a small device (10 nm-100  $\mu\text{m}$ ) will not function as accurately when compared to a device with larger dimensions (>100  $\mu\text{m}$ ). Radiation detection relies on using a large capture surface to try to increase the probability to detect an incident photon. Hence, a small device dimension only restricts the ability to predict the incidence of radiation. For this reason, a mask with larger dimensions is required. Chalcogenide glasses are highly resistive material, a very large device will be difficult to be sensed because the signal to noise ratio degrades with an increase in the device dimension. A mask design is required with various device dimensions to adjust for various radiation doses.

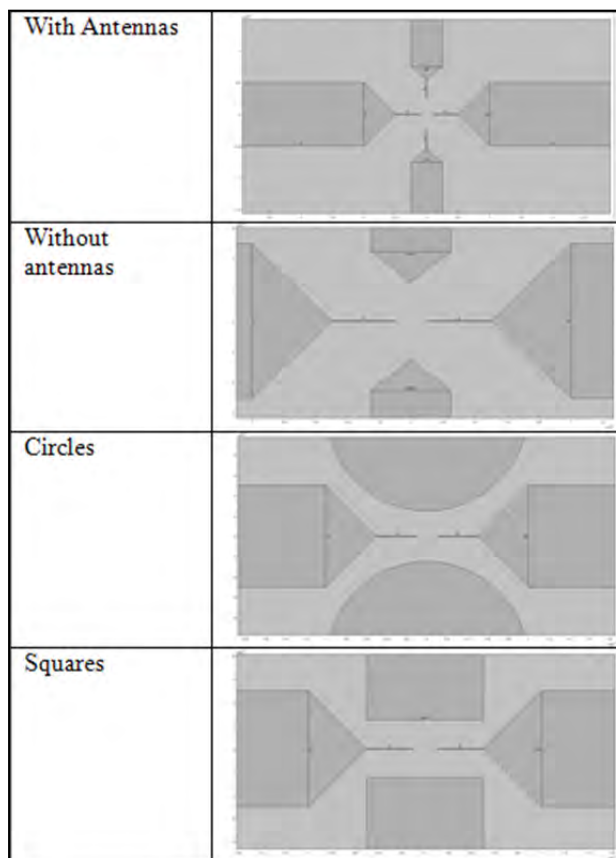
To reduce the cost of mask production, transparency masks were produced using a Hewlett-Packard LaserJet HP4014dn printer. Before fabrication of the masks, the transparencies were cleaned with deionized water, and wiped dry using a lint free cloth wipe. After cleaning, the transparencies were inspected for any remaining contaminants, and if there were any contaminants still present after the first cleaning, the transparencies were cleaned a second time. Only the transparencies that were defect free after the second

cleaning were then stored away from any light source, and used for mask production. The transparencies were only handled using gloves, and always covered with a lint free cloth, and when the transparencies were not in use, they were placed under vacuum to prevent any surface contaminants.

A precise printer is required for creating these masks, since all laser jet printers use similar technology of spraying ink dots onto the surface, but if the settings are not properly adjusted, then a line on the transparency would end up becoming a series of unconnected dots. All the masks were printed on various printers, and the resolution of the printers were adjusted, and verified using microscopes. The final verdict was to use the HP4014dn printer, and adjusting the printer settings to 180 lpi, provided the best resolution.

After choosing the correct printer, and settings, the next major task was to create an appropriate mask design. The COMSOL simulations have shown a specific type of electrodes for the aluminum electrodes, but the silver electrodes can be created with different geometries since the electric fields are confined to areas between the aluminum electrodes. For this reason, four types of electrode geometries (antenna, no antenna, circle, and square) were created on the transparency mask. These masks were prepared using Microsoft Visio software, and the devices were measured to precise dimensions, which will be described below.

**Table 14** Four types of silver source geometries used in the mask design for device fabrication.



The benefit that arises from the four types of geometries is that each type is unique, but each is an effective means of providing silver towards the area between the aluminum electrodes. Using these four basic shapes, 6 masks were created for fabricating devices. Various Al spacing ranging from 10 mm to 250  $\mu\text{m}$  were created such that there are 20 devices for each type of Ag geometry. The various device parameters are shown in the table below.

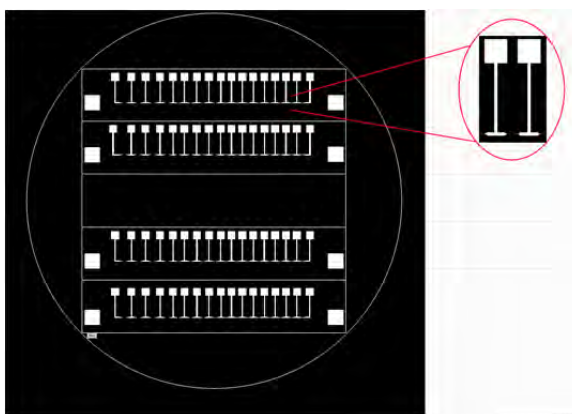
**Table 15 Aluminum electrode, and Silver source spacing on the small device mask to fabricate devices with relatively small dimensions.**

Al Spacing	1 mm	1 mm	1 mm	1 mm	.5 mm	.5 mm	.5 mm	.5 mm	.35 mm	.35 mm	.35 mm	.35 mm	.25 mm	.25 mm	.25 mm	.25 mm
Ag Spacing	1.25 mm	0.625 mm	0.300 mm	0.15 mm	1.25 mm	.625 mm	.300 mm	.15 mm	1.25 mm	.625 mm	.300 mm	.15 mm	1.25 mm	.625 mm	.300 mm	.15 mm

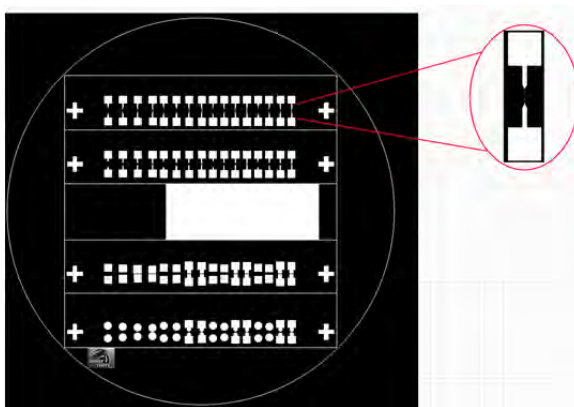
**Table 16 Aluminum electrode, and Silver source spacing on the big device mask to fabricate devices with relatively large dimensions.**

Al Spacing	10 mm	10 mm	5 mm	5 mm
Ag Spacing	12.5 mm	6.25 mm	6.25 mm	1.25 mm

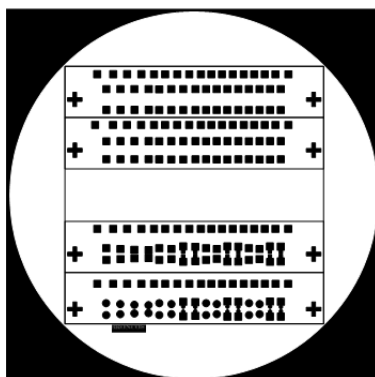
Therefore, using two wafers, and the completion of one process flow, 80 different devices can be fabricated. The devices were separated into two parts, large devices, and small devices, such that all 80 devices can fit onto the fewest number of 4" wafers. The various masks are shown below, and their respective uses will be described in the process flow section.



**Figure 91 Mask for creating Al electrodes for small devices.**

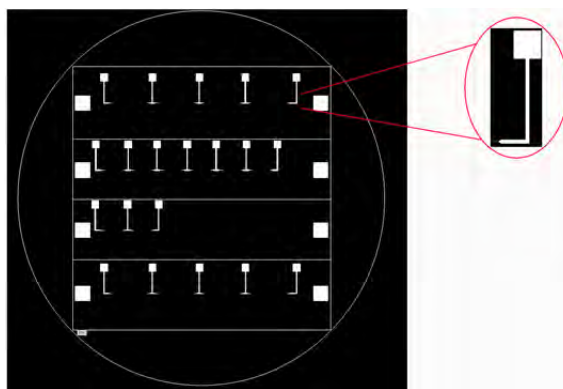


**Figure 92** Mask for creating Ag electrodes for small devices.

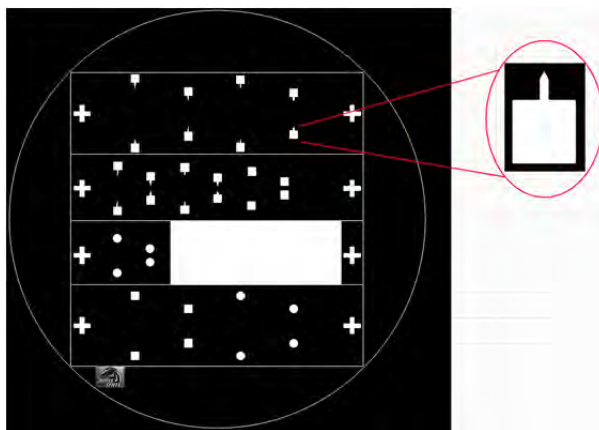


**Figure 93** Mask for depositing chalcogenide films for small devices.

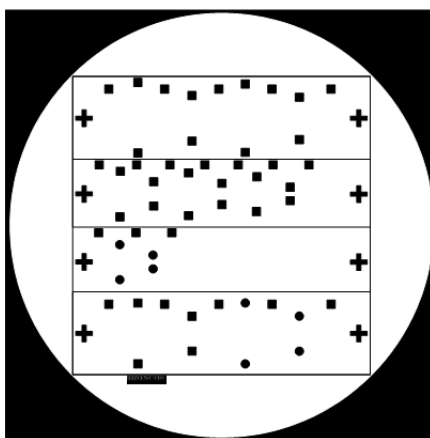
The devices fabricated using the small masks are arranged according from 1 mm to 250  $\mu\text{m}$  Al spacing, and each row has a different Ag geometry. Refer to Table 15 for information about the device dimensions.



**Figure 94** Mask for creating Al electrodes for large devices.



**Figure 95** Mask for creating Ag electrodes for large devices.



**Figure 96** Mask for depositing Chalcogenide films for small devices.

The devices that have been fabricated using the large device masks are arranged according to the following table.

**Table 17 Device sizes, and location on the large device masks: Antenna geometry (A), No antenna (NA), Circle (C), and Square (S).**

	Device 1	Device 2	Device 3	Device 4	Device 5	Device 6
Row 1	10mm x 12.5mm (A)	10mm x 6.25mm (A)	10mm x 12.5mm (NA)	10mm x 6.25mm (NA)	--	--
Row 2	5mm x 6.25mm (A)	5mm x 1.25mm (A)	5mm x 6.25mm (NA)	5mm x 1.25mm (NA)	5mm x 6.25mm (S)	5mm x 1.25mm (S)
Row 3	5mm x 6.25mm (C)	5mm x 1.25mm (C)				
Row 4	10mm x 12.5mm (S)	10mm x 6.25mm (S)	10mm x 12.5mm (C)	10mm x 6.25mm (C)	--	--

### Process Flow

This is a very useful sensor design, since it provides the ability to be CMOS compatible. The radiation sensor can be embedded to a suitable IC structure, and its fabrication can be completed at the Back End of Line (BEOL) after creating the last metal layers, and before packaging the devices. The main obstacle in using conventional photolithography techniques is that the developer, and photoresist stripper are both basic solutions, and chalcogenide glasses are dissolvable in basic solutions. Therefore, exposure to basic solutions will inadvertently etch the thin films, and to avoid this problem, the process flow for fabricating devices must be designed in a specific manner such that the chalcogenide thin film has minimal exposure of the basic solutions. This specialized process flow was separated into three different steps, which are described below.

The devices were fabricated on a silicon substrate, and a thermally grown oxide as described in the fabrication of Gen. 1 devices, and the remaining processes are segregated into three parts: Al deposition, Ag deposition, and ChG deposition, which are described below.

### Al Deposition

Photolithography processes were applied to a silicon wafer with <100> orientation was used with thermally grown oxide insulator. Approximately 5 ml of Hexamethyl-di-silazane (HMDS) was measured using a pipette, and deposited onto the wafer surface, which was then followed by spinning the wafer at 5000 rpm for 60 seconds such that the HMDS would evenly cover the entire surface of the wafer. After the HMDS has completely covered the wafer surface, 15 ml of SPR 220-3.0 photoresist (PR) was measured using a different pipette, and deposited onto the wafer. The maximum wafer spin speed achieved during the PR coating process was 6000 rpm. A rapid increase in the spin speed from stationary to 6000 rpm will result in uneven thicknesses, and streaks on the wafer surface because SPR 220-3.0 is a highly viscous liquid. The recipe was programmed such that the wafer will achieve the maximum spin speed after ramping up the speed at 200 rpm/sec for 30 seconds. Then the wafer was maintained at 6000 rpm for one minute, which was then followed by a ramp down at 600 rpm/sec for 10 seconds since at this point spin coating the film was fairly consistent, and will not be affected by a fast ramp down. After the wafer has slowed down to a stop, the wafer was then baked at 115°C on a hot plate for 90 seconds.

Aluminum electrodes were defined by exposing the photoresist, and HMDS covered wafer using a Quintel Q-4000 contact aligner, and either the large or small device mask. Since this is no ordinary mask, it does not have the mechanical stability of a soda lime or glass mask, a transparent 1" thick acrylic slab was used in addition to the transparency. The transparency was adhered to the acrylic slab using static electricity. This method ensures structural stability similar to a conventional mask, and accomplishes



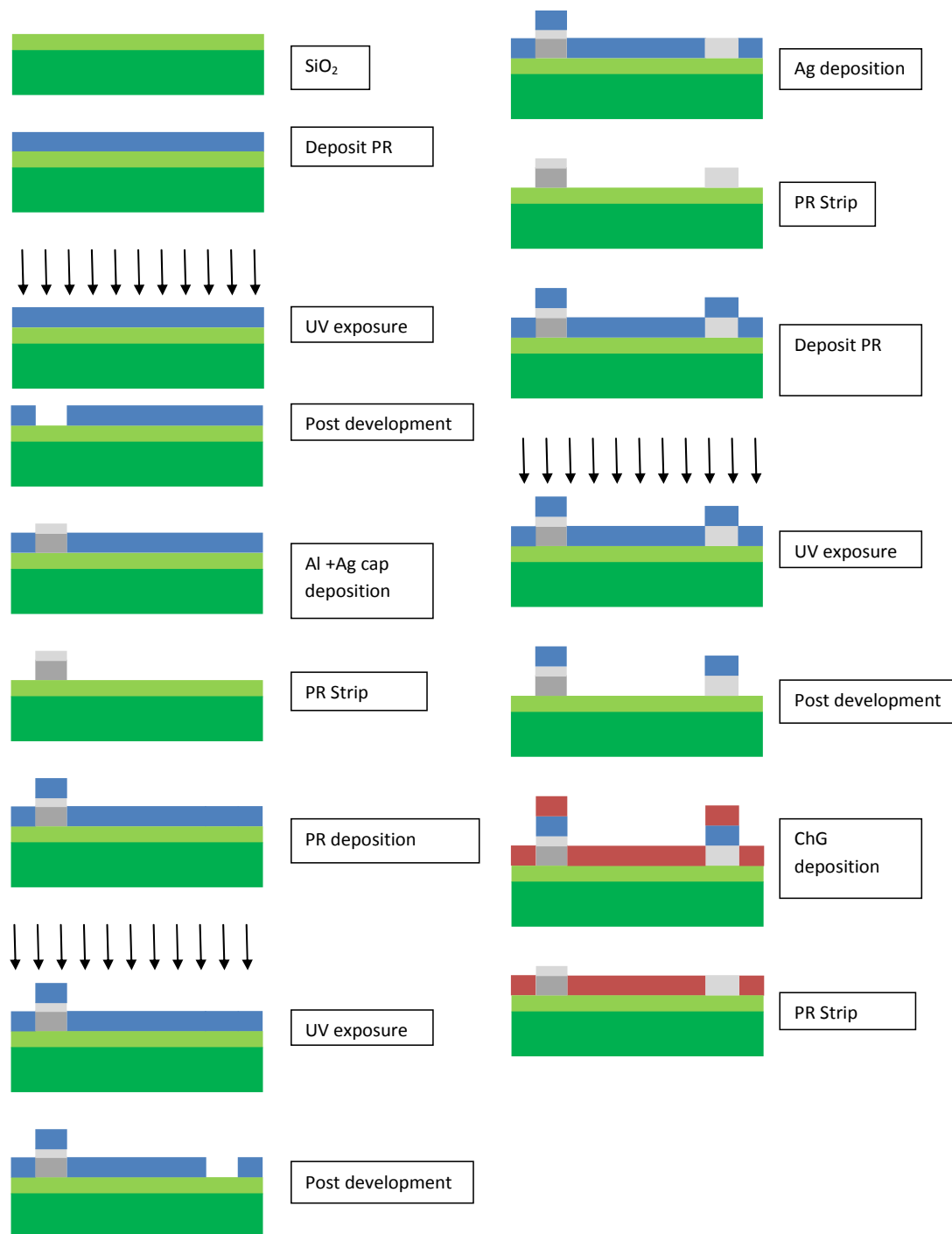
the same purposes as an expensive quartz mask. The mask was aligned such that printed side of the transparency was in contact with the acrylic. If the printed side of the transparency was in contact with the wafer, the wafer, and the mask could become contaminated by ink deposition on the wafer or photoresist deposition on the mask. After the mask, acrylic slab, and the wafer were properly aligned, a UV lamp exposes the wafer for 10 seconds. Following the UV exposure, the wafer was submerged into a beaker containing MF-26A (photoresist developer) for 90 seconds followed by a thorough rinse with deionized water. Now openings were created on SiO<sub>2</sub> for thermally evaporated aluminum, and a thin silver cap as described in the process flow for the Gen. 1 devices.

After a blanket deposition of Al on the wafer, the excess aluminum was removed using 1165 photoresist remover at room temperature. The removal of the excess Al must be performed with care since some of the silver can be inadvertently removed during the liftoff process. If sufficient silver is removed such that aluminum is exposed, then the aluminum can begin to dissolve in solvent solutions or worse the aluminum can become oxidized preventing the capability to accurately sense the radiation device. There are two solutions to this problem, either increase the thickness of the silver cap or perform the Al deposition step after the silver deposition step.

#### Ag, and ChG Deposition

Silver deposition was also performed in a same manner as the aluminum deposition with the only exception being the use of Ag mask, alignment with the Al alignment markers, and thermal deposition of silver as described in the Gen. 1 device fabrication. Finally, the last lithography step was performed, which at the end of this process, covers the Al, and Ag pads on the wafer with photoresist while the rest of the

wafer was covered with thermally evaporated chalcogenide glass thin film. The entire fabrication process is summarized in Figure 97.



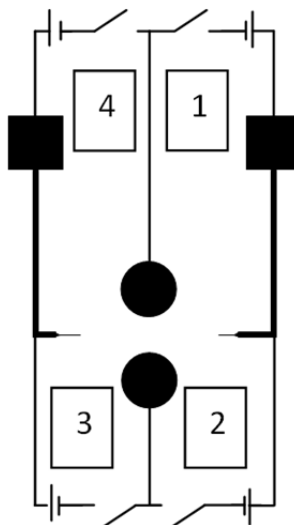
**Figure 97** Gen 2. device fabrication process flow.



**Figure 98** Microscope image of Gen. 2 devices post fabrication.

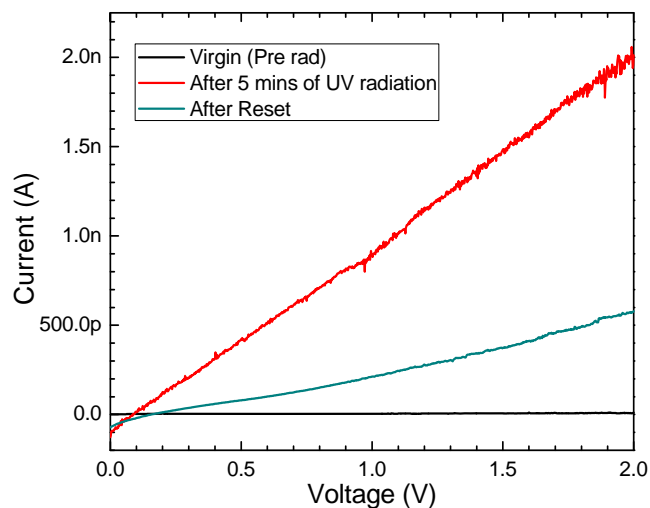
### UV Characterization

After fabrication, the devices were tested to verify the functionality, and performance using a UV lamp. For this purpose, a device was fabricated using chalcogenide glass thin film fabricated from  $\text{Ge}_{20}\text{Se}_{80}$  bulk glass, and a device with 5 mm Al spacing with 1.25 mm circular Ag electrodes was measured. The device was measured using a voltage sweep between 0, and 2V before, and after UV radiation. Since this type of structure is very conducive for resetting the device post irradiation, the device was reset after the UV radiation by biasing the Al electrode at a positive voltage, and the Ag electrode at 0V. This reset procedure was performed using a probe station, so only two pads were biased at a time. After making contact with the proper pads, five sweeps between 0, and 2V were performed at medium integration in the manner shown in the figure below where 1 corresponds to the first two electrodes that were biased.



**Figure 99** Reset procedure using a probe station to return the diffused silver to the silver source, and reuse the sensor.

This procedure is ideal when device is wire bonded where both the silver electrodes were shorted to the cathode, and the aluminum electrodes were shorted together to the anode. In this manner, the device can be reset simultaneously from all directions by attracting the ions back towards either of the silver pads.

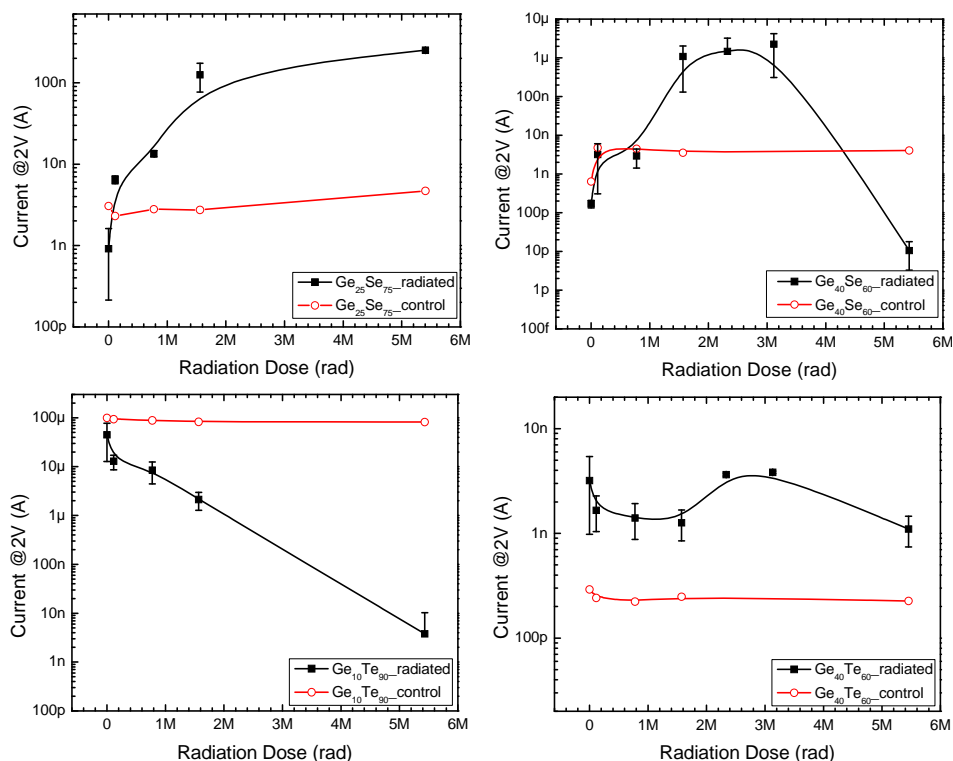


**Figure 100** Current vs. Voltage plot for UV irradiated Gen. 2 device Prerad (black), 5 min rad (red), and post reset (green) characteristics.

The current vs. voltage characteristics for the UV shows a very high resistivity before radiation, and after only five minutes of radiation, there is a sharp increase in current illustrating that this type of device structure is a viable alternative to the Gen. 1 devices. Measurement after the reset procedure shows an increase in the resistivity but the current is not as low as the before radiation level. This revealed that the reset procedure was unable to return all the silver diffused ions towards the silver electrode. Either more sweeps, or a longer bias will ensure the resistivity of the film returns to its original state.

### Gamma Ray Characterization

Devices of various compositions were fabricated, and measured at various radiation doses. These measurements are shown in the figures below.



**Figure 101** Radiation dose vs. current characteristics for a)  $\text{Ge}_{20}\text{Se}_{80}$ , b)  $\text{Ge}_{40}\text{Se}_{60}$ , c)  $\text{Ge}_{10}\text{Te}_{90}$ , and d)  $\text{Ge}_{50}\text{Te}_{50}$

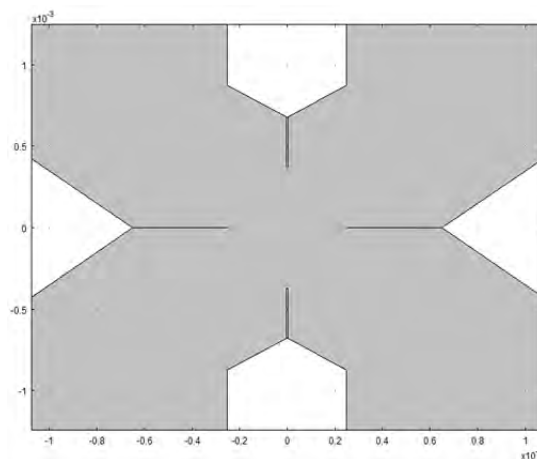
Examination of the results from the Gen. 2 device testing shows a significant change in conductivity as a function of radiation in three out of the four device compositions. In the  $\text{Ge}_{20}\text{Se}_{80}$  devices, the observed initial change in the conductivity during the low radiation doses in the Gen. 1 devices holds true with these types of devices. Up to 2 Mrad of radiation, there is a consistent change observed in the devices. Increasing the radiation dose by 1 Mrad corresponds to approximately one order of magnitude increase in the conductivity of the device. This consistent trend is a direct correlation to the formation of defects therefore, due to the increasing radiation dose there is a linear increase in the number of defect formation, which is then represented by an increase in the conductivity. The observed trend in this device changes after 2 Mrad, due to recombination of defects.

In the  $\text{Ge}_{40}\text{Se}_{60}$  devices, there is a significant rise in the conductivity up to 3 Mrad, which is followed by a decrease in conductivity. There are many small periods where specific changes develop, and are exhibited within this overall trend in this device. Initially, within the first 100 krad, there is a sharp rise in the conductivity. This region has not been visible in the Gen.1 devices due to their large dimensions, but with the ability to adjust the sizes of the devices this region has been revealed in these devices. The sharp increase in conductivity is attributed to the formation of defects since at this low dose, the probability of structural changes is minimal but there is a high likelihood that defects play a role at this early stage. This subsides after the initial exposure to radiation until 1Mrad when the structural changes described in the film analysis begin to dominate the performance of the device. These structural changes in addition to the silver diffusion create a haven for high conductivity change. There is more than a 3 orders of change in

the conductivity within 2 Mrad of absorbed dose. The final trend observed in these results occurs after 3 Mrad, where the effect of oxygen overwhelms the effect of the structural changes, and silver diffusion induced conductivity change.

The  $\text{Ge}_{20}\text{Te}_{80}$  devices have a consistent trend, which is similar but a more pronounced result than in the Gen. 1 device. In the Gen. 1 device, there was a small decrease in the conductivity due to the difference in conductivity of the  $\text{Ag}_2\text{Te}$ , and a-Te, as well as polarizability of Te atoms as discussed in the film analysis (see Table 4). These devices undergo a 6 order of magnitude decrease with 5.5 Mrad radiation dose. With further enhancement of the device structure, it is possible to achieve as close to a 1:1 ratio of change in conductivity to Mrad of radiation dose, which is ideal for radiation sensing purposes. This change that is observed in the tellurium-rich devices is also evident in the germanium-rich devices within the first 100 krad. This trend subsides after the initial radiation dose due to the overwhelming effect of oxygen, which dominates from the initial radiation dose onwards. The specific structure, and the fabrication methods for Gen. 2 devices enhanced the repeatability of the devices, which was lacking in the Gen. 1 devices.

Until this point, the silver diffusion, and other investigations have only provided a few glimpses of the silver diffusion processes. With the power of simulations, it is possible to piece together a time lapse of the silver diffusion during the radiation experiment. Using the diffusion coefficients previously described, it can be manipulated to the geometry to the Gen. 2 devices, and correlate the conductivity results to determine the underlying silver diffusion effect on these changes. The dimensions of the devices are 500  $\mu\text{m}$  spacing between the Al electrodes, and 750  $\mu\text{m}$  spacing between the Ag sources.

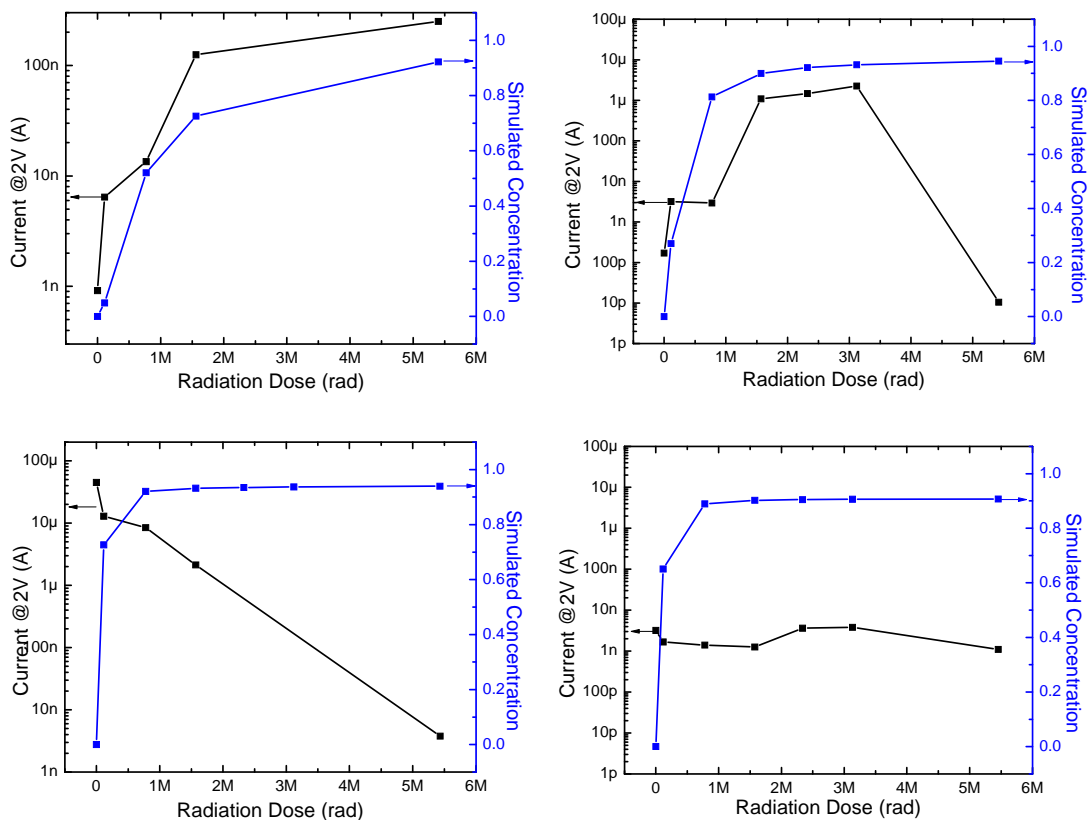


**Figure 102** Geometry of the simulated device to study the silver diffusion using COMSOL multiphysics software.

The silver source has been simulated as the source of silver species, and the highest concentration of the silver species was normalized to 1. Aluminum electrodes on the other hand have been placed at a floating potential where silver is not attracted towards or a repelling. This ensures that the silver is allowed to diffuse in all directions, which coincides with the characteristics of silver. A cutline was created between the two Al electrodes, where the silver concentration in this region was measured, and the data was compared to the change in conductivity at the specific radiation doses.

Since silver diffusion has a step-like characteristic, it is important to place a threshold silver concentration that corresponds to the step-like behavior. The simulation does not have the capability of representing the step-like behavior of silver, therefore an appropriate silver threshold level must be assigned. An appropriate silver threshold is 90%, therefore once the silver concentration between the two electrodes reaches 0.9, it can be inferred that silver has diffused between the Al electrodes.



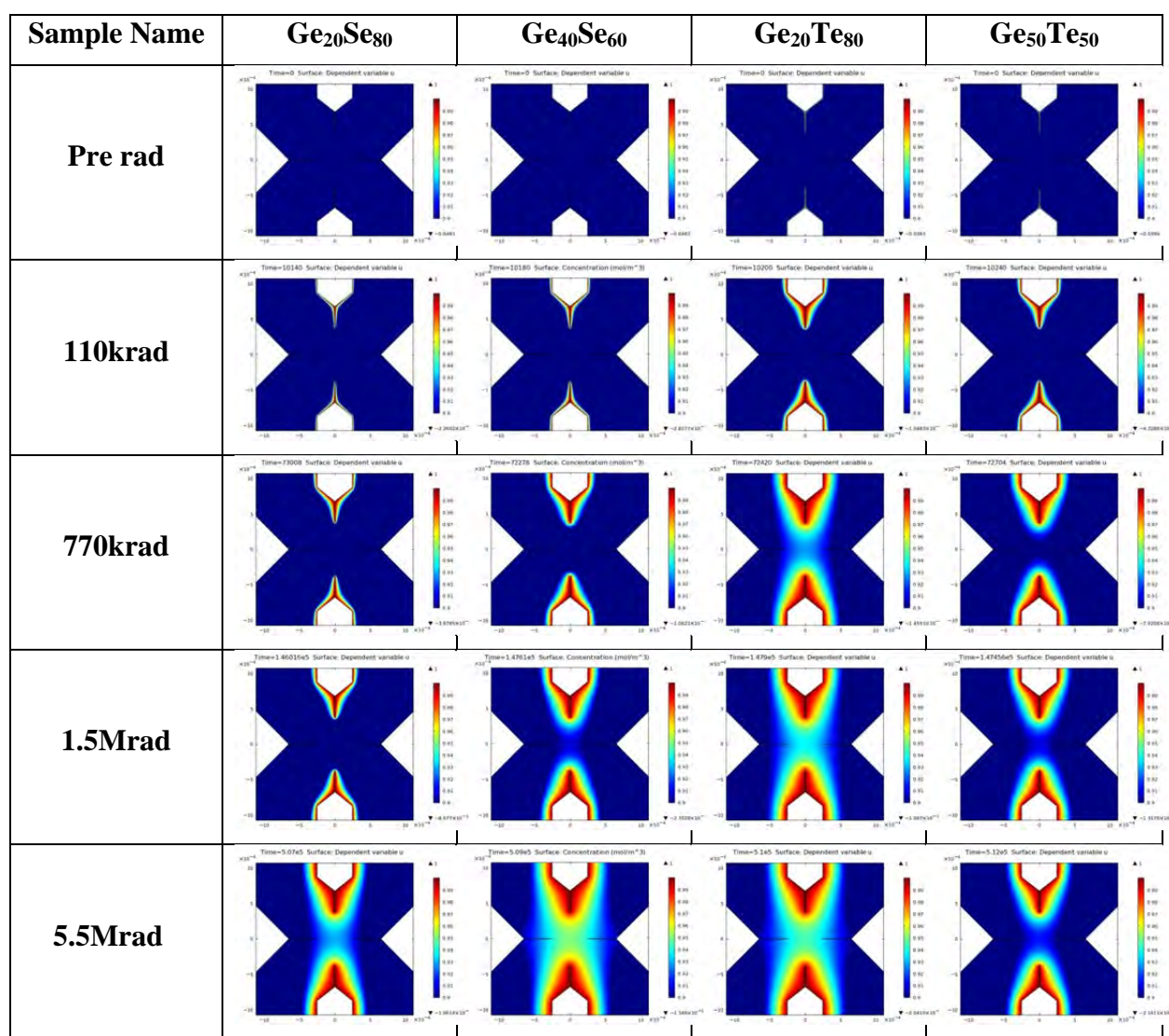


**Figure 103 Simulated Silver diffusion compared to the change in conductivity of the Gen. 2 devices as a function of radiation dose. The blue graph corresponds to the normalized silver concentration, and the black graph represents the change in conductivity of the device at discrete radiation doses.**

Close inspection of all the graphs show a clear trend, when the silver concentration becomes 0.9 or greater, there is a sharp change in the conductivity of the devices. In the  $\text{Ge}_{40}\text{Se}_{60}$  devices, the simulations revealed that the concentration reaches 0.9 at 1.5 Mrad, similarly, there is an increase of 2.5 orders in the conductivity at this radiation dose. The  $\text{Ge}_{20}\text{Te}_{80}$  devices reach a steady conductivity decline after the silver concentration reaches 0.9 at 500 krad. Prior to the silver saturation region, the conductivity has a different rate of decline than post silver saturation, which stabilizes the effects, and continues a uniform trend.

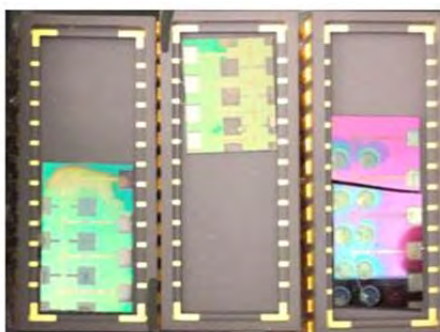
In the  $\text{Ge}_{20}\text{Se}_{80}$  simulations, the silver does not achieve the saturation level until 5.5 Mrad, which confirms the findings that the measured changes are defect formation, and recombination dominant. Finally, the  $\text{Ge}_{50}\text{Te}_{50}$  reaches a value close to the threshold concentration at an early radiation dose level, but the concentration does not cross this threshold value as illustrated in the table below. The lack of silver diffusion added to the oxidation effects affects the conductivity of this device composition.

**Table 18 Silver diffusion simulations captured at various radiation doses.**



## Conclusion

Gen. 1 devices are highly applicable for measuring radiation doses at discrete radiation dose intervals, but the main advantage of creating an inexpensive thin film radiation sensor (Gen. 2 device) is the versatility for applications as *in situ* or discrete radiation dose measurements. Simulations with the aid of COMSOL Multiphysics software, and after a myriad of iterations on the geometry has given rise to the Gen. 2 device, which fulfils the only application that Gen. 1 device cannot offer, and much more. A proprietary lithography masks, and process flow were created allowing the fabrication of 82 unique devices. These devices were tested under UV radiation, and expounded a reduction in resistance after exposure in addition to the capability to reset the devices, and return the conductivity of the device to a current level near the pre-exposure state. After exposure to gamma radiation, the devices perform in a similar manner, providing the repeatability that is vital for radiation sensing. The radiation-induced changes in the device's electrical performance range from at least 2-3 orders of magnitude change to certain device compositions exhibiting a magnitude change of 5+ orders. The silver diffusion for the measured devices was simulated and exhibited a direct correlation of the change in the device conductivity to the silver concentration.



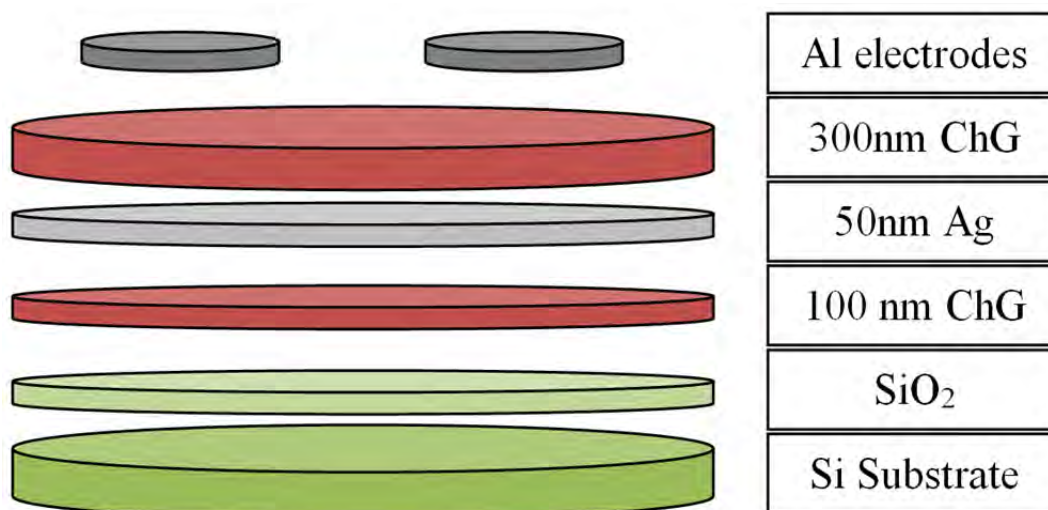
**Figure 104** Final product of the wire bonded Gen. 2 devices.

## GENERATION 3 DEVICES

This generation of devices are significantly different from the other two types of devices since the silver diffusion mechanics in the prior two types is lateral, while silver in this device structure diffuses vertically. The aim for these types of devices was to determine whether vertical silver diffusion would enhance the observed changes in laterally diffusing devices.

### **Device Fabrication**

The intricate structure of these devices was created on oxidized silicon wafers, and then placed into the Cressington 308R evaporation chamber for device, and film preparation. Multiple layers were deposited onto the substrate without breaking vacuum to protect against the introduction of contaminants between the films. Initially, 100 nm of  $\text{Ge}_{40}\text{Se}_{60}$  film was deposited followed by a 50 nm continuous film of Ag, after which a 300 nm film  $\text{Ge}_{40}\text{Se}_{60}$  was evaporated. Part of the wafer was set aside after this step to be used for the film study, while on the remaining portion of the wafer radiation-sensing devices were created by placing of non-diffusive aluminum (Al) electrodes. These electrodes were thermally evaporated, and selectively deposited in specific regions of the wafer with the aid of a circular mask. This mask generated final device with 2 mm diameter circles with 1 mm spacing, whose cross section is shown below.

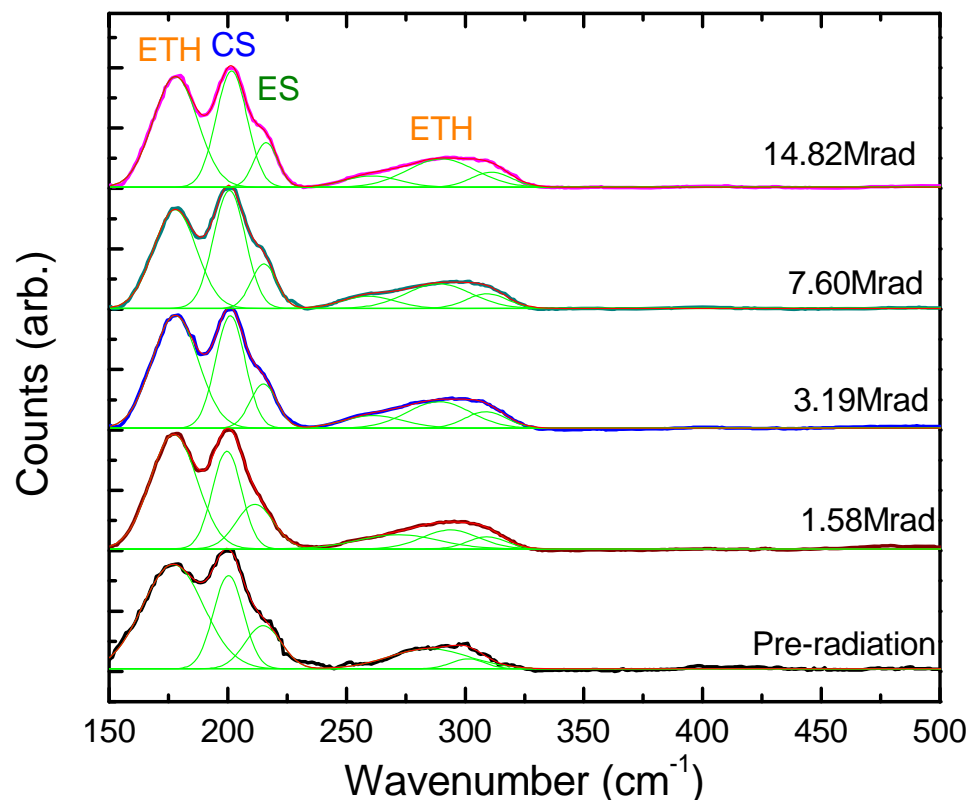


**Figure 105** Gen. 3 device cross section with film labels, and corresponding thicknesses.

### Results

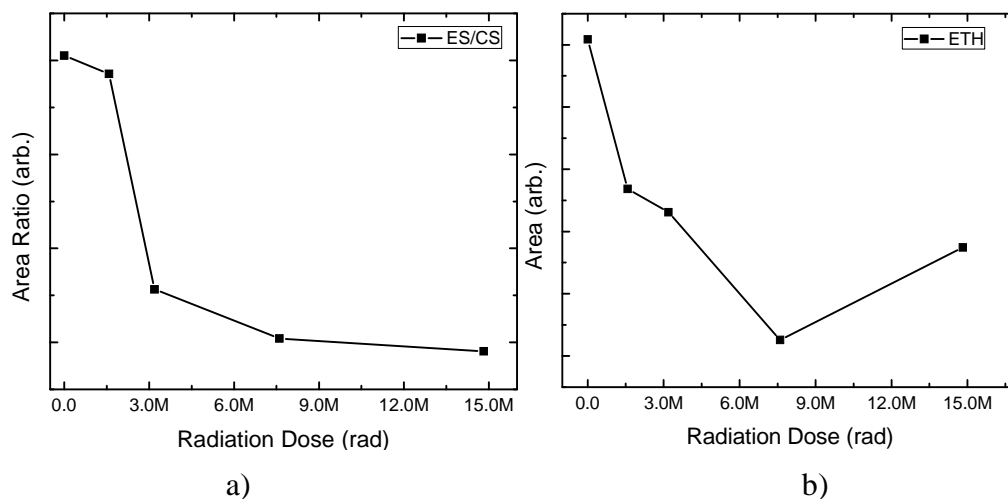
The film analysis in the prior chapter pertains to the radiation-induced effects in bare films, and lateral silver diffusion, but due to the unique structure of these films, and devices, the changes could vary. Material analysis was performed on films without the measuring electrodes to relate the changes in conductivity to the observed material characteristics. EDS has been performed on five locations on each sample such that 25 points were used to determine the uniformity of the film composition. The average deposited film composition was  $\text{Ge}_{37.65}\text{Se}_{62.35}$  with a standard deviation of 0.93, which suggests that the overall film composition is uniform.

Raman spectra of the sandwich structure (chalcogenide glass/silver/chalcogenide glass), mode assignments, and corresponding structural units for characterized studied structures are shown below.



**Figure 106** Fitted Raman spectra of films at various radiation doses.

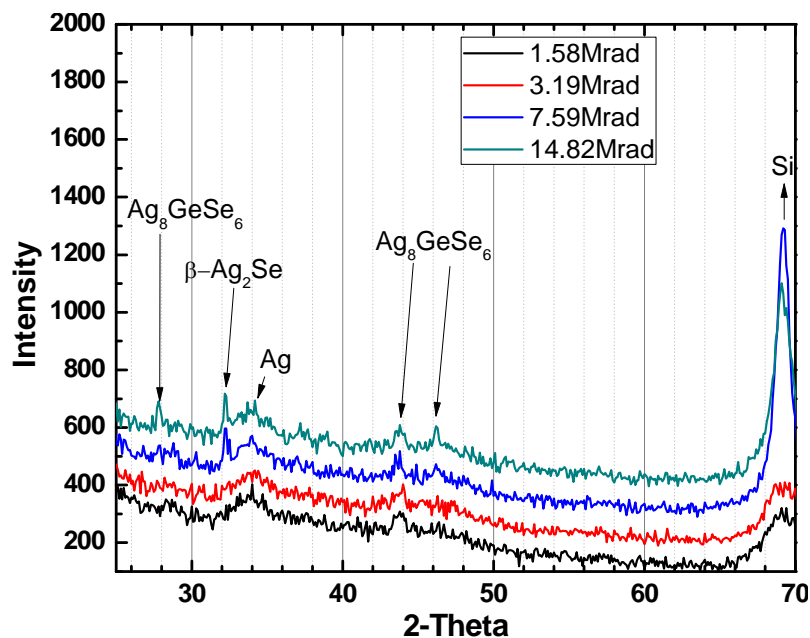
The spectra show the peaks located at  $178\text{ cm}^{-1}$ ,  $195\text{ cm}^{-1}$ , and  $219\text{ cm}^{-1}$  which correspond to ETH, CS, and ES structural units, respectively [128]. Development of the spectra as a function of the applied radiation exhibited a decrease in the intensity of the peaks relating to the ethane-like (ETH), and the edge-shared (ES) modes when compared to the corner-shared (CS) mode. A close observation of the area ratio between ES, and CS modes demonstrates a constant decrease in the ratio as shown in Figure 107 a). The comparison of the areas of the fitted ETH structure revealed a continued decrease with increase in the radiation dose up to 7.58 Mrad, after which the areal intensity of this mode increases as shown in Figure 107b).



**Figure 107** Analysis of the Raman spectra a) ES/CS Area ratio and b) ETH Area change

The x-ray diffraction spectra for four radiation doses are presented in Figure 108, and respective peaks have been assigned for the formation of various diffusion products.

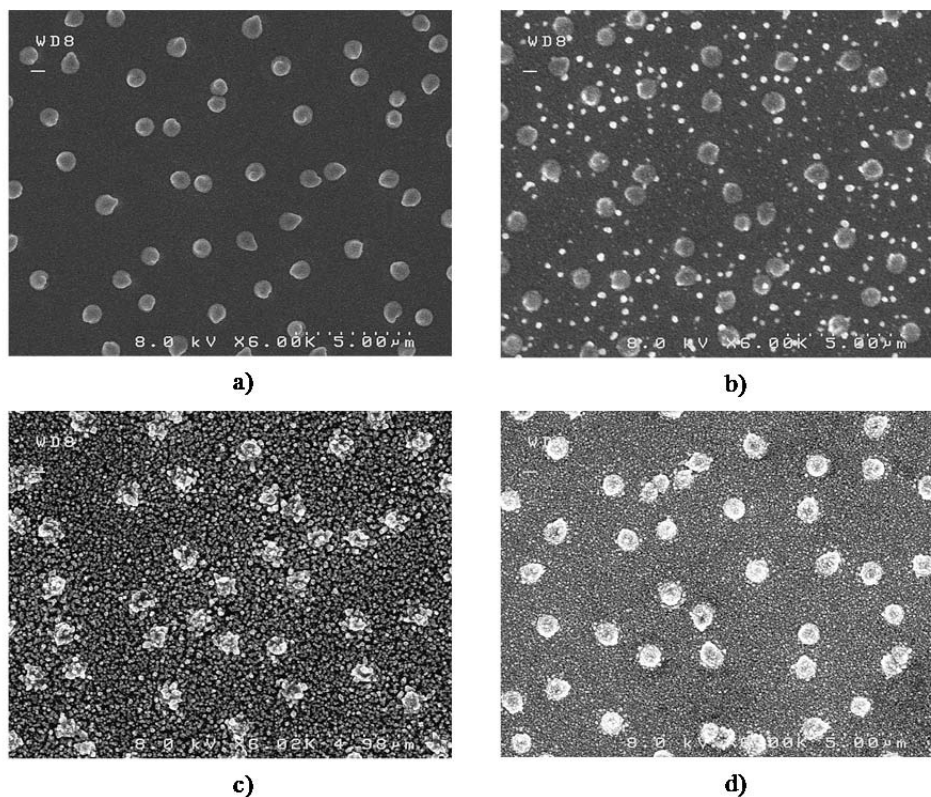
The XRD data obtained at very low radiation dose reflects a pattern of an amorphous film, as was also the non-radiated film, while the higher radiation doses affirm the notion of silver diffusion, and the formation of Ag-containing compositions within the chalcogenide film. There are three main peaks that are evident from the spectra, which have been identified with JCPDS cards 04-0783, 71-190, 24-1041, corresponding to pure Ag,  $\text{Ag}_8\text{GeSe}_6$ , and  $\beta\text{Ag}_2\text{Se}$ , respectively.



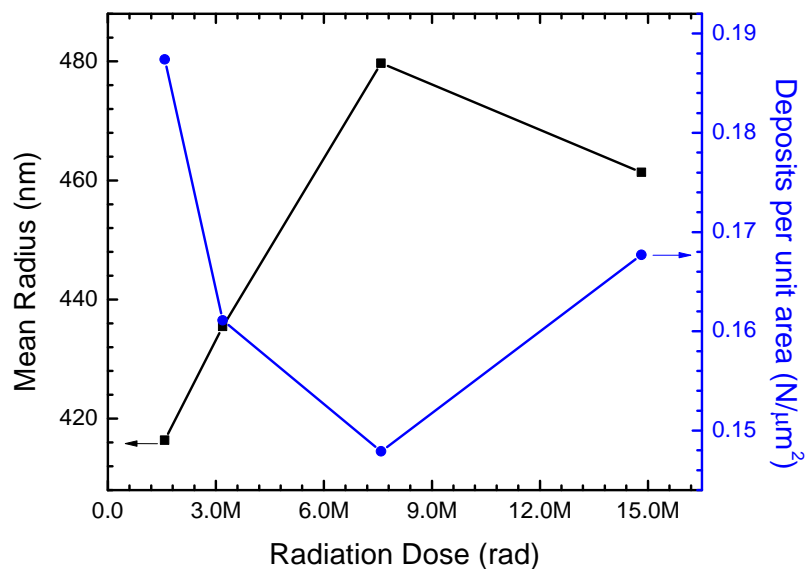
**Figure 108** XRD pattern revealing the formation of various silver phases at different radiation dose exposures.

Analysis of the SEM images exhibits the presence of silver surface deposition occurs because of the Ag diffusion within the chalcogenide film, and Ag-containing clusters are visible. The radius of the silver deposits, and the distribution density of the deposits are inversely related. Increasing the radiation dose resulted in an increase in the silver surface deposits, and concurrently a decrease in the density of nucleation of the silver islands per unit area up to 7.59 Mrad. Above this radiation dose, the radius of the deposits decreases while the density increases. Simultaneously, a second phase with a smaller size is also formed at the higher radiation doses. The SEM images are presented in Figure 109, and the analysis of these images is summarized in Figure 110.



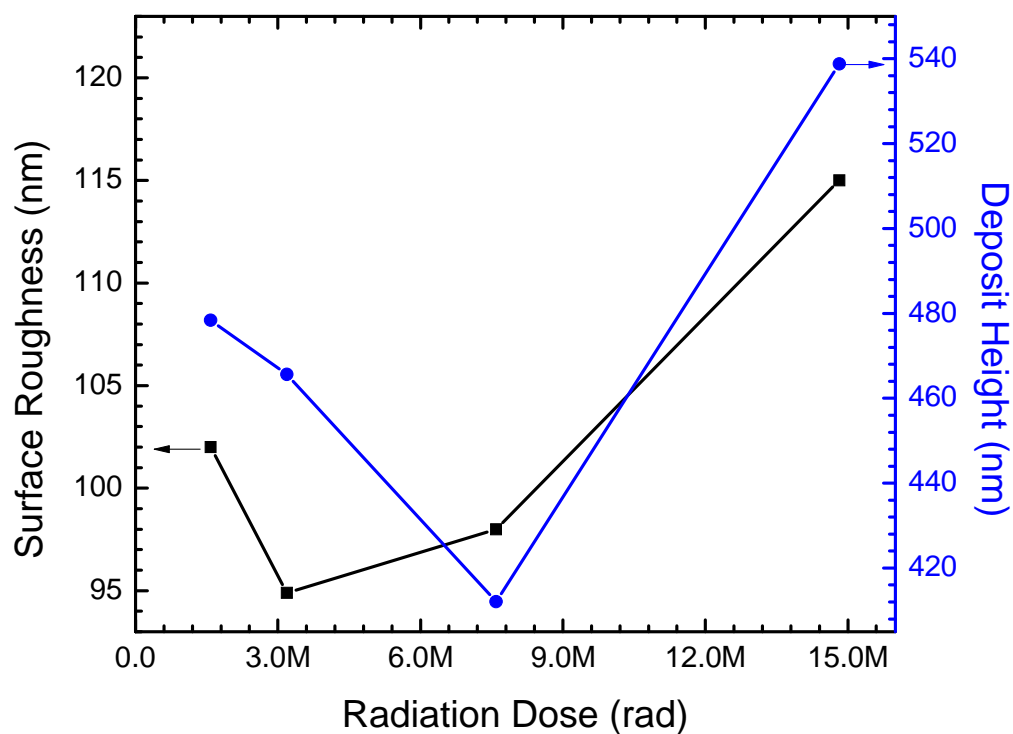


**Figure 109** SEM surface images at various radiation doses a) 1.58 Mrad, b) 3.19 Mrad, c) 7.59 Mrad, and d) 14.82 Mrad. The clusters on the surface correspond to silver surface deposition due to radiation-induced silver diffusion.



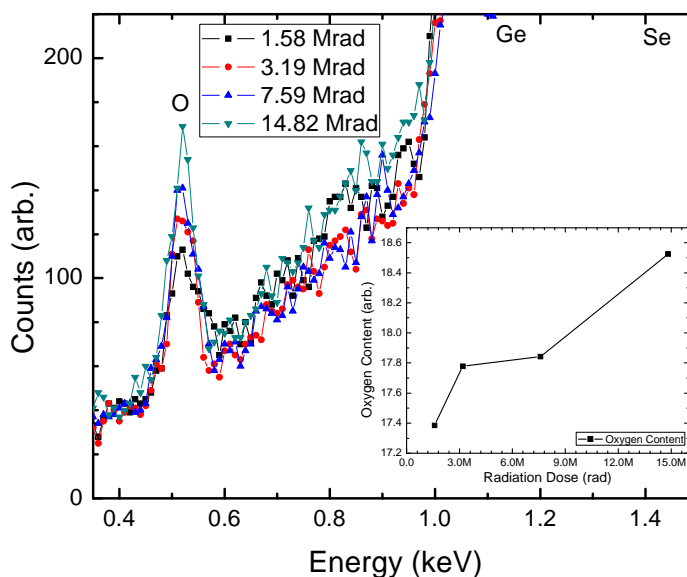
**Figure 110** SEM analysis of the silver clusters on the film surface; the black graph corresponds to the mean radius of the clusters, and the blue graph represents the number of deposits per unit area.

The AFM study illustrates that the height of these deposits decreases with increasing radiation doses. This trend is opposite to the mean radius of the deposits as illustrated through the SEM analysis mentioned above. Another aspect that was studied using AFM was the topological roughness. The surface roughness of the films was measured by excluding the areas occupied by the deposits to study roughness of the film attributed to the presence of smaller silver deposits, and the radiation-induced changes due to structural reorganization. The AFM scans were performed on the same areas where the SEM images were taken to maintain consistency between the two types of studies. Analysis of the AFM films is presented in Figure 111.



**Figure 111** AFM analysis of the surface of the films representing the film surface roughness (black), and the height of the silver clusters (blue).

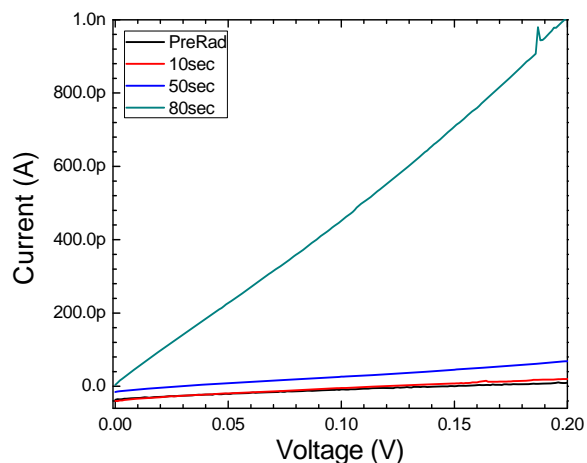
Detailed inspection of the EDS spectra revealed the presence of oxygen within the films. Based on this analysis, it was expounded that the oxygen content in the films increases with radiation dose as presented below.



**Figure 112 EDS analysis confirming the oxidation in the studied system. Inset shows the development of the oxygen concentration with radiation dose.**

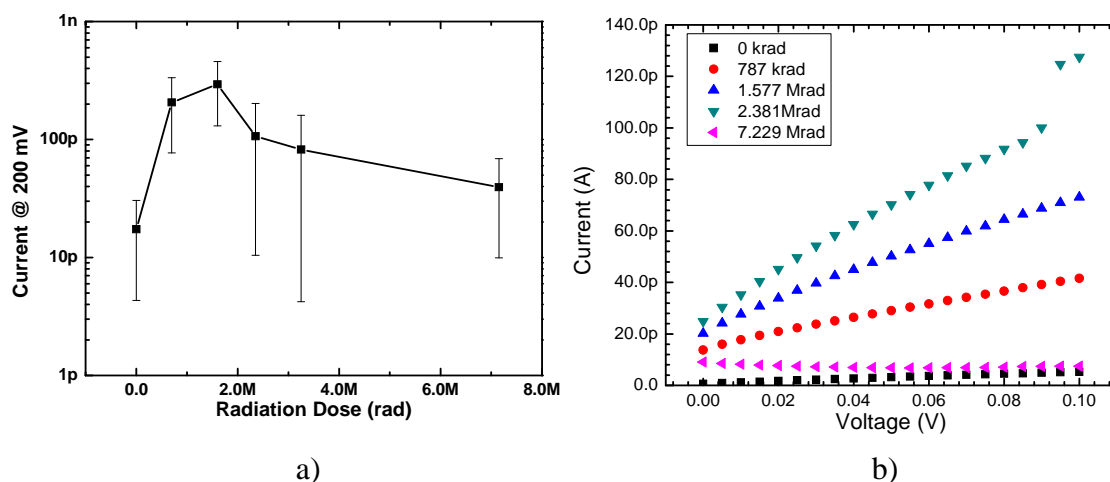
Current vs. Voltage (I-V) curves have been measured using an Agilent 4156C signal analyser using two Source Measuring Units (SMU) connected to the device. Specific voltage sweep conditions were experimentally verified since the application of large voltage bias could induce silver diffusion due to the close proximity of the silver source to the measuring electrodes. The device was initially measured using an impedance meter with a  $V_{ac}$  of 10 mV followed by a current vs. voltage (I-V) sweep, and this process was repeated. The secondary impedance spectra, and I-V was compared to the first sweep measurements. It was determined that a voltage sweep from 0 V to 200 mV was a suitable one, which does not affect the device behavior.

This generation devices, similar to the other generation devices were initially verified using UV, which is shown in the figure below.



**Figure 113** UV characterization of Gen. 3 devices measured at different exposure times.

Several devices were irradiated, and direct current (DC) I-V measurements were performed after discrete radiation dose steps, which are presented in Figure 114a. An I-V curve of one such device is also presented in Figure 114b. The trend observed from the various devices shows an immediate increase in the current from the pre radiation measurement to the first radiation dose. After this sharp increase, the current stabilizes with increasing radiation dose, and then the current begins to decrease with additional radiation dose.



**Figure 114** a) Current vs. Radiation dose measurements illustrating the development of the current and b) Current vs. Voltage curves of one of the radiated devices, measured at discrete radiation doses.

### Discussion

First, it is important to distinguish the type of films that were characterized in these studies. This distinction can be made through XRD, EDS, and Raman analyses. Based on the XRD spectra, it can be stated that the films are amorphous in nature. Additionally, the EDS analysis revealed that the films consisted of 37.65% Ge content, categorizing them to be germanium-rich in comparison to various other Ge-chalcogen binary compounds. The large peak at  $178\text{ cm}^{-1}$  in the Raman spectra corresponding to the ETH structure, also affirms the claim that these films are germanium-rich [149]. This bond is the weakest in the system. One can expect that gamma radiation will cause a destruction of these bonds, and consequently the areal intensity of the ETH structures will decrease. The destruction of the Ge-Ge bonding creates defect sites located on the germanium atom, which can be influenced by the presence of oxygen. Since the radiation experiments have been carried out at ambient environment, oxidation can easily occur as illustrated by the EDS data presented in Figure 112. Even though the presence of oxygen

in the Ge-rich glasses is well documented, there are plenty of discussions as how exactly it reacts with them. Indeed, the problem persists, since it is not easy to give a direct proof for the formation of chalcogenide oxides, and because of this, secondary data like film shrinking, and weight loss have been used in support of the formation of gaseous chalcogen-oxide products leaving the system. In some cases shrinking of the films has been observed [150] in support of the idea that the chalcogen atoms are oxidizing, while other authors [31, 151] reported direct evidence, studying the infrared spectra, for the appearance of Ge–O bonds. Considering the standard potential data for the formation of the particular bivalent oxides  $E_0/E_{n-2}$ , it turns out that germanium is much easier to oxidize with potential  $V_{Ge} = 0.23$  compared to that for selenium ( $V_{Se} = 0.35$ ). Consequently, after the radiation, and formation of defects on germanium sites, even if Se defect sites exist, germanium will be oxidized first. As a result of this, one can expect that the oxygen atoms will replace part of the chalcogen atom location on Ge bonding sites. In this manner, the number of selenium atoms ready to build structural units with germanium increases, and formation of CS units, which consume the highest number of chalcogen atoms grows. In other words, the Ge:Se ratio will decrease giving rise to the formation of units, characteristic for compositions richer in selenium. It is for this reason that there is an increase of the areal intensity of the CS units in the system, which otherwise are not expected to appear with such intensity in the initially regarded system. One other evidence of this fact is the light shift of the CS peak to lower wave numbers from  $202.82 \text{ cm}^{-1}$  to  $201.86 \text{ cm}^{-1}$ .

The bonding strength of Ge-O is 6.83 eV, which is significantly greater than the Ge-Se 2.38eV, and Ge-Ge 1.92eV, and this stabilizes the presence of oxygen in the films.

The bond length of the Ge-O bond is much shorter - 1.62 Å, compared to 2.35 Å, and 2.45 Å for Ge-Se, and Ge-Ge, respectively. The significantly strong Ge-O bond, and the shorter bond length create a constriction of the films, limiting the amount of passages and free volume for silver to diffuse within the films. Due to these limiting factors, XRD only exhibits very small crystalline phases, and the nucleation sites of the surface deposited silver dendrites decrease in size with increased radiation dose. There is one more effect that can be related to oxygen—at low radiation doses, the ternary  $\text{Ag}_8\text{GeSe}_6$  forms, while at higher radiation due to the reduced amount of Ge to react, and form the Ag-containing diffusion products, formation of  $\text{Ag}_2\text{Se}$  is documented on the XRD spectra. However, both types of products are Raman silent, and not visible on the Raman spectra.

The nucleation, and growth of Ag clusters on the surface of the film up to a radiation dose of 7.59 Mrad coincides with the data discussed by T. Kawaguchi, and S. Maruno [152] for the Ag surface deposition in Ag-As-S glasses, and can be related to the increased Ag diffusion with increase of the radiation. This brings about the further growth, and agglomeration of the existing nuclei, which reduces the number of the Ag containing sites. However, the radius of these clusters increases. One could ask about the reason behind the lack of continuation of these processes with increased radiation over 7.59 Mrad, i.e. why does the radius of the deposits decreases beyond this radiation dose? The reason is that at that point, the majority of Ag is reacting to form  $\beta\text{Ag}_2\text{Se}$ , which depletes the formation of  $\text{Ag}_8\text{GeSe}_6$  clusters. The resolution of our EDS system does not allow distinguishing the elements embedded in the big, and small crystals visible on the SEM image but it can be stated that the small crystals that appear at radiation with 3.19 Mrad and higher, are those of  $\beta\text{Ag}_2\text{Se}$ . Their nucleation is restricted at lower radiation

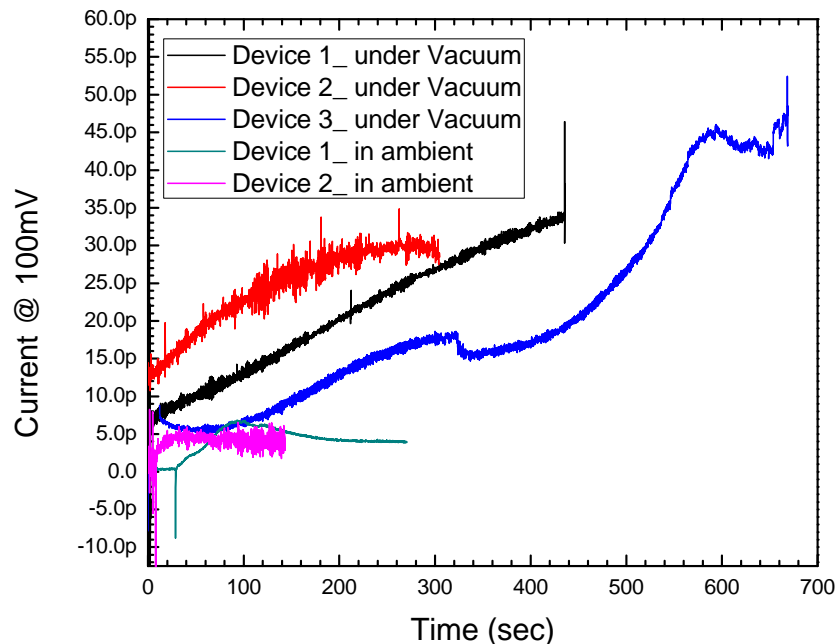
doses, and because of this, they have not been registered by the XRD system. At radiation with a dose of 7.59 Mrad, and over, their appearance is obvious with the high number of nucleation sites increasing with radiation, which suppresses the growth of the  $\text{Ag}_8\text{GeSe}_6$  clusters. In accordance to the  $\beta\text{Ag}_2\text{Se}$  nucleation on the surface, its roughness increases as shown on Figure 111. The formation of  $\beta\text{Ag}_2\text{Se}$  contributes to a new depletion of the hosting film of Se, and because of this, a new increase of the aerial intensity of the ETH units occurs at radiation of 14.82Mrad. The formation of  $\beta\text{Ag}_2\text{Se}$ , and the concurrent depletion of the Se atoms contributes to the occurrence of the ES/CS ratio saturation, and even a small increase in the areal intensity of the ES units. There are a significant number of effects, which goes through an inflection point at a radiation dose of 7.59 Mrad. It seems that this dose is a threshold one, for many of the studied processes.

The last, and indeed the most important, from the application point of view, is how to understand the device performance. The largest increase in the conductivity occurs between pre-radiation condition, and 2 Mrad radiation, where the structural changes (observed by the Raman spectroscopy), and silver incorporation (as exhibited by the XRD) are dominant. After 2 Mrad, the oxygen-induced effects begin to dominate the device performance. To reduce the consequences of oxygen on the device performance, the designed radiation sensor can be encapsulated in a vacuum environment, and in this manner the silver and structural dominant region of the device performance can be enhanced, creating a sensor that can sense a large spectrum of radiation doses. However, there could be another hypothesis. Considering the chalcogenide film, there is published data about the dual role of light within the chalcogenide systems [59]. These effects are related to changes in the band gap of the glasses, and thus would contribute to an initial



increase followed by a decrease of the conductivity. In the studied case, Ag, and oxygen are introduced in the system, which considerably change the situation. To check which influence (the effect of oxidation that occurs in the chalcogenide films or the presence of Ag) will prevail, studies in completely encapsulated devices were also performed.

Current vs. irradiation time measurements under vacuum, and in ambient conditions were performed to determine whether the behavior of the devices varies due to the presence of oxygen during the irradiation. Strict care has been taken to use only the devices with the same fabrication processes, and other environmental conditions to ensure the results were comparable. A  $1.5\text{W}/\text{cm}^2$  UV lamp provided the source of radiation, and a Keithley picoammeter was used to measure the current, while simultaneously placing a 100mV voltage bias across the device. This constant voltage bias was placed on each device, and the performance of each device was monitored for 15 minutes before the start of the experiment to ensure that the constant voltage bias did not affect the device behavior. Some devices were placed in ambient room temperature inside a closed chamber to prevent the introduction of additional light sources, while other devices were placed inside a cryostat at a pressure of  $1 \times 10^{-5}$  mbar in the same dark conditions. After assuring the stability of the experiment at dark conditions, illumination with the UV lamp was performed. The results for this experiment are presented in Figure 115 where it was observed that devices in ambient behaved in a similar manner as the  $\gamma$ -irradiated devices, where there was an initial increase in the current followed by stabilization, and a subsequent decrease in the current.



**Figure 115** *In situ* measurement of current vs illumination time of Gen. 3 devices in vacuum, and in ambient using a UV light source.

Devices under vacuum, on the other hand, showed a linear increase in the current as a function of radiation dose without any decrease in the current even up to a total energy absorption density of  $1000 \text{ J/cm}^2$  ( $>600$  seconds). The non-linearity of the devices is attributed to the contact between the probe tips, and the Al contact, which can be improved by wire bonding the devices. Without wire bonding, a near ohmic contact was achieved in Device 1 under vacuum, which demonstrated that up 400 seconds of UV irradiation there is a constant increase in the current. From this result, it can be suggested that oxygen does play a major role on the device performance. The final devices that are useful for commercial use will include an encapsulation procedure, which is conventional for any fabricated semiconductor based devices. Hence, the observed device performance under vacuum conditions correlates to the commercially available devices.

## Simulations

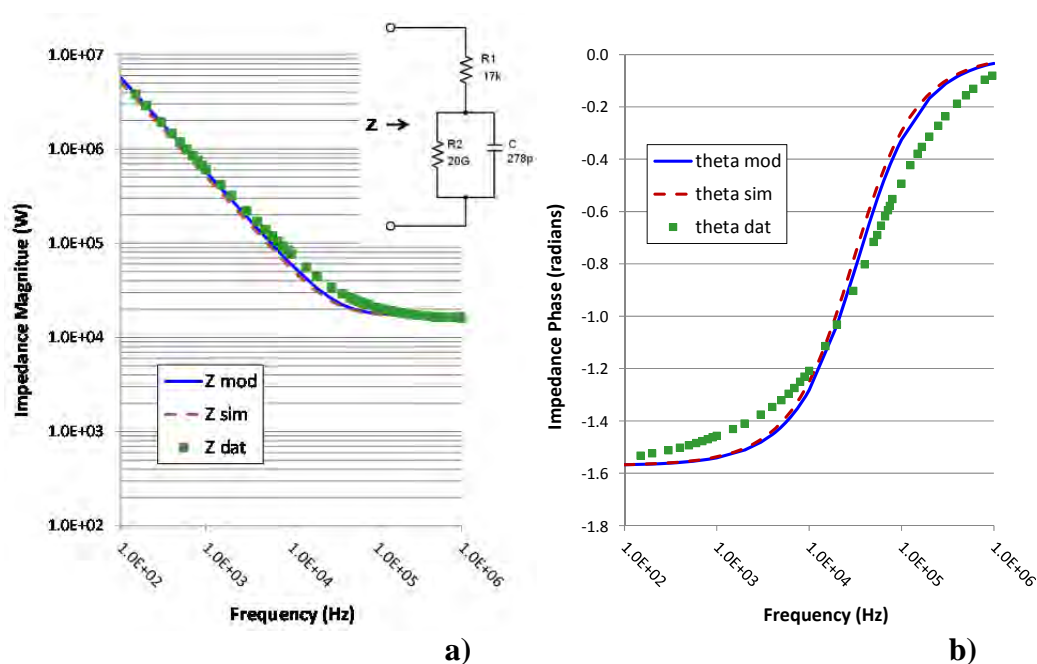
The next step in the study of these devices was to simulate their performance. The motivation for pursuing these simulations is to model the device using discrete components, leading towards creating an external sensing circuitry to become embedded onto a semiconductor chip. Impedance measurements were performed on the devices, and then the spectra was compared with analytical models as well as simulated results from the Silvaco Atlas device simulator. The device has been modeled using the same thicknesses, and parameters as the fabricated devices, and the material parameters are shown in Table 19.

**Table 19**      **Material Properties used for Silvaco device modeling**

Aluminum Workfunction	4.3 eV
Silver Workfunction	4.6 eV
Ge <sub>2</sub> Se <sub>3</sub> parameters	
Affinity	3.45 eV
Bandgap	2.5 eV
Dielectric Constant	6
Carrier Mobility	100 cm <sup>2</sup> /Vs
Density of States	10 <sup>19</sup> cm <sup>-3</sup>

In order to verify the Silvaco model, mixed mode electrical simulations were performed on the device structure. The simulations entail simulating the frequency response of the device with a constant 10 mV amplitude AC voltage applied between the Al electrodes. From these results, the magnitude, and phase of the device impedance can be extracted, and compared to an equivalent circuit model as well as experimentally measured data. The equivalent circuit model proposed is a 1-pole network, composed of a resistor (R1) in series with a second resistor (R2) in parallel with a capacitor (C). The resistor R1 corresponds to the contact resistance comprising of both of the Al electrodes,

and the chalcogenide glass film consisting of R, and C component. Modeling the device with this 1-pole circuit, and using the materials parameters for the Silvaco software correlates very well with the measured data, which suggests that this device can be replaced with this simple circuit model. The impedance measurement data, and comparison with the simulated results are depicted in Figure 116. This is a good validation of the methodology used for these device simulations.

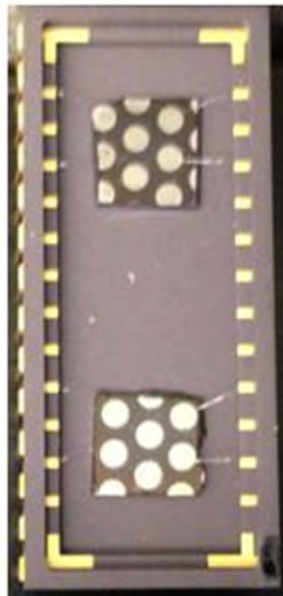


**Figure 116** a) Magnitude of impedance vs. frequency, and b) Phase of impedance vs. frequency for analytical model (Zmod, theta mod), device simulations (Zsim; Theta sim), and experimental data (Zdat; theta dat) for prerad impedance characteristics of one of the investigated devices.

## Conclusion

Sandwich structures of Ge<sub>37.65</sub>Se<sub>62.35</sub> glass-silver- Ge<sub>37.65</sub>Se<sub>62.35</sub> glass with Al electrodes on top of them were studied in order to understand the nature of the effects occurring in them under radiation with different doses of gamma radiation. It was shown that under radiation, the chalcogenide films undergo structural changes related to an

increase of the CS structural units, and a decrease of the ETH, and ES structural units up to radiation dose of ~7 Mrad. This effect is connected to the reaction of the chalcogenide matrix with Ag diffusing within the films, and the oxidation from the environment in which the experiments have been conducted. The diffusion products that are formed due to the reaction of Ag with the chalcogenide matrix is initially  $\text{Ag}_8\text{GeSe}_6$  with the development of a second phase— $\beta\text{Ag}_2\text{Se}$  once the amount of oxygen, reacting with the chalcogenide matrix, increases due to radiation. The Ag diffusion in the chalcogenide matrix results in silver surface deposits, which are built initially by clusters from  $\text{Ag}_8\text{GeSe}_6$ , whose growth at high radiation doses is retarded due to formation of a new phase— $\beta\text{Ag}_2\text{Se}$  surface nucleates. The introduction of Ag, and the intrinsic radiation-induced effects in the chalcogenide matrix lead initially to an increase of the conductivity of the structures, which later, due to the dominant role of oxidation, the conductivity decreases. It has been proved that oxidation occurs when all these processes are carried out in an oxygen-containing environment. This type of device is highly applicable for sensing different ranges of radiation doses with a linear response of current as a function of irradiation time. However, oxidation of the films should be avoided during preparation, and normal functionality to harness the full sensing capability of these devices. These devices have been analyzed, and modeled using Silvaco software. The simulated results are in harmony with the measured impedance results. The final device can be modeled using circuit elements as revealed through these simulations.



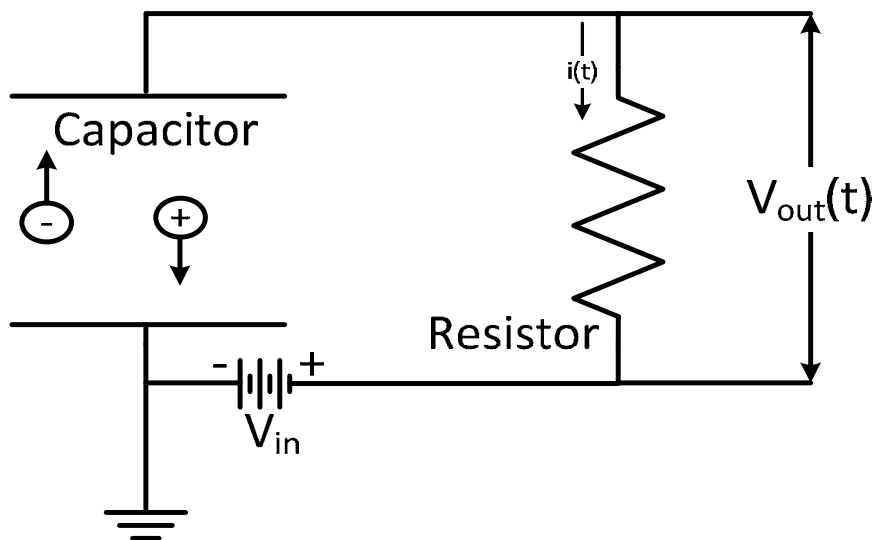
**Figure 117** Final product of the wire bonded Gen. 3 device.

## RADIATION SENSING CIRCUITRY

### **Background, and Circuit Requirements**

There is a prevalent need to investigate new semiconductor materials capable of effectively sensing radiation. One of the main requirement for determining whether a material is suitable for radiation sensing is that it must have a high resistivity  $>10 \text{ M}\Omega$  [153]. Assuming a 1V bias is applied to this material with  $10 \text{ M}\Omega$  resistivity creates a 100 nA current. New radiation sensors must be able to have at least  $10 \text{ M}\Omega$  resistance [153], but current sensing circuitry using MOSFETs have an internal noise level near 1-10nA range. This limits the number of materials because the resistance of a potential material must lie between 1-2 orders of magnitude range, while increasing this range will allow greater freedom for developing new materials.

Due to these limitations, current radiation sensors increase the applied voltage to try to sense higher currents to circumvent this issue [5]. This is not an ideal solution for two reasons. A higher voltage requires voltage converter circuits, which increases the complexity of embedding the circuit, and the radiation sensing material. The other issue that can occur due to increasing the voltage applied to the sensors is the possibility that this large voltage could couple with other devices on the same silicon substrate. This coupling effect can change the device operation, and to prevent this issue very good insulators are required. The application of larger applied voltage will significantly strain the insulators, and increases the probability of oxide degradation. An example of a large voltage sensing circuit is shown in the figure below.



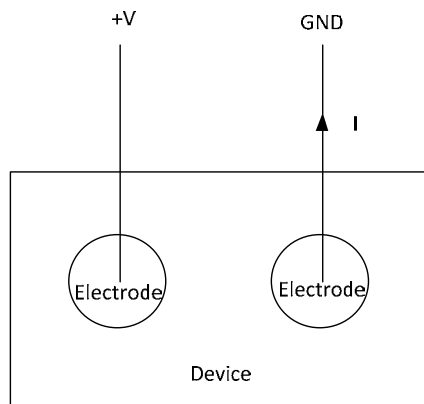
**Figure 118 Large voltage external sensing differentiating circuit [154]**

Even though sensing low current issues can be averted by using large voltages, this is not an ideal solution for creating smaller devices that could run on batteries. The ideal solution will not use a very large voltage (1V) to run all the devices on the chip as well as provide the appropriate voltage bias to the radiation sensing device.

### Circuit Design, and Simulations

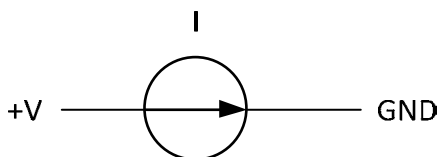
Before delving into detail about the measuring circuit, it is important to model the device as conventional circuit elements. The material, and device characterizations have shown that the device resistance changes as a function of radiation dose. Additionally, resistance is a passive quantity, and has a linear relationship between the voltage, and current. Therefore, it is justified to model the device as a variable current source since the applied voltage bias will be constant so the current through the device will be directly proportional to the resistance. The issue that still persists is regarding the direction of the current. The device measurements have been conducted in the following manner using semiconductor parameter analyzer.





**Figure 119** Device measurement setup using a semiconductor parameter analyzer.

This setup is analogous to the using the following circuit element, and can be substituted into circuit simulations.



**Figure 120** Analogous circuit element substitution for radiation sensor.

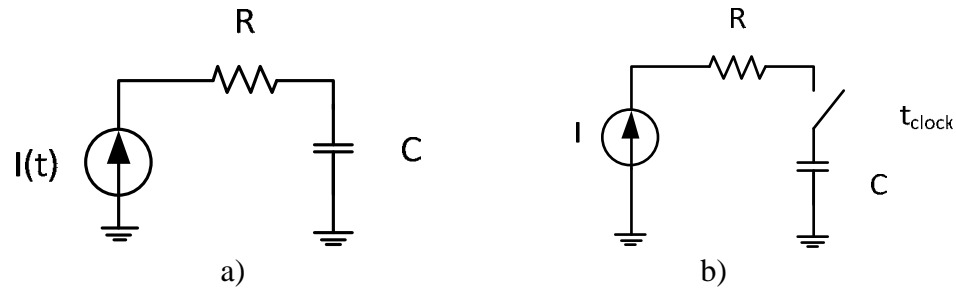
As shown in the previous data regarding the device measurements, at the pre radiation state and low irradiation levels, the device current is on the orders of pico amps, which is within the noise of any MOSFET. This makes it difficult to differentiate the signal from the noise, which is why using any type of MOSFET within this circuit must be done very carefully as to not confuse the noise from the signal. For such reasons, conventional current to voltage converters cannot function at such low current levels, but by sacrificing micro second, and nano second sensing capability, it is possible to devise a circuit that can measure these low currents.

The basic circuit elements are resistors, capacitors, and inductors, where the resistor is a passive device, and the capacitor, and inductors are active devices. Unlike inductors, capacitors are widely used in VLSI, and ULSI technology, easily fabricatable in CMOS processing, and it is a charge-based device. The charge within the capacitor is a linear function of capacitance, and voltage as well as current, and time shown in the following equations.

$$Q = C * V \quad (31)$$

$$Q = I * t \quad (32)$$

Using these two equations, current can be converted into voltage by using a constant capacitance, and the time variables. This is the theory behind the circuit implementation that can sense such low currents. In such low current circuits, it is necessary to work at very low frequencies. Thermal noise is the primary source of noise in low frequency circuit, which is approximately 25 mV so the lowest sensing voltage has to be twice this voltage so 50 mV. The lower limit for the theoretical calculations was performed with 100 mV to try to avoid this issue. Additionally, the size of the capacitor is also very important. The smaller the capacitor size, the faster it will achieve the target 100 mV limit with the least amount of time, and for the smallest current. On the other hand, this limits the highest current that is capable of sensing because the highest voltage in a circuit cannot exceed the voltage applied to the entire system. These simulations were performed using a 1 micron design with a VDD of 1V so the highest voltage cannot exceed 1 volt. The initial circuit diagram is presented in the figure below.

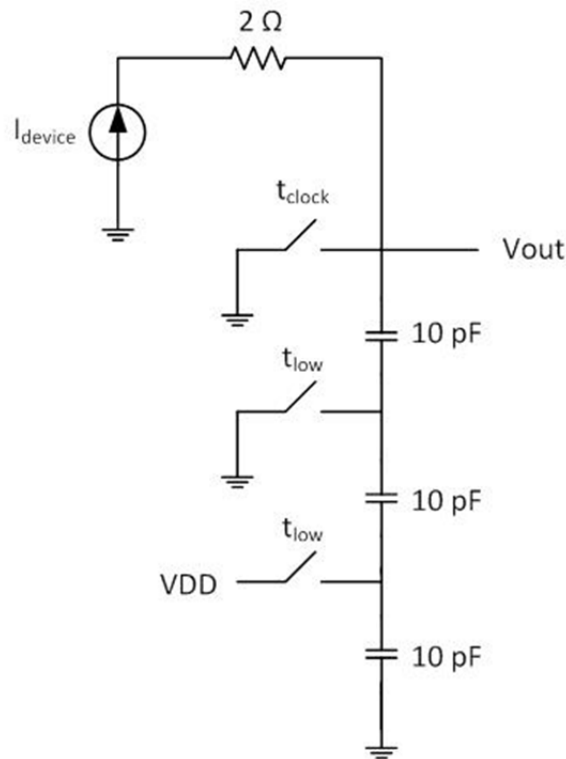


**Figure 121** Circuit schemes for a) charging, and b) discharging a capacitor.

Based on these limitations, and using a 10 pF capacitor, and 20 ms period with 50% duty cycle, the sensing current range is between 1nA, and 100 pA. This cannot sense current levels near 1 pA so there are two options: either increase the clock period or decrease the capacitor size. Varying the clock is not advisable in case other elements are dependent on this clock, while decreasing the capacitor size is a fabrication challenge. The latter is easily achievable at the expense of fabrication area, which is not a big issue since the radiation sensor dimensions are large enough to accommodate this large fabrication area. Capacitance is directly proportional to the cross sectional area so the bigger the capacitor the larger the required area to build such a capacitor, which takes valuable silicon real estate. Since the approach is to use different capacitors rather than varying the clock speeds, there are two methods to derive these various capacitances. Achieving different capacitance values is either possible by placing capacitors in series or parallel to obtain an effective capacitance value. Placing capacitors in parallel will result in the addition of the capacitance values, resulting in a bigger capacitor, while placing capacitors in series creates a smaller capacitor whose value is derived from the following equation.

$$C_{eff} = \frac{(C_1 * C_2 * C_3)}{(C_1 + C_2 + C_3)} \quad (33)$$

Using capacitors in parallel is more mathematically convenient, but to enable specific capacitors without having the current from the device traverse a MOSFET makes this topology extremely difficult to accomplish. The advantage of this circuit design is that it offers not only one capacitor, but rather it offers two different capacitors, by enabling a single switch. The described circuit is shown in the figure below.



**Figure 122** Circuit concept design for measuring low currents.

The radiation sensor is represented by the current source to offer a conceptual view of the current range that is capable of being sensed, and the  $2\ \Omega$  resistor represents the contact resistance as well as other miscellaneous resistances that are naturally present in fabricated devices. Capacitance values that are achievable using this topology are  $10\ \text{pF}$ , and  $3.33\ \text{pF}$  where the former is capable of sensing comparably higher currents, and the latter for sensing low currents. The lower capacitance value is achievable by keeping

the  $t_{low}$  switch open, creating 3 capacitors in series, and for sensing higher currents the switch is closed, creating a 10 pF capacitor. The charging of the capacitors occurs by periodically opening, and closing the  $t_{clock}$  switch that allows the current to go directly to ground (discharging the capacitors or removing all the accumulated charge within the capacitors) or directing the current from the device to pass into the capacitors. The charging time selected for this circuit was 10 msec, and 10 msec of discharging time, which allows 50 measurements to be made within a second. By averaging these 50 points will ensure that faulty readings, and any other anomalies are completely avoided due to the natural redundancy of this sensing methodology.

Using this circuit design, it is possible to convert a current value into a corresponding voltage. The voltage range that can be sensed is from 100 mV to VDD, where VDD is the largest voltage applied to the entire circuit. Any node within the circuit cannot exceed this voltage so this limits the high-end range. Keeping the minimum voltage at 100 mV will avoid the interference of any flicker or thermal noise, which can inflict signal integrity. Using these limitations, the calculated current sensing range is from 33 pA to 1 nA, which is a significant range that will increase the current sensing range by 2 extra orders of magnitude.

This design was also verified using simulations, where all the switches were replaced with MOSFETs, and the entire circuit is split into 4 blocks. The first block is a voltage reference [155], and other external conversions required for accurate functionality of the entire circuit, which is followed by the sensing circuit represented in Figure 124. After the current is converted into a voltage, this voltage cannot be immediately converted into the user-specific method because this conversion could affect

the functionality of the capacitors; for such reasons, a voltage buffer is required that will have a wide range to duplicate the voltage values achieved at the output of the current to voltage converter circuit. The advantage of using a buffer is that the output of the current to voltage conversion circuit goes to a high impedance node, which does not accept any current but only senses the voltage at that node. Finally, it was observed that the two types of buffers used in the buffer stage have the capability to sense either very low voltages (close to 0 V) or a high voltage range (close to VDD). Combining the two outputs will offer some of the benefits, and provide a larger voltage range than using only one of the buffers, but at the smallest, and largest voltages, the weaker buffer will dominate, and overwhelm the effect of the other buffer circuit. To resolve this issue, two pass gates were created, which when provided sufficient voltage, will pass the input voltage to the output. The layout of these pass gates will allow the buffer with the low voltage sensing ability to be passed when  $t_s$  is open, and once  $t_s$  is closed the output of the other buffer will be passed to the output while blocking the output of the other buffer to prevent any interference.

The switch corresponding to the  $t_{low}$  will be closed once the voltage reaches a user specific value; this enables the high current sensing circuit regime. Switch designated by  $t_s$  will be triggered on if, and only if  $t_{low}$  is closed, and a specific threshold current has been achieved. The circuit diagrams for these various blocks, and the results of these simulations are shown in the figures below.

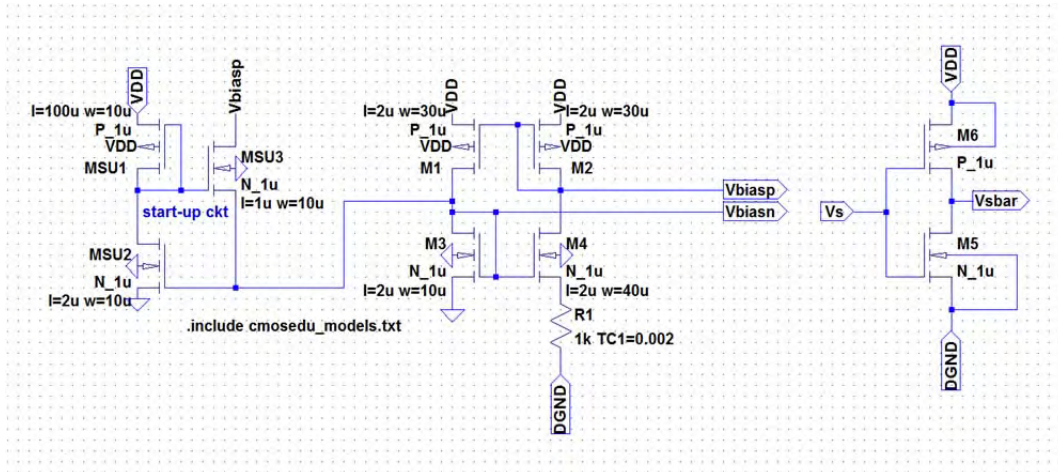


Figure 123 Voltage reference Circuit block

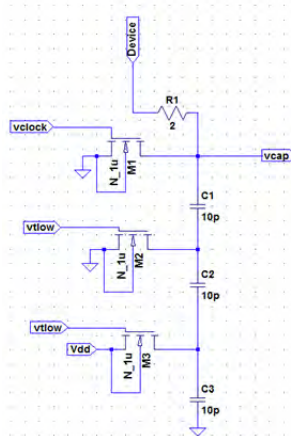


Figure 124 Radiation Sensing Circuit block

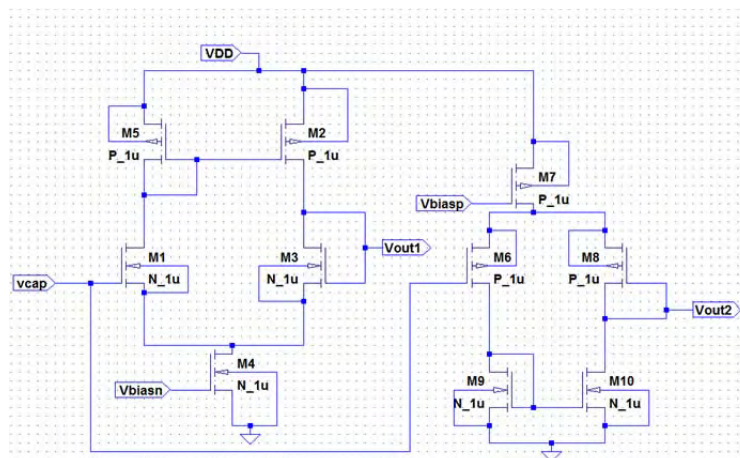
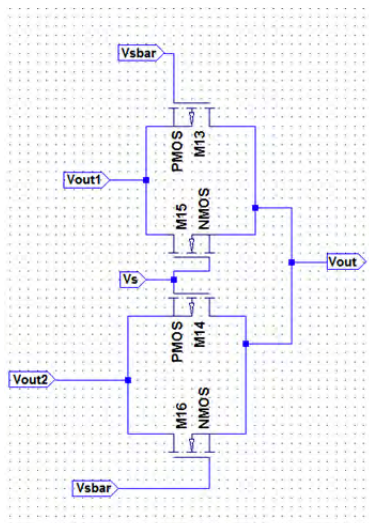
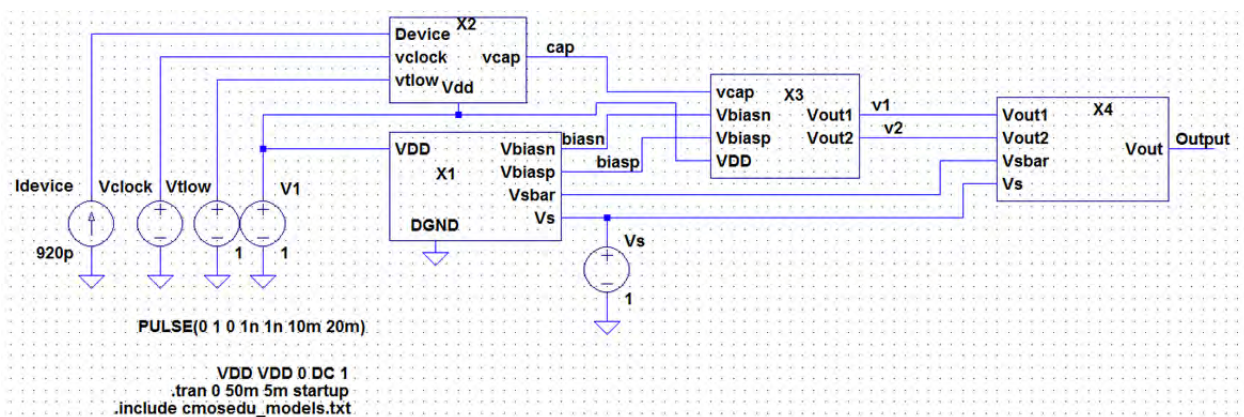


Figure 125 Buffer Circuit block



**Figure 126** Output pass gates Circuit block

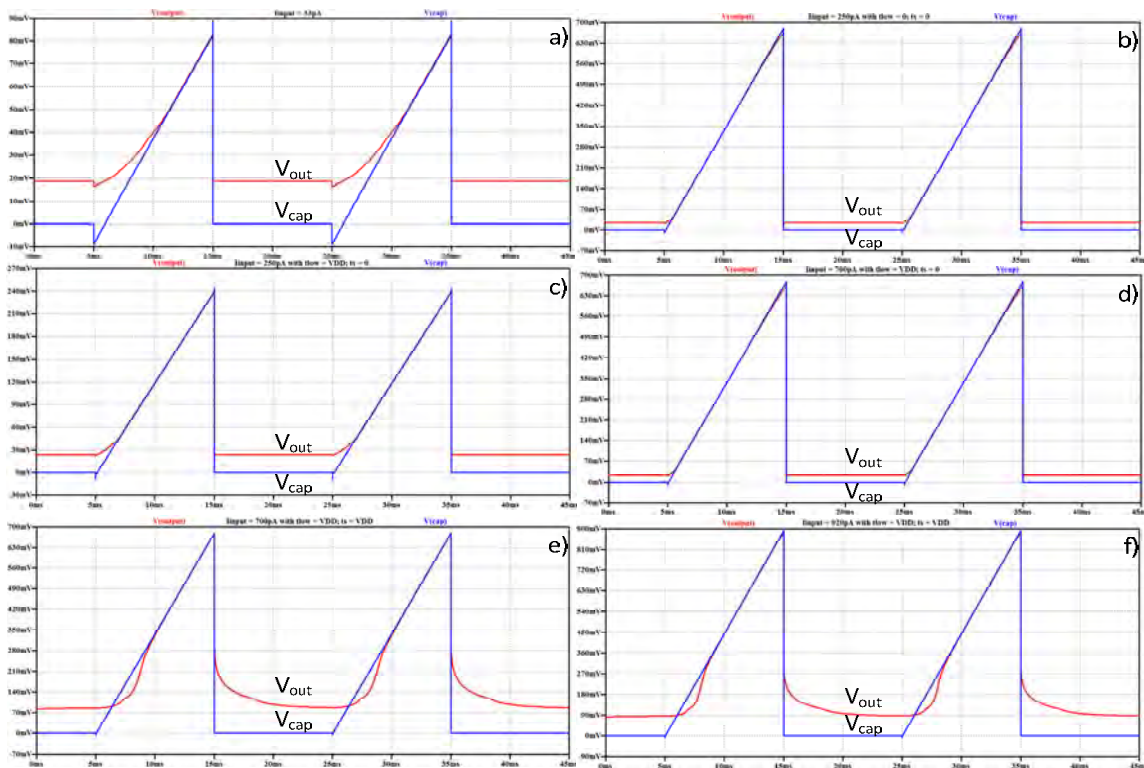


**Figure 127** Top view of all circuit blocks, and their corresponding connections

Note that the device circuit block does not have any VDD affecting any active capacitors, this block is completely independent of any other reference voltage, and the radiation-sensing device is the only source of power for the capacitors. The VDD in that circuit is merely to ensure that all nodes are driven to specific voltages to reduce the effect of any radiation-induced changes. This node is described in more detail in the fabrication of the rad hard device. All the devices were simulated using a 1-micron process, and this circuit is adaptable towards smaller devices less than 1 micron. The



clock used for this simulation is a square pulse with a 20 msec period, and 1 nano second rise, and fall time. The results of the simulations are shown below where the red graph refers to the circuit output while the blue graph refers to the output voltage of the device sensing circuit block.



**Figure 128** Simulation results for (a)  $I_{input}=33pA$ , (b)  $I_{input}=250pA$ , (c)  $I_{input}=250pA$  with  $t_{low}$  closed, (d)  $I_{input}=700pA$  with  $t_{low}$  closed, (e)  $I_{input}=700pA$  with  $t_{low}$ , and  $t_s$  closed, and (f)  $I_{input}=920pA$  with  $t_{low}$ , and  $t_s$  closed

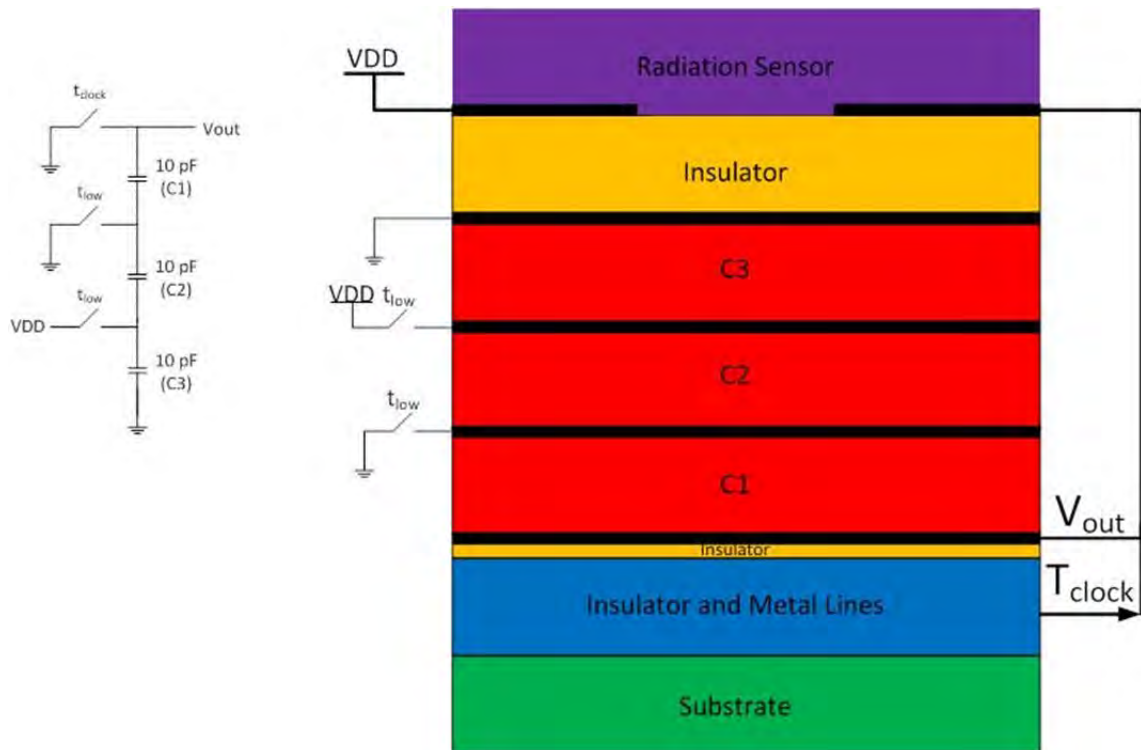
The second part of the circuit design is making this entire circuit radiation hard, which is aided by the unique circuit design. When radiation interacts with a material, it generates an electron of significant high energy, which can penetrate deep into any material substrate, and cause damage to various electronics. This issue is a very important issue that affects the performance of all circuits in the presence of radiation, and for this reason there has been a significant amount of research to investigate this issue [156-170].

The interaction of this high-energy electron with a single device causes a sharp increase in voltage/current, which can burn out devices or cause inaccurate readings, which has to be avoided at all costs. It is important to either capture or slow down these electrons to reduce the damage. The use of such large capacitors, and this topology is made with a purpose since these capacitors can hide all the devices, and prevent any radiation to penetrate, and alter the devices that are created on the silicon substrate. These capacitors could be created using the low-k dielectric material currently used to insulate the various metal lines on top of the devices. The capacitors of various capacitance values are created using the following equation [148].

$$C = \frac{\epsilon_0 \epsilon_r * A}{d} \quad (34)$$

Where A is the cross sectional area, d is the distance between the two capacitor plates,  $\epsilon_0$  is a constant value, and  $\epsilon_r$  is material dependent. The material utilized between metal lines usually has a very low  $\epsilon_r$  to try to limit the capacitance between two adjacent lines. In this design, this low  $\epsilon_r$  material has a dual role: to capture any radiation-induced charges, and to form the capacitor, which is used for sensing, making this material very beneficial. The capacitor thickness increases the probability of capturing all incident radiation, thus a thicker capacitor will protect the underlying devices. In case these electrons have the ability to penetrate to the substrate, the capacitors will be energized to have a constant electric field to slow down these electrons. Electrons have a natural negative charge so an application of an electric field can change the path of these electrons because the applied electric field can slow down these electrons. An electron is attracted to higher voltage, and thus the topology is created while keeping this in mind. The following cross section details the layout of these devices.

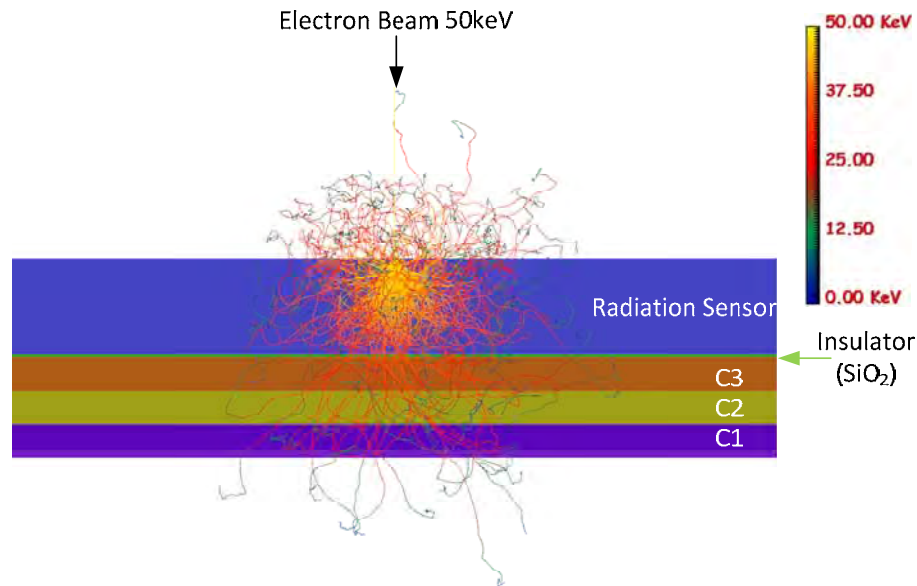
### Fabricated Sensor Topology



**Figure 129** Concept of the cross section of final fabricated device.

When a high-energy electron at low radiation doses ( $t_{low}$  is open), and passes through the insulator layer underneath the radiation sensor, the electron enters the C3 capacitor, is in close proximity of the ground node, which is a source of electric fields, and can disturb the path of the electron. By the time this electron reaches C1, it will have significantly reduced velocity, and is likely to have been stopped within the capacitor stack. The disturbances created by this one electron at low doses are offset by averaging 50 measurements within a second. At high radiation doses on the other hand, the electron will experience not only one electric field, but it will experience 3 electric fields because of the VDD applied to the metal contact between capacitors C2, and C3. This will

significantly alter the electron energy, and it will aid in preventing the electron from entering C1.



**Figure 130 Electron beam simulations validating the circuit topology using Casino Monte Carlo simulator.**

Verification of this topology was performed using Casino simulator, which uses a Monte Carlo method to determine the trajectory, penetration depth, and interactions with material [171]. Certain assumptions were taken into consideration, resembling the environment these radiation sensors experience during  $\gamma$ -ray exposure. When gamma rays interact with material, an electron of high energy is generated, whereas in the simulation, the original electrons are specified with certain energy, and angled at a specific direction. To accommodate this discrepancy, the thickness of the radiation sensor was increased by 1 order of magnitude ( $1\ \mu\text{m}$ ) to ensure the incident electron beam interacts with the sensor prior to entering the capacitors at different angles. The energy of the electrons was chosen to be large enough that without the capacitor barrier, the devices on the Si substrate will be substantially damaged. The simulations were performed without metal

lines, electric field, and standard densities of SiO<sub>2</sub> for the insulator, which were specified within the simulation [171]. The capacitor thicknesses were calculated using a dielectric constant of 2.5 [172] with a cross section area of 900 μm, which is larger than the 500 μm device dimensions, and adjusted for other discrepancies, resulting in a capacitor thickness of 1.7 μm. After the simulation, note that only very weak electrons have penetrated through the capacitors, confirming that this topology can reduce the radiation-induced effects on the silicon substrate.

### **Conclusion**

In this chapter, a radiation sensing circuit is presented, which is applicable for sensing low currents without traversing through any MOSFETs. A novel circuit topology is also presented that reduces the effect of radiation-induced high energy electrons. This topology is also verified by the application of a Monte Carlo simulator. The benefit of this design is the capability to create a portable radiation sensing device using low voltages.

## CONCLUSIONS

The main goal of this dissertation was to engineer, design, fabricate, and test a new generation of radiation sensing devices for which there were no preliminary data. As a result of the successes achieved in this dissertation, an independent research group in China started working on other combination of chalcogenide glass structures for radiation sensing [173], referring to our work. Therefore, as a byproduct of this research, we have started to build the roots of a new research area. This was made possible through the following research achievements:

1. Detailed structural characterization, and radiation-induced changes in the studied films, using Raman spectroscopy, Energy Dispersive x-ray Spectroscopy (EDS), Atomic Force Microscopy (AFM), X-ray Photoelectron spectroscopy (XPS), and Optical bandgap measurements. With the aid of these characterization methods, we discovered the response to radiation in the studied materials as a function of the atomic radius cross section, chemical bonding, and initial structural organization. These studies, not published by any other research group before us, showed that:
  - a. The Se containing glasses have the highest sensitivity because the bigger atomic cross-section, and lower strength of the chemical bonding in them, when compared to S containing system. Selenium containing glasses do not exhibit the polarization, which is a

characteristic for the Te-containing system. The changes in the S-rich, and Se-rich glasses are primarily attributed to the formation of defects, which have been detected in the bandgap measurements.

- b. In all systems, Ge-rich films demonstrate higher radiation sensitivity due to the active role of the Ge-Ge bonding as well as easier switching from corner-sharing units to edge-sharing units, which reduces the entropy of the system. Radiation-induced oxidation is also a characteristic feature, as detected in these systems. Surface of Ge-rich films from all the studied systems exhibits a reduction in roughness with increasing radiation dose.
2. Pioneering a comprehensive study of radiation-induced Ag diffusion. This has been possible by examining the molecular structure using the XRD studies, EDS, and silver diffusion simulations:
    - a. Exposure to gamma radiation causes Ag diffusion, and the formation of different molecular structures in the hosting material. In the chalcogen richer films, the predominant silver containing diffusion products are the binary phases  $\text{Ag}_2\text{X}$  ( $\text{X} = \text{S}, \text{Se}, \text{or Te}$ ). In germanium richer films, a mixture of the binary phase, and the ternary  $\text{Ag}_2\text{GeS}_3$ ,  $\text{Ag}_8\text{GeSe}_6$ , or  $\text{Ag}_8\text{GeTe}_6$  depending on the film system.
    - b. Silver diffusion simulations were able to replicate the experimentally measured diffusion captured by EDS or photographs. The outcome of the simulation was the ability to generate a diffusion rate for the

analyzed compositions, which proved to be an asset for designing a radiation sensing device.

3. Three unique sensor designs were conceived, fabricated, tested under UV, and gamma conditions, and reset.
  - a. Gen. 1 devices were fabricated, and revealed that the device spacing is an important parameter for consideration. The performance of the  $\text{Ge}_{20}\text{Se}_{80}$  devices exhibited a high sensitivity towards low radiation doses. These devices present a 5-6 order of magnitude increase in the conductivity. The  $\text{Ge}_{20}\text{Te}_{80}$  devices also present the ability to exhibit a change with increasing radiation dose.
  - b. Gen. 2 devices were carefully chosen after an intensive investigation into the electric fields present during the sensing procedure using COMSOL Multiphysics software. A unique process flow was created, which empowers the ability to integrate these devices with current CMOS semiconductor fabrications. The Se, and Te-rich films behave in a similar manner as the Gen. 1 devices, but due to the reduction of device sizes, the sensitivity is enhanced. Similar to the Gen. 1 devices, the Se-rich devices have the capability of sensing low radiation doses, the  $\text{Ge}_{40}\text{Se}_{60}$  devices presented the sensitivity to higher radiation doses.
  - c. Gen. 3 devices are unique when compared with the other two device generations. These devices were created to utilize vertical diffusion of silver. Raman spectroscopy demonstrated a different insight into the effect of silver in the presence of structural changes. The XRD, silver



surface deposition, and AFM contribute towards understanding the device performance. The outcome of the material analysis expounded the existence of two main regimes: radiation-induced structural change dominant, and an oxidation dominant. In the radiation-induced structural change dominant regime, destruction, and reorganization of the chalcogenide network occurs in addition to silver diffusion, and silver crystal growth. These changes contribute to an increase in the device conductivity. In the oxidation dominant regime, the crystal size decreases, structural changes are not as exaggerated, highly dense binary molecules are formed, and the conductivity of the devices decreases. Devices that were measured under vacuum using UV lamp present the capability to extend the radiation-induced structural change regime, and the conductivity of the devices show an increasing trend up to an absorbed dose of  $1000 \text{ J/cm}^2$ .

4. A radiation sensor is only as good as the accompanying external sensing circuitry. To demonstrate the sensing methodology, a rudimentary sensing circuit, which has the sensing ability from 33 pA to 1 nA, was designed, and simulated. Simultaneously, a unique topology is also presented for reducing the effect of radiation on the silicon substrate, and any devices that it may contain.

In conclusion, the original goal to create an inexpensive, small, portable gamma radiation-sensing sensor has been achieved combining the radiation sensitivity that is

intrinsic to containing chalcogenide glasses, and radiation-induced silver diffusion within them. The material properties can be adjusted to fit the requirement of the end user.

## REFERENCES

- [1] D. A. Neamen, *Semiconductor physics and devices : basic principles*. Chicago: Irwin, 1997.
- [2] F. H. Attix, *Introduction to radiological physics and radiation dosimetry*. New York: Wiley, 1986.
- [3] J. R. Cooper, K. Randle, and R. S. Sokhi, *Radioactive releases in the environment: impact and assessment*: J. Wiley, 2003.
- [4] B. G. Harvey, *Introduction to nuclear physics and chemistry*. Englewood Cliffs, N.J.: Prentice-Hall, 1969.
- [5] W. H. Tait, *Radiation detection*. London; Boston: Butterworths, 1980.
- [6] M. Mladenovic, *Radioisotope and radiation physics; an introduction*. New York: Academic Press, 1973.
- [7] D. Reilly, N. Ensslin, and H. Smith, *Passive Nondestructive Assay of Nuclear Materials*: The Commission, 1991.
- [8] W. J. Price, *Nuclear radiation detection*. New York: McGraw-Hill, 1964.
- [9] G. A. Armantrout, S. P. Swierkowski, J. W. Sherohman, and J. H. Yee, "What can be expected from high-Z semiconductor detectors?," *Nuclear Science, IEEE Transactions on*, vol. 24, pp. 121-125, 1977.
- [10] K. Vetter, "Recent developments in the fabrication and operation of germanium detectors," *Annual Review of Nuclear and Particle Science*, vol. 57, p. 363, 2007.
- [11] R. Hall and T. Soltys, "High purity germanium for detector fabrication," *Nuclear Science, IEEE Transactions on*, vol. 18, pp. 160-165, 1971.
- [12] R. H. Pehl, R. C. Cordi, and F. S. Goulding, "High-purity germanium: Detector fabrication and performance," *Nuclear Science, IEEE Transactions on*, vol. 19, pp. 265-269, 1972.
- [13] T. E. Schlesinger, J. E. Toney, H. Yoon, E. Y. Lee, B. A. Brunett, L. Franks, and R. B. James, "Cadmium zinc telluride and its use as a nuclear radiation detector material," *Materials Science and Engineering: R: Reports*, vol. 32, pp. 103-189, 2001.
- [14] Y. Eisen and A. Shor, "CdTe and CdZnTe materials for room-temperature X-ray and gamma ray detectors," *Journal of Crystal Growth*, vol. 184-185, pp. 1302-1312, 1998.
- [15] J. Steininger, A. J. Strauss, and R. F. Brebrick, "Phase Diagram of the Zn-Cd-Te Ternary System," *Journal of The Electrochemical Society*, vol. 117, pp. 1305-1309, 1970.
- [16] T. H. Prettyman, M. A. Hoffbauer, J. A. Rennie, S. Cook, J. C. Gregory, M. A. George, P. N. Luke, M. Amman, S. A. Soldner, and J. R. Earnhart, "Performance of CdZnTe detectors passivated with energetic oxygen atoms," *Nuclear Instruments and Methods in Physics Research Section A: Accelerators, Spectrometers, Detectors and Associated Equipment*, vol. 422, pp. 179-184, 1999.

- [17] U. Lachish, "Semiconductor crystal optimization of gamma detection," *Journal of Crystal Growth*, vol. 225, pp. 114-117, 2001.
- [18] C. H. Su and S. L. Lehoczky, "Growth of CdZnTe Crystals the Bridgman Technique with Controlled Overpressures of Cd," 2008.
- [19] J. Franc, P. Höschl, E. Belas, R. Grill, P. Hlidek, P. Moravec, and J. Bok, "CdTe and CdZnTe crystals for room temperature gamma-ray detectors," *Nuclear Instruments and Methods in Physics Research Section A: Accelerators, Spectrometers, Detectors and Associated Equipment*, vol. 434, pp. 146-151, 1999.
- [20] P. N. Luke, M. Amman, J. S. Lee, and C. Q. Vu, "Pocket-size CdZnTe gamma-ray spectrometer," *Nuclear Science, IEEE Transactions on*, vol. 52, pp. 2041-2044, 2005.
- [21] S. Ovshinsky, "Optically induced phase changes in amorphous materials," *Journal of Non-Crystalline Solids*, vol. 141, pp. 200-203, 1992.
- [22] O. I. Shpotyuk, "Radiation-induced effects in chalcogenide vitreous semiconductors," in *Semiconducting chalcogenide glass*, R. Fairman and B. Ushkov, Eds., ed Amsterdam; London: Elsevier Academic Press, 2004.
- [23] J. C. Phillips, "Topology of covalent non-crystalline solids I: Short-range order in chalcogenide alloys," *Journal of Non-Crystalline Solids*, vol. 34, pp. 153-181, 1979.
- [24] P. Boolchand, G. Lucovsky, J. C. Phillips, and M. F. Thorpe, "Self-organization and the physics of glassy networks," *Philosophical Magazine*, vol. 85, pp. 3823-3838, Nov 2005.
- [25] D. J. Jacobs and M. F. Thorpe, "Generic rigidity percolation: the pebble game," *Physical Review Letters*, vol. 75, p. 4051, 1995.
- [26] M. Thorpe, "Continuous deformations in random networks," *Journal of Non-Crystalline Solids*, vol. 57, pp. 355-370, 1983.
- [27] M. Thorpe, D. Jacobs, M. Chubynsky, and J. Phillips, "Self-organization in network glasses," *Journal of Non-Crystalline Solids*, vol. 266, pp. 859-866, 2000.
- [28] M. F. Thorpe, D. J. Jacobs, N. Chubynsky, and A. Rader, "Generic rigidity of network glasses," *Rigidity Theory and Applications*, Kluwer Academic/Plenum Publishers, New York, pp. 239-278, 1999.
- [29] P. Boolchand, D. Georgiev, and B. Goodman, "Discovery of the intermediate phase in chalcogenide glasses," *Journal of Optoelectronics and Advanced Materials*, vol. 3, pp. 703-720, 2001.
- [30] F. Wang, S. Mamedov, P. Boolchand, B. Goodman, and M. Chandrasekhar, "Pressure Raman effects and internal stress in network glasses," *Physical Review B*, vol. 71, p. 174201, 2005.
- [31] L. Tichý, H. Tichá, and K. Handlír, "Photoinduced changes of optical properties of amorphous chalcogenide films at ambient air pressure," *Journal of Non-Crystalline Solids*, vol. 97, pp. 1227-1230, 1987.
- [32] M. T. Shatnawi, C. L. Farrow, P. Chen, P. Boolchand, A. Sartbaeva, M. Thorpe, and S. J. Billinge, "Search for a structural response to the intermediate phase in  $\text{Ge}_x\text{Se}_{1-x}$  glasses," *Physical Review B*, vol. 77, p. 094134, 2008.
- [33] P. Boolchand, X. Feng, and W. J. Bresser, "Rigidity transitions in binary Ge-Se glasses and the intermediate phase," *Journal of Non-Crystalline Solids*, vol. 293-295, pp. 348-356, 2001.

- [34] K. Chopra, S. Barthwal, and D. Pandya, "Structural sensitivity of transport and optical properties of amorphous GeTe," *physica status solidi (a)*, vol. 35, pp. 761-768, 1976.
- [35] V. Lyubin, M. Klebanov, A. Bruner, N. Shitrit, and B. Sfez, "Transient photodarkening and photobleaching in glassy GeSe<sub>2</sub> films," *Optical Materials*, vol. 33, pp. 949-952, 2011.
- [36] R. Fairman and B. Ushkov, *Semiconducting chalcogenide glass*. Amsterdam; London: Elsevier Academic Press, 2004.
- [37] D. Linke, "Vzaimosvyazi sostav-svoistvo v khal'kogenidnuikh steklakh i ikh strukt? mo-khimicheskaya interpretaciya (russ.)," in *Proc. Conf. Amorphous Semiconductors*, 1978, pp. 57-64.
- [38] K. Gupta and S. Das, "X-ray study of selenium in the liquid and colloidal state," *Indian J. Phys*, vol. 15, pp. 401-409, 1941.
- [39] J. Stuke, "Review of optical and electrical properties of amorphous semiconductors," *Journal of Non-Crystalline Solids*, vol. 4, pp. 1-26, 1970.
- [40] G. Lucovsky, "Average energy gaps in the binary glass-alloy systems: Ge<sub>1-x</sub>Se<sub>x</sub> and As<sub>1-x</sub>Se<sub>x</sub>," *Physical Review B*, vol. 15, p. 5762, 1977.
- [41] V. Kumar, S. Kr Sharma, T. Sharma, and V. Singh, "Band gap determination in thick films from reflectance measurements," *Optical Materials*, vol. 12, pp. 115-119, 1999.
- [42] A. Lakatos and M. Abkowitz, "Electrical Properties of Amorphous Se, As<sub>2</sub>Se<sub>3</sub>, and As<sub>2</sub>S<sub>3</sub>," *Physical Review B*, vol. 3, p. 1791, 1971.
- [43] S. R. Elliott and A. Zakery, "An Introduction to Chalcogenide Glasses," in *Optical Nonlinearities in Chalcogenide Glasses and their Applications*. vol. 135, ed: Springer Berlin Heidelberg, 2007, pp. 1-28.
- [44] Y. Utsugi and Y. Mizushima, "Optically broadened lattice vibrational spectra in amorphous arsenic chalcogenides," *Journal of Applied Physics*, vol. 50, pp. 1494-1496, 1979.
- [45] Y. Utsugi and Y. Mizushima, "Photostructural change in the Urbach tail in chalcogenide glasses," *Journal of Applied Physics*, vol. 51, pp. 1773-1779, 1980.
- [46] Y. Utsugi and Y. Mizushima, "Photostructural change of lattice vibrational spectra in Se-Ge chalcogenide glass," *Journal of Applied Physics*, vol. 49, pp. 3470-3475, 1978.
- [47] S. M. Alekperova, A. Aliyev, K. D. Jalilova, and I. Ahmedov, "Optical filters on the basis of  $\alpha$ -Ag<sub>2</sub>Te thin films," in *Moscow, Russia*, 2005, pp. 384-387.
- [48] T. S. Moss, *Photoconductivity in the Elements*: Butterworths Scientific Publications, 1952.
- [49] A. Ganjoo, Y. Ikeda, and K. Shimakawa, "In situ measurements of photo-induced volume changes in amorphous chalcogenide films," *J. of Non-Cryst. Sol.*, vol. 266, pp. 919-923, 2000.
- [50] F. Yakuphanoglu, D. Arsova, and E. Vateva, "Photoinduced changes of the optical parameters of thin films from Ge<sub>30.8</sub>As<sub>5.7</sub>S<sub>63.5</sub> glass," *Journal of optoelectronics and advanced materials*, vol. 9, pp. 334-336, 2007.
- [51] V. Kornelyuk, I. Savitskii, L. Khirunenko, O. Shpotyuk, and I. Yaskovets, "Photoinduced defect formation in chalcogenide vitreous semiconductors," *Journal of Applied Spectroscopy*, vol. 50, pp. 310-313, 1989.

- [52] K. Shimakawa, A. Kolobov, and S. Elliott, "Photoinduced effects and metastability in amorphous semiconductors and insulators," *Adv. in Phys.*, vol. 44, pp. 475-588, 1995.
- [53] N. Terakado and K. Tanaka, "Photoinduced Phenomena in GeO<sub>2</sub>-GeS<sub>2</sub> Glasses," *Japanese Journal of Applied Physics*, vol. 46, p. L265, 2007.
- [54] S. Rajagopalan, K. S. Harshavardhan, L. K. Malhotra, and K. L. Chopra, "Photo-optical changes in Ge-chalcogenide films," *Journal of Non-Crystalline Solids* vol. 50, pp. 29-38, 1982.
- [55] K. Tanaka, Y. Kasanuki, and A. Odajima, "Physical properties and photoinduced changes of amorphous Ge-S films," *Thin Solid Films*, vol. 117, pp. 251-260, 1984.
- [56] A. Zakery and S. R. Elliott, *Optical nonlinearities in chalcogenide glasses and their applications* vol. 135: Springer, 2007.
- [57] K. Tanaka, "Mechanisms of photodarkening in amorphous chalcogenides," *Journal of Non-Crystalline Solids*, vol. 59, pp. 925-928, 1983.
- [58] D. Jacobs and M. Thorpe, "Generic rigidity percolation in two dimensions," *Physical Review E*, vol. 53, p. 3682, 1996.
- [59] D. Arsova and E. Vateva, "Dual action of light in photodarkened Ge-As-S films," *phys. stat. sol. (b)*, vol. 249, pp. 153-157, 2012.
- [60] A. Barik, R. Naik, and K. Adarsh, "Unusual observation of fast photodarkening and slow photobleaching in a-GeSe<sub>2</sub> thin film," *Journal of Non-Crystalline Solids*, 2013.
- [61] P. Khan, A. Barik, E. Vinod, K. Sangunni, H. Jain, and K. Adarsh, "Coexistence of fast photodarkening and slow photobleaching in Ge<sub>19</sub>As<sub>21</sub>Se<sub>60</sub> thin films," *Opt. Express*, vol. 20, pp. 12416-12421, 2012.
- [62] Q. Yan, H. Jain, G. Yang, J. Ren, and G. Chen, "Millisecond kinetics of photodarkening/bleaching in x(Ge<sub>45</sub>Se<sub>55</sub>) - (1-x)(As<sub>45</sub>Se<sub>55</sub>) chalcogenide amorphous films," *Journal of Applied Physics*, vol. 112, p. 053105, 2012.
- [63] R. R. Kumar, A. Barik, E. Vinod, M. Bapna, K. Sangunni, and K. Adarsh, "Crossover from photodarkening to photobleaching in a-Ge<sub>x</sub>Se<sub>100-x</sub> thin films," *Optics Letters*, vol. 38, pp. 1682-1684, 2013.
- [64] A. Kovalskiy, H. Jain, A. C. Miller, R. Y. Golovchak, and O. I. Shpotyuk, "A Study of Reversible  $\gamma$ -Induced Structural Transformations in Vitreous Ge<sub>23.5</sub>Sb<sub>11.8</sub>S<sub>64.7</sub> by High-Resolution X-ray Photoelectron Spectroscopy," *The Journal of Physical Chemistry B*, vol. 110, pp. 22930-22934, 2012/09/03 2006.
- [65] S. Chakravarty, D. Georgiev, P. Boolchand, and M. Micoulaut, "Ageing, fragility and the reversibility window in bulk alloy glasses," *Journal of Physics: Condensed Matter*, vol. 17, p. L1, 2005.
- [66] P. Boolchand, D. Georgiev, and M. Micoulaut, "Nature of glass transition in chalcogenides," *J. Optoelectron. Adv. Mater*, vol. 4, p. 823, 2002.
- [67] M. Mitkova, "Three-component chalcogenide glasses as inorganic photoresists," *Thin Solid Films*, vol. 182, pp. 247-254, 1989.
- [68] K. Tanaka, "Configurational and structural models for photodarkening in glassy chalcogenides," *Jap. J. Appl. Phys.*, vol. 25, pp. 779-786, 1986.
- [69] S. S. Sarsembinov, E. Abdulgafarov, M. Tumanov, and N. Rogachev, "Radiation-induced defects influence on the electrical, photoelectrical and optical properties

- of chalcogenide glasses," *Journal of Non-Crystalline Solids*, vol. 35, pp. 877-882, 1980.
- [70] O. Shpotyuk, "Influence of gamma-irradiation on optical transmission spectra and microhardness of vitreous  $\text{As}_2\text{S}_3\text{-Sb}_2\text{S}_3$ ," *Visn. Lviv Univ*, vol. 19, pp. 25-31, 1985.
- [71] O. Shpotyuk and A. Kovalskiy, "Compositional trends in radiation-optical properties of chalcogenide glasses," *J. Optoelectron. Adv. Mater*, vol. 4, p. 751, 2002.
- [72] F. Xia, S. Baccaro, D. Zhao, M. Falconieri, and G. Chen, "Gamma ray irradiation-induced optical band gap variations in chalcogenide glasses," *Nuclear Instruments and Methods in Physics Research Section B: Beam Interactions with Materials and Atoms*, vol. 234, pp. 525-532, 2005.
- [73] D. Zhao, H. Wang, G. Chen, S. Baccaro, A. Cecilia, M. Falconieri, and L. Pilloni, "Gamma-ray-induced multi-effect on properties of chalcogenide glasses," *Journal of the American Ceramic Society*, vol. 89, pp. 3582-4, 2006.
- [74] F. Xia, S. Baccaro, H. Wang, W. Hua, H. Zeng, X. Zhang, and G. Chen, " $\gamma$ -ray irradiation-induced multiple effects on Ge-As-Se chalcogenide glasses," *Journal of Non-Crystalline Solids*, vol. 354, pp. 1365-1368, 2008.
- [75] M. Shpotyuk, O. Shpotyuk, R. Golovchak, and P. Demchenko, "FSDP-related correlations in  $\gamma$ -irradiated chalcogenide semiconductor glasses: The case of glassy arsenic trisulphide  $\text{g-As}_2\text{S}_3$  revised," *Journal of Physics and Chemistry of Solids*, 2013.
- [76] S. K. Sundaram, J. S. McCloy, B. J. Riley, M. K. Murphy, H. A. Qiao, C. F. Windisch, E. D. Walter, J. V. Crum, R. Golovchak, and O. Shpotyuk, "Gamma Radiation Effects on Physical, Optical, and Structural Properties of Binary As-S Glasses," *Journal of the American Ceramic Society*, vol. 95, pp. 1048-1055, 2012.
- [77] A. Kovalskiy, "Compositional trends of radiation-induced effects in ternary systems of chalcogenide glasses," *Radiation Effects and Defects in Solids*, 158, vol. 1, pp. 391-397, 2003.
- [78] O. Shpotyuk, R. Y. Golovchak, T. Kavetsky, A. Kovalskiy, and M. Vakiv, "Radiation-optical effects in glassy Ge-As (Sb)-S systems," *Nuclear Instruments and Methods in Physics Research Section B: Beam Interactions with Materials and Atoms*, vol. 166, pp. 517-520, 2000.
- [79] O. Shpotyuk, A. Matkovsky, A. Kovalsky, and M. Vakiv, "Radiation-induced changes of amorphous  $\text{As}_2\text{S}_3$  physical properties," *Radiation effects and defects in solids*, vol. 133, pp. 1-4, 1995.
- [80] O. I. Shpotyuk, "Radiation-induced effects in chalcogenide vitreous semiconductors," *Semiconductors and Semimetals*, vol. 78, pp. 215-260, 2004.
- [81] M. Al-Ewaisi, M. Imran, O. A. Lafi, and M. d. W. Kloub, "Effect of gamma irradiation on some electrical properties and optical band gap of bulk  $\text{Se}_{92}\text{Sn}_8$  chalcogenide glass," *Physica B: Condensed Matter*, vol. 405, pp. 2643-2647, 2010.
- [82] A. Abu El-Fadl, A. S. Soltan, and A. A. Abu-Sehly, "Effect of gamma doses on the optical parameters of  $\text{Se}_{76}\text{Te}_{15}\text{Sb}_9$  thin films," *Journal of Physics and Chemistry of Solids*, vol. 68, pp. 1415-1421, 2007.

- [83] A. A. Shaheen, M. M. A. Imran, O. A. Lafi, M. d. I. Awadallah, and M. r. K. Abdullah, "Optical properties of a- $\text{Se}_{90}\text{In}_{10-x}\text{Sn}_x$  chalcogenide thin films before and after gamma irradiation," *Radiation Physics and Chemistry*, vol. 79, pp. 923-928, 2010.
- [84] S. M. El-Sayed, "Electron beam and gamma irradiation effects on amorphous chalcogenide  $\text{SbSe}_{2.5}$  films," *Nuclear Instruments and Methods in Physics Research Section B: Beam Interactions with Materials and Atoms*, vol. 225, pp. 535-543, 2004.
- [85] M. El-Hagary, M. Emam-Ismail, E. Shaaban, and A. El-Taher, "Effect of  $\gamma$ -irradiation exposure on optical properties of chalcogenide glasses  $\text{Se}_{70}\text{S}_{30-x}\text{Sb}_x$  thin films," *Radiation Physics and Chemistry*, vol. 81, pp. 1572-1577, 2012.
- [86] B. R. Johnson, J. V. Crum, S. Sundaram, R. M. Van Ginhoven, C. E. Seifert, B. J. Riley, and J. V. Ryan, "DC Ionization Conductivity of Amorphous Semiconductors for Radiation Detection Applications," *Nuclear Science, IEEE Transactions on*, vol. 56, pp. 863-868, 2009.
- [87] T. Minami, A. Yoshida, and M. Tanaka, "Gamma-ray induced conductivity of vitreous semiconductors in the systems As-S-Te and As-Se-Te," *Journal of Non-Crystalline Solids*, vol. 7, pp. 328-336, 1972.
- [88] M. N. Kozicki, M. Park, and M. Mitkova, "Nanoscale memory elements based on solid-state electrolytes," *Nanotechnology, IEEE Transactions on*, vol. 4, pp. 331-338, 2005.
- [89] M. Mitkova, T. Petkova, P. Markovski, and V. Mateev, "Photoinduced changes by polarisation holographic recording in  $\text{Se}_{70}\text{Ag}_{15}\text{I}_{15}$  thin films," *Journal of non-crystalline solids*, vol. 164, pp. 1203-1206, 1993.
- [90] M. Mitkova, I. Iliev, V. Boev, and T. Petkova, "Influence of an electrical field on optical recording in chalcogenide glasses," *Journal of non-crystalline solids*, vol. 227, pp. 748-751, 1998.
- [91] M. Mitkova, T. Petkova, P. Markovski, and V. Mateev, "Photoinduced changes in the selenium-silver-iodine system," *The Journal of Physical Chemistry*, vol. 96, pp. 8998-9001, 1992.
- [92] A. Husmann, J. Betts, G. Boebinger, A. Migliori, T. Rosenbaum, and M.-L. Saboungi, "Megagauss sensors," *Nature*, vol. 417, pp. 421-424, 2002.
- [93] M. Schöning, C. Schmidt, J. Schubert, W. Zander, S. Mesters, P. Kordos, H. Lüth, A. Legin, B. Seleznev, and Y. G. Vlasov, "Thin film sensors on the basis of chalcogenide glass materials prepared by pulsed laser deposition technique," *Sensors and Actuators B: Chemical*, vol. 68, pp. 254-259, 2000.
- [94] M. Frumar and T. Wagner, "Ag doped chalcogenide glasses and their applications," *Current Opinion in Solid State and Materials Science*, vol. 7, pp. 117-126, 2003.
- [95] A. V. Kolobov and S. R. Elliott, "Photodoping of amorphous chalcogenides by metals," *Advances in Physics*, vol. 40, pp. 625-684, 1991/10/01 1991.
- [96] J. Phillips, "Microscopic origin of anomalously narrow Raman lines in network glasses," *Journal of non-crystalline solids*, vol. 63, pp. 347-355, 1984.
- [97] R. El Ghrandi, J. Calas, and G. Galibert, "Ag dissolution kinetics in amorphous  $\text{GeSe}_{5.5}$  thin films from "In-situ" resistance measurements versus time," *physica status solidi (a)*, vol. 123, pp. 451-460, 1991.



- [98] M. Kostyshin and Y. V. Ushenin, "He-Ne laser radiation-stimulated diffusion of Ag into vitreous  $\text{As}_2\text{S}_3$ ," *physica status solidi (a)*, vol. 66, pp. K47-K50, 1981.
- [99] T. Wagner, E. Marquez, J. Fernandez-Pena, J. Gonzalez-Leal, P. Ewen, and S. Kasap, "The kinetics of the photo-induced solid-state chemical reaction in  $\text{Ag}/\text{As}_{33}\text{S}_{67}$  bilayers and its reaction products," *Philosophical Magazine B*, vol. 79, pp. 223-237, 1999.
- [100] A. Kolobov And G. Bedelbaeva, "Effect of conductive substrate on dissolution and lateral diffusion of metals in vitreous chalcogenides," *Philosophical Magazine B*, vol. 64, pp. 21-32, 1991.
- [101] T. Wagner, "Photo-and thermally-induced diffusion and dissolution of Ag in chalcogenide glasses thin films," *Journal of Optoelectronics and Advanced Materials*, vol. 4, pp. 717-727, 2002.
- [102] S. Elliott, "A unified mechanism for metal photodissolution in amorphous chalcogenide materials," *Journal of non-crystalline solids*, vol. 130, pp. 85-97, 1991.
- [103] T. Wagner and M. Frumar, "Photoenhanced dissolution and diffusion of Ag in As-S layers," *Journal of non-crystalline solids*, vol. 116, pp. 269-276, 1990.
- [104] M. Mitkova, M. Kozicki, H. Kim, and T. Alford, "Local structure resulting from photo and thermal diffusion of Ag in Ge-Se thin films," *Journal of Non-Crystalline Solids*, vol. 338, pp. 552-556, 2004.
- [105] M. Mitkova, Y. Sakaguchi, D. Tenne, S. K. Bhagat, and T. L. Alford, "Structural details of Ge-rich and silver-doped chalcogenide glasses for nanoionic nonvolatile memory," *Physica Status Solidi a-Applications and Materials Science*, vol. 207, Mar 2010.
- [106] T. W. Kang, C. Y. Hong, C. S. Chong, and T. W. Kim, "Effects of electric fields on the silver photodoping of  $\text{As}_2\text{Se}_3$  films," *Journal of Materials Science*, vol. 27, pp. 5620-5622, 1992.
- [107] D. Tsiulyanu and I. Stratan, "On the photodissolution kinetics of silver in glassy  $\text{As}_2\text{S}_3$ ," *Journal of Non-Crystalline Solids*, vol. 356, pp. 147-152, 2010.
- [108] D. Goldschmidt, T. Bernstein, and P. Rudman, "The kinetics of photodissolution of silver in amorphous  $\text{As}_2\text{S}_3$  Films," *physica status solidi (a)*, vol. 41, pp. 283-287, 1977.
- [109] A. Kolobov, V. Lyubin, and J. Tröltzsch, "On the mechanism of anomalous surface diffusion of silver in an amorphous chalcogenide/silver structure," *physica status solidi (a)*, vol. 115, pp. K139-K141, 1989.
- [110] A. Feltz, H. Aust, and A. Blayer, "Glass formation and properties of chalcogenide systems XXVI: Permittivity and the structure of glasses  $\text{As}_x\text{Se}_{1-x}$  and  $\text{Ge}_x\text{Se}_{1-x}$ ," *Journal of Non-Crystalline Solids*, vol. 55, pp. 179-190, 1983.
- [111] M. Aniya and J. Kawamura, "Medium range structure and activation energy of ion transport in glasses," *Solid State Ionics*, vol. 154, pp. 343-348, 2002.
- [112] V. Sousa, "Chalcogenide materials and their application to Non-Volatile Memories," *Microelectronic Engineering*, vol. 88, pp. 807-813, 2011.
- [113] A. Abu El-Fadl, M. M. Hafiz, M. M. Wakaad, and A. S. Aashour, "Influence of  $\gamma$ -radiation on the optical parameters of  $\text{Ag}_{10}\text{Te}_{90}$  thin films," *Radiation Physics and Chemistry*, vol. 76, pp. 61-66, 2007.

- [114] K. Shahi, "Transport studies on superionic conductors," *physica status solidi (a)*, vol. 41, pp. 11-44, 1977.
- [115] M. Ribes, E. Bychkov, and A. Pradel, "Ion transport in chalcogenide glasses: Dynamics and structural studies," *Journal of Optoelectronics and Advanced Materials*, vol. 3, Sep 2001.
- [116] M. Ureña, A. Piarristeguy, M. Fontana, and B. Arcondo, "Ionic conductivity ( $\text{Ag}^+$ ) in AgGeSe glasses," *Solid State Ionics*, vol. 176, pp. 505-512, 2005.
- [117] M. A. Ureña, M. Fontana, B. Arcondo, and M. T. Clavaguera-Mora, "Crystallization processes of Ag-Ge-Se superionic glasses," *Journal of Non-Crystalline Solids*, vol. 320, pp. 151-167, 2003.
- [118] Y. Sakaguchi, D. A. Tenne, and M. Mitkova, "Structural development in Ge-rich Ge-S glasses," *Journal of Non-Crystalline Solids* vol. 355, pp. 1792-1796, 2009.
- [119] M. Tanaka, T. Minami, and M. Hattori, "Thermal Expansion and Its Related Properties of Arsenic-Sulfur Glasses," *Japanese Journal of Applied Physics*, vol. 5, pp. 185-186, 1966.
- [120] X. Feng, W. J. Bresser, and P. Boolchand, "Direct Evidence for Stiffness Threshold in Chalcogenide Glasses," *Physical Review Letters*, vol. 78, pp. 4422-4425, 1997.
- [121] I. Kotsalas and C. Raptis, "Structural Raman studies of  $\text{Ge}_x\text{S}_{1-x}$  chalcogenide glasses," *Journal of Optoelectronics and Advanced Materials*, vol. 3, pp. 675-684, 2001.
- [122] S. Sugai, "Stochastic random network model in Ge and Si chalcogenide glasses," *Physical Review B*, vol. 35, pp. 1345-1361, 1987.
- [123] K. Inoue, O. Matsuda, and K. Murase, "A model calculation of the characteristic Raman modes in the tetrahedral network structures of  $\text{GeSe}_2$ ," *Physica B: Condensed Matter*, vol. 219-220, pp. 520-522, 1996.
- [124] K. Jackson, "Electric Fields in Electronic Structure Calculations: Electric Polarizabilities and IR and Raman Spectra from First Principles," *physica status solidi (b)*, vol. 217, pp. 293-310, 2000.
- [125] T. G. Edwards and S. Sen, "Structure and Relaxation in Germanium Selenide Glasses and Supercooled Liquids: A Raman Spectroscopic Study," *The Journal of Physical Chemistry B*, vol. 115, pp. 4307-4314, 2011.
- [126] G. Lucovsky, C. K. Wong, and W. B. Pollard, "Vibrational properties of glasses: Intermediate range order," *Journal of Non-Crystalline Solids*, vol. 59-60, pp. 839-846, 1983.
- [127] G. Lucovsky and F. L. Galeener, "Intermediate range order in amorphous solids," *Journal of Non-Crystalline Solids*, vol. 35-36, pp. 1209-1214, 1980.
- [128] K. Jackson, A. Briley, S. Grossman, D. Porezag, and M. Pederson, "Raman-active modes of a- $\text{GeSe}_2$  and a- $\text{GeS}_2$ : A first-principles study," *Phys. Rev. B Physical Review B*, vol. 60, pp. R14985-R14989, 1999.
- [129] P. M. Bridenbaugh, G. P. Espinosa, J. E. Griffiths, J. C. Phillips, and J. P. Remeika, "Microscopic origin of the companion  $A_1$  Raman line in glassy  $\text{Ge}(\text{S},\text{Se})_2$ ," *Physical Review B*, vol. 20, pp. 4140-4144, 1979.
- [130] E. Sleetx, L. Tich, P. Nagels, and R. Callaerts, "Thermally and photo-induced irreversible changes in the optical properties of amorphous  $\text{Ge}_x\text{Se}_{100-x}$  films," *Journal of Non-Crystalline Solids*, vol. 198-200, pp. 723-727, 1996.

- [131] K. Andrikopoulos, S. Yannopoulos, G. Voyiatzis, A. Kolobov, M. Ribes, and J. Tominaga, "Raman scattering study of the a-GeTe structure and possible mechanism for the amorphous to crystal transition," *Journal of Physics: Condensed Matter*, vol. 18, p. 965, 2006.
- [132] K. Andrikopoulos, S. Yannopoulos, A. Kolobov, P. Fons, and J. Tominaga, "Raman scattering study of GeTe and Ge<sub>2</sub>Sb<sub>2</sub>Te<sub>5</sub> phase-change materials," *Journal of Physics and Chemistry of Solids*, vol. 68, pp. 1074-1078, 2007.
- [133] R. Mazzarello, S. Caravati, S. Angioletti-Uberti, M. Bernasconi, and M. Parrinello, "Signature of tetrahedral Ge in the Raman spectrum of amorphous phase-change materials," *Physical Review Letters*, vol. 104, p. 085503, 2010.
- [134] P. Boolchand, "Insulating And Semiconducting Glasses," in *Series on Directions in Condensed Matter Physics*. vol. 17, P. Boolchand, Ed., ed: World Scientific, 2000.
- [135] T. S. Kavetskiy, O. I. Shpotyuk, A. P. Kovalskiy, and V. M. Tsmots, "Structural-chemical approach for compositional dependences of gamma-induced optical effects in chalcogenide glasses of Ge-Sb-S system," *Journal of Optoelectronics and Advanced Materials*, vol. 7, pp. 2299-2308, 2005.
- [136] T. Edwards and S. Sen, "Structure and relaxation in germanium selenide glasses and supercooled liquids: a Raman spectroscopic study," *The Journal of Physical Chemistry B*, vol. 115, pp. 4307-4314, 2011.
- [137] P. J3v3ari, A. Piarristeguy, R. Escalier, I. Kaban, J. Bednar3ik, and A. Pradel, "Short range order and stability of amorphous Ge<sub>x</sub>Te<sub>100-x</sub> alloys (12 ≤ x ≤ 44.6)," *Journal of Physics: Condensed Matter*, vol. 25, p. 195401, 2013.
- [138] A. V. Kolobov, P. Fons, and J. Tominaga, "p-Type conductivity of GeTe: The role of lone-pair electrons," *physica status solidi (b)*, vol. 249, pp. 1902-1906, 2012.
- [139] E. I. Kamitsos, J. A. Kapoutsis, G. D. Chryssikos, G. Taillades, A. Pradel, and M. Ribes, "Structure and Optical Conductivity of Silver Thiogermanate Glasses," *Journal of Solid State Chemistry*, vol. 112, pp. 255-261, 1994.
- [140] C. A. Angell, K. L. Ngai, G. B. McKenna, P. F. McMillan, and S. W. Martin, "Relaxation in glassforming liquids and amorphous solids," *Journal of Applied Physics*, vol. 88, pp. 3113-3157, 2000.
- [141] O. I. Shpotyuk, in, R. Fairman, and B. Ushkov, "Properties of Chalcogenide Glasses," in *Semiconducting chalcogenide glass / Robert Fairman; Boris Ushkov*, ed: Elsevier Acad. Press, 2004, pp. 215-255.
- [142] P. Scherrer, "G3ttinger Nachrichten Math," *Phys*, vol. 2, pp. 98-100, 1918.
- [143] P. Dandamudi, M. N. Kozicki, H. J. Barnaby, Y. Gonzalez-Velo, M. Mitkova, K. E. Holbert, M. Ailavajhala, and W. Yu, "Sensors Based on Radiation-Induced Diffusion of Silver in Germanium Selenide Glasses," *Nuclear Science, IEEE Transactions on*, vol. 60, pp. 4257-4264, 2013.
- [144] V. K. Kudoyarova, "The effect of DC electric field on Ag migration in glassy Ge<sub>2</sub>S<sub>3</sub>," *Journal of Non-Crystalline Solids*, vol. 90, pp. 593-596, 1987.
- [145] R. Coltman, C. Klabunde, D. McDonald, and J. Redman, "Reactor Damage in Pure Metals," *Journal of Applied Physics*, vol. 33, pp. 3509-3522, 1962.
- [146] G. P. Pells, "Radiation damage effects in alumina," *Journal of the American Ceramic Society*, vol. 77, pp. 368-377, 1994.

- [147] K. Srivastava and A. Vohra, "Complex impedance and dipolar behaviour of a silver-doped chalcogenide," *Philosophical Magazine B*, vol. 61, pp. 201-216, 1990.
- [148] S. O. Kasap, *Principles of electronic materials and devices*. Boston: McGraw-Hill, 2006.
- [149] A. Owens. (2012). *Compound semiconductor radiation detectors*. Available: <http://public.eblib.com/EBLPublic/PublicView.do?ptiID=893019>
- [150] K. S. Harshavardhan and M. Hegde, "Origin of anomalous photoinduced transformations in amorphous Ge-based chalcogenide thin films," *Physical review letters*, vol. 58, p. 567, 1987.
- [151] L. Tichý, A. Tříška, H. Ticha, and M. Frumar, "On the nature of bleaching of amorphous Ge<sub>30</sub>S<sub>70</sub> films," *Philosophical Magazine B*, vol. 54, pp. 219-230, 1986.
- [152] T. Kawaguchi and S. Maruno, "Photoinduced surface deposition of metallic silver in Ag-As-S glasses," *J. of Appl. Phys.*, vol. 77, pp. 628-634, 1995.
- [153] A. Owens, *Compound Semiconductor Radiation Detectors*: Taylor & Francis, 2012.
- [154] N. Tsoulfanidis, *Measurement and detection of radiation*: Taylor & Francis Group, 1995.
- [155] R. J. Baker, *CMOS: circuit design, layout, and simulation* vol. 18: Wiley-IEEE Press, 2011.
- [156] P. Adell, R. Schrimpf, H. Barnaby, R. Marec, C. Chatry, P. Calvel, C. Barillot, and O. Mion, "Analysis of single-event transients in analog circuits," *Nuclear Science, IEEE Transactions on*, vol. 47, pp. 2616-2623, 2000.
- [157] Y. Boulghassoul, P. Adell, J. Rowe, L. Massengill, R. Schrimpf, and A. Sternberg, "System-level design hardening based on worst-case ASET simulations," *Nuclear Science, IEEE Transactions on*, vol. 51, pp. 2787-2793, 2004.
- [158] S. Buchner, D. Wilson, K. Kang, D. Gill, J. Mazer, W. Raburn, A. Campbell, and A. Knudson, "Laser simulation of single event upsets," *Nuclear Science, IEEE Transactions on*, vol. 34, pp. 1227-1233, 1987.
- [159] S. P. Buchner and M. P. Baze, "Single-event transients in fast electronic circuits," in *IEEE NSREC Short Course*, 2001.
- [160] P. Dodd, F. Sexton, G. Hash, M. Shaneyfelt, B. Draper, A. Farino, and R. Flores, "Impact of technology trends on SEU in CMOS SRAMs," *Nuclear Science, IEEE Transactions on*, vol. 43, pp. 2797-2804, 1996.
- [161] P. E. Dodd and L. W. Massengill, "Basic mechanisms and modeling of single-event upset in digital microelectronics," *Nuclear Science, IEEE Transactions on*, vol. 50, pp. 583-602, 2003.
- [162] A. Johnston, G. Swift, T. Miyahira, and L. Edmonds, "A model for single-event transients in comparators," *Nuclear Science, IEEE Transactions on*, vol. 47, pp. 2624-2633, 2000.
- [163] L. Massengill, "SEU modeling and prediction techniques," in *IEEE NSREC Short Course*, 1993, pp. 1-93.
- [164] D. McMorro, W. T. Lotshaw, J. S. Melinger, S. Buchner, Y. Boulghassoul, L. W. Massengill, and R. L. Pease, "Three-dimensional mapping of single-event

- effects using two photon absorption," *Nuclear Science, IEEE Transactions on*, vol. 50, pp. 2199-2207, 2003.
- [165] R. L. Pease, A. Sternberg, L. Massengill, R. Schrimpf, S. Buchner, M. Savage, J. Titus, and T. Turflinger, "Critical charge for single-event transients (SETs) in bipolar linear circuits," *Nuclear Science, IEEE Transactions on*, vol. 48, pp. 1966-1972, 2001.
- [166] R. L. Pease, A. L. Sternberg, Y. Boulghassoul, L. W. Massengill, S. Buchner, D. McMorrow, D. S. Walsh, G. L. Hash, S. D. LaLumondiere, and S. C. Moss, "Comparison of SETs in bipolar linear circuits generated with an ion microbeam, laser light, and circuit simulation," *Nuclear Science, IEEE Transactions on*, vol. 49, pp. 3163-3170, 2002.
- [167] V. Pouget, D. Lewis, H. Lapuyade, R. Briand, P. Fouillat, L. Sarger, and M.-C. Calvet, "Validation of radiation hardened designs by pulsed laser testing and SPICE analysis," *Microelectronics Reliability*, vol. 39, pp. 931-935, 1999.
- [168] M. Savage, T. Turflinger, J. Titus, H. Barsun, A. Sternberg, Y. Boulghassoul, and L. Massengill, "Variations in SET pulse shapes in the LM124A and LM111," in *Radiation Effects Data Workshop, 2002 IEEE*, 2002, pp. 75-81.
- [169] M. Savage, T. Turflinger, J. Titus, R. Pease, and C. Poivey, "Characterization of SET response of the LM124A the LM111, and the LM6144," in *Radiation Effects Data Workshop, 2003. IEEE*, 2003, pp. 121-126.
- [170] A. L. Sternberg, L. Massengill, S. Buchner, R. Pease, Y. Boulghassoul, M. Savage, D. McMorrow, and R. Weller, "The role of parasitic elements in the single-event transient response of linear circuits," *Nuclear Science, IEEE Transactions on*, vol. 49, pp. 3115-3120, 2002.
- [171] P. Hovington, D. Drouin, and R. Gauvin, "CASINO: A new Monte Carlo code in C language for electron beam interaction—part I: Description of the program," *Scanning*, vol. 19, pp. 1-14, 1997.
- [172] M. Baklanov and K. Mogilnikov, "Non-destructive characterisation of porous low-k dielectric films," *Microelectronic Engineering*, vol. 64, pp. 335-349, 2002.
- [173] W. Shen, J. Ren, G. Chen, S. Baccaro, A. Cemmi, I. D. Sarcina, M. Falconieri, and F. Menchini, "Controllable gamma-ray sensitivity of Ag-doped and/or AgI-modified Ge–Ga–S glasses," *Nuclear Instruments and Methods in Physics Research Section B: Beam Interactions with Materials and Atoms*, vol. 280, pp. 36-38, 2012.